Universidad de Oviedo

PROGRAMA DE DOCTORADO EN INGENIERÍA ENERGÉTICA

DOCTORAL THESIS

Numerical Analysis of the Damping-Controlled Fluidelastic Instability of Tube Arrays Subject to Cross-Flow

Beatriz de Pedro Palomar

Supervisors: *Jorge Parrondo Gayo*
Jesús Fernández Oro

A thesis submitted in fulfillment of the requirements for the degree of Doctor

Department of Energy
Polytechnic School of Engineering of Gijón

June 2016

RESUMEN DEL CONTENIDO DE TESIS DOCTORAL

1.- Título de la Tesis	
Español: "Análisis numérico de la excitación de vibraciones por inestabilidad fluidoelástica en tubos de intercambiadores de calor bajo flujo cruzado"	Inglés: "Numerical Analysis of the Damping-Controlled Fluidelastic Instability of Tube Arrays Subject to Cross-Flow"

2.- Autor	
Nombre: BEATRIZ DE PEDRO PALOMAR	
Programa de Doctorado: Ingeniería Energética	
Órgano responsable: Comisión Académica del Programa de Doctorado en Ingeniería Energética	

RESUMEN

Los haces de tubos sometidos a flujo cruzado (como los de intercambiadores de calor de carcasa y tubos), pueden desarrollar vibraciones de gran amplitud, capaces de provocar roturas rápidamente, por el fenómeno llamado inestabilidad fluidoelástica (FEI). La FEI engloba las vibraciones auto-excitadas debidas a dos mecanismos: uno controlado por amortiguamiento, que solo requiere un grado de libertad (o sea, un solo tubo vibrando), y otro controlado por rigidez, que requiere de varios tubos con vibración acoplada. La FEI ha sido muy estudiada experimentalmente en el pasado para medir valores críticos de velocidad que garanticen operación estable, pero los datos recogidos para cada configuración muestran mucha dispersión. Esto se atribuye al gran número de factores que afectan al fenómeno: la relación de paso P/d, el número de filas y columnas en el haz, los grados de libertad de los tubos, la exactitud de posicionado de los tubos, la intensidad de turbulencia o el solapamiento con otros mecanismos de excitación. También se han propuesto varios modelos teóricos simples que, en general, capturan parte de los procesos subyacentes en la FEI, pero sus hipótesis simplificadoras y su necesidad de datos empíricos limitan su efectividad como herramientas predictivas.

Como alternativa, los modelos de Fluido-Dinámica Computacional (CFD) ofrecen gran potencial para obtener predicciones más fiables e, incluso, para simular la respuesta dinámica del sistema flujo-estructura cuando opera en régimen inestable, con términos no lineales dominantes. Esto es clave para explorar posibles aplicaciones de la FEI, como en la conversión de energía hidrocinética. Por ello como objetivo de esta tesis se planteó el desarrollo de una metodología numérica CFD consistente y validada para simular la generación de vibraciones por FEI, a fin de aplicar esa metodología como instrumento de análisis del fenómeno. En concreto, el estudio se centró en la FEI controlada por amortiguamiento (haces con un solo tubo flexible) pues este caso permite caracterizar más fácilmente la relación entre el movimiento del tubo y las perturbaciones inducidas en el flujo, aspecto que se considera clave en el mecanismo de excitación.

La metodología CFD propuesta incluye movimiento estructural y mallado dinámico a fin de incorporar tubos en vibración. En el estudio, se modelaron varias geometrías triangular normal y

paralela con distintos valores de P/d, simulándose el flujo no estacionario (URANS 2D) con el software Fluent complementado con código propio externo (UDF). Los parámetros del modelo (finura de malla, condiciones de contorno, modelo de turbulencia, paso temporal, etc) se ajustaron tras análisis de sensibilidad y contraste con medidas en condiciones estáticas (Mahon-Meskell 2009).

Esta metodología CFD se aplicó sucesivamente sobre varias configuraciones dinámicas con datos experimentales disponibles, cada una relacionada con distintos niveles de cálculo:
a) Fluctuaciones de presión con tubo en vibración forzada (medidas hechas por la autora tras diseñar y construir un banco experimental específico).
b) Retraso temporal de la fuerza de sustentación sobre tubo en vibración forzada (medidas de Mahon-Meskell 2013).
c) Fluctuaciones de la velocidad con tubo oscilando por FEI (medidas de Khalifa et al. 2013).
d) Velocidades críticas para FEI en haces triangulares normales (medidas de Austermann-Popp 1995).

En general las predicciones obtenidas con los modelos numéricos desarrollados son satisfactorias, y su análisis lleva a nuevas conclusiones sobre el retraso entre fuerza de sustentación y movimiento del tubo, la localización de las fuentes de perturbación asociadas a la oscilación de cilindros, la velocidad de propagación de perturbaciones y la propia velocidad crítica de inestabilidad. La metodología desarrollada también se empleó para explorar el efecto sobre la FEI del número de Reynolds, la relación de paso y los grados de libertad (uno o dos) del cilindro vibrante.

SUMMARY

Tube arrays subject to cross-flow such as in shell-and-tube heat ex-changers may undergo large amplitude vibrations —capable of producing structural damage in short operating time— due to the phenomenon known as fluidelastic instability (FEI). FEI is a type of self-excited vibration that can be triggered by either a fluid-damping-controlled mechanism, which only requires one degree of freedom (i.e. one vibrating tube), or a fluid-stiffness-controlled mechanism, which requires several tubes with coupled motion. In the past FEI has been widely studied experimentally in order to measure critical flow velocities below which the operation is stable. However, the data collected for each configuration usually show notorious scatter, due to the variety of factors that can affect the phenomenon: pitch ratio, number of rows and columns in the array, degrees of freedom, accuracy of tube position in the array, Reynolds number, turbulence intensity and presence of other excitation mechanisms. Besides, several simplified theoretical models have been proposed that, in general, capture some of the essential features of the FEI phenomenon up to some extent, but their flow assumptions and the need for empirical data limit their effectiveness as prediction tools.

Alternatively, computational fluid-dynamic models (CFD) offer high potential for more reliable predictions, including the possibility of simulating the dynamic response of the flow-structure system even when operating at unstable regimes, for which the non-linear terms are dominant. This is key to explore new situations involving FEI, such as in the area of fluid kinetic energy conversion. Therefore, the prime purpose of this thesis was the development of a well validated CFD methodology to simulate the generation of vibrations due to FEI, in order to apply it as a

consistent tool for the analysis of the phenomenon. In particular the study focused in the case of damping-controlled FEI in arrays with only one single flexible tube, because it is very convenient to correlate the tube motion and the associated flow fluctuations, and this relationship is recognized as a key issue in FEI excitation.

A CFD methodology involving structure motion and dynamic re-meshing has been put into practice to simulate the unsteady flow across tube arrays with normal and parallel triangular geometries, each with several pitch ratios. URANS 2D computations were performed with the Fluent code complemented with User Defined Functions to account for the flexible tube motion. Appropriate model parameters regarding mesh refinement, boundary conditions, turbulence model and time step were selected after sensitivity analysis and comparison to experimental data under static conditions (Mahon-Meskell 2009).

This CFD methodology was contrasted by comparing predictions to several sets of experimental data, each related to a different level of calculation:
a) Pressure fluctuations with one tube under forced vibration (exp. data by the author after designing and setting up a specific test rig).
b) Time lag of lift force on a tube under forced vibration (exp. data by Mahon-Meskell 2013).
c) Velocity fluctuations in the cross-flow with one tube under FEI (exp. data by Khalifa et al. 2013).
d) Critical velocity for FEI in normal triangular arrays (exp. data by Austermann-Popp 1995).

In general the predictions obtained with the numerical models developed are satisfactory. Besides, the results obtained represent a significant contribution of data on the retardation parameter between lift force and tube motion, on the location of the perturbation sources associated to the oscillation of cylinders, on the speed of disturbance propagation along the stream and, indeed, on the critical threshold for the onset of the instability. Finally, the numerical methodology was used to explore the effect on the critical velocity for FEI of the Reynolds number, the pitch ratio and the degrees of freedom of the vibrating cylinder.

Abstract

Cylinder arrays subject to cross-flow, such as in shell-and-tube heat ex-changers, may undergo flow induced vibrations due to a number of different excitation mechanisms. The highest potential for large amplitude vibrations —capable of unacceptable structural damage in short operating time— corresponds to the phenomenon known as fluidelastic instability (FEI), which denotes a type of self-excited vibrations. FEI vibrations can be triggered by either a fluid-damping controlled mechanism, which only requires one degree of freedom (i.e. one flexible tube capable of vibrating in one direction), or a fluid-stiffness controlled mechanism, which requires the coupled motion of several tubes. FEI has been largely studied experimentally in the past, with the main purpose of establishing critical flow velocities as the limiting conditions that ensure stability for heat exchangers and other related equipment. However, the data collected of critical velocity for each main geometrical configuration usually show significant scatter. This is attributed to the wide variety of factors with potential to influence the phenomenon, including pitch ratio (P/d), number of rows and columns in the array, degrees of freedom, accuracy of cylinder position in the array, details of structural parameters of each cylinder in the array, Reynolds number, turbulence intensity and presence of other excitation mechanisms.

Additionally, several theoretical models have been proposed based on different simplifying assumptions, such the so-called quasi-steady model by Price and Paidoussis (1984), quasi-unsteady model by Granger and Paidoussis (1996) or the flow inertia model by Lever and Weaver (1986). In general these models capture the essential features of the FEI phenomena up to some extent, but their flow simplifications and the need for empirical data limit their effectiveness as prediction tools. Indeed, the best potential for the detailed description of the flow without empirical data corresponds to CFD models and that capability should allow for more reliable predictions of the critical velocity for FEI. Moreover, CFD offers the possibility of simulating the dynamic response of the flow-structure system even operating at unstable regimes, for which the non-linear terms are dominant. The latter is key to explore possible new situations involving FEI phenomena, such as in the area of fluid kinetic energy conversion.

In line with some other recent investigations, this thesis presents a CFD study on the fluid-dynamic vibrations due to FEI in tube arrays subject to cross-flow. Two main objectives were considered for this research:
i) The establishment of a consistent and well-validated numerical methodology to simulate this type of fluid-structure interaction.
ii) The use of that numerical tool to deepen our current understanding of the FEI phenomenon. In particular the study was focused in the case of damping-controlled FEI in arrays with only one single flexible tube, because it is very convenient to analyze the correlation between tube motion and the associated flow fluctuations. Indeed, this is an important issue in FEI excitation because it is widely recognized that it depends strongly on how the disturbances induced by the oscillating cylinder are transmitted through the cross-flow.

A CFD methodology involving structure motion and dynamic re-meshing has been put into practice to simulate the flow across arrays of cylinders including cylinder vibration. The configurations considered have been the normal triangular and the parallel triangular geometries, each with several pitch-to-diameter ratios. URANS 2D computations were performed with the commercial code Fluent 12.1 complemented with User Defined Functions to account for the flexible tube motion, which was always located at the third row. Appropriate model parameters regarding mesh refinement, boundary conditions, turbulence model and time step were selected by comparing calculations to experimental data under static conditions (Mahon and Meskell, 2009) as well as to ensure minimum influence on predictions. In particular, large-scale disturbances downstream the array were avoided by using parallel guide plates instead of truncating the computation domain at the last row like in other precedent models.

This CFD methodology was contrasted by comparing predictions to several sets of experimental data, each related to a different level of calculation. These sets of data included:
i) Pressure fluctuations on the surface of the static cylinders of a parallel triangular array with P/d=1.57 and one cylinder under transverse forced vibration. This test series was conducted by the author after designing and building a specific laboratory set-up.
ii) Time lag of lift coefficient under transverse forced vibrations for a normal triangular array with P/d=1.32. These data were obtained by Mahon and Meskell (2009).
iii) Velocity fluctuations along the streamtubes though a parallel triangular array with P/d=1.54 with one oscillating tube under FEI. These data were obtained by Khalifa et.al.(2013). iv) Critical velocity for 1 degree-of-freedom FEI in normal triangular arrays with P/d=1.25 and P/d=1.375 over a range of the mass-damping parameter. These

data were obtained by Austermann and Popp (1995).

In general the predictions obtained with the numerical models developed can be considered satisfactory. Besides, the results obtained represent a significant contribution of data on the retardation parameter between lift force and tube motion, on the location of the perturbation sources associated to the oscillation of cylinders, on the speed of disturbance propagation along the stream and, indeed, on the critical threshold for the onset of the instability. Finally, the numerical methodology was used to explore the effect of different parameters of the system on the critical velocity for FEI, including the Reynolds number, the pitch-to-diameter ratio and the degrees of freedom of the vibrating cylinder.

Resumen

Un haz de cilindros sometido a flujo cruzado (como un cambiador de calor de carcasa y tubos), en ciertas condiciones, puede desarrollar vibraciones flujo-inducidas debido a distintos mecanismos de excitación.
El mecanismo con mayor potencial para desarrollar vibraciones de gran amplitud – capaces de provocar, en un corto periodo de operación un daño inaceptable– es el fenómeno denominado como inestabilidad fluidoeslástica (FEI). La FEI es una forma de vibración auto-excitada dentro de la que se engloban dos mecanismos, uno controlado por el amortiguamiento, que solo requiere un grado de libertad (es decir, un solo tubo flexible vibrando en una dirección), y otro controlado por la rigidez que se produce cuando aparece un acoplamiento en la vibración entre varios tubos. El fenómeno de la FEI ha sido ampliamente estudiado experimentalmente, con el propósito de establecer un valor crítico de la velocidad que garantice condiciones de seguridad en la operación de los cambiadores de calor y otros equipos. Sin embargo, los datos experimentales de velocidad crítica recogidos para cada configuración geométrica particular muestran habitualmente una dispersión significativa. Esto puede atribuirse al gran número de factores que pueden potencialmente influir en el desarrollo del fenómeno, entre los que se encuentran entre otros el pitch (P/d), el número de filas y columnas en el haz, los grados de libertad, la exactitud con la que se haya localizado el tubo en la matriz del haz, la intensidad de turbulencia o el solapamiento con otros mecanismos de excitación.

Basándose en distintas simplificaciones se han propuesto varios modelos teóricos, como el denominado modelo “quasi-estacionario” de Price y Paidoussis, el modelo “quasi-no-estacionario” de Granger y Paidoussis o el modelo de hipótesis inercial para el flujo de Leaver y Weaver. En general estos modelos son capaces de capturar los procesos involucrados en el fenómeno de FEI hasta cierto punto, pero las hipótesis simplificadoras que aplican al flujo, así como la necesidad de datos empíricos, limitan su efectividad en la práctica como herramientas predictivas. Por otra parte, los modelos con mayor capacidad para caracterizar detalladamente el flujo, sin la necesidad de ningún dato de entrada empírico, serían los modelos de Fluido Dinámica Computacional (CFD), cuyo potencial podría hacer posible predicciones más realistas de la velocidad critica para la FEI. Además, los modelos CFD actuales posibilitan la simulación de la respuesta dinámica del sistema flujo-estructura, incluso cuando éste opera en régimen inestable, pare el que los términos no lineales son dominantes.

Dichos términos no lineales son claves de cara a la investigación de nuevos posibles escenarios relaccionados con la FEI, por ejemplo en el ámbito de la generación energética por aprovechamiento de la energía cinética.

En la misma línea que algunos otros grupos investigadores recientes, esta tesis plantea un estudio CFD acerca de las vibraciones fluido-dinámicas debidas a la FEI en tubos sometidos a flujo cruzado. En esta investigación los objetivos principales considerados fueron dos:
i) El establecimiento y de una metodología numérica consistente y sólidamente validada para la simulación de este mecanismo de interacción flujo-estructura.
ii) El uso de la metodología numérica desarrollada como herramienta para la profundización en el conocimiento actual del fenómeno de FEI.
Particularmente, el presente estudio se centró en el caso de FEI controlada por el amortiguamiento, con haces de un solo tubo flexible, ya que este escenario permite una identificación muy clara de la relación entre el movimiento del tubo y las perturbaciones del flujo asociadas. Como está ampliamente reconocido, la manera en la que estas perturbaciones inducidas por el tubo vibrante se propagan en el flujo es de hecho clave en la FEI.

Se ha desarrollado una metodología CFD, incluyendo movimiento estructural y mallado dinámico, de cara a simular el flujo cruzado a través de un haz de cilindros, considerando con esta metodología la vibración del propio cilindro.
Se consideraron las configuraciones triangular normal y paralela, cada una para un rango de relaciones paso dinámetro (P/d). Las simulaciones (U RANS 2D) se realizaron con el software Fluent 12.1 al que se le incorporo un código externo (user defined function, udf) que calcula el movimiento del tubo flexible, siempre localizado en la tercera línea.

El ajuste de los parámetros del modelo, en lo referente a: refinado de la malla, condiciones de contorno, modelo de turbulencia y paso temporal, se realizó tanto por comparación con datos experimentales (Mahon y Meskell, 2009) como por evaluación paramétrica de los resultados obtenidos, con el objetivo de minimizar su influencia en las predicciones numéricas.
En particular, las perturbaciones de gran escala aguas abajo del haz fueron controladas empleando placas guía paralelas tras la última fila de tubos en lugar de truncar el dominio computacional aguas debajo de estos como se proponía en modelos precedentes.

La presente metodología CFD fue contrastada por comparación de las predicciones con varios conjuntos de datos experimentales, cada uno relacionado con distintos niveles de cálculo. Dichos conjuntos de medidas incluyeron:

i) Fluctuaciones de presión en la superficie de ciertos tubos estáticos de un haz triangular paralelo con P/d=1.57 y en el que un cilindro estaba sometido a vibración forzada. Este conjunto de medidas fueron realizadas por la autora tras el diseño y construcción de un montaje experimental específico.

ii) Retraso temporal del coeficiente de sustentación en vibración forzada para un haz triangular normal con P/d=1.32. Estos datos fueron obtenidos por Mahon y Meskell (2013).

iii) Fluctuaciones de la velocidad a lo largo de tubos de corriente a través de un haz triangular paralelo con P/d=1.54 con un tubo oscilando en inestabilidad fluido elástica (FEI). Estos datos fueron obtenidos por Khalifa et al. (2013).

iv) Velocidad crítica para FEI con un grado de libertad en haces triangulares normales con P/d=1.25 y P/d=1.375 a lo largo de un rango de parámetros de masa amortiguamiento. Estos datos fueron obtenidos por Austermann y Popp (1995).

En general las predicciones obtenidas con los modelos numéricos desarrollados pueden considerarse satisfactorias. Además, los resultados obtenidos representan una contribución significativa a los datos existentes en cuanto al parámetro de retraso entre la fuerza de sustentación y el movimiento del tubo, a la localización de las fuentes de perturbación asociadas a la oscilación de cilindros, a la velocidad crítica para el desarrollo de la inestabilidad. Finalmente, la metodología numérica se empleó para explorar el efecto de diferentes parámetros del sistema en la velocidad crítica para la FEI, incluyendo el número de Reynolds, el ratio pitch-diámetro y los grados de libertad del cilindro vibrante.

Acknowledgements

First, I would like to thank my supervisors, Dr. Jorge Parrondo and Dr. Jesús Fernández Oro, who I am greatly indebted to. Thank you for believe in me since the beginning of this work, for your continuous support and encouragement, for patiently teaching and guiding me through these years and for your boundless help and time. Thank you for the tons of knowledge, smart ideas and wise advises you gave me away. I could never have done any of this without you. It was really an honor working with both.

I would also like to express my deep gratitude to Dr. Craig Meskell, for receiving me in his research group of Trinity College Dublin and sharing his wide and extremely valuable experience on the subject of this thesis with me. Thank you for your very powerful insights and advices, they were a priceless inspiration in this work. It was a great pleasure to meet you.

Thanks to Dr. Eduardo Blanco for his always very wise advises both for the numerical model and for the design and construction of the experimental setup used in this thesis. Thanks also to Dr. Carlos Suárez, from the Fabrication Department, for his essential help with the machining of the crucial tube section of the bank.

Thank you to the external supervisors: Dr. José Antunes, Dr. Sergio Lavagnoli, Dr. Tomomichi Nakamura and Dr. Guillaume Riccardi, for dedicating some of their time and widely recognized knowledge to reviewing this thesis. Their very interesting and experienced comments had certainly improved the quality of the present study.

Many thanks to the professors and colleges of the Fluid Mechanics Area that provided me with invaluable and selfless advices on both my research and my future career plans.

Finally, I would like to dedicate this work to my family, to my mother Pilar who had believed in me all the days of my life, to my husband Rodo for his neverending encouragement and love, and to my beloved little daughter Nuria.

Contents

List of Figures

List of Tables

Nomenclature

C_D	Drag coefficient
C_L	Lift coefficient
C_P	Mean pressure coefficient
d	Tube diameter
f	Frequency (Hz)
F_D	Drag force
F_L	Lift force
F_y	Fluidelastic force
FEI	Fluidelastic instability
l	Tube length
m	Tube mass
$m_r\delta$	Mass damping parameter ($= m\delta/\rho d^2$)
P	Pitch
P/d	Pitch ratio
P_θ	Mean pressure at a given position angle
P_o	Mean pressure at stagnation point
Re	Reynolds number

To Rodo and Nuria.

Chapter 1

Introduction

1.1 Flow-induced vibrations in tube arrays

As the global demand for energy is constantly increasing and the fossil fuel supply is limited, alternative energy resources, including wind, solar or nuclear energies, are becoming more important.

In the nuclear industry, large shell-and-tube heat exchangers and steam generators, are essential equipments for the energy conversion, which performance is crucial to maximize the efficiency. These elements are frequently composed of cylinder arrays subjected to cross-flow which, at certain conditions, are susceptible for the arising of Flow-Induced Vibration (FIV) of high amplitude and the subsequent possibility of structural damage [4], [5]. FIV can be a major problem in these large heat exchangers, including short term failures , and leading to a limitation for the performance of the device and also in the overall power output of the nuclear plant. Figs 1.1 and 1.2, show typical configuration of the reactor and the steam generators in a nuclear plant, where large tube bundles are illustrated. Although support plates are installed to limit these vibrations, finite gaps between the tubes and their supports must be introduced due to functionality constraints. As a consequence, large amplitude tube vibrations with large amplitude may still occur leading to early failures by impact and fretting wear at the supports as shown in Figs. 1.3(a), 1.3 (b), 1.3 (c), by thinning due to mid-span collision as observed in Fig. 1.3(d), or fatigue caused due to high bending stressess. Moreover, four main excitation mechanisms are identified in most of the situations with flow-induced vibrations [6]: Turbulent Buffeting, Vortex Shedding, Acoustic Resonance, and Fluidelastic Instability.

The most destructive form of these vibrations is uidelastic instability (FEI), which is characterized by an abrupt and dramatic increase in the vibration amplitude when the cross-ow velocity exceeds a certain critical value. This detrimental phenomenon can

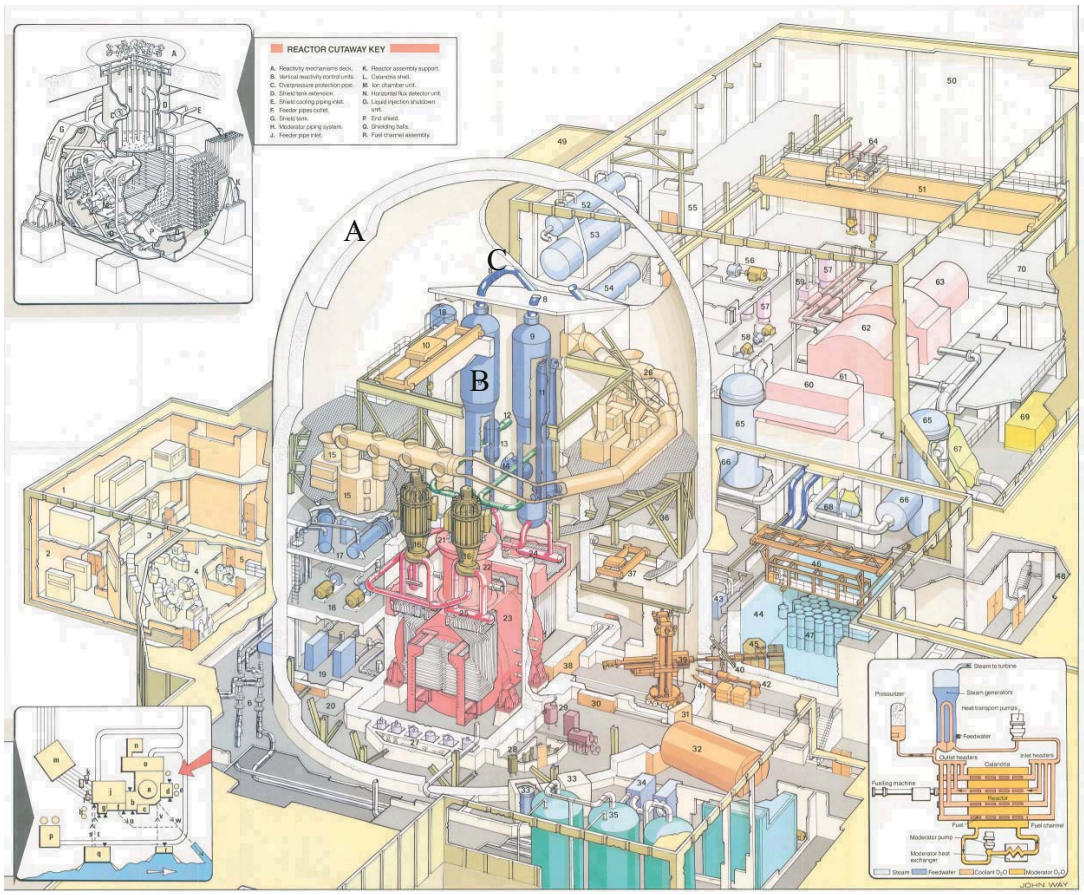

FIGURE 1.1: Typical configuration of a CANDU reactor.

cause in just few hours the same damage that the other three mechanisms can produce in several years of service. FEI has been largely studied experimentally in the past, with the main purpose of establishing critical flow velocities as the limiting conditions that ensure stability. However, the data collected on critical velocity for each main geometrical configuration usually show significant scatter. This is attributed to the variety of factors that have influence on the phenomenon, such as the number of lines and rows, degrees of freedom, accuracy of tube position in the array, details of structural parameters of each tube in the array, Reynolds number, turbulence intensity and even the presence of other excitation mechanisms, as the FEI phenomenon, can be triggered by either a fluid damping or a fluid stiffness controlled mechanism [7], [8].

1.2 Scope of the work

In addition to a large number of experimental studies, several theoretical models have been proposed over recent times to predict stability thresholds regarding FEI conditions.

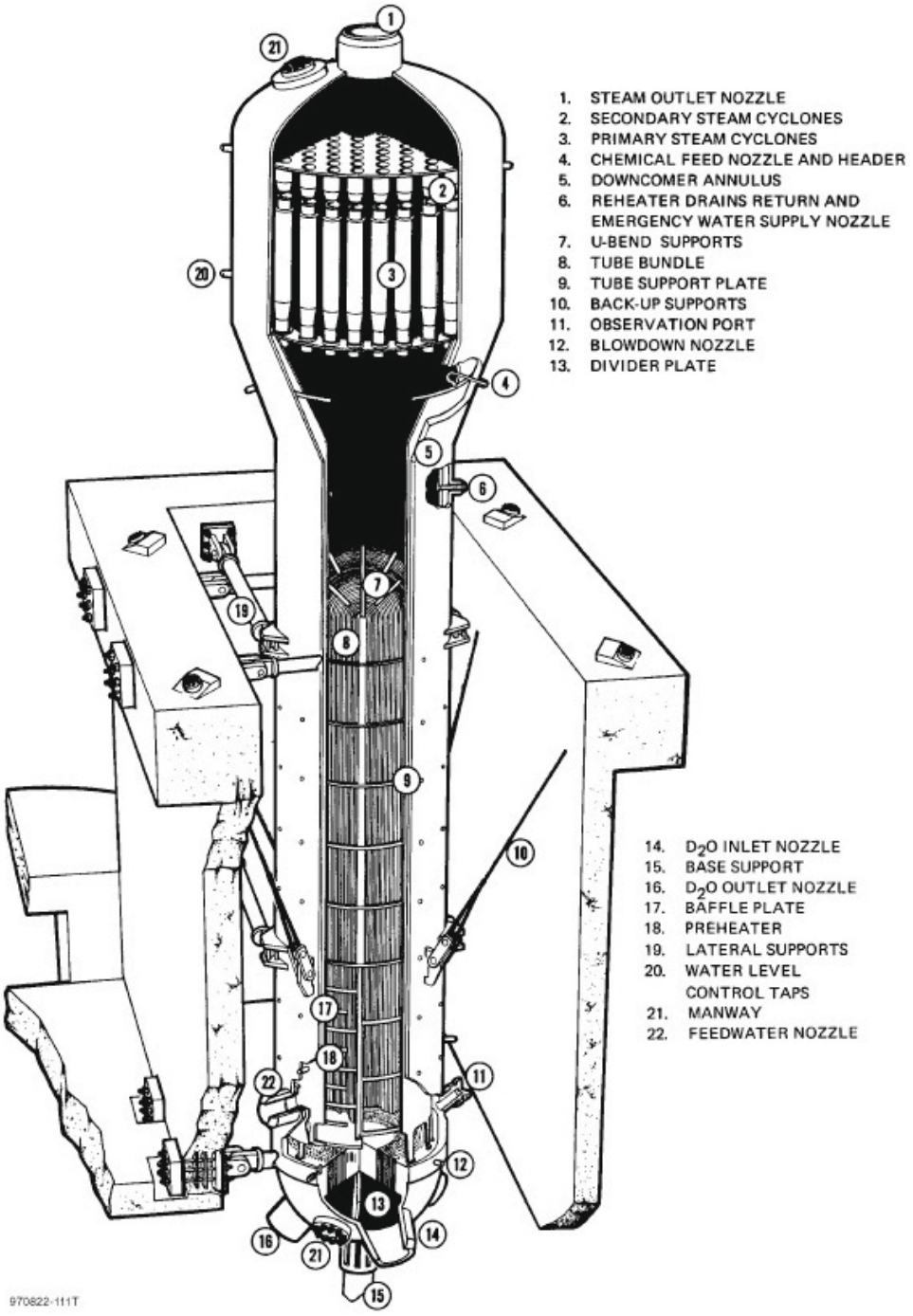

FIGURE 1.2: Typical configuration of a steam generator.

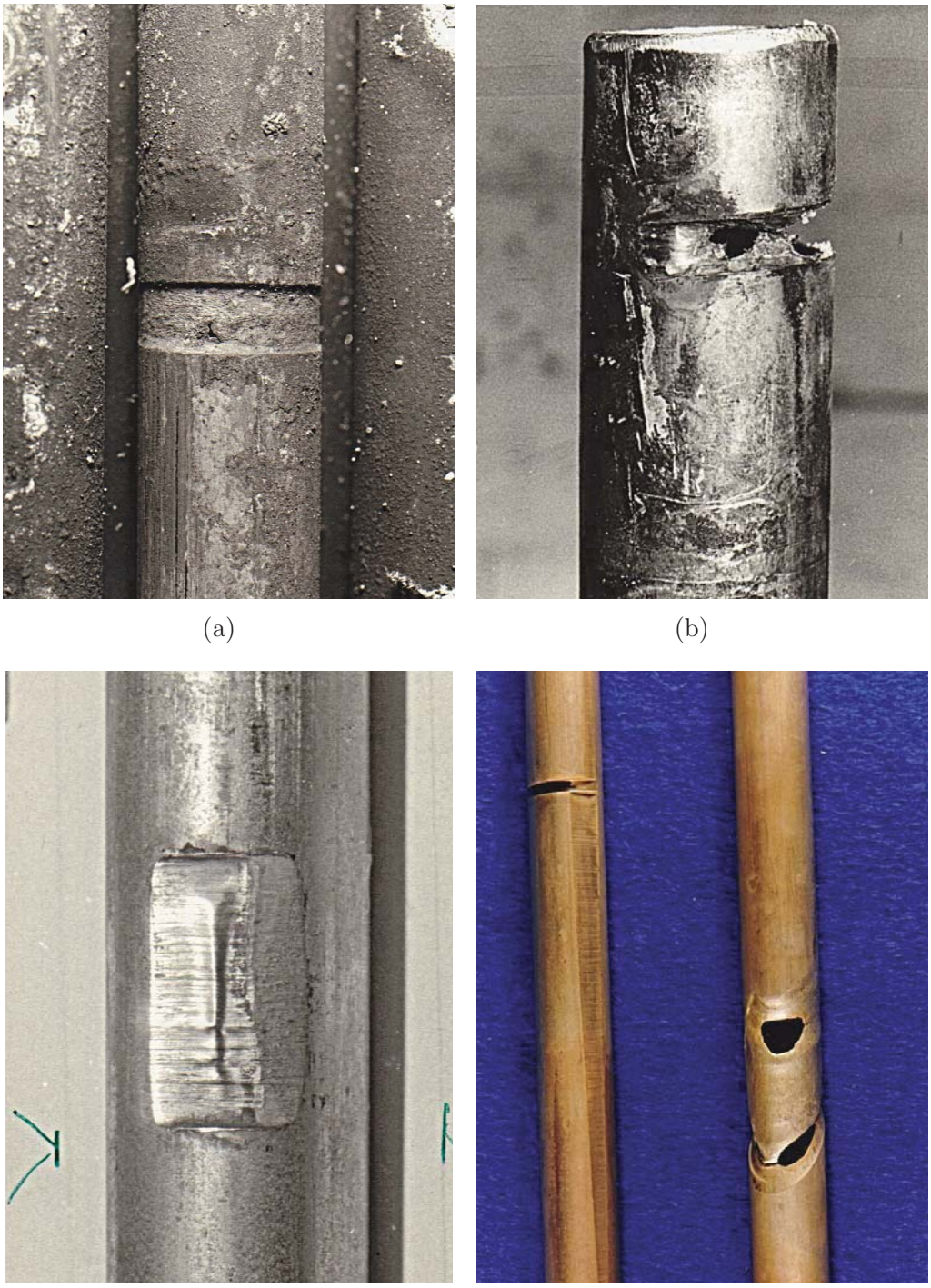

(a) (b)

(c) (d)

FIGURE 1.3: Samples of steam generator tube failures due to flow-induced vibrations. (a), (b), and (c) show the effect of fretting wear at the support (AECL). (d) Left tube shows both fretting wear at support and tube-to-tube clashing while right tube shows damage caused by a broken piece of a tube that hit other tubes in its path (UKAEA Harwell).

Despite of the different flow assumptions and simplifications involved, their predictions have provided reasonable accuracy at least for specific system configurations [9]. For instance, the so-called quasi-steady models [10] and quasi-unsteady models [11] assume that the fluid-dynamic forces on the tubes can be obtained by performing static flow calculations with a cylinder slightly shifted from equilibrium and then introducing a phase lag term on the resulting static forces. Lever and Weaver [12] proposed a semi-analitical model in which it is considered that the motion of the cylinder is considered to cause a redistribution of the streamtube area that is in phase with the tube position for the attached flow. But, due to the flow inertia, this area is lagging behind the cylinder motion in the detached flow (both upstream and downstream), causing a phase lag between the tube motion and the fluid pressure distribution on the cylinder. Eventually, it is this phase lag the responsible to produce motion-dependent fluid forces on the tubes that do not oppose their oscillation but reinforce it.

However, the models with best capability for a detailed description of the flow features are those based on CFD calculations. In fact, they should allow for more reliable predictions of the critical velocity for FEI situations. Several authors have explored the possibility of coupling CFD prediction and theoretical models to estimate critical velocities in the recent years. Hassan et. al.[13] investigated pitch-to-diameter ratio and Reynolds number effects on critical velocity for in-line tube arrays, obtaining coefficients for a theoretical unsteady model from the numerical simulations. Khalifa et. al. [14] investigated the interaction between tube vibrations and flow perturbations at lower reduced velocities and Reynolds numbers, coupling numerical predictions of the phase lag with the semi-analytical model of Lever and Weaver [12] to estimate the reduced critical velocity. Anderson et. al. [15] developed a model to account for temporal variations in the flow separation for in-line arrays. In this case, numerical simulations in the separation zone were coupled with a structural model and a far-field flow model, to obtain the stability threshold.

Furthermore, CFD offers the possibility of simulating the dynamic response of the flow-structure system even operating at unstable regimes, for which the non-linear terms are dominant. The latter is key to explore possible new applications involving FEI phenomena, for instance in the area of fluid kinetic energy conversion.

Under that perspective, this thesis presents an investigation on fluidelastic instability, with a CFD methodology complemented with experimental tests for validating purposes. The proposed CFD methodology allows the simulation of the fluid-dynamic vibrations of one or more flexible tubes oscillating either in the transverse direction only or with two degrees of freedom. Numerical methodology was compared with 6 different experimental data sets, including measurements obtained in the laboratory facility developed for this work. Main focus has been placed in the retrievement of those parameters that are considered for the onset of fluidelastic instability in the literature.

The case of one single flexible tube oscillating in the transverse direction has been widely analyzed in this study. Such case is convenient to study the correlation between the tube motion and the associated flow fluctuations because FEI vibrations can only be developed due to the damping mechanism in this particular situation [7], [8]. Differences in behavior of the coupled system, regarding flow pattern, tubes trajectories, net damping and instability thresholds obtained with one or more flexible tubes in different relative positions are also discussed along the study. The validated numerical methodology was finally used to discuss the flow patterns through the different array geometries and to explore the effect on the critical velocity of several parameters as the Reynolds number, the mass ratio, the pitch ratio or the number of degrees of freedom in the vibrating tube motion.

1.3 Objectives

This thesis is focused on the analysis of those conditions resposible for the onset of Fluidelastic Instability, a self-excited mechanism that can cause short term tube failure in steam generators. Although, there has been a large amount of research conducted in this field over the past five decades, there is still no consensus on the basic mechanisms of FEI, or even a well-accepted agreement upon the existence of a comprehensive model for its prediction. While there are several sophisticated FEI models available in the literature, the ASME design guidelines for heat exchangers are still based on an empirical relationship developed by Connors' in 1970 [16]. Although this engineering standards may seem conservative, the nuclear power industry has been facing failures due to fluidelastic instability in steam generators designed according to this ASME criteria, as noted by Paidoussis (2006) [17] and Weaver (2008) [18]. In fact, Paidoussis (2006) [17] estimated that the use of this relationship for the design of heat exchangers has resulted in damages worth US$1 billion. Moreover, this design patterns don't provide any physical insights to the problem, and the exact physical nature of this phenomenon remains unknown.

The purpose of the research reported in this thesis is to develop a better understanding of the fluidelastic instability phenomenon in tube bundle heat exchangers in order to achieve more reliable predictions of critical velocity. To provide these new insights, both numerical and experimental studies were undertaken investigating some of the key details in the theoretical models, like the propagation of perturbations in the stream tube [12] and also the time delay between the tube vibrations and the fluid response. The latter is considered to be an important aspect of the instability mechanism by most of the theoretical models [10] [12] [11].

A major goal of this thesis is to propose a systematic, accurate and consistent CFD methodology , so successful simulations of tube arrays under fluidelastic instability conditions may be conducted. The proposed methodology will be compared with six different experimental data including new experimental results obtained specifically for the present work [19], [1], [2] and [3]. The validated numerical procedure will be used to improve the prediction of the onset of fluidelastic instability through verification of common hypothesis, analyzing the effect of different parameters effect in the stability threshold. Another objective has been placed in a detailed characterization the transmission of the perturbations through the tube bundle as defined by Lever and Weaver [12] and how it varies as a function of a reduced flow velocity U_r.This final objective will be achieved by using both numerical and experimental results of forced vibrations in which pressure and velocity fluctuations will be correlated with the tube motion.

1.4 Thesis structure

The thesis is divided into 7 chapters. After this first chapter regarding the introduction to the problem, forthcoming chapter 2 provides a comprehensive state-of-the-art of the research conducted on fluidelastic instability over the last decades. Following, chapter3 describes the numerical methodology proposed, including the calculation levels, the validation milestones for comparison with experimental data and the characteristics of the numerical model that are common to all the numerical routines. Chapter 4 contains the results obtained in static calculations, including the comparison of the pressure coefficient in the tube surface with the experimental data from Mahon and Meskell (2009) [19], as well as the estimation of stability thresholds obtained with the static CFD force coefficients and the quasi-unsteady theory [11] [20] against the critical velocities reported by Austermann and Popp (1995) [1] . This chapter also explores the effect of a number of typical parameters in the definition of the critical velocity. In chapter 5, the results obtained forcing the vibrations of the tube in the CFD computations are revealed. This level of calculation is validated against the experimental results for time delays coming from the work by Mahon and Meskell (2013) [2]. Finally, a discussion of the observed flow patterns for the different cylinder arrays is also included, introducing the comparison of the propagation velocity of flow perturbations with the results obtained by Khalifa et al. [3]. As the final approach, chapter 6 summarizes the results obtained for self-excited oscillations, including the experimental comparison with results given by Austermann and Popp (1995) [1] and also the analysis of the effect of introducing a second degree of freedom in the tube array. The behavior observed when another flexible tube is allowed to vibrate in different relative positions is also analyzed in terms of trajectory and net

damping. To conclude, chapter 7 provides a summary of this work and describes plans for future contributions.

Chapter 2

Background

2.1 Flow-induced vibrations

Steam generators and large heat exchangers are long, slender structures composed of bundles of tubes with thin walls to promote heat transfer. This makes them suspceptible for Flow-Induced Vibrations and, specially, for Fluidelastic Instability when operated under cross-flow conditions. Since Fluidelastic Instability is potentially the most destructive phenomenon [21], the determination of the critical velocity to assure stability represents a must in the design and regular operation of such equipments. Moreover, significant research effort has been dedicated over the last decades to understand and predict this detrimental limitation in a reliable way.

The analysis of Fluidelastic Instability in tube arrays has been reviewed in detail by many authors. In particular, the current state of knowledge, the existing models available for prediction or the establishment of appropiate design guidelines can be found in Chen (1982) [21], Paidoussis (1983) [22] and (1988)[23], Weaver and Fitzpatrick (1988) [24], Gelbe et al. (1995) [25], Price (1995) [9] and (2001) [26], Goyder (2002) [27], and Pettigrew and Taylor (2003a,b) [4] [5]. This chapter presents a complete literature survey of the excitation mechanisms and the theoretical models developed for fluidelastic instability in heat exchanger tube arrays.

2.1.1 Physical discussion

The physical variables involved in the fluidelastic instability problem were detailed in the non-dimesional analysis conducted by Blevins (1994) [6]. He established six basic

non-dimensional groups with n0, n1, n2, n3 and n4 as possible constant exponents:

$$\frac{U}{fd} \propto (\frac{m}{\rho d^2})^{n0} \delta^{n1} (\frac{P}{d})^{n2} (\frac{\rho U d}{\mu})^{n3} (\frac{'}{U})^{n4} \tag{2.1}$$

The left hand side of Relation 2.1 refers to the reduced velocity term (U/fd), which represents the relative magnitude of flow velocity with respect to the velocity. This term is used as an indicator of the stability threshold for fluidelastic instability. The mean gap velocity U_g is often used to represent the flow velocity in the array instead of the upstream flow velocity U_0. Equation 2.2 can be used to obtain the mean gap velocity based on the upstream flow velocity which is often more convenient to measure. This equation is based on continuity and represents the mean flow velocity in the minimum gap between the tubes, although it is strictly valid only for normal triangular and rotated square arrays. However, it is generally used as the mean interstitial flow velocity for all types of tube arrays.

$$U_g = \frac{P}{P-d} U_0 \tag{2.2}$$

The right hand side of Relation 2.1 includes all the contributing factors to determine the reduced velocity threshold. The first term on the right hand side refers to the mass ratio $m/\rho d^2$, which stands for the ratio between the mass of dynamic tube per unit length (which includes the added mass corresponding to the fluid) and the displaced mass of the surrounding fluid. In fact this term represents the tube/fluid inertia ratio. Heat exchangers operate over a wide range of mass ratios associated with various working fluids inside and outside the tubes.

The second term at the right hand side of Relation 2.1 refers to the logarithmic decrement δ, which is a measure of the amount of energy dissipated by the array per oscillation cycle.

The third term refers to the array pitch-ratio P/d , which is the ratio between the diameter of the tube and their spacings. This represents the compactness of the tube array, and it is frequently obviated by the predictions models when estimating the critical velocity. The array pitch angle (see Fig. 2.1) is an additional geometrical parameter, not included in the previous Relation 2.1 because it is typically neglected as a relevant contribution (see for instance the ASME design guidelines). Nevertheless, Weaver and Fitzpatrick (1988) [24] have shown that a classification of the available experimental data according to the array pitch angle allows a significant reduction in the amount of data scatter, as can be seen in Figs. 2.2 to 2.5 Those figures, corresponding to the configurations sketched in Fig. 2.1, provide typical maps with correlations to obtain the stability regions free of Fluidelastic Instability. Fig. 2.6 summarizes all the mathematical expressions for the design correlations derived from the maps.

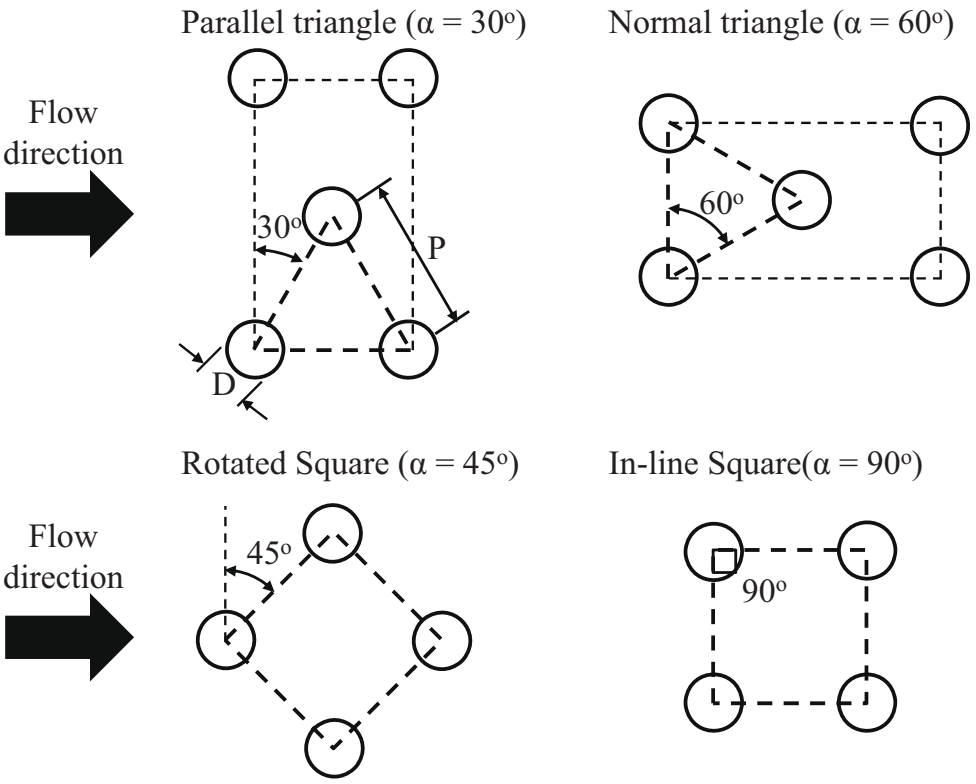

FIGURE 2.1: Common geometrical configurations of tube arrays.

The fourth term refers to the Reynolds number $= \rho U_g d/$ which represents the classical ratio between fluid inertia forces to fluid viscous forces. Most analysis ignore Reynolds number dependence because little evidence of its relevance has been observed in the past.

The last term is the turbulence intensity $'/U$, which is the ratio between the statistical variance of the flow velocity to the mean velocity. It causes random small vibration of the tubes, typically known as turbulent buffeting. However the exact effect of the turbulence level in FEI, Polak and Weaver (1995) [28] found that the turbulence generated by the tube bundle itself overwhelms the upstream turbulence from the fourth or fifth row. Similarly, Rzentkowski and Lever (1998) [29] have found that the fluidelastic instability is virtually unaffected by the turbulence level. On the other hand, Rottmann and Popp (2003) [30] have found that the threshold for FEI is reduced when the turbulence levels are increased. Finally, another phenomenon not included in the dimensional analysis is vortex shedding. Under certain conditions (particular flows and geometries) if there is coincidence between vortex shedding and fluidelastic instability frequencies, resonance phenomena could appear. The Strouhal number , as expressed in Equation 2.3, where f_v is the vortex shedding frequency, characterize the frequency of vortex shedding from

a particular tube array the tube at a given flow velocity.

$$_t = \frac{f_v d}{U} \tag{2.3}$$

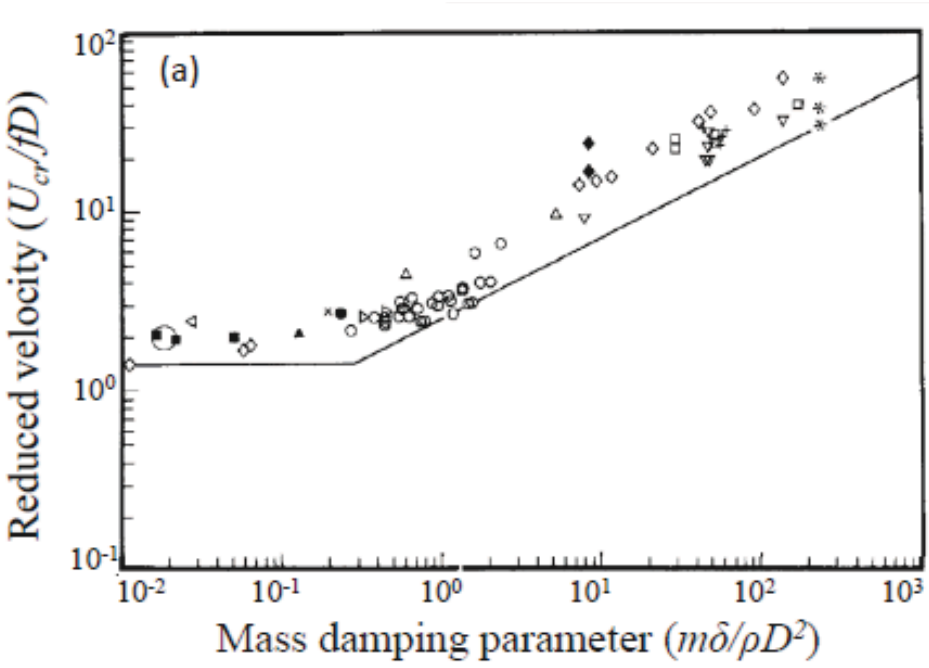

FIGURE 2.2: Critical flow velocities for fluidelastic instability in the square array. (Weaver and Fitzpatrick, 1988).

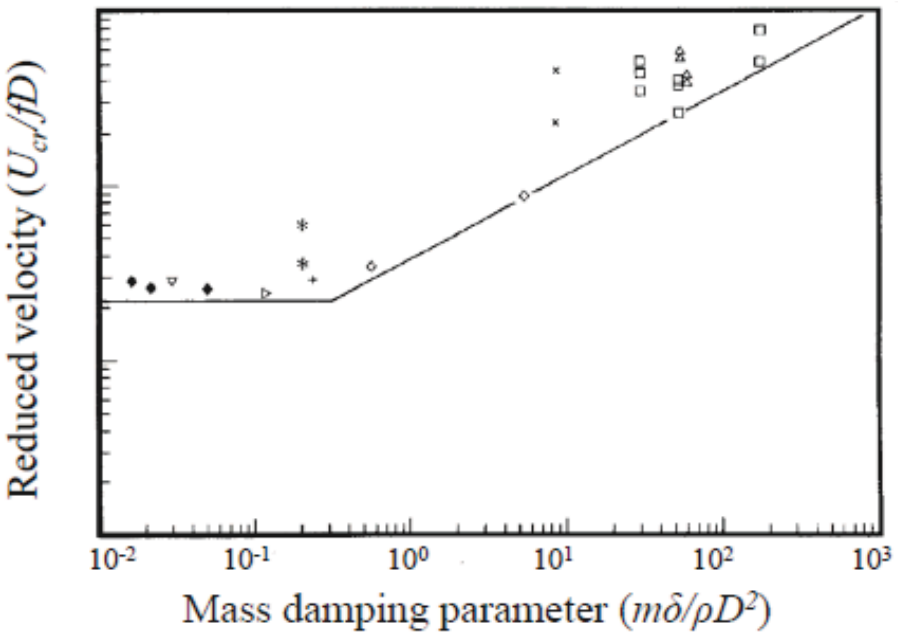

FIGURE 2.3: Critical flow velocities for fluidelastic instability in the rotated square array. (Weaver and Fitzpatrick, 1988).

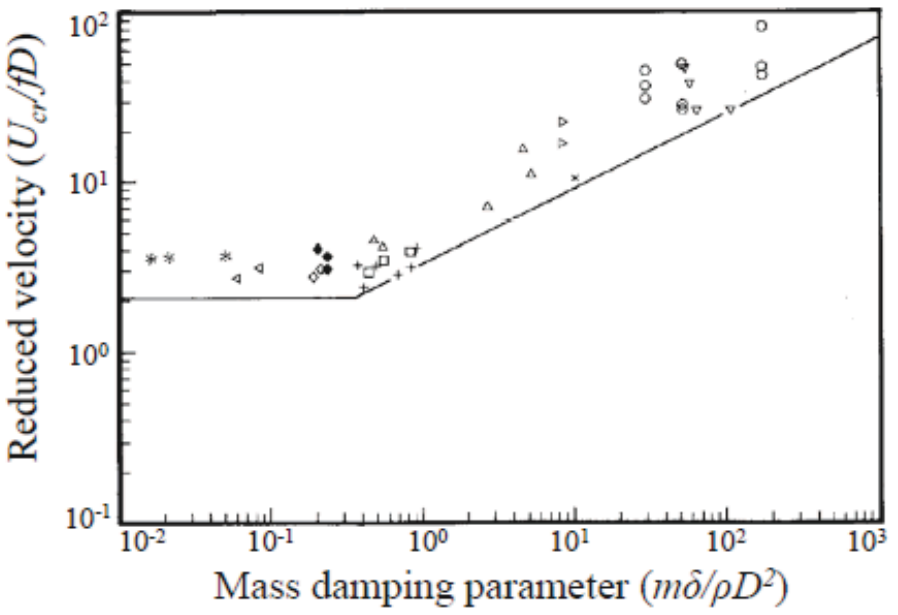

FIGURE 2.4: Critical flow velocities for fluidelastic instability in the normal triangular array. (Weaver and Fitzpatrick, 1988).

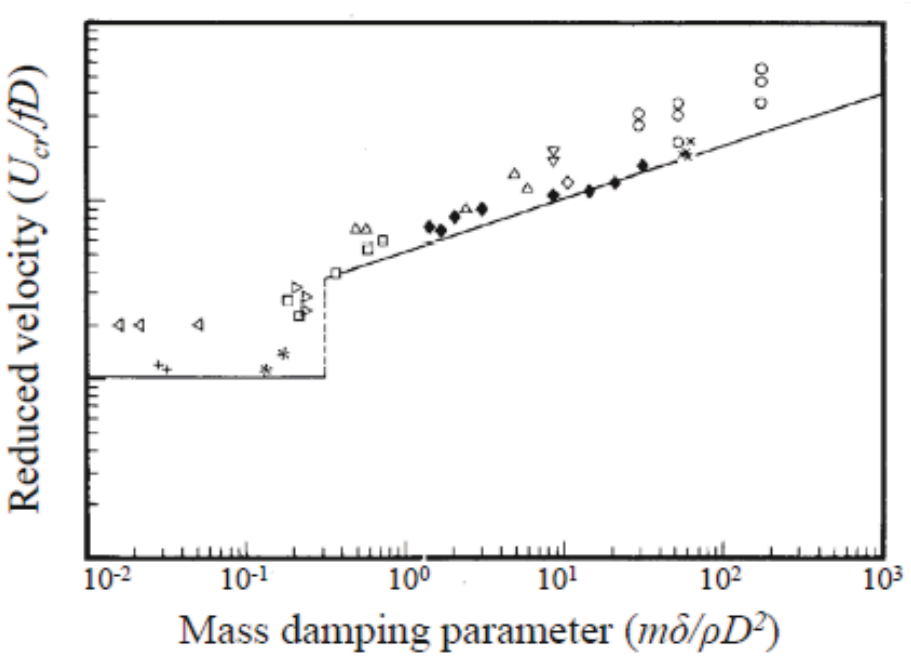

FIGURE 2.5: Critical flow velocities for fluidelastic instability in the parallel triangular array. (Weaver and Fitzpatrick, 1988).

ARRAY GEOMETRY	CHEN (1984)			WEAVER-FITZPATRICK (1988)		
	RANGE	K	α	RANGE	K	α
IN-LINE SQUARE ARRAY (90°)	$\frac{m\,\delta}{\rho\,d^2} < 0.7$	2.1	0.15	$\frac{m\,\delta_A}{\rho\,d^2} < 0.3$	1.4	0.0
	$\frac{m\,\delta}{\rho\,d^2} > 0.7$	2.35	0.5	$\frac{m\,\delta_A}{\rho\,d^2} > 0.3$	2.5	0.48
ROTATED SQUARE ARRAY (45°)	$\forall \frac{m\,\delta}{\rho\,d^2}$	3.54(T/d-0.5)	0.5	$\frac{m\,\delta_A}{\rho\,d^2} < 0.3$	2.2	0.0
				$\frac{m\,\delta_A}{\rho\,d^2} > 0.3$	4.0	0.48
PARALLEL TRIANGULAR ARRAY (30°)	$\frac{m\,\delta}{\rho\,d^2} < 2.0$	3.58(T/d - 0.9)	0.1	$\frac{m\,\delta_A}{\rho\,d^2} < 0.3$	1.0	0.0
	$\frac{m\,\delta}{\rho\,d^2} > 2.0$	6.53(T/d - 0.9)	0.5	$\frac{m\,\delta_A}{\rho\,d^2} > 0.3$	4.8	0.30
NORMAL TRIANGULAR ARRAY (60°)	$\frac{m\,\delta}{\rho\,d^2} < 1.0$	2.8	0.17	$\frac{m\,\delta_A}{\rho\,d^2} < 0.3$	2.0	0.0
	$\frac{m\,\delta}{\rho\,d^2} > 1.0$	2.8	0.5	$\frac{m\,\delta_A}{\rho\,d^2} > 0.3$	3.2	0.40

FIGURE 2.6: Design correlations for fluidelastic instability in different array configurations and pitch angles. (Comparison between Chen, 1984 and Weaver and Fitzpatrick, 1988).

2.1.2 Mechanisms of flow-induced vibrations

Naudascher and Rockwell (2005)[31] classified the four main excitation mechanisms in tube bundles of heat exchangers according to their response to cross-flow conditions. They considered firstly the turbulence buffeting, which is a forced vibration mechanism, as a steady state response. Following, they catalogued the vortex shedding and the acoustic resonance, which are self-controlled mechanisms, as a resonant response. And finally, the FEI, a self-excited mechanism, as an instability. A typical response of a tube in a bundle subjected to cross flow is shown in Figs. 2.7 and 2.8[32] [33]. Initially, as the flow velocity is increased, there is a gradual enlargement in the amplitude of the tube vibration due to turbulent buffeting. When the vortex shedding frequency coincides with the tube natural frequency, tube acoustic resonance may take place in a phenomenon called "lock-in" where the tubes may experience relatively larger vibration amplitudes. If the flow velocity is further increased, then the tube comes out from the lock-in zone and the response amplitude is restablished following the vibration trend due to turbulent buffeting. Finally, when the flow velocity reaches the critical velocity threshold for fluidelastic instability, a dramatic increase of the vibration amplitude takes place.

Turbulence buffeting is a quasi-random excitation resulting in the order of a few percent of the tube diameter. Although this can result in long term wear due to impact and also fretting wear at the tube supports, turbulent buffeting enhances convective heat transfer so the heat exchanger performance is improved. It is hence not recommendedt to minimize this source of excitation of heat exchangers; specially for certain array geometries, which are employed to increase turbulent mixing. Nevertheless, it is important to ensure that the tube-support interaction does not cause premature wear. For instance, Hassan et al. (2003) [34]. and Axisa et al. (1990) [35] have conducted a detailed theoretical investigation of the turbulent buffeting in tube bundles of heat exchangers theoretically relating the vibration amplitude to the flow dimensionless force spectrum. Additionally, modelling techniques for turbulent buffeting have been reviewed in detail by Weaver et al. (2000b) [36].

Vortex shedding and acoustic resonance can result in relatively large amplitudes of vibration if their frequencies are close and get coupled. Vortex shedding is a periodic excitation with a frequency f that is linearly related to the flow velocity U through the Strouhal Number. When the frequency of the vortex shedding matches the tube's natural frequency, resonance occurs and large amplitude oscillations are set off over the lock-in region. That is manifested by a sudden peak in the amplitude of the oscillations as shown in Figs. 2.7 and 2.8. In most cases, vortex shedding resonance can be avoided by operating the heat exchanger away from the lock-in region. A general review of both mechanisms can be found in Weaver (1993) [37] and Ziada (2006) [38].

An added problem is that this phenomena are quite dependent to the array geometry.

So, different configurations have to be tested before giving any definitive guideline. For that purpose, Ziada et al. (1989a,b) [39] [40] conducted an experimental investigation of the acoustic resonance in staggered and in-line tube bundles subjected to air and water cross flows. They found that there are multiple Strouhal numbers for each array which are not necessarily harmonic between them. Also, detailed investigation of the vortex shedding in an in-line array conducted by Ziada and Oengoren (1992) [41], suggested that the instability of the jet flow between the cylinders is the source of vortex shedding excitation. They concluded that this jet instability distinguishes the vortex shedding phenomenon for in-line tube arrays from that in staggered tube arrays. Ziada and Oengoren (2000)[42] also studied the vortex shedding and acoustic resonance in staggard parallel triangular tube arrays. The authors found multiple Strouhal numbers for the vortex shedding excitation in this array pattern. Lately, numerical simulations of vortex shedding in tube bundles were acomplished for Sweeney and Meskell (2003)[43], Liang and Papadakis (2007)[44], and Liang et al. (2009) [45]. The last mechanism of fluid induced vibrations, is discussed with some more detail in the next section.

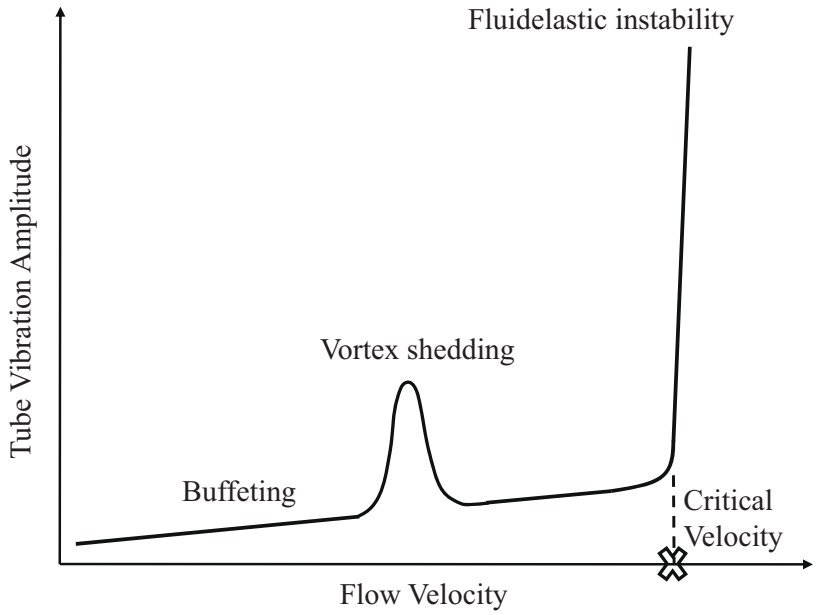

FIGURE 2.7: Typical tube response pattern in a tube array subjected to cross flow.

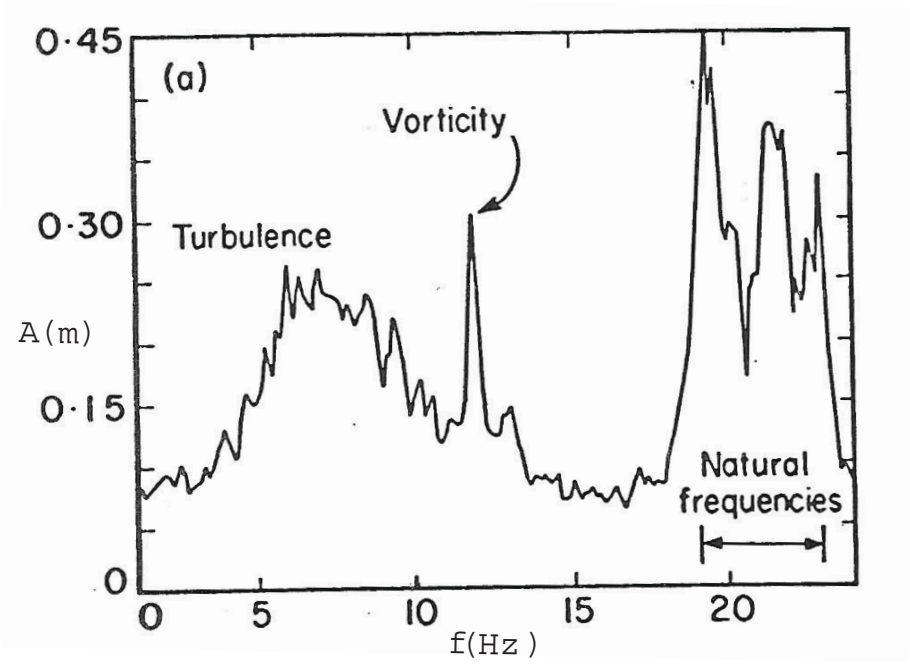

FIGURE 2.8: Typical spectral response pattern in a tube array subjected to cross flow.

2.2 Fluidelastic Instability mechanisms

When a tube bundle is subjected to cross-flow, it is typical to find tubes vibrating with an amplitude proportional to the upstream velocity. The system is considered to be stable if the response motion decays with time, while the system is considered to be unstable if the response motion increases (Rao, 2004) [46]. Fluidelastic instability takes place when the cross-stream reaches a threshold limit, called the critical velocity. Suddenly, the response of the system is dramatically increased, putting in risk the integrity of the installation. This phenomenon can be described as a self-excited feedback mechanism between the tube motion and the fluid forces.

The mechanisms involvend in this process can be theoretically discussed analyzing the equation of motion for the system

$$[\quad _s + m_f]\ddot{} + [C_s + \quad _f]\dot{} + [\quad _s + \quad _f] \quad = \sum F \tag{2.4}$$

where $[\quad _s]$, $[C_s]$ and $[\quad _s]$ are the mass, damping and stiffness matrices respectively. The equation also includes m_f, $\quad _f$ and $\quad _f$ representing the added mass, the fluid damping and the fluid stiffness. The system is considered stable if both total damping, $[C_s + \quad _f]$

and total stiffness [$_s$+ $_f$] terms in Equation 2.4 are positive. Physically, a positive total damping means that there is a net energy dissipated by the structure per oscillation cycle, while a positive total stiffness indicates that structural forces are stabilizing the system.

Static instability or divergence appears when a negative fluid stiffness exceeds the structural stiffness leading to a negative total stiffness term. This instability is rarely observed in heat exchanger tube arrays because dynamic instability takes place first.

Dynamic instability can be caused by only one or even a combination of three main mechanisms. The first mechanism requires at least two degrees of freedom, so fluid stiffness produces out-of-diagonal terms in the total stiffness matrix leading to instability. The second mechanism is due to the nonlinear hysteresis provoked by fluid forces which depend on the tube vibration mode. However, the third and most significant dynamic instability is caused by a negative fluid damping exceeding the positive damping in the system. Therefore, with a total negative damping in the system, the flow transfers a net energy per cycle into the structure, so the amplitude of the system response is abruptly increased up to dramatic levels, as sketched in Fig. 2.7.

2.3 Fluidelastic Instability models

A review of the existing models for fluidelastic instability in cylinder arrays is presented in this section. These models are focused in the mutual interaction between the structural displacement and the resulted fluid forces in order to attempt an accurate prediction of the critical velocity for FEI onset. Unfortunately, it is not sufficient to determine the fluid forces on an individual cylinder when it is mounted statically at its equilibrium position. The effect of cylinder motion must be taken into account to obtain a reliable description [47]. In fact, this is an essential component of any of the models that will be introduced in the present section.

2.3.1 Jet-switch model

The jet-switching model, developed by Roberts (1962) [48] [49], was conceived as a purely analytical model with no need for any additional experimental data. In his preliminary experiments, Roberts noticed that instability occurred predominantly in the stream-wise direction, hence his analysis was limited to one directional (in-flow) motion. Furthermore, based on flow visualizations, he assumed that the flow downstream of two adjacent cylinders could be represented by two wake regions, one larger than the other, with a classic jet-flow between them. Figs. 2.9 and 2.10 shows the behavior proposed by Roberts. In particular, Fig. 2.9 corresponds to an instant in which alternative pairs

tubes, with initially the same in-flow position, are displaced downstream as a consequence of their in-flow vibration [32] [33].

Because only in-flow motion was allowed, Roberts suggested that a hypothetical channel involving two half cylinders and imaginary boundaries could be representative of the flow through a row of cylinders (Fig. 2.10). He considered this flow pattern similar to a jet passing between two parallel flat plates: the jet from the wake regions is curved and impinges onto the plates, while a portion of the jet flow is recirculated upstream so the wake region is preserved. Hence, the positions where the jet is impinging the imaginary plates are maintained fixed. The main constraints of Roberts' model are that the flow separation from the cylinder occurs at the minimum gap between the tubes centers (at 90 degrees) and also that the cylinder wakes are regions of constant pressure. In other words, the pressure difference across the jet in not varying in the in the in-flow direction. Additionally, the flow upstream of the separation points and in the jet region was considered to be inviscid.

Employing basic dynamic and kinematic considerations, Roberts obtained the pressure coefficient of both cylinders as a function of its position in the in-flow direction. As a result, a considerable hysteresis around the non-displaced position was found with this formulation. When the cylinders change their in-flow positions due to their vibration the jet is forced to switch its direction. Since a finite pressure difference is required to initiate this switch, and because the cylinder is moving in the opposite direction, the jet switch will not occur at the same position. Therefore, around the non displaced position the flow would have two stable configurations.

The hysteresis of the drag forces play an important role in Roberts model, for a cylinder oscillating in the in-flow direction causing the jet switch the drag force aiding the downstream motion is greater than opposing the upstream motion, hence Roberts concluded that energy would be extracted from the flow resulting in fluidelastic instability.

Another significant contribution of this model is that it accounts for the unsteady nature of the instability, considering that a finite time is needed to allow for the jet to witch.

With all these characteristics in mind, Roberts formulated the equation of motion for a cylinder in a row and obtained the reduced velocity required to initiate limit cycle oscillations for any mass-damping parameter:

$$U_c/\ _n\ d = \quad (m\delta/\rho d^2)^{1/2} \tag{2.5}$$

where is the ratio between the fluidelastic frequency and the natural frequency (~ 1). The theoretical values obtained by Roberts show in general a poor agreement with the experimental data. Paidoussis et. al.(2011) [47], have attributed that to the assumption of the instability taking place in the in-flow direction is not accurate. In fact, later experimental results indicate that the vibration is predominantly normal to the flow.

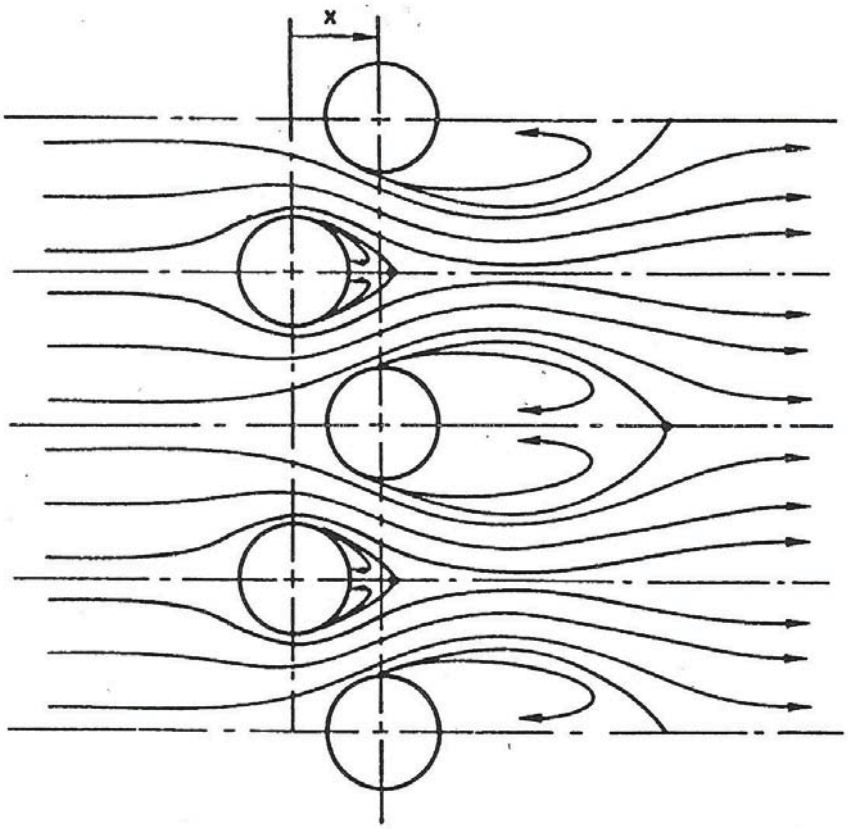

FIGURE 2.9: Idealized model of the jet-flow for a row of cylinders(Roberts, 1962).

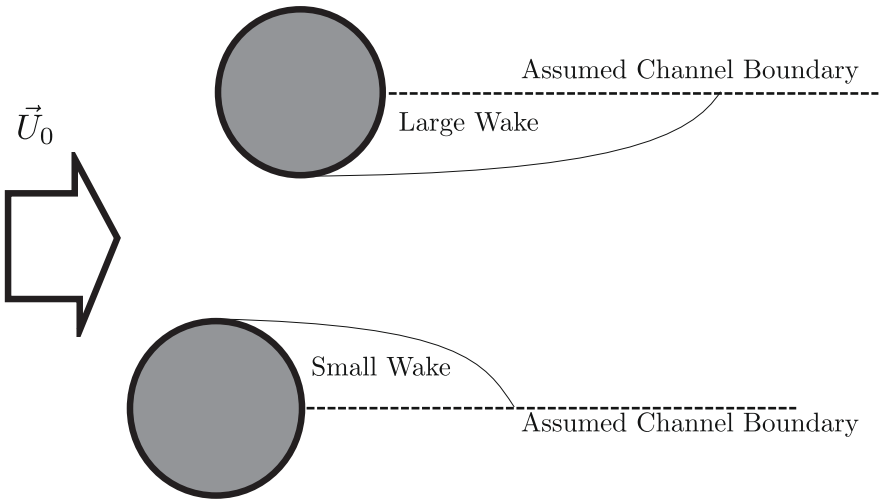

FIGURE 2.10: Idealized model of the jet-flow between two imaginary plates for a cell of a two half tubes. (Roberts, 1962).

2.3.2 Quasi-static model

The most famous expression predicting fluidelastic instability for cylinder arrays subjected to cross-flow is the one usually atributed to Connors (1970) [16], who derived it using a quasi-static analysis. However, it was Roberts [48] the first one to obtain such expression as shown in the preceding subsection.

The quasi-static model developed by Connors (1970) [16] considered the instability of a single row of tubes subjected to normal flow. He observed that the tubes were oscillating in elliptical orbits, either stream or cross-stream wise. He simulated this pattern by moving the two adjacent tubes for a cylinder in both symmetrical and antisymmetrical elliptical orbits, to measure the fluid forces coefficients (See Fig. 2.11).

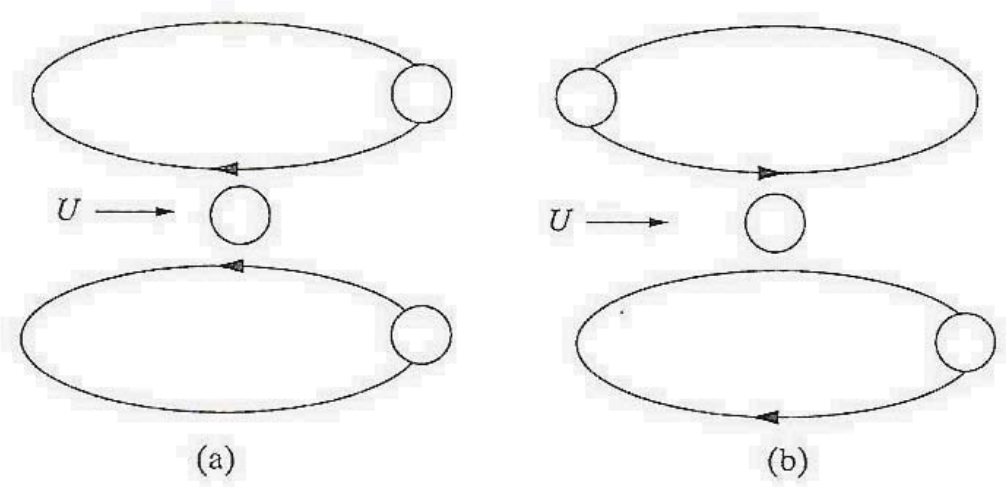

FIGURE 2.11: Elliptical motion of the neighbouring cylinders employed by Connors (1970): (a) symmetric motion (b) antisymmetric motion.

Performing an energy balance for both stream and cross-stream wise directions, Connors derived the most used expression for predicting fluidelastic instability:

$$U_{cr}/f_n d = \quad (m\delta/\rho d^2)^n \tag{2.6}$$

U_{cr} is the critical flow velocity, f_n is the tube natural frequency, d is the tube diameter, m is the tube mass per unit length including the fluid added mass, δ is the tube logarithmic decrement, ρ is the fluid density, and and are constants which values were initially proposed by Connors (1970) [16] to be 9.9 and 0.5, respectively. Although, the values of these constants and also the linear relationship between the damping term δ and the mas-ratio term $m/\rho d^2$ have been widely debated by many authors in the last decades.

Gorman (1978) [50], Pettigrew et. al. (1978) [51], Paidoussis (1980)[52], Au-Yang et. al.

(1991) [53] and Pettigrew and Tailor (1991) [54] found different values of K=3.3, 3.3, 0.8, 2.4 and 3 respectively (independent of P/d). Blevins (1974) found these constants to be dependent on the array geometry and the fluid characteristics. Weaver and Elkashlan (1981a) [55] investigated the effect of damping and mass ratio on the stability of a tube array, founding that the tube damping term δ is not linearly related to the mass ratio term $m/\rho * d^2$. A correction to previous equation 2.6 was introduced in the following form:

$$U_{cr}/f_n \quad = \quad (m/\rho d^2)^{n1}\delta^{n2} \tag{2.7}$$

where 1 and 2 are the new non-linear exponents. They also found that the response of a single row of tubes is different from a tube array so threshold is affected by the number of rows in an array. A minimum number of six tube rows was recommended to obtain a typical stability behavior of a tube array [56]. Following, Weaver and Koroyannakis (1982)[57] carried out an experimental study on tube array response in air and water flows. They observed significant variations of the tube response frequency in water flows , much more pronounced than in the case of air flows. This phenomenon was attributed to the effect of the vibration mode of the surrounding tube on the added mass term, more significant for water than for air flows.
Alternatively, Blevins (1974, 1977, 1979)[58],[59],[60] carried out a series of studies in which he re-formulated Equation 2.7 using a different approach where the fluid forces are considered to be a function of the relative tube displacement. This assumption was later questioned by Price and Paidoussis (1986a) [61].
Finally, as a concluding remark, Price (1995) [9] and Paidoussis et. al. [47] discussed the evidences of experimental support for the different quasi-static models. In Fig. 2.12 the different model predictions and the experimental data are shown. The authors noted that all the models overestimated the critical velocity for $m_r\delta$ 5 and that all of them failed to predict the discontinuity in the stability threshold between lower and higher mass damping parameters.

2.3.3 Unsteady models

In the models presented in this section the unsteady forces on the oscillating cylinder were obtained empirically. Tanaka and Takahara (1980, 1981) [62] [63] measured the unsteady fluid forces on an in-line square array. The authors carried out an experimental study in which a centered tube in an in-line tube array was excited harmonically and the fluid forces acting on the surrounding tubes were measured. They assumed that the fluid forces affecting a tube in the array are a function of the tube motion as well as the motions of the four adjacent tubes only, namely U, R, L and D in Fig.

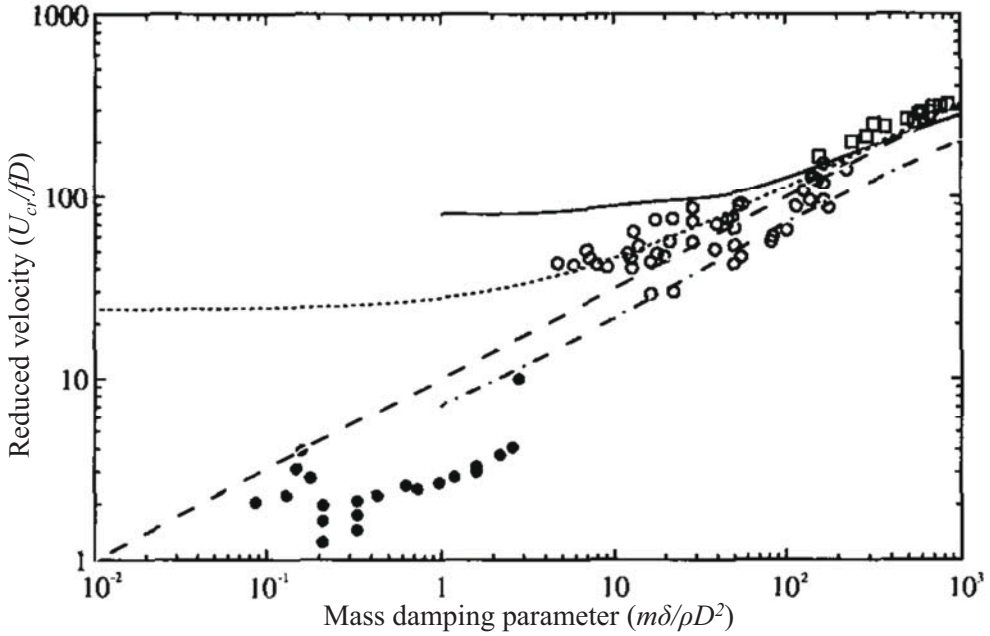

FIGURE 2.12: Theoretical stability boundaries for fluidelastic instability compared to various experimental data. Multiple flexible tubes in liquid flow (white circle), multiple flexible tubes in gaseous flow (black circle), single flexible tube in gaseous flow (white square), Roberts solution 1966 (line), Connors solution 1970 (dash), Blevins solution 1974 (dot).

2.13. Amplitude and phase measurements of the lift and drag forces were carried out over a range of Reynolds number and reduced velocities. They reported a discontinuity in the stability boundary for values of the of mass-damping parameter in the range of $(m/\rho d^2 = 50 \rightarrow 500)$, concluding that the instability mechanism below this range is different from the one above it. Tanaka and Takahara's model provided a good agreement with the experimental results. However, the number of force coefficients and measurements required to complete this model is considerably high. Later, Tanaka et al. (1982) [64] published an experimental study in which a single flexible tube in a rigid array was set free to oscillate in the lift direction only (disregarding the stiffness mechanism). In addition to an upper shift in the stability threshold, they found that the discontinuity in the stability threshold remained in the stability maps, suggesting that this characteristic is not exclusive to a change in the instability mechanisms. Paidoussis et. al (2011)[47] have proposed the rapid shift in the phase angle between the cylinder motion and the resulting fluid forces as a likely explanation.

Chen (1983a,b) [7] [8] found that there are two basic mechanisms causing fuidelastic instability; the first is controlled by fluid damping while the second is controlled by fluidelastic forces. The damping-controlled instability, or dynamic instability caused by fluid damping forces, is known as the "damping mechanism". These fluid damping forces

are a function of flow velocity resulting that when the flow velocity is increased, the fluid damping decreases. Moreover, when the flow velocity exceeds a certain value, the total damping becomes negative and the system becomes unstable. The second mechanism, controlled by fluidelastic forces, is known as the"stiffness mechanism". The coupling between the tube vibrations and the fluid flow produces fluidelastic forces which contribute to the total system stiffness. As the flow velocity increases the fluidelastic forces increases as well. Ultimately, at a certain velocity threshold, the system becomes fluidelastically unstable.

Later, Paidoussis and Price (1988) [23] introduced another study on the nature of fluidelastic instability which supports the existence of the aforementioned mechanisms. Chen (1983a,b) [7] [8] used the force measurements obtained by Tanaka and Takahara as an empirical input to a mathematical model which couples the fluid forces with the tube equations of motion. The stability boundaries obtained using Chen's model were in good agreement with the experimental data of Tanaka and Takahara (1981) [63] as shown in Fig. 2.14. Chen attributed the discontinuity of the experimental results reported by Tanaka and Takahara to the existence of multiple stability boundaries as predicted by his model. Chen (1983a) [7] was the first to introduce the existence of multiple stability boundaries.

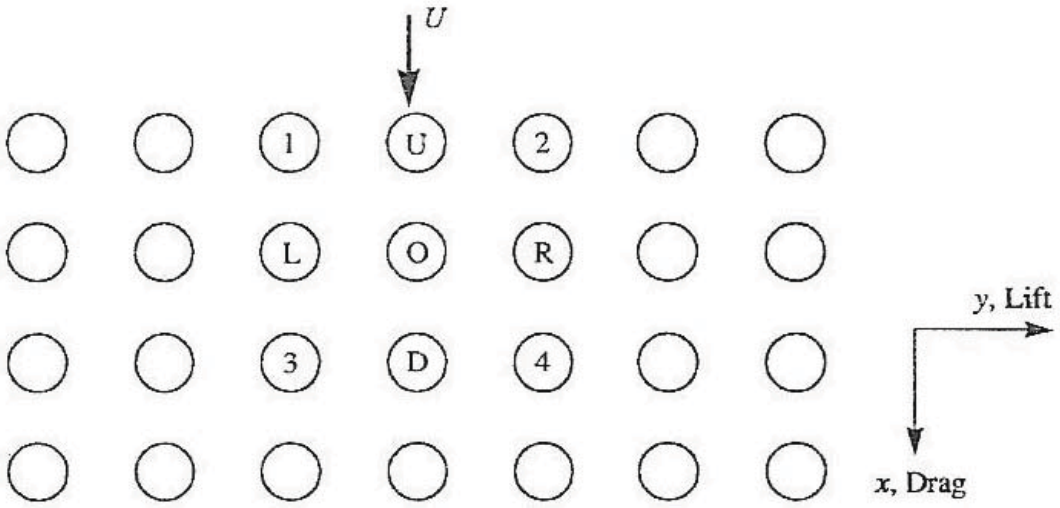

FIGURE 2.13: Cylinder notation employed by Tanaka and Takahara (1980, 1981).

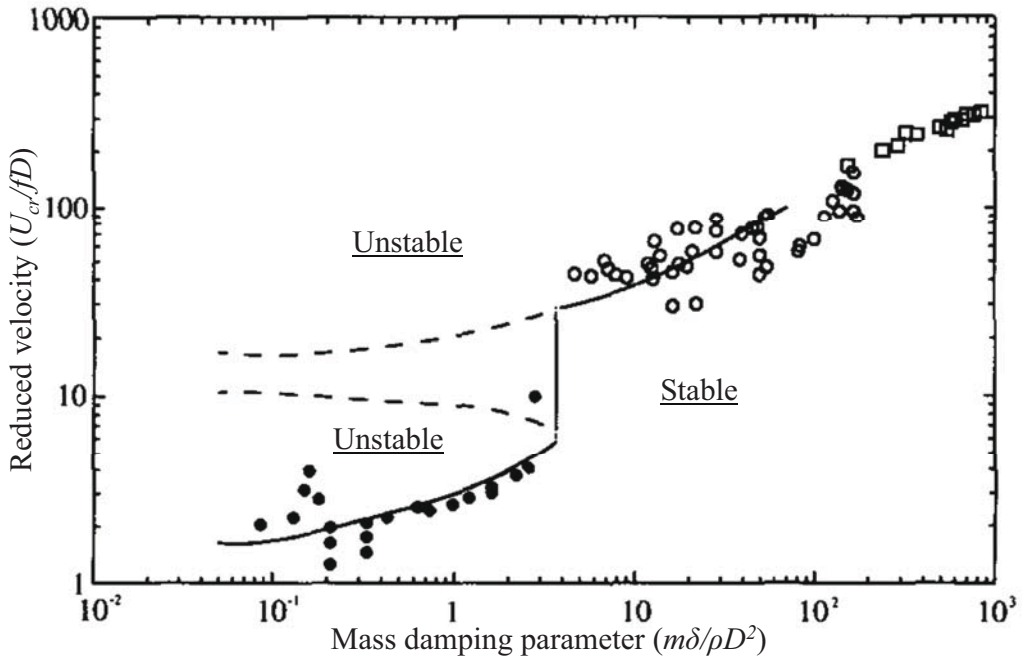

FIGURE 2.14: Theoretical stability boundaries developed by Chen (1983a,b) compared to the experiments of Tanaka and Takahara (1981). Multiple flexible tubes in liquid flow (white circle), multiple flexible tubes in gaseous flow (black circle), single flexible tube in gaseous flow (white square), practical stability boundaries (line), theoretical stability boundaries (dash).

These multiple stability boundaries were generated by most of the later theoretical models. However, their practical existence was disscussed firstly by Paidoussis et al., 1996 [65]. Besides, the generalizations in the applicability of Chen's model was questioned by Weaver (2008) [18], who argued that the model depends mainly on the empirical values of the fluid forces which are in turn a function of the array geometry.

2.3.4 Semianalitical model

Lever and Weaver (1982) [66] found experimentally that a single flexible tube in a rigid array could have essentially the same stability threshold than that of a fully flexible array. In particular, they carried out their analysis based on a single flexible tube in a cell of rigid tubes subjected to cross flow. The flow through the array was divided into wake regions and flow channels which were called stream-tubes, as seen in Fig. 2.15. The cross-sectional area of the stream-tubes was assumed to fluctuate about a constant value which is equal to the entrance sectional area. The flow in these stream-tubes was assumed to be inviscid, one dimensional, and the friction losses were introduced using a pressure drop term. Lever and Weaver assumed that the tube motion will disturb the

stream-tube area proportionally to its magnitude. The stream-tube disturbance over the flow attachment length is in phase with the tube motion, while a finite delay time is required for the disturbance caused by tube vibration to propagate upstream. They attributed this time delay to the fluid inertia considering that a finite time would be required to reorganize the flow pattern when the tube oscillates. Fig. 2.16 shows the flow inertia and finite time delay assumed by the authors. In this figure, the concept of fluid inertia is illustrated with a simplified canonical 2D flow in a rectangular channel, where a plate is moving in the cross-flow direction.

The delay time was proposed to be in the form of a phase lag function (*) - see Eq. 2.8 , where is a phase angle that represents the delay time, U_g is the mean gap flow velocity, is the frequency, and * is the curvilinear coordinate which represents the distance from the vibrating tube.

$$(\ ^*) = 2 \ _n \ /U_g \tag{2.8}$$

Knowing the stream-tube cross-sectional area in terms of time and space, Lever and Weaver used the one dimensional unsteady Bernoulli's equation to solve the flow field in the stream-tubes (see Figs. 2.17, 2.18 and 2.19). By integrating the pressures over the flow attachment length on both sides of the tube, they obtained the fluid forces which are coupled with the tube equation of motion to predict the tube response. The stability boundaries are obtained by setting the damping term in the tube equation of motion to zero, which corresponds to the system switching from a positive to a negative damping value. Despite the relative simplicity of this model, the stability boundaries are quite consistent with the experimental data trend, as shown in Fig. 2.20. It is important to note here that the theoretical model of Lever and Weaver predicted multiple stability loops in the lower mass damping parameter regions similar to what Chen (1983a) [7] found lately.

Price (1995) [9] questioned the flow delay model shown in Equation 2.8 and pointed out that this semi-analytical model needs some empirical terms to be employed such as the pressure drop term used to present the friction losses in the array, the attachment and separation points in the stream tube, and the length of the stream tubes.The effect of these parameters was later investigated by Lever and Weaver (1986) [12] showing that they have minor effects on the stability boundaries. However, the stability boundaries are significantly modified depending on the selection of the time delay, which it is considered a major deficiency of the model by Weaver (2008) [18].

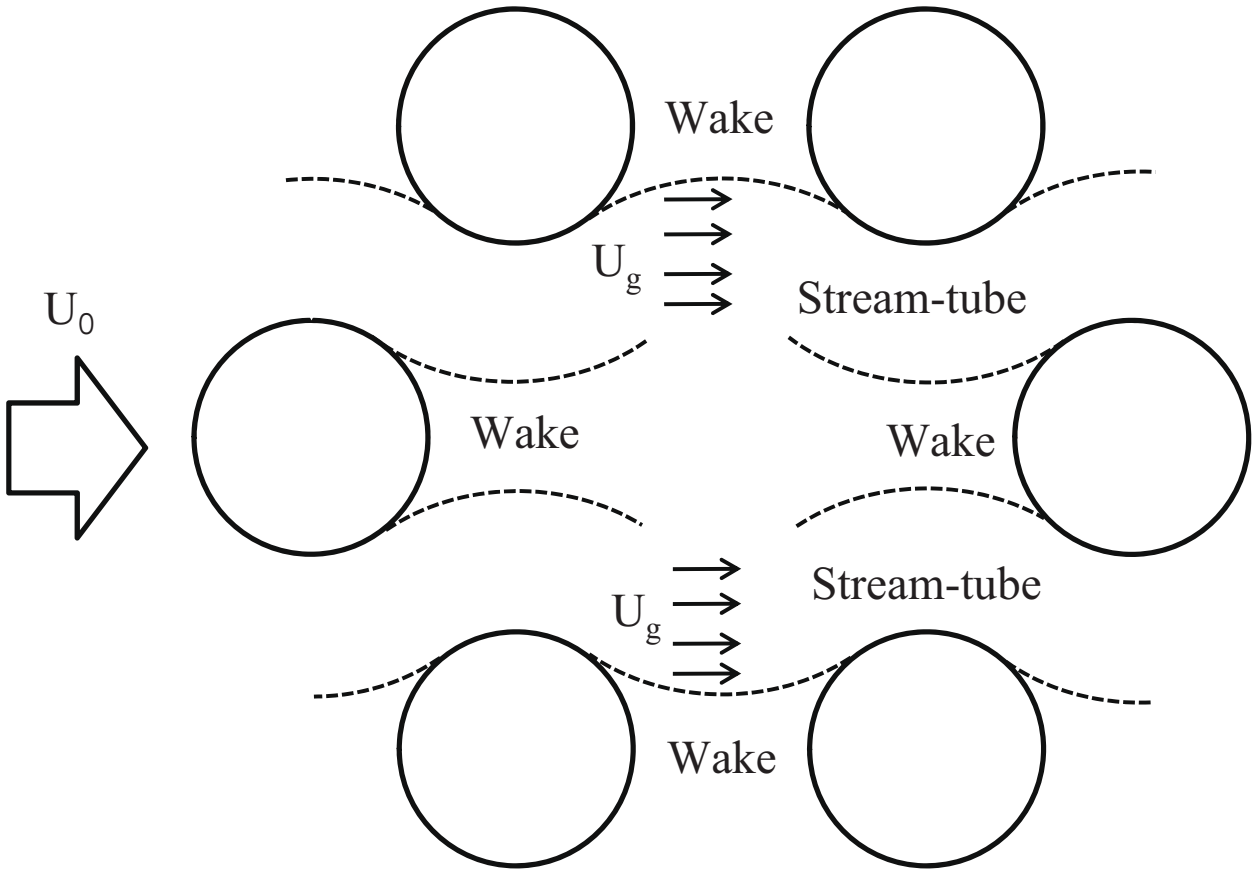

FIGURE 2.15: Sketch of the idealized flow pattern through a stagger tube array, as proposed by Lever and Weaver (1982).

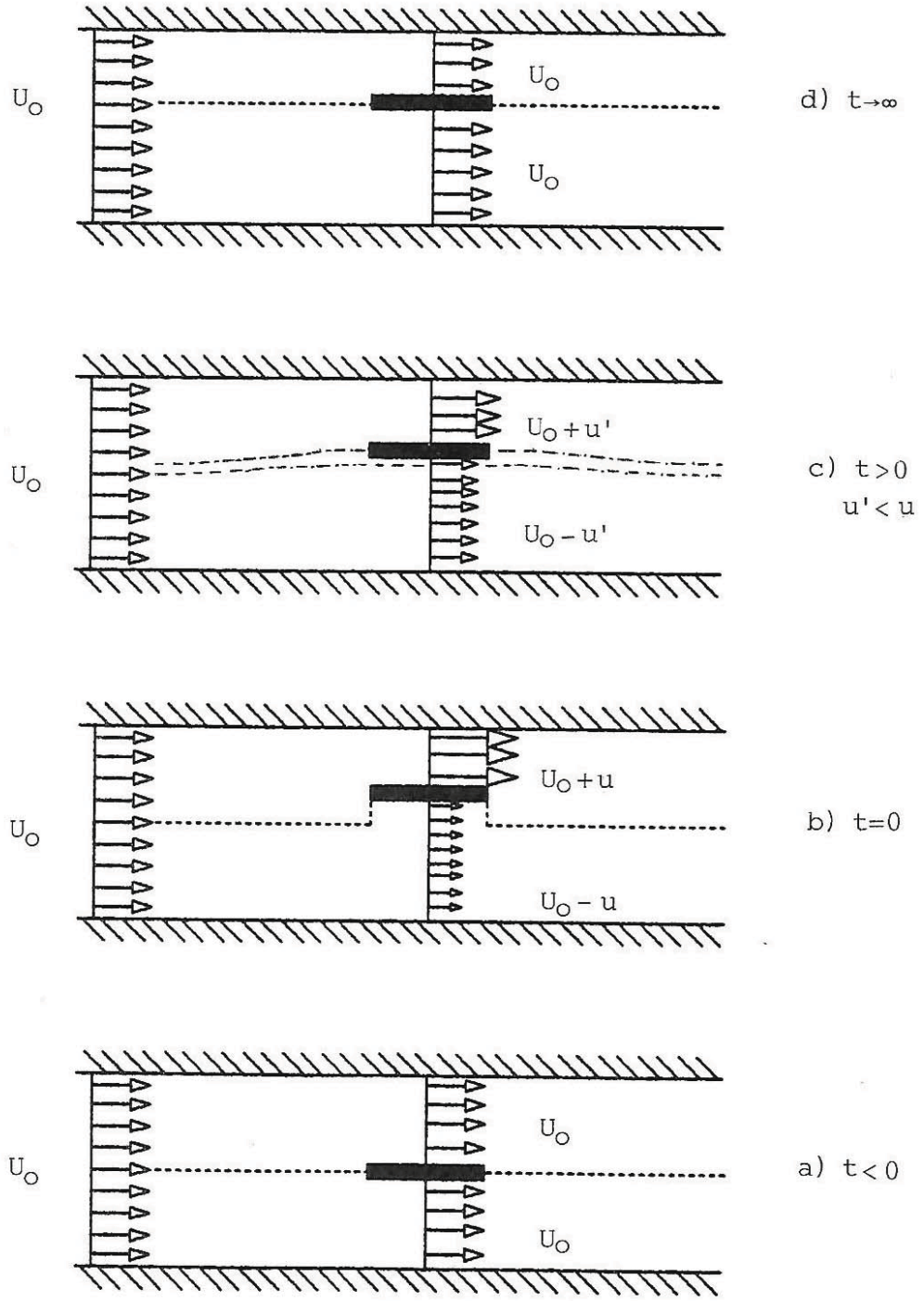

FIGURE 2.16: Idealized sketch of the flow inertia and finite time delay concepts.

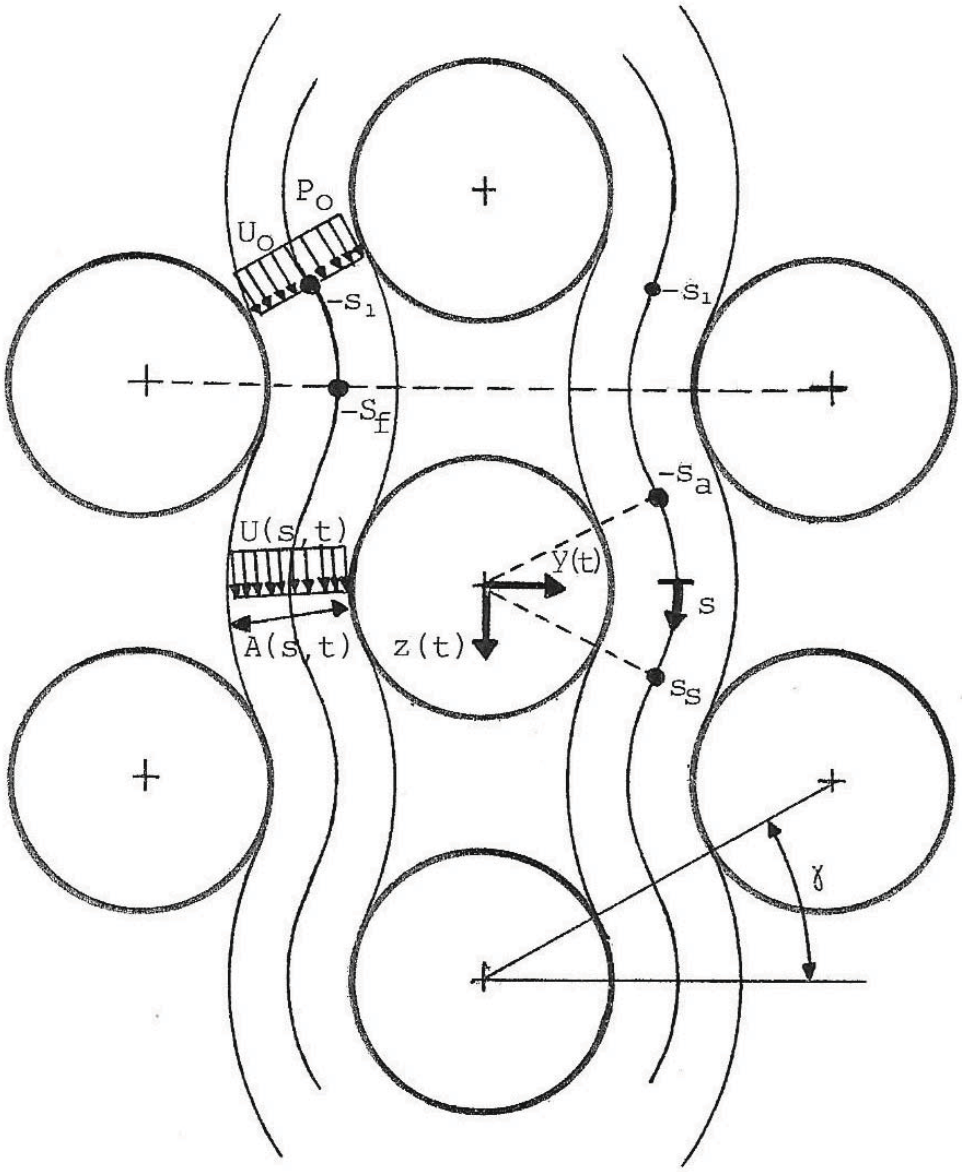

FIGURE 2.17: Schetch of the stream-tube flow with curvilinear coordinates.

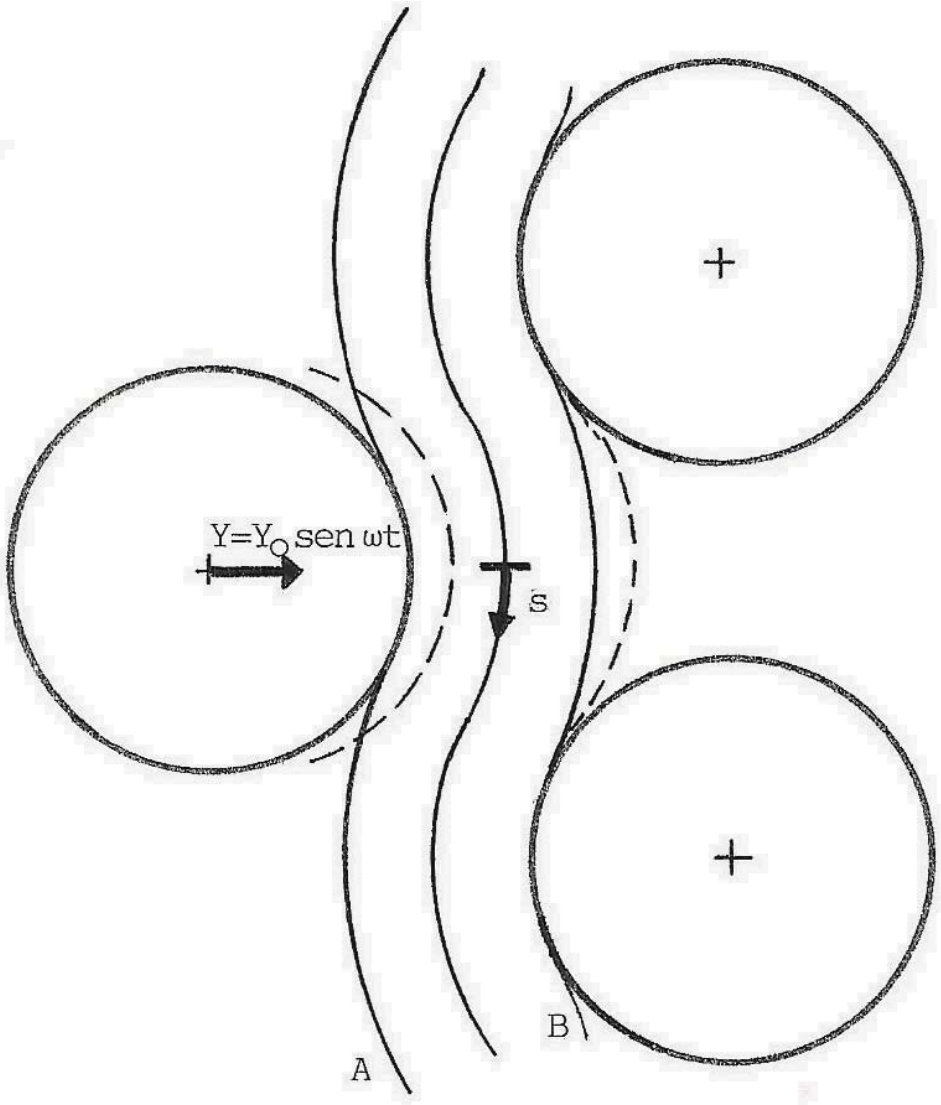

FIGURE 2.18: Effect of the tube motion.

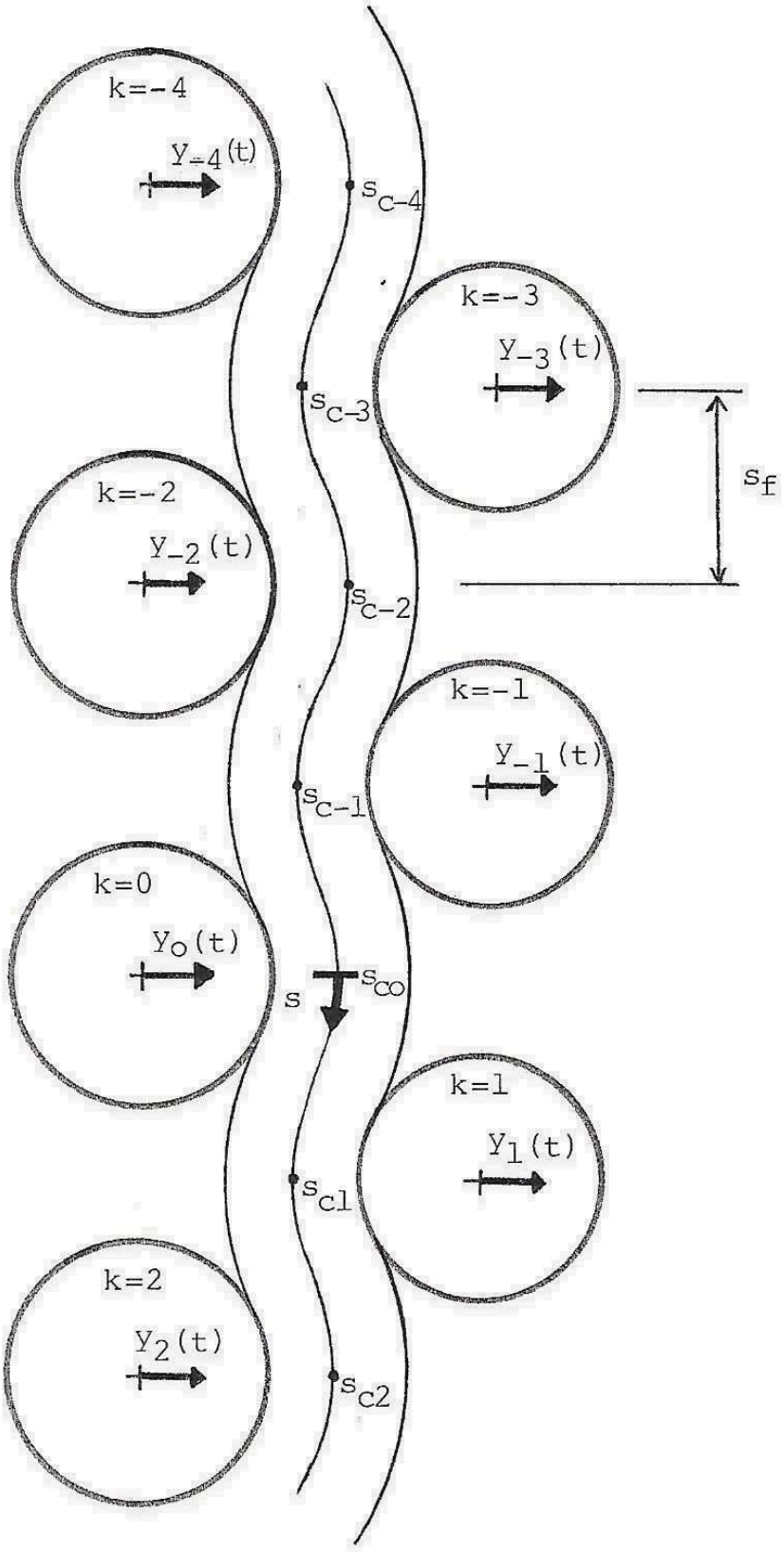

FIGURE 2.19: Schetch of the stream-tube with the surrounding tubes.

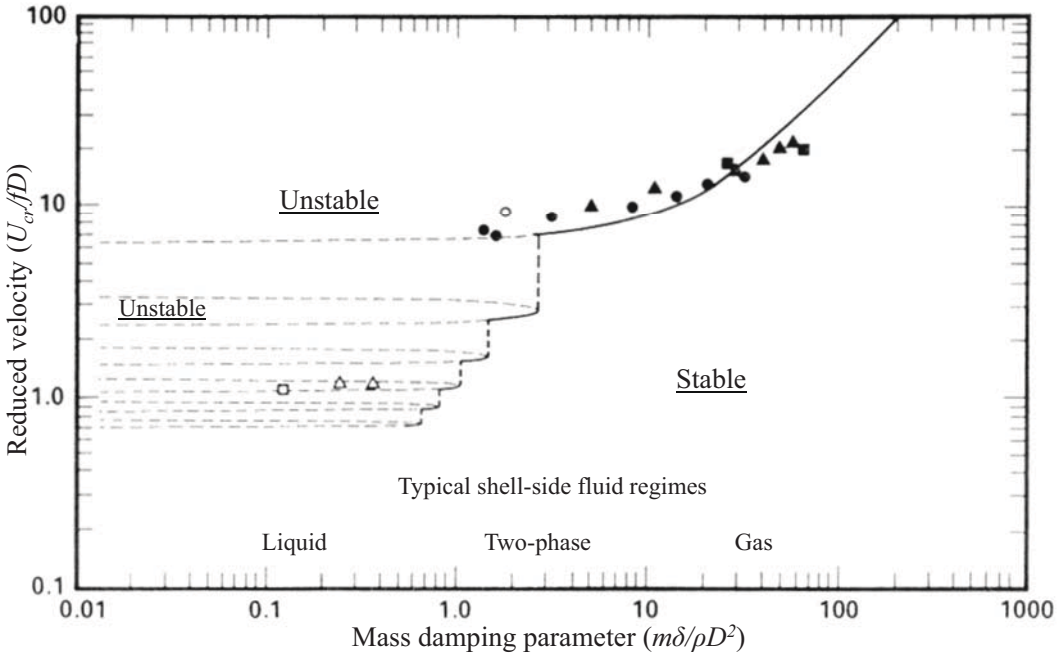

FIGURE 2.20: Stability boundaries developed by Lever and Weaver's (1982). Theoretical model for parallel triangular tube array (P/d = 1 375). Practical stability boundaries (line), theoretical stability boundaries (dash).

Afterwards, Yetisir and Weaver (1993) [67] introduced some refinements to the theoretical model of Lever and Weaver, accounting for the stream-wise tube motion and considering flexible all the tubes in the array. They also introduced a generic function to model the upstream decay of the perturbations caused by tube vibrations, and unconstrained the tube response frequency (Lever and Weaver (1982) [66] to be equal to the tube natural frequency). The modifications introduced by Yetisir and Weaver showed that at low mass-damping parameters, the fluidelastic instability is attributed mainly to the damping mechanism while at high mass damping parameters the instability is attributed to the stiffness mechanism. Numerical results presented by Yetisir and Weaver (1993a) [67] for parallel triangular and in-line square arrays with P/d=1.375 showed that the exponent on $m\delta/\rho d^2$ tends to 0.5 as the mass damping parameter is enlarged (valid for $m\delta/\rho d^2 < 200$ only), rather than tending to 1 as obtained with the original Leaver and Weaver model [66][12]. A very similar analysis accounting for multiple flexible cylinders was proposed by Parrondo et. al. (1993) [68] who reached essentially the same conclusions as those outlined above [47].

2.3.5 Quasi-steady model

The quasi-steady assumption states that for an oscillating body, such as a cylinder, the effect of its motion on the resulting fluid forces leads to the modification of the

velocity vector relative to the body. Consequently, the resultant lift and drag forces are reoriented to become normal and parallel, respectively, to this relative velocity vector, as seen in Fig. 2.21

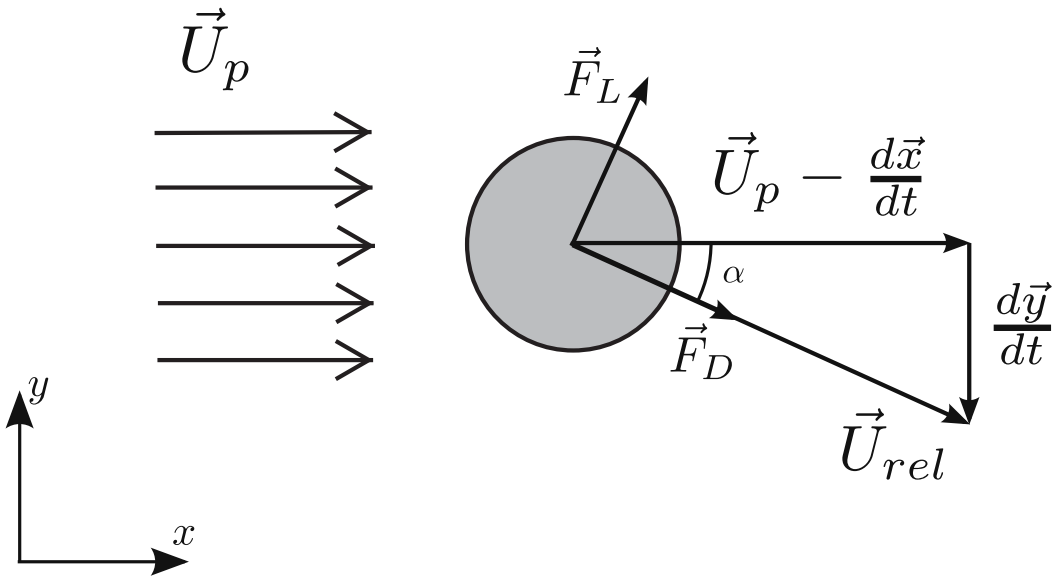

FIGURE 2.21: Schetch of the quasi-steady approach applied to tube bundles.

As the tube oscillates, the relative pitch velocity U_p oscillates as well, resulting in dynamic lift and drag forces. The first quasi-steady analysis, conducted by Gross (1975)[69], developed the analysis for the cross-flow motion of a single flexible cylinder. He assumed a linear variation of C_L with the pitch angle and after approximating that $\approx \dot{d}/U_p$, he obtained an aerodynamic damping force proportional to $\delta C_L/\delta$. Instability occurs when the sum of the fluid and structural damping is zero, giving

$$\frac{U_{pc}}{f_n d} = \frac{m\delta}{\rho d^2(-\delta C_L/\delta)} \tag{2.9}$$

Price and Paidoussis (1984) [10] also developed a mathematical model for fluidelastic instability based on the quasi-steady approach. These authors considered an array of flexible tubes, and assuming that the motion of a tube is affected by the motion of the two adjacent tubes. The transverse fluid force was then written as:

$$F_y = \frac{1}{2}\rho d l U_g^2 (C_L - \frac{\dot{d}}{U_g} 2C_L - \frac{\dot{d}}{U_g} C_D) \tag{2.10}$$

In this work a time delay between the tube motion and the fluid response was also incorporated to take into account the time required for the mean flow to travel one tube row downstream. They presented a first order time delay expression in the form of Eq. 2.11 where is the delay time between the tube motion and the fluid response, is a constant, d is the tube diameter, and U_g is the mean gap velocity.

$$= \frac{d}{U_g} \tag{2.11}$$

Based on reasonable assumptions and considerations [47] Price and Paidoussis (1984) [10] suggested for the constant to be order unity $\sim$ (1). Fluid forces for displaced tubes were coupled through the system equations of motion to determine the tube response. Fluidelastic instability was obtained by setting the damping term to zero as discussed previously. The model was improved later by Price and Paidoussis (1986) [61]. Next, Paidoussis and Price (1988) [23] showed the effects of damping and stiffness mechanisms by comparing the stability boundaries for a fully flexible array to those for a single flexible tube in a rigid array. The authors concluded that instability for mass-damping parameters less than 300 is predominantly due to damping mechanism, while for mass-damping parameters more than 300 stiffness mechanism is predominant. Obviously, around a mass-damping parameter of 300 both mechanisms are active. The stability boundaries obtained from Price and Paidoussis (1984, 1986) [10] [61] with this theoretical model showed multiple stability regions which were considered impractical. Finally, a conservative stability threshold was considered as shown in Fig.2.22. While the quasi-steady model is more complex than the the semi-analytical model of Lever and Weaver, the stability boundaries predicted by Price and Paidoussis (1986)[61] underestimated the stability threshold as shown in Fig.2.22.The delay time constant adopted in this model was shown to significantly affect the stability predictions.

2.3.6 Quasi-unsteady model

Granger and Paidoussis (1996) [11] included the unsteady effects which were previously neglected in the theoretical model of Price and Paidoussis (1984), introducing the quasi-unsteady model. The authors considered the model of a single flexible tube in a rigid array, which implies that the instability is attributed to the damping mechanism only. They solved the continuity and Navier-Stokes equations to predict the fluid response to an impulse motion of the tube.

They concluded that due to the impulse motion of the tube, a finite layer of small vortices is generated at the tube surface. These vortices are responsible for the evolution of the disturbance from the tubes to the flow around them. They attributed the time delay between the tube vibration and fluid response to the time required to form these layers

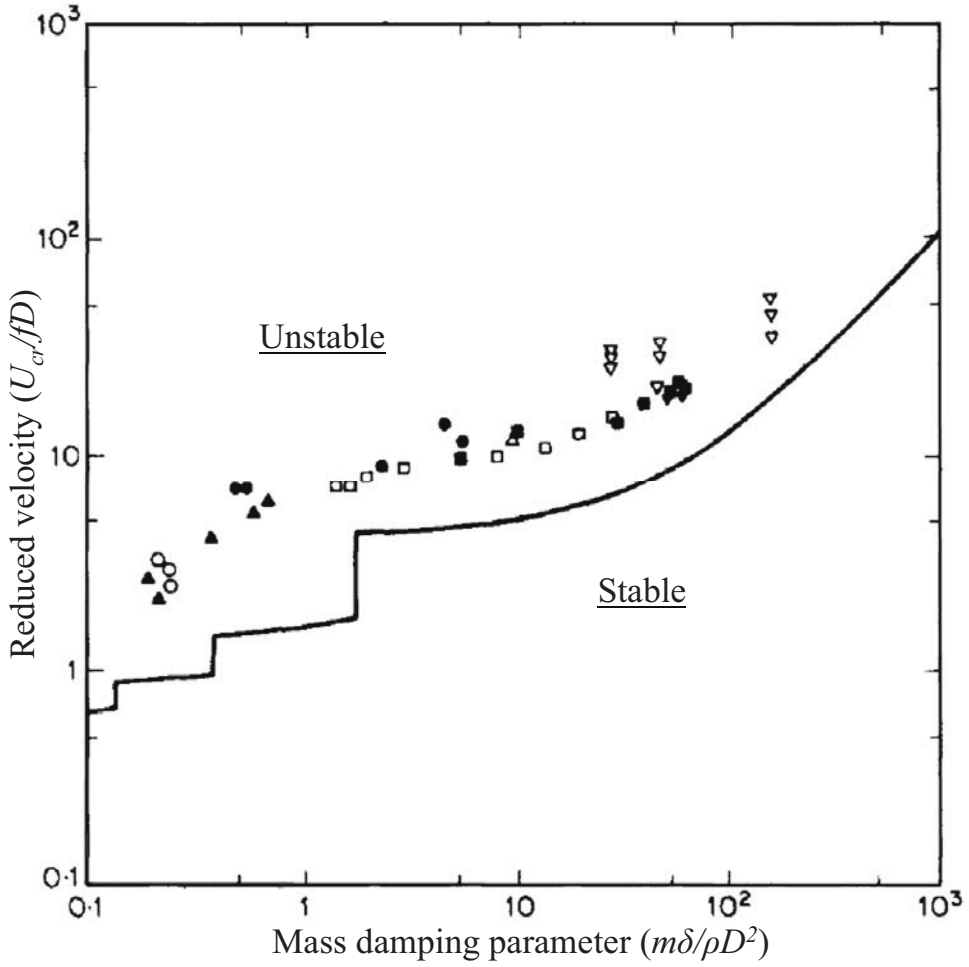

FIGURE 2.22: Stability boundaries developed by Price and Paidoussis (1986); $\delta = 0.05$; $= 1.0$; parallel triangular tube array ($P/d = 1\ 375$).

of vortices. Price and Paidoussis (1984) [10] had assumed in their model that time delay had to be a constant time shift, as seen in Fig. 2.23. Conversely, in this Granger and Paidoussis (1996) model [11], a memory effect to model the time delay resulted from the generation and convection of vorticity on the tube surface was proposed, as shown in Fig. 2.24. This memory effect can be modeled using either a first-order or second-order empirical equations in which a set of factors (dependent on the equation order) is obtained from experimental measurements of the tube array.

Anyway, the quasi-unsteady model developed by Granger and Paidoussis provided better prediction of fluidelastic instability than the quasi-steady model. The agreement

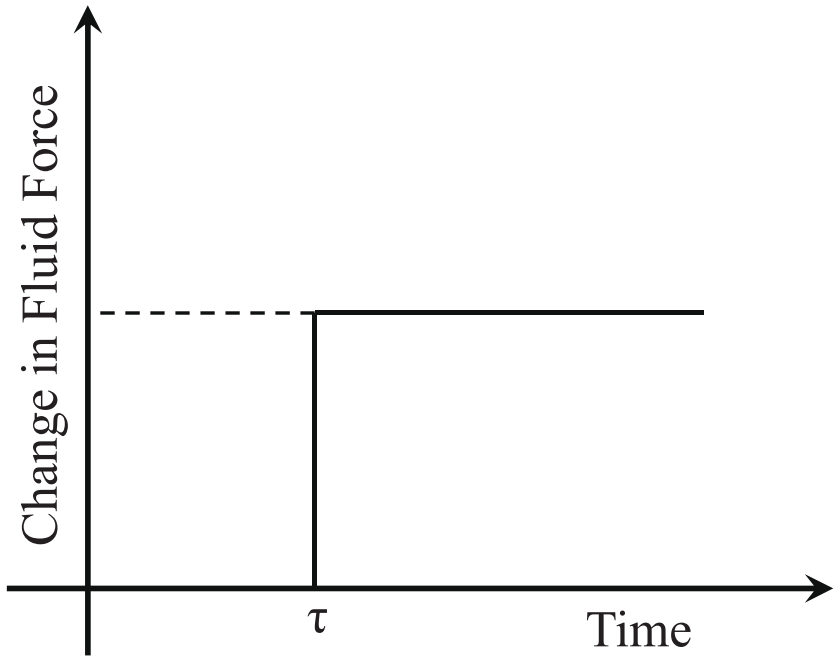

FIGURE 2.23: Transient variation of the fluid force coefficient induced by a step tube displacement. (Price and Paidoussis, 1984).

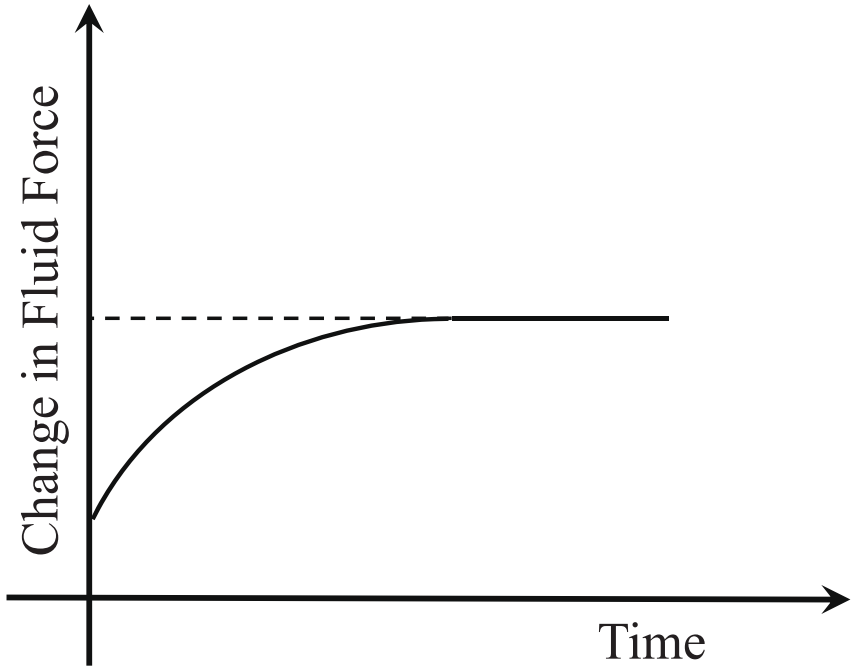

FIGURE 2.24: Transient variation of the fluid force coefficient induced by a step tube displacement. (Granger and Paidoussis, 1996).

between the quasi-unsteady stability boundaries and the experimental data was improved by increasing the order of the function for the memory effect, as seen in Fig. 2.25.

Meskell (2009) [20] predicted analytically the memory function proposed by Granger and Paidoussis [11] via analytical considerations. This author assumed that the memory function could be represented by the normalized instantaneous bound circulation on a vibrating cylinder due to a sudden change in its transverse position. The instantaneous flow field in the array was modeled as a circular cylinder with a bound circulation, giving the static lift and drag forces, and a trailing vortex sheet which represented the transient nature of the fluielastic forces. The approach of the memory function obtained with this model can be seen in Fig. 2.26.

In addition, an estimation of the coefficients, assuming N=1, were obtained for a normal triangular array with $P/d = 1\,375$. The stability boundaries obtained by Meskell [20] performing an stability analysis (see Fig. 2.11) are very coincident with both experimental data and the second-order results from Granger and Paidoussis model [47].

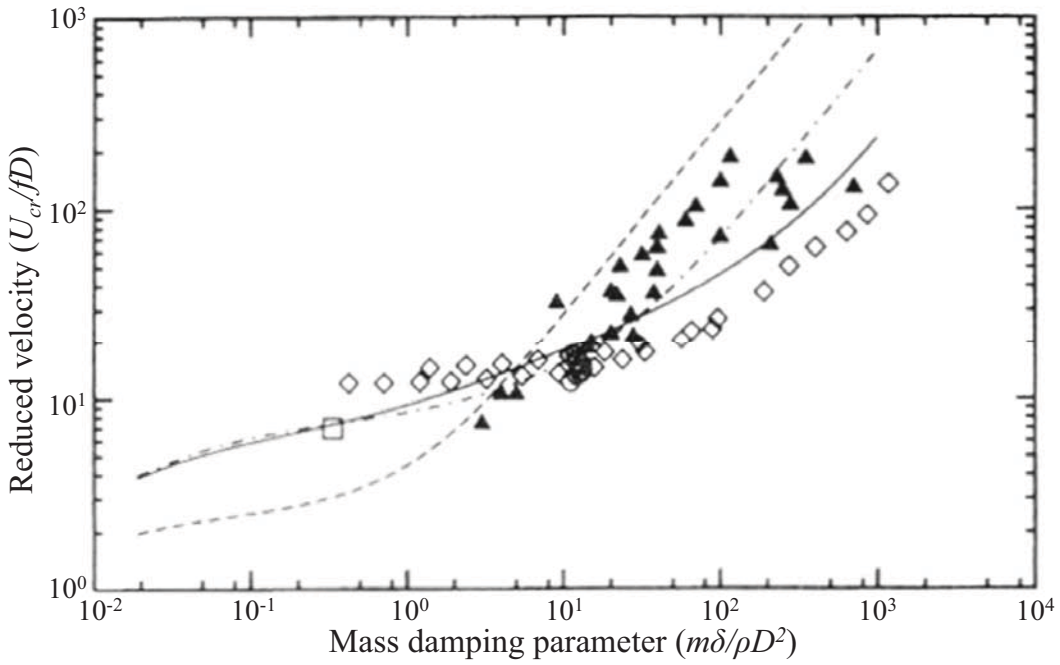

FIGURE 2.25: Comparison of the stability boundaries for a single flexible tube in a rigid normal triangular array between the quasi-steady model (dash), quasi-unsteady model with first order (line) and quasi-unsteady model with second order (dash-dot).

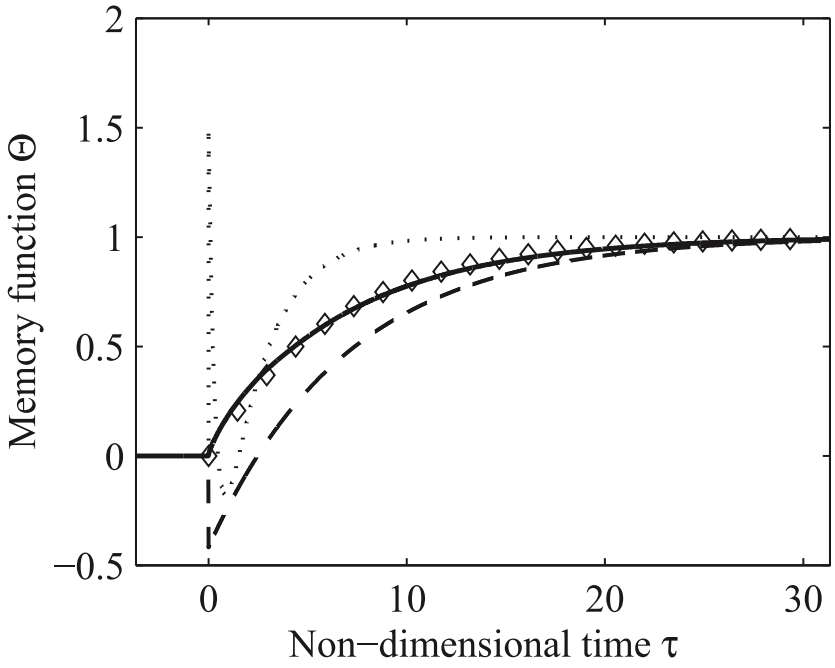

FIGURE 2.26: Transient variation of the fluid force coefficient induced by a step tube displacement. (Granger and Paidoussis, 1996). Memory function for P/d=1.375; first order empirical function (dash), second order empirical function (dot), theoretical model of Meskell, 2009 (line), first order approximation of the theoretical model of Meskell, 2009 (diamonds).

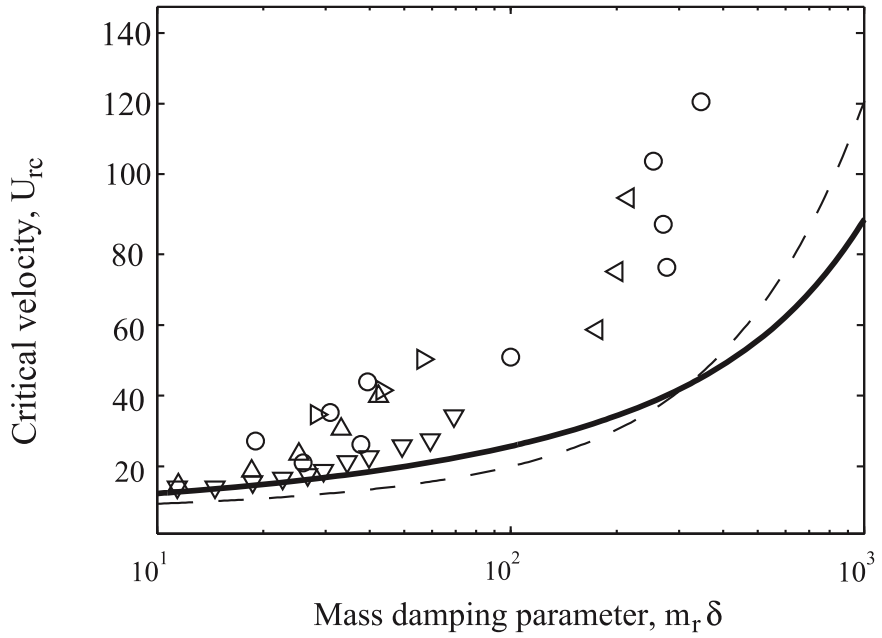

FIGURE 2.27: Stability boundaries obtained by Meskell (2009) with experimental data and the second-order model of Granger and Paidoussis.

2.3.7 Non-linear models

Manufacturing tolerances and thermal constraints there are responsible for the appearance of small clearances between heat-exchanger tubes and other structural elements like tube supports, antivibration bars or baffle plates. This results in "inactive" or ineffectual supports, and also in the existence of large lengths of unintentionally unsupported tubes with very low natural frequencies. These low frequency modes may suffer from fluidelastic instability at relatively low velocities U_{pc} (Weaver and Schneider 1983 [70]). Once the tubes go unstable, they will impact at the initially inactive supports and higher modes of vibration will be excited.

Numerous researchers have investigated the post-instability behavior of cylinder arrays subjected to cross-flow.

The first nonlinear analytical model was that of Roberts (1962, 1966) [48] [49] who employed the Krylov and Bogoliubov method of averaging to solve the nonlinear equations associated with the jump in C_D on an oscillating cylinder. Since then, most of the analysis were based on linear assumptions until the mid 80's.

The more recent nonlinear analysis were initially concentrated on impacting (e. g. with baffle plates). A typical example is given by Axixa et. al. (1988) [35] where the impacting is represented via an equivalent bilinear spring stiffness. A similar analysis similar was developed by Fricker (1991, 1992) [71], [72], who allowed for the variation of the vibration frequency. Cai et. al. (1992) [73] and Cai and Chen (1993) [74] [75] attempted to investigate theoretically a two-span tube using the unsteady fluid-dynamic analysis of Chen (1983a) [7]. The predicted behavior agreed very well with the experiments on the same system, but once the active tube-support coupling become unstable there is no other dissipation mechanism so the theory predicts that the amplitude increases indefinitely.

Chen and Chen (1993) [76] considered the chaotic response of three rigid tubes, mounted on a flexible platform, impacting against rigid support plates. Chaotic motion from bifurcation diagrams was presented and Lyapunov exponents were predicted from the results. At the same time, Paidoussis and Li (1992) [77] attempted a three dimensional analysis of a clamped-clamped beam, with an inactive support at midspan and that was set to vibrate free in the transversal direction only. They employed the linear fluidelastic instability model of Price and Paidoussis (1986) [61], and the effect of impacting was modeled by using a bilinear stiffness, as proposed by Axisa et. al. (1988) [35], or a cubic spring stiffness. For the cubic spring, Paidoussis and Li presented results in terms of bifurcation diagrams as th one shown in Fig.2.28. They found that the instability is lost at a Hopf bifurcation as far as the non-dimensional velocity is further increased. At this point, a limit cycle oscillation is established followed by a post-Hopf bifurcation with a double-period sequence and, eventually, chaos.

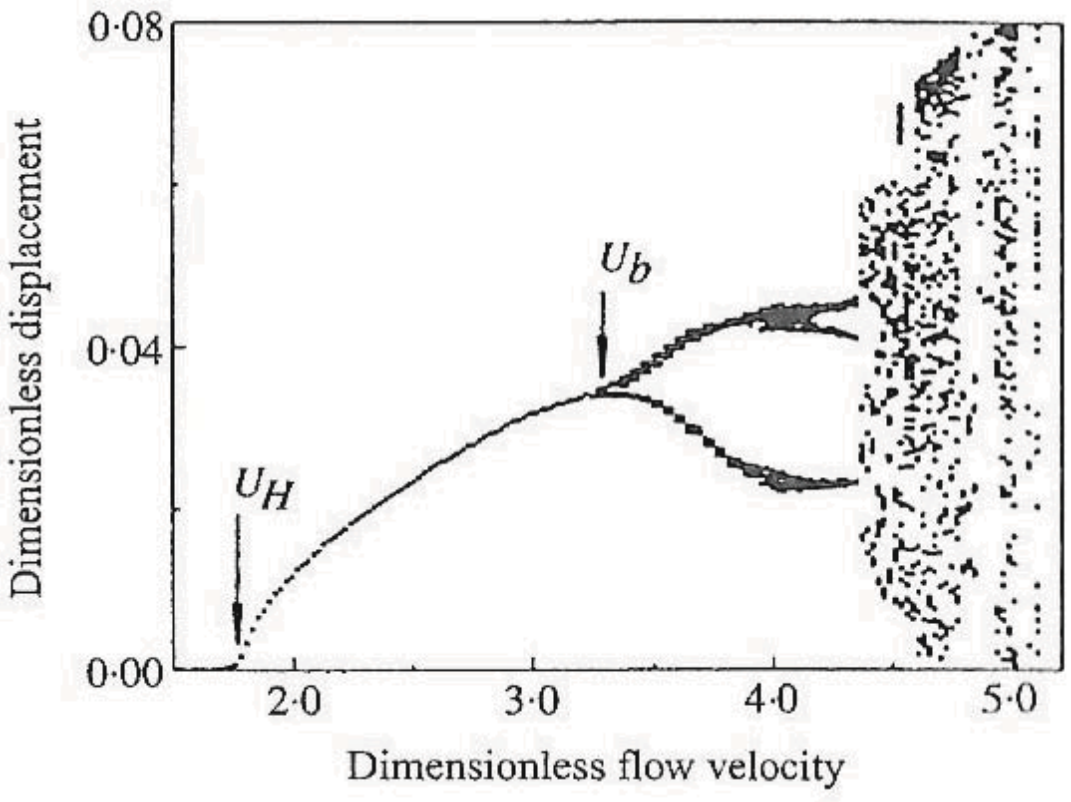

FIGURE 2.28: Bifurcation diagram, based on dimensionless flow velocity, for a single flexible cylinder in an in-line square array ($P/d = 1\ 5$).

Langre et. al. (1992) considered the effect of using three different fluidelatic instability models: the negative.fluid-damping model, the Blevins (1974) [58] coupled model and the Price and Paidoussis (1984) [10] quasi-steady model. All these models are considering linear fluid-dynamic effects only. The most interesting conclusion is that all of them predicted the same type of bifurcation as the flow velocity is increased above its critical value, although, the bifurcations were observed at different velocities every model.

Meskell and Fizpatrick (2003)[78] performed an experimental study on triangular tube arrays ($P/d = 1\ 32$ and 1.58) with a single flexible tube vibrating in the transverse direction only. Based on detailed measurements of the free-vibrational response as a function of the flow velocity, an empirical non-linear model for was proposed for the fluidelastic damping and stiffness forces. It was assumed that the fluidelastic force can be decomposed in three functions, all of them depending on the flow velocity: the first one is in phase with the tube displacement, the second one with the tube velocity and the third one depending on both displacement and velocity. This can be expressed as follows:

$$f(\ ,\dot{\ },U) = \ _1(\ ,U) - \ _3(\ ,\dot{\ },U) - \ _2(\dot{\ },U) \tag{2.12}$$

Using free-response measurements from the vibration of the tube at different flow velocities along with a force-state mapping technique (Masri and Caughey 1979; Meskell et. al. 2001) [79] [80] it was possible to propose a mathematical expression in the form of cubic polynomials for those functions: $_1 = \ ^3 \ _f \dot{} \ $ and $\ _3 = \ ^{\cdot 3} + \ _f \dot{}$; while $\ _2 \approx 0$; $_f$ and $\ _f$ being respectively, the fluid stiffness and damping terms. Considering the variation with the flow velocity, it was shown that $\ _f$, $\ _f$ and $\ $ were linear functions of U, whereas the cubic fluid damping term $\ $ was represented by a third order polynomial in U. Using the inferred functions $\ _1$ and $\ _3$, Meskell and Fitzpatrick predicted the vibrational amplitude of the flexible tube as a function of the flow velocity [47].

2.3.8 Non-uniform flow

Direct application of two-dimensional theoretical models to real flows in three-dimensional tube arrays of heat exchangers requires the existence of inlet flow uniformity: if the flow over the tubes is uniform then the models can be used with the equivalent modal terms. However, there are many situations where the flow velocity is not uniform so it is necessary to modify the stability analysis to account for this effect. Since most of the experiments on which correlations are based were conducted under uniform flow conditions, and it is mandatorry to know how to modify the stability conditions to validate them for non-uniform flows. The method suggested in several design guides is to introduce the concept of a so-called "effective velocity" (Au-Yang 1991 [53]; Pettigrew and Taylor 1991 [54]) that would be depending the velocity shape function $\ $ and the structural mode shape Φ.

Different experimental verifications and some theoretical approaches have been undertaken to introduce the effect of non-uniformity in the system response. Waring and Weaver (1988) [81] conducted experiments in a non-uniform flow extended for one, two and even three span tubes, comparing the results for those with uniform flow over a portion of a single span tube. They found that the theory of an "effective velocity" could be unconservative and in some cases it could predict incorrectly which was the unstable mode.

Consequently, Weaver and Goyder (1990) [82] modified the theory to account for different modes of vibration for a multispan tube. For the $\ $th mode of an $\ $-span array with velocity distribution $U_P \ _n$ the critical velocity U_{pci} was given by

$$U_{pci} \sum_{n=1}^{N} (\frac{n}{f d_i}) \ _{in}^{0.5} = \ (\frac{m\delta_i}{\rho d^2})^{0.5} \tag{2.13}$$

where $_i$ is the so-called energy fraction given by

$$_{in} = \int_{l_1}^{l_2} \Phi^2 d \ / \int_0^l \Phi^2 d \tag{2.14}$$

where $l_2 - l_1$ represents the length of the th span.

The energy fraction idea was further developed by Weaver and Parrondo (1991) who suggested a modified expression for the critical velocity according to:

$$U_{pci} \sum_{n=1}^{N} (\frac{n}{f d_i}) \ _{in}^{0.5} = \quad (\frac{m}{\rho d^2 \ _{in}})^{\alpha} \delta_i^{\beta} \tag{2.15}$$

with the new exponents and to be determined from experiments.

Weaver and Parrondo (1991) [83] conducted seven different sets of experiments with airflow over one span of a three-span parallel triangular array with $P/d = 1\ 47$. They compared the experimental results with the estimations given by Eq. 2.15 for $= 3\ 3$ and $= = 0\ 5$ (suggested by Petigrew et. al. (1978) [51]); $= 4\ 8$ and $= = 0\ 3$ (suggested by the experimental correlation of Weaver and Fitzpatrick (1988) [24]) and $= 4\ 6$ and $= 0\ 29$, $= 0\ 21$ (suggested by the experimental correlation of Weaver and El-Kashlan (1981) [55]). Weaver and Fitzpatrick or Weaver and El-Kashlan correlations lead to conservative results, predicting the unstable mode in all the cases. The error in the estimation of the critical velocity, U_{pc} was less than 37% for the Weaver and El-Kashlan correlation while for the Weaver and Fitzpatrick correlation provided less accurate results (77% error). On the other hand, with the Petigrew correlation the error was less than 57% but became unrealible because it could underestimate or even overestimate U_{pc} value. Also, the mode that went unstable was sometimes not predicted correctly. Based on these results Weaver and Parrondo suggested that Eq. 2.15 should be used with $= = 0\ 3, 0\ 4, 0\ 48$ and $0\ 48$ and $= 4\ 8, 3\ 2, 2\ 5$ and $4\ 0$ for parallel triangular, normal triangular, in-line square and rotated square arrays, respectively (see Fig. 2.1).

2.3.9 Computational Fluid Dynamic models

Computational Fluid Dynamic (CFD) techniques has being gaining potential since the early 1990's in the study of the phenomenon of fluidelastic instability in tube bundles. There are a number of limited CFD studies intended to understand particular issues of the flow-induced vibration phenomena or to supply any of the previous theoretical models with the inputs needed to predict the critical velocity.

As a starting point, Marn and Catton (1990) [84] developed a relatively simple code based on the one dimensional unsteady integral approach to investigate the flow induced vibrations in tube bundles. Later, Marn and Catton (1991) [85] considered a

two dimensional analysis to solve the problem, but the prediction of the tube bundle response did not provide good agreement with the experimental data. Eisinger et al. (1995) [86] presented a finite element model of an in-line tube array using the commercial finite element package ABAQUS. In the numerical solution, the fluid forces were obtained from the Unsteady model developed by Chen (1983a,b) [7] [8]. In this case, the results obtained using the simulations were in good agreement with the results provided by Chen (1983a,b) [7] [8]. Besides, Kassera and Strohmeier (1997) [87] developed a two dimensional model for flow-induced vibrations in tube bundles subjected to cross flow. The model solves the unsteady Navier-Stokes equations including the tube motion. The simulations provided a relatively good prediction of the velocity and pressure fields at low Reynolds numbers, but the model was unable to predict the fluidelastic instability correctly. Afterwards, Barsamian and Hassan (1997) [88] investigated the fluid forces fluctuations due to turbulent buffeting in an in-line tube array using a Large Eddy Simulation (LES) technique. The power spectral data obtained using the (LES) simulations were in good qualitative agreement with the experimental results for the same array geometry, although the quantitative comparison was not as good. Later, Schroder and Gelbe (1999) [89] developed two and three dimensional models for a row of flexible tubes in an attempt to improve the design guidelines for fluidelastic instability. Their pressure coefficients obtained in the simulation agreed well with the experimental results, but the same agreement was not achieved for fluidelastic instability patterns. Longatte et al. (2003) [90] introduced a study of the numerical methods used to predict tube bundle vibrations in cross-flow. They used the Arbitrary Lagrange Euler technique to couple the fluid forces coefficients obtained from the CFD solution to the finite element code used to solve the structure motion. Although this work was a first step to develop a real CFD code capable of predicting fluidelastic instability, a relatively good agreement of the tube response frequency was reported. In addition, Sweeney and Meskell (2003) [43] carried out a numerical investigation of the vortex shedding excitations in tube bundles subjected to cross flow. They used the discrete vortex method for a relatively low Reynolds number (= 2200) in order to compare the predicted Strouhal number from the simulations to the experimental results available in the literature. They reported an overall agreement with just a 6% error.

Schneider and Farge (2005) [91] investigated numerically the flow patterns in both staggered and in-line arrays of different tube shapes. The simulations provided reasonable agreement for Reynolds numbers 1000. Complementarily, Liang and Papadakis (2007) [44] used a Large Eddy Simulation (LES) technique to model the vortex shedding in staggered tube arrays subjected to cross flow for Reynolds numbers 8600. The Strouhal number obtained from the simulations was in good agreement with the experimental results.

More recently, Hassan et al. (2010) [13] introduced a numerical estimation of the fluidelastic instability threshold in tube arrays. The authors solved the flow using Reynolds averaged Navier-Stokes equations to obtain the fluid forces coeffcients, and used the unsteady-model developed by Chen (1983a) [7] to predict fluidelastic instability. The stability boundaries predicted by Hassan et al. (2010) [13] with this numerical solution were in a relatively good agreement with the experimental results in the literature.
Fundamental research using CFD has been improved significantly in the last few years. However, the present computational techniques are restricted to low Reynolds numbers and most of the times, they still depend on one of the aforementioned theoretical models to predict fluid elastic instability. Therefore, the ability to solve the fully coupled Navier-Stokes equations with the tubes equations of motions for practical Reynolds numbers [32] is still a formidable task. One of the objectives of this thesis is the development of a numerical numerical tool capable to provide reliable prediction of the onset of fluidelastic instability in tube arrays without the need of any analytical additional approach, neither for the fluid forces nor the tube motion parts.

2.3.10 Comparison of the models

The stability boundaries obtained with a number of relevant theoretical analysis is compared with available experimental data for four different array geometries are presented in Figs. 2.29 to 2.34.
It should be noticed that experimental results exhibit considerable scatter in Upc/fnd in both normal triangular (Fig. 2.29) and rotated square (Fig. 2.31) arrays. If the results for the case of a single flexible cylinder are removed, the scatter is notably reduced for the normal triangular array (Fig. 2.30).
The theoretical models of Tanaka and Takahara (1981) [63], Chen (1983a, b) [7] [8], Price and Paidoussis (1984) [10] and Lever and Weaver (1986) [12] have been all included in the figure for the triangular array. As usual, several jumps are observed in the stability boundaries due to the multiple instability regions occurring at low $m\delta/\rho d^2$. For clarity, only the envelope of the lower boundaries are given. For this normal triangular array, the theoretical model of Lever and Weaver with $P/d = 1\ 2$ tends to underestimate the experimental results. The theoretical curve for $P/d = 2\ 0$ provides a reasonable lower limit, but P/d a typical experimental value. However, comparing Figs. 2.29 and 2.30 it can be seen that many experimental data points with the single flexible cylinder tend to overestimate $U_{pc}/f_n d$ with respect to the case of multiple flexible cylinders. Austermann and Popp (1995)[1] found significant differences in the stability threshold for a single flexible tube in a rigid array, depending on the row in which this tube was located. In general, the lower values were those corresponding with a flexible tube in the third row.

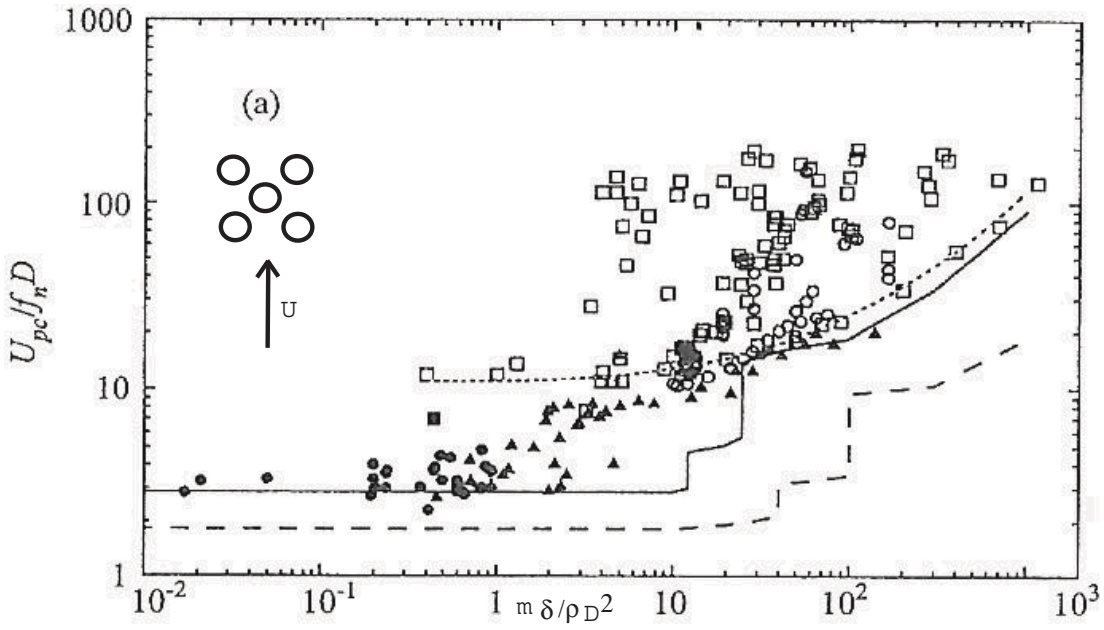

FIGURE 2.29: Stability maps for the normal triangular array. Comparison of model results and different experimental data.

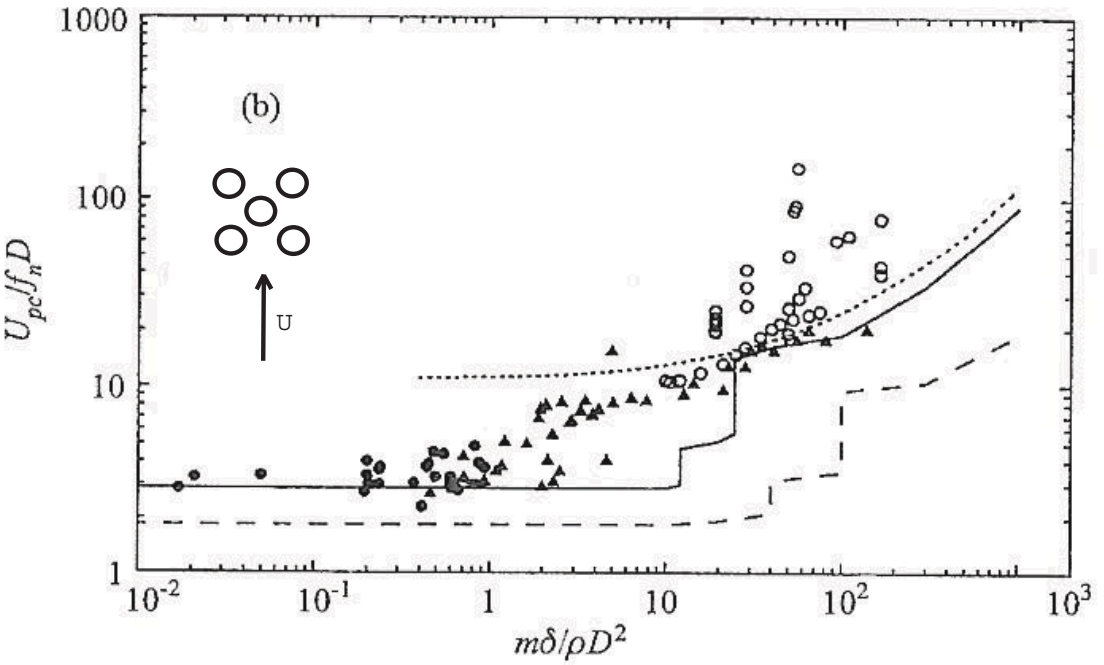

FIGURE 2.30: Stability maps for the normal triangular array. The results from experiments with a single flexible tube have been removed.

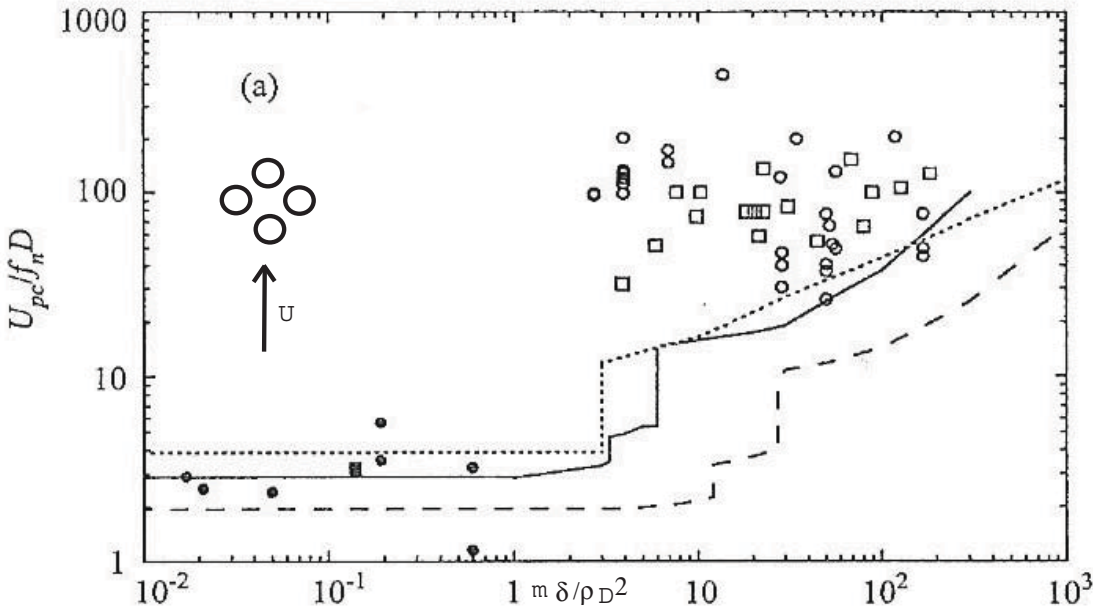

FIGURE 2.31: Stability maps for the rotated square array.

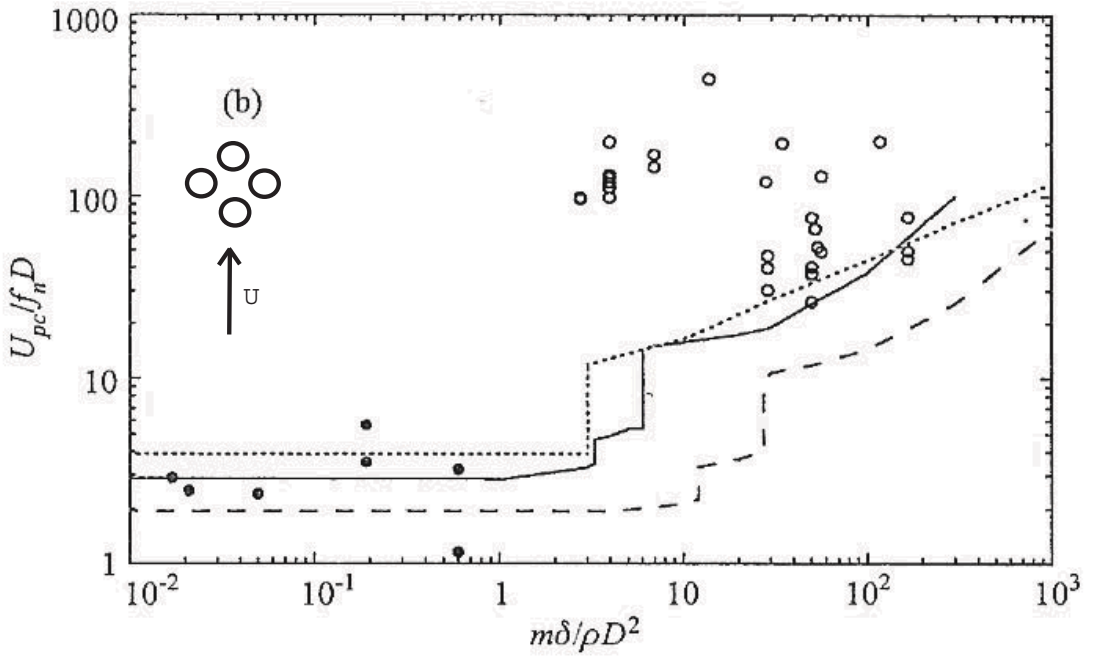

FIGURE 2.32: Stability maps for the rotated square array. The results from the single flexible tube have been removed.

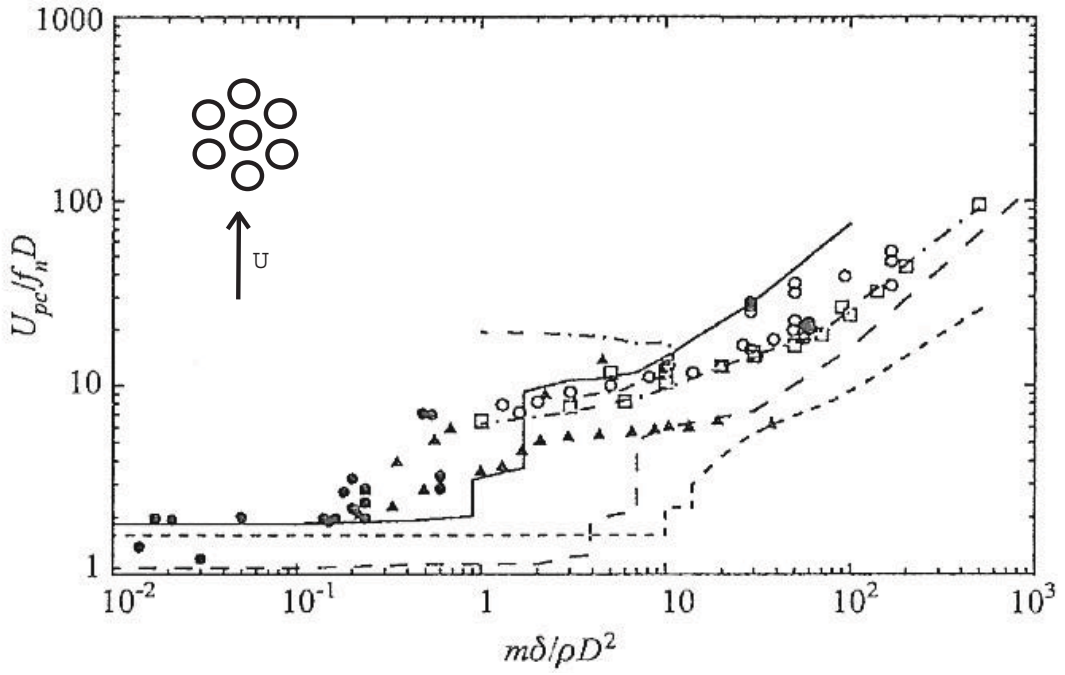

FIGURE 2.33: Stability maps for the parallel triangular array.

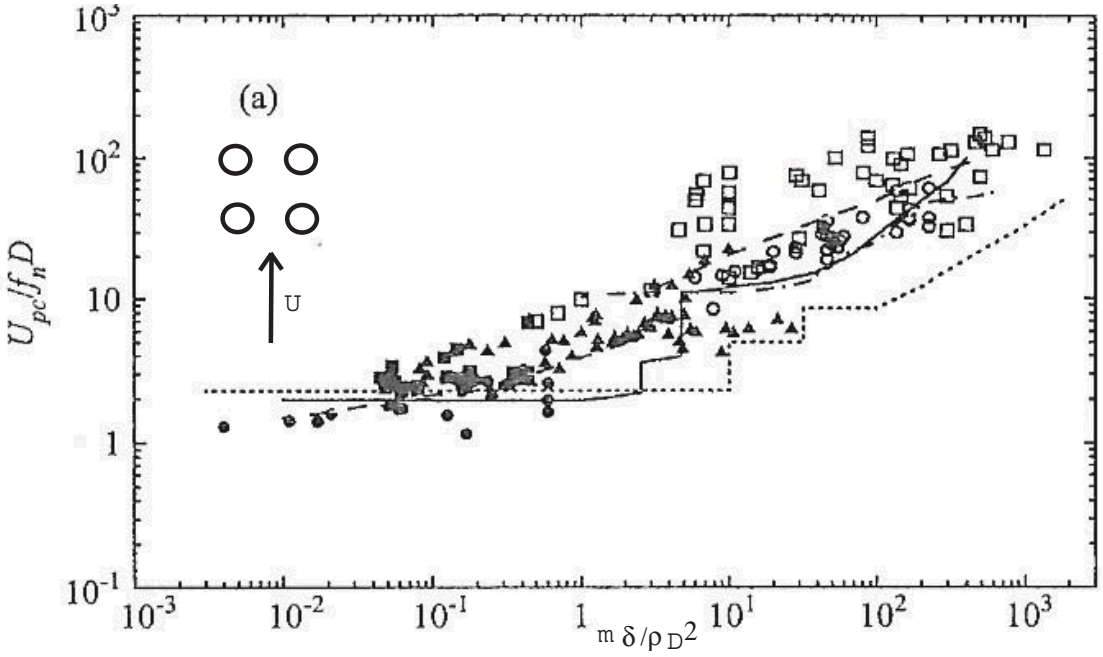

FIGURE 2.34: Stability maps for the in-line square array.

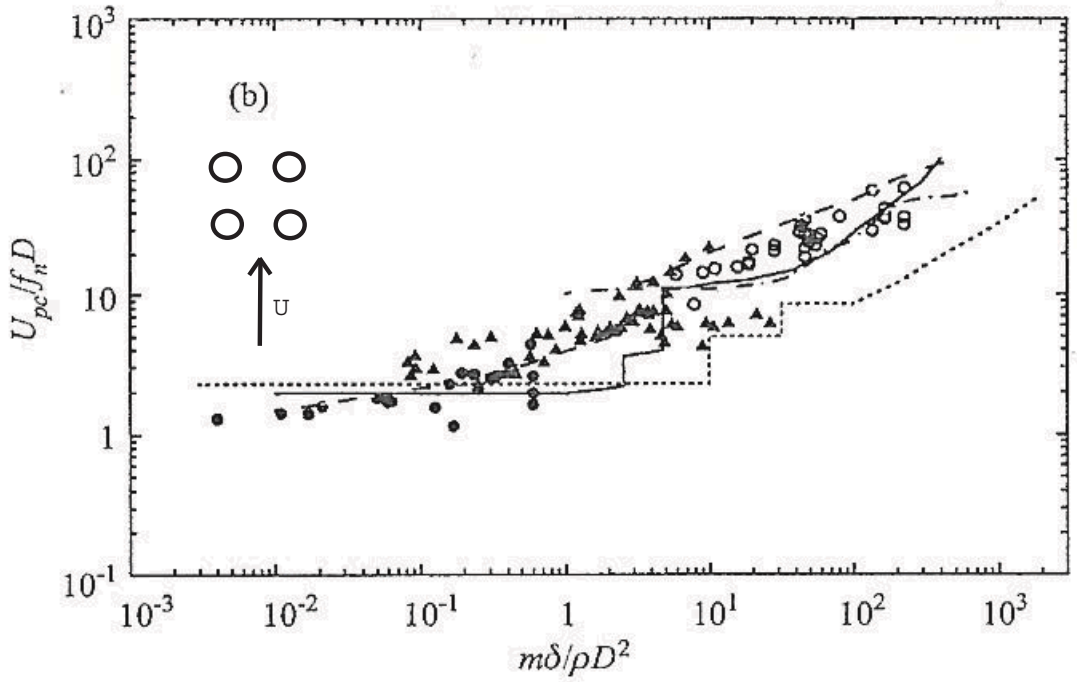

FIGURE 2.35: Stability maps for the in-line square array. Experimental data from single flexible tube have been removed.

Similarly, Khalifa et. al. (2012) [92] found for a parallel triangular array little differences between critical velocities in a rigid array with only one flexible tube in the third row, or with a fully flexible array.

Secondly, a similar comparison is now presented for the case of a rotated square array (see Fig. 2.31). The theoretical stability curve from Lever and Weaver's model (obtained with a single flexible cylinder for P/d=2.0) is very similar to the curve obtained by Price and Paidoussis (with multiple flexible cylindersfor P/d=2.12). Once again, Fig. 2.32. reduces the experimental scatter due to the removal of the results from the experiments with a single flexible cylinder.

Thirdly, Fig. 2.33 shows the comparison between the models and the experiments for the case of a rotated triangular array. For this array, the results obtained from single and multiple flexible cylinders are very similar, so only one data set including all the experimental points is presented. The stability thresholds predicted by either Price and Paidoussis or Lever and Weaver with (P/d = 1 2) tend to underestimate the experimental stability boundary, specially at high mass-damping value. On the contrary, reasonable agreement is obtained at low values of $m\delta/\rho d^2$.

Finally, in the case of in-line square array, excellent agreement is obtained between the experimental results and the theoretical predictions of Chen, Lever and Weaver and

Price and Paidoussis (see Fig. 2.34), especially when only the experimental data from multiple flexible cylinder experiments are considered (Fig. 2.35) [47].

2.3.11 Concluding remarks

Over the recent years, a wide number of theoretical models have been proposed to predict practical stability thresholds for Fluidelastic Instability in the case of tube bundles subjected to cross-flow in heat exchangers. Based on diffferent assumptions and simplifications, they provide reasonable predictions of the critical velocity with acceptable accuracy in most of the typical configurations. An in-depth review of the different proposals has been performed in this chapter, with special focus on the analysis of the hypothesis, the experimental inputs required and the overall level of uncertainty in every model. It has been concluded that most of the models yields reasonable predictons, but many of them need for significant experimental data to be completed. Besides, some models are accurate just for particular configurations, with important lack of fidelity for other conditions. For instance, the ASME design guidelines for heat exchangers, based on conservative empirical correlations developed by Connors' in 1970 [16]are well-accepted and considered reliable by manufacturers and the nuclear engineering community. However, the nuclear power industry is still facing failures due to fluidelastic instability in steam generators [17] [18], indicating that the current knowledge of the fluidelastic instability do not completely captures the complexity of the phenomenon.

Recent advances in computational dynamics (CFD) presents a formidable tool in the investigation of unsteady flows of highly turbulent nature, such those present in the interstitial flows within oscillating tube arrays [47]. This numerical methods also are characterized by its potential for the detailed spatial description of the flow features, which in turn should allow for a more reliable prediction of the critical velocity for FEI. In the last years, several authors have investigated the interaction between tube vibrations and flow perturbations under particular conditions. Moreover, the possibility of coupling CFD predictions and theoretical models to define accurate critical velocities has been explored intensively. However, while many aspects of CFD are mature and well understood, it is often clear what appropriate modeling strategies are the best selection for a particular system configuration.

The possibility of simulating the dynamic response of the flow-structure interaction is already available in the commercial CFD codes. This is essential to explore numerically possible different situations involving FEI phenomena, even operating at unstable regimes with dominant non-linear terms (for instance in the area of fluid kinetic energy conversion). Taking advantage of the current state-of-the-art of computational tools, this thesis pretends to develop a CFD methodology able to simulate the self-excited

response of tube arrays under fluidelastic instability. As a secondary objective, it is also necessary to provide a tool for further analysis of the characteristics of the interstitial flow in vibrating tube bundles.

Chapter 3

CFD Methodology.

3.1 Calculation levels and validation plan

A CFD methodology with capability for dynamic meshes has been developed to simulate the fluid-structure interaction in arrays involving cylinder vibration response to cross-flow conditions. Both normal and parallel triangular arrays with different pitch-to-diameter ratios have been selected as simulation geometries in order to compare the numerical results with the published experimental data. In addition, the numerical model developed for this study has been tested at three different calculation levels: static calculations, forced vibration and self-excited oscillations. In the case of unsteady simulations, one or several tubes were allowed to vibrate either in the transverse direction only or with two degrees of freedom, taking advantage of the features of the dynamic meshes. With these characteristics, it was possible to investigate the onset of Fluidelastic Instability for different possible scenarios. In particular, the situation with one single flexible tube oscillating only in the transversal direction has been widely analyzed in this work because FEI vibration can only be developed due to damping mechanisms [7] , [8] in this case. Moreover, this condition is really convenient to study the correlation between the tube motion and the associated flow fluctuations. It must be noted that experimental evidence [1], [92] indicates that the FEI critical velocity for arrays with one single flexible tube can be very dependent on the location of the flexible cylinder in the array. Previous works have concluded that the lowest critical velocities were observed when the flexible tube is placed in the third row. Furthermore, Khalifa et al. (2012) [92] have found, collecting and analyzing data in the bibliography, that lowest critical velocity for arrays with one flexible tube is very close to the FEI critical velocity for fully flexible arrays.

The proposed methodology, which has been developed with the commercial code ANSYS-Fluent 12.1 [93], includes the motion of vibrating cylinders by means of a special User Defined Function. With this capability, the domain is remeshed at every time step in the dynamic simulations , allowing the description of the time-resolved interaction between the vibrating tube and the incoming cross-flow.

Five different validation tests have been conducted to contrast the three calculation levels. Experimental data, available in the literature, has been employed for that purpose. Moreover, an experimental facility has been specifically designed to obtain additional measurement in the case of forced vibration. Following, a detailed analysis of the effect of different parameters (geometrical and functional) on the stability thresholds has been performed for the different stages of the study. Also, the interstitial flow pattern, the propagation of the perturbations through the cross-flow [67] and the associated time delays have been discussed extensively. The results, discussion and conclusions obtained have been structured in separated chapters according to the calculation level (see also Fig. 3.1):

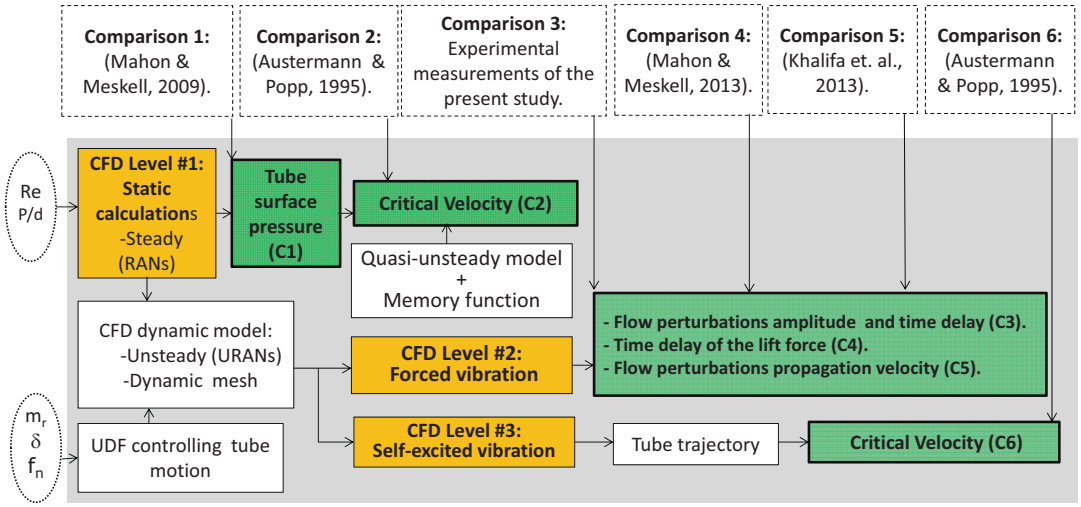

FIGURE 3.1: Road map for the CFD Methodology: Calculation levels and check-points for validation with experimental data.

Level #1: Static calculations (Chapter 4). As a starting point, the influence of the mesh refinement, the selection of the boundary conditions (type and position) or the turbulence closure were addressed comparing the static CFD results with two empirical data sets. Firstly the numerical pressure distribution on the cylinders was compared with the measurements conducted by Mahon and Meskell [19] for the normal triangular array with P/d=1.32. Secondly, the force coefficients obtained from the CFD simulation with a displaced static tube were introduced as input data for the quasi-unsteady model

of Granger (1996). The required memory function was taken from the Meskell theoretical approach [20] and the stability threshold was finally obtained to be compared with experimental data. In particular, the numerical critical velocities for $P/d = 1\ 25$ and $P/d = 1\ 32$ were compared with the empirical stability thresholds of Austerman and Popp [1]. After the validation of this hybrid methodology using CFD input data for an unsteady theoretical model, the effect of the Reynolds number and both mass and pitch ratios in the critical velocity was investigated.

Level #2: Forced oscillations (Chapter 5) Unsteady simulations with forced vibration of one of the tubes in the transverse direction were carried out next. On the one hand, the set of configurations tested by [2] in the case of a normal triangular array with P/d=1.32 were reproduced numerically. On the other hand, a parallel triangular array with P/d=1.57, corresponding to the home-made experimental facility, was also simulated under conditions of forced vibration. The time step for these transient CFD simulations was carefully checked in order to balance the consistency of the results with the optimization of the CPU time. The validation was conducted using the time delay between the tube motion and the lift force as the reference indicator to compare the numerical estimations with the experimental results. Both experimental data from Mahon and Meskell (2013) [2] and from our own laboratory tests were used at this level. This unsteady approach has allowed to describe the flow pattern of the interstitial flow and to quantify the non-dimensional time delay, a key parameter for the description of the fluidelastic instability. Also, the transmission of flow perturbations through the array was discussed for both normal and parallel triangular geometries. The obtained results were analyzed in terms of amplitude and phase lag of flow perturbations, representing maps of velocity magnitude and static pressure.

Level #3: Self-excited oscillations (Chapter 6) The simulation of the spontaneous response of a flexible tube in a cylinder array, which at this stage, basic structural parameters for the vibrating tube, as well as its equation of motion have been introduced in the computations by means of a User Defined Function. The validation of the numerical predictions has been focused on the critical velocity for the two sets of tube arrays tested experimentally by Austermann and Popp (1995) [1]. The numerical routine consisted on the increment of the cross-flow velocity in discrete intervals (5% of experimental U_c) and also in the analysis of the trajectories of the oscillating tube in order to determine the sign of the net damping. At this point, the good agreement with the experimental data allowed to analyze the effect of the Reynolds number, the Pitch ratio and also the number of degrees of freedom of the vibrating tube. Hence, orbital trajectories and net damping evolution with increasing U_c were analyzed for both triangular patterns.

Finally, the effect of a second flexible tube oscillating at different relative positions was studied for the case with the parallel triangular array (P/d=1.57).

3.2 CFD basic characteristics

The numerical simulations carried out for this work are based on 2D URANS computations with a commercial CFD code, complemented with user defined functions to incorporate the motion of the vibrating tubes. In particular, this model has been applied to several configurations in order to reproduce the experimental set-ups with available measured data in the literature or those conducted in the lab for this investigation. Three different calculating levels, including static conditions, forced vibrations and self-excited vibrations were progressively performed. The interstitial flow pattern, the propagation of perturbations along the cross-flow and, finally, the effect on the critical velocity of the Reynolds number, the pitch-to-diameter ratio and the degrees of freedom of the vibrating cylinder were studied.

Several triangular tube arrays were considered for this investigation, with pitch-to-diameter ratios ranging from 1.25 to 1.58. The 1.32 value was used by [19] in their experiments, while the values of 1.25 and 1.375 were used by [1] in a normal triangular array. Also, and the $P/d = 1\ 57$ value was selected for the simulation of the parallel triangular array of the home-made experimental facility. The calculation domain was extended a total length equivalent to nine tube diameters in both upstream and downstream directions. Fig. 3.2 shows the typical triangular configuration valid for all the different P/d ratios. In this figure label V corresponds to the tube that can became unstable, under the different calculation levels conditions, while T1-T8 are fixed tubes referenced at several points in the study.

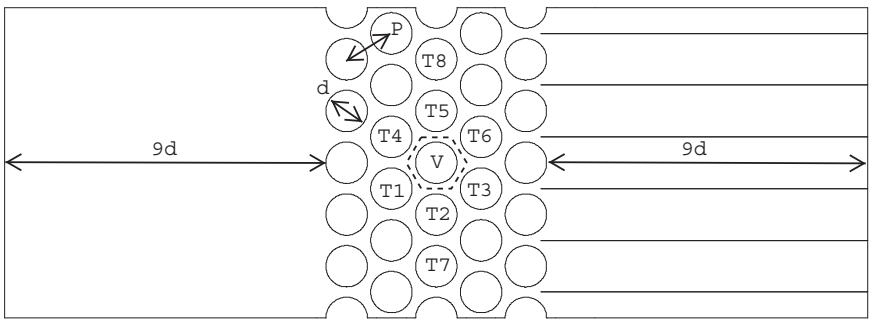

FIGURE 3.2: Triangular array configuration. Extension of the computational domain as proposed.

Preliminary steady flow calculations static conditions (all cylinders rigid), showed the interference during the iterative process of large scale oscillations in the region downstream as can be seen in Fig. 3.3. This was attributed to instability in the numerical procedure since it does not correspond to the experimental observations. This type of oscillations had also been reported by [13], that decided to truncate the domain from the last column of the array as a means to suppress the appearance of those large scale structures. However this procedure implies imposing boundary conditions (constant outlet pressure) at the flow through the array itself, and that may not be realistic to model properly the propagation of disturbances throughout the flow, which is crucial for the development of the FEI phenomenon. As an alternative strategy, full-slip guide plates were placed behind each tube of the last row, parallel to main stream (see Fig.3.2) in order to allow for a reasonable distance between the array and the domain outlet while preventing large scale oscillations. The flow pattern obtained with the proposed solution is shown in Fig. 3.4.

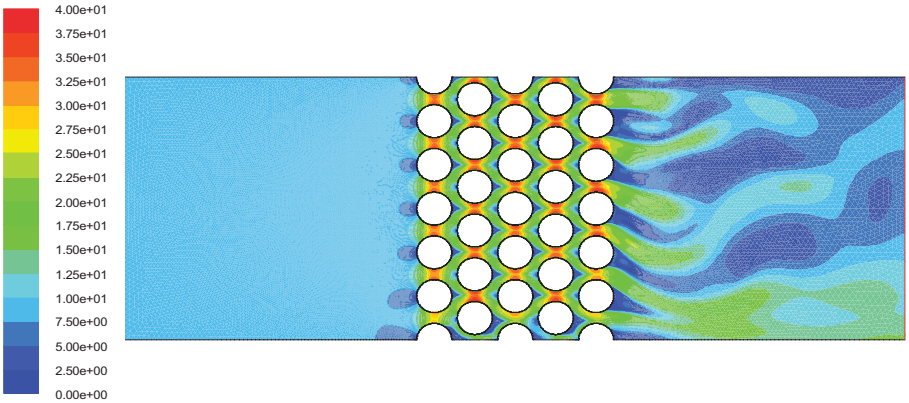

FIGURE 3.3: Example of large wake oscillations downstream the array.

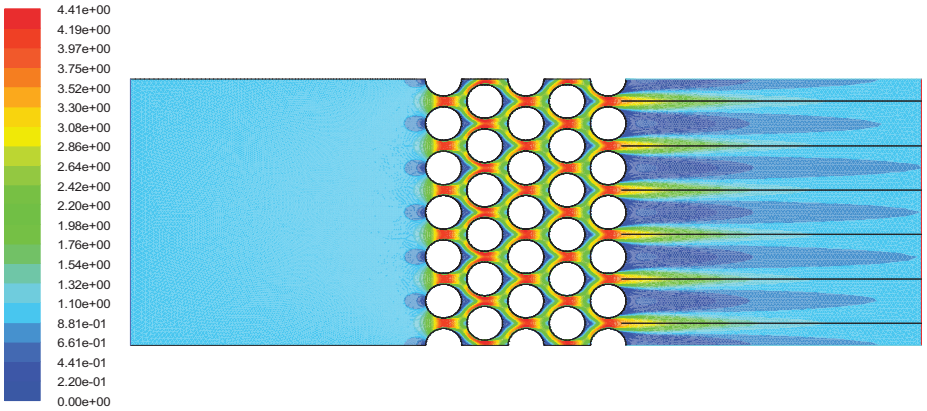

FIGURE 3.4: Typical velocity contours obtained with the proposed configuration.

Another important feature is the correct definition of the mesh design and the corresponding sensitivity analysis. Fig. 3.5 shows a general view of the meshed domain with its relevant characteristics. To discretize this domain, an hybrid mesh strategy was followed as the most convenient for the expected dynamic behaviour of the vibrating tubes. In particular, a specially refined grid was used around each cylinder in the array, composed of quadrilateral elements with an initial thickness of 0.06 mm and a growth factor of 1.15 until the 13th row of cells. This element discretization was found to produce $^{+}$ values in the tube "V" surface of the order of 1 for all the simulations conducted. The rest of the inter-cylinder domain was meshed using triangular elements of progressively greater size when separating from the tubes (see Fig. 3.6).
Furthermore, in order to prepare the model to deal with cylinder oscillations, a hexagonal region was defined surrounding the vibrating tube, in which the triangular cells could either shrink or expand depending on the instantaneous tube position (see Fig. 3.7). It was found that triangular cells are needed in these areas because they prevent the mesh degradation observed in the case of quadrilateral elements (due to cell sides normal to motion direction). On the contrary, the 13 lines of refined mesh with quadrilateral cells were allowed to move attached to the oscillating tube, without undergoing deformation and hence not suffering from degradation. The rest of zones, both upstream and downstream the array, were meshed using quadrilateral cells in order to provide a more homogeneous, symmetric and economic mesh (see Fig. 3.8).Using these mesh guidelines, it was observed during computations involving cylinder motion, that the grid did not suffer an excessive distortion, even in the cases with cylinder displacements above a 4% of the tube diameter and for the smallest pitch-to-diameter ratios (P/d=1.25, Fig. 3.7).

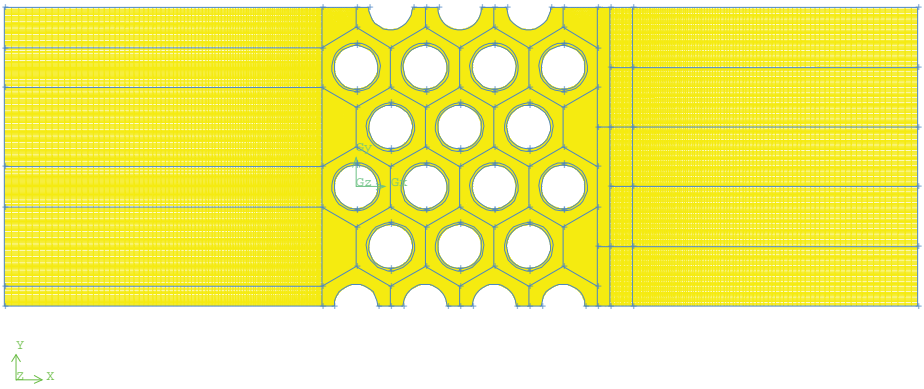

FIGURE 3.5: Example of a typical domain mesh configuration.

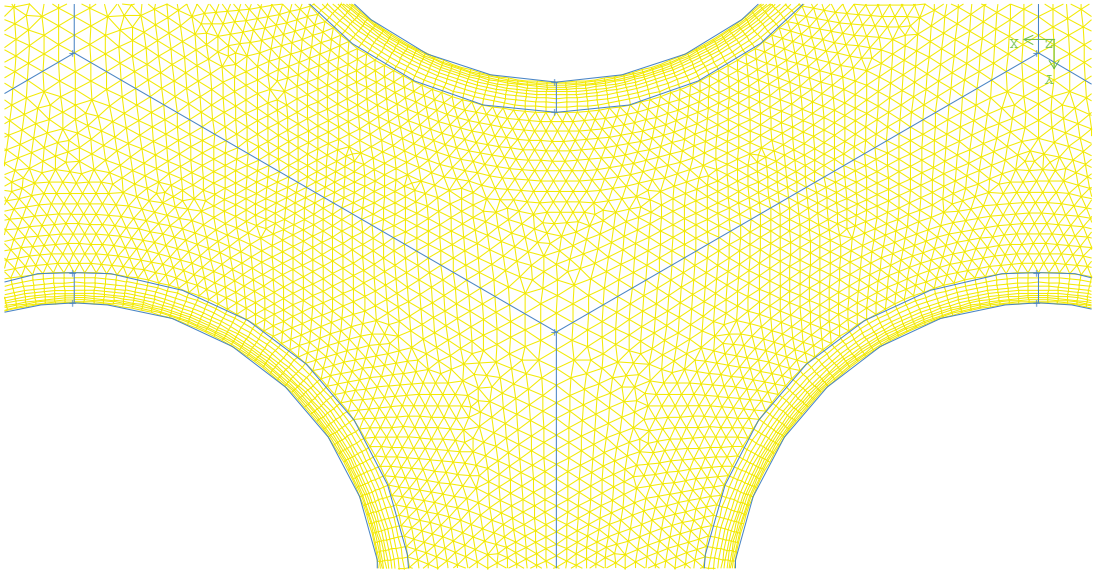

FIGURE 3.6: Detail of the intercylinder mesh.

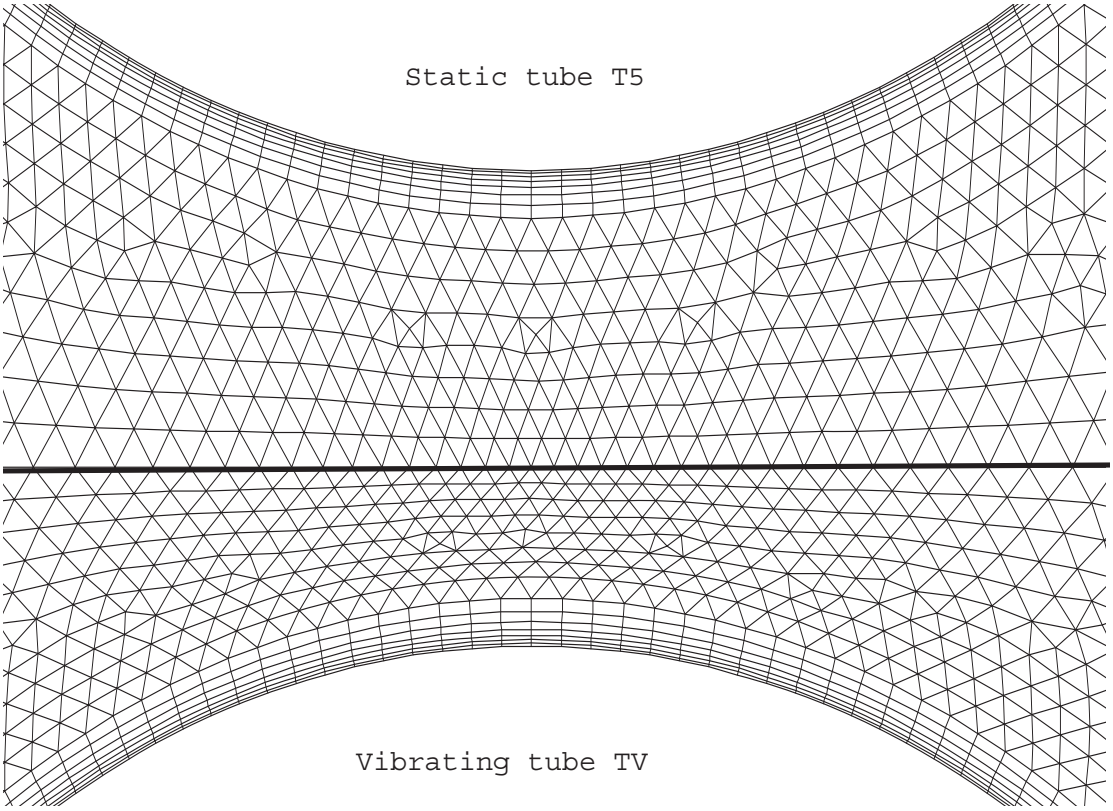

FIGURE 3.7: Mesh deformation in the region between cylinders T5 (static) and TV (shifted 5% of tube diameter upwards), P/d=1.25.

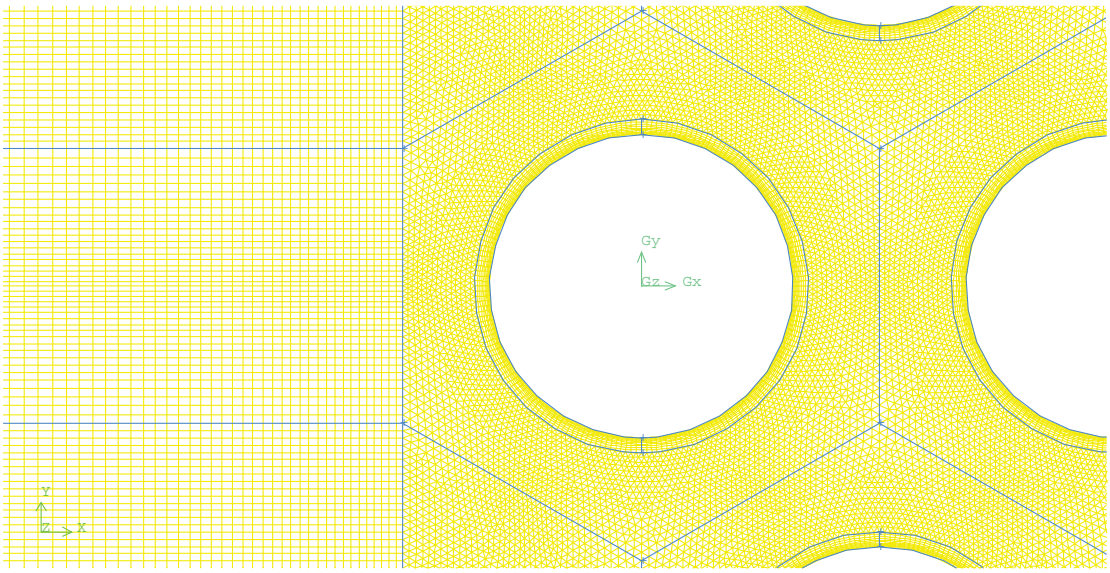

FIGURE 3.8: Detail of the mesh for the structured, quadrilateral mesh in the region upstream.

Finally, the effect of cell size was analyzed by comparing the fluid forces computed for meshes with four different refinement degrees. Each mesh was characterized by the number of nodes along the tube nodes along the tube perimeter, which varied between 100 and 250. Two different parameters were monitored for the analysis: the derivative of the lift coefficient on the central tube TV (Fig.3.2) with respect to its transverse position and drag coefficient of the cylinder. These variables have been selected because they are the relevant parameters used in the quasi-steady and quasi-unsteady models to predict stability critical conditions [10],[11]. The derivative of the lift coefficient was estimated with a first order central difference scheme obtained when the tube TV was displaced out of its center a +/- 0.5% of the tube diameter in the transverse direction.
Fig. 3.9 shows the results obtained for the different mesh densities, with respect to the data for the most refined mesh. It is observed that above the 150-node mesh, the control variables are practically unaffected to further refinements. Consequently, a typical mesh density corresponding to a 200-node mesh on the tubes has been employed for the simulations of this thesis, with differences lower than 1.6% for the left derivation, and 0.06% for the drag coefficient with respect to the 250-node case. The corresponding total number of cells in the domain ranged from 0 28 million for $P/d = 1$ 25 to 0 4 million for P/d=1.58.

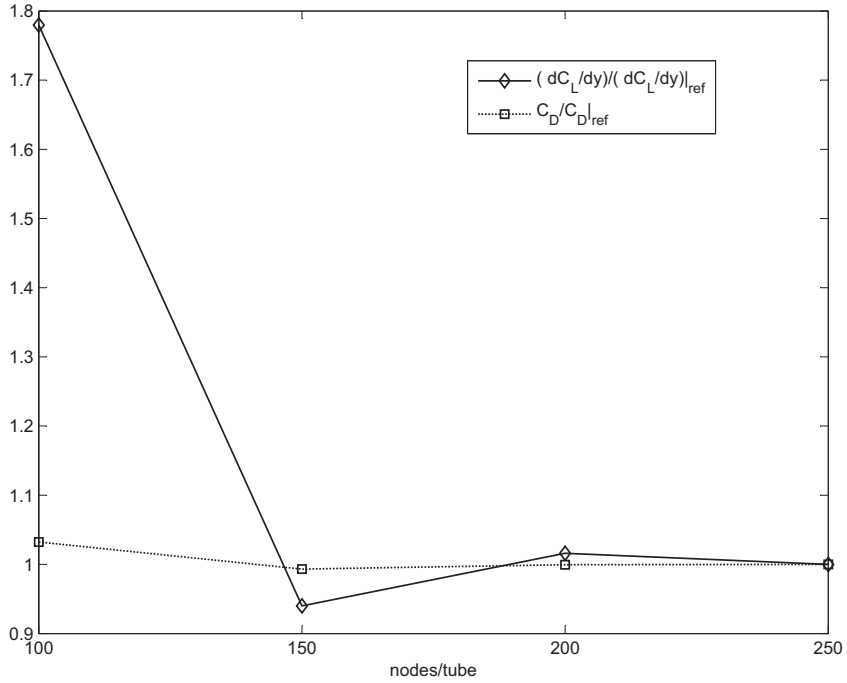

FIGURE 3.9: Effect of the number of nodes along the cylinder surface. (P/d=1.25).

Chapter 4

Static Calculations

In this chapter, an hybrid approach using the theoretical quasi-unsteady model of Granger and Paidousis (1996) [9], with CFD results as input data, has been employed to study damping-controlled Fluidelastic Instability in the case of normal triangular tube arrays. This model requires the force coefficients on the cylinders as well as a memory function to predict the maps of critical velocity. The former have been estimated in a CFD steady simulation while the latter were obtained theoretically using the simple wake model proposed by Meskell (2009) [20]. The combined methodology allows the prediction of stability thresholds using structural parameters only, with no need for further experimental data.

Five normal triangular tube arrays, with pitch-to-diameter ratios of 1 25, 1 30, 1 32, 1 375 and 1 44, were investigated. CFD pressure distributions in the tube surface for the $P/d = 1\ 32$ array, predicted by the CFD, were compared with empirical measurements available in [17], allowing for a first validation of the proposed numerical simulation.

Following, force coefficients, obtained with the validated CFD model, were used to predict stability thresholds for the $P/d = 1\ 25$ and $P/d = 1\ 375$ tube arrays. Moreover, results were employed for a second comparison, with experimental critical velocities measured in [1].

Finally, the proposed theoretical-CFD hybrid methodology, depicted in Fig. 4.1 was used to analyze and quantify the dependence of the critical velocity on three different parameters: the mass ratio, the Reynolds number and the pitch ratio.

4.1 Comparison #1: Pressure coefficient on tube surface

Steady Navier-Stokes equations have been resolved in the numerical domain and mesh density described in Chapter 3 to obtain the pressure coefficients on the cylinder under

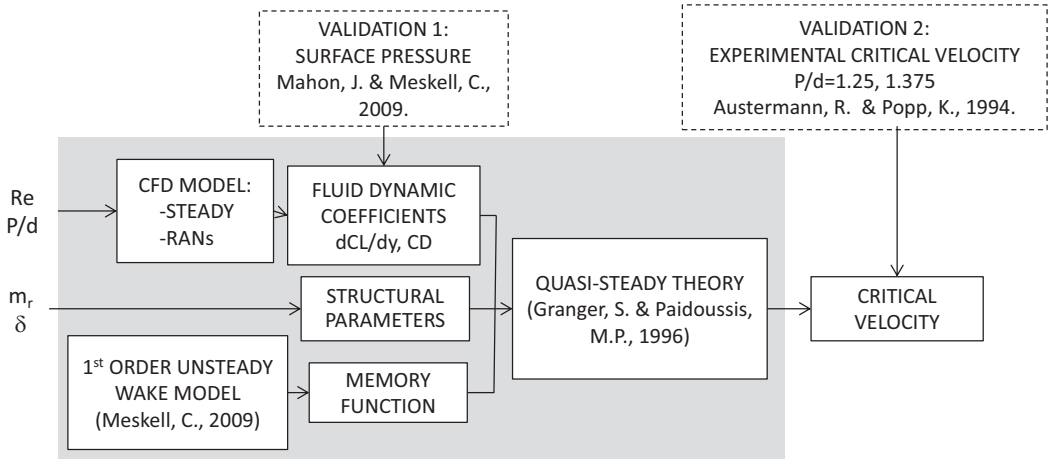

FIGURE 4.1: Sketch of the hybrid methodology proposed and validation plan for in level #1, static calculations.

static conditions. A series of computations have been performed. To select the most appropriate calculation parameters in order to match the CFD predictions to the wind tunnel data presented in [17]. In particular, the static pressure distribution around the surface of the central cylinder (labeled as "TV" in Fig.3.2) has been obtained in the case of P/d=1.32 for several cross-flow velocities. These pressure data have been non-dimensionalized according to the following definition of a pressure coefficient:

$$P^* = \frac{P_\Theta - P_\Theta|_{max}}{(P_\Theta|_{max} - P_\Theta|_{min})} \tag{4.1}$$

where $P_\Theta|_{max}$ is the stagnation pressure (i.e., P at $\Theta = 0°$). The denominator computes the maximum pressure difference in the cylinder (between $\Theta = 0°$ and $\Theta = 90°$ or $\Theta = 270°$, approximately) pressure values. First of all, the effect of the turbulence model on the numerical results is addressed in Fig. 4.2, where Mahon and Meskell's experimental data are compared to a set of CFD predictions. Three different turbulence models, for an upstream air velocity of 2 m/s, were considered: a standard − , a − with shear stress transport corrections (− -SST) and a − with renormalization group (− -RNG) complemented with non-equilibrium wall treatment corrections [93]. The results show that all the numerical predictions are reasonably close to the experimental data, although the standard − model gives the closest fit in the wake region. On the other hand, the two − models seem to yield more asymmetric results than the − -RNG. However, the accurate estimation of the lift forces is crucial in this case because FEI phenomena is usually associated to vibrations in hte traverse direction. Also, note that these forces are mostly determined by the pressure at those regions, where the static pressure is minimum. Precisely, the best predictions were obtained for the − -RNG model. As a consequence, and because of the overall good agreement of

all the models this was the model selected for the subsequent computations.

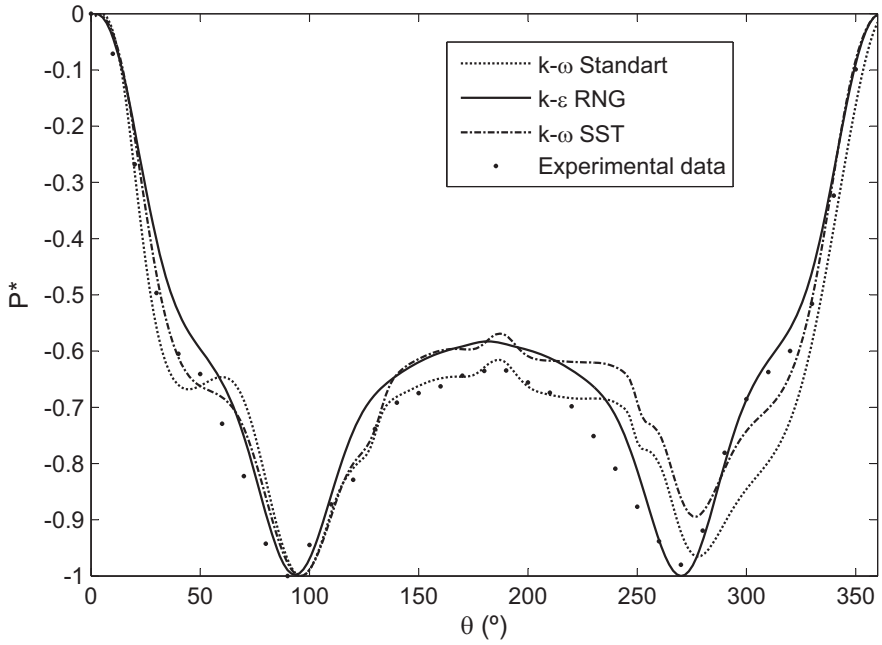

FIGURE 4.2: Pressure coefficient on the central tube (TV). Comparison between different turbulence models and Mahon and Meskell's experimental data.

Following, another computation series explored the effect of the boundary conditions imposed at the channel lateral edges, downstream the array. Firstly, they were modeled as full-slip solid walls, neglecting any perpendicular flow (similar to symmetry conditions). Secondly, those planes were considered as periodic boundaries with repetition of flow features (perpendicular flow is no longer restricted). Figs.4.3 and 4.4 show the pressure distributions obtained with both boundary conditions around the reference cylinders T1, T3 and D, as depicted in Fig.3.2. Though the three cylinders belong to the same row, the periodic boundary condition (Fig.4.4) is seen to produce the most symmetrical flow in the domain, with almost identical pressure distributions around the three cylinders.

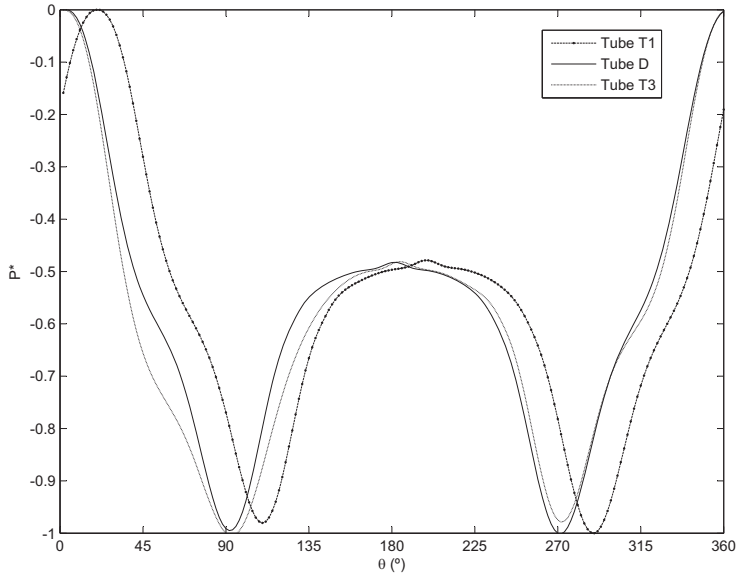

FIGURE 4.3: Pressure coefficient in tubes T1, T3 and D. Phase lag observed between then when solid walls are set as boundary conditions array downstream.

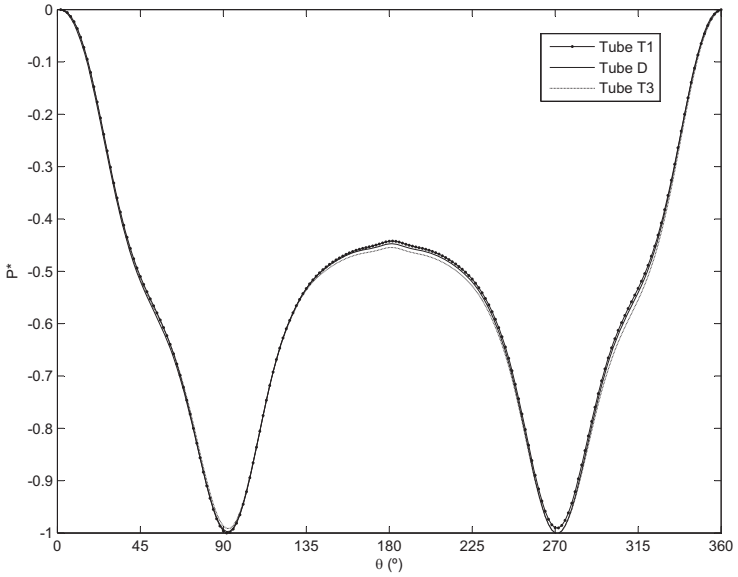

FIGURE 4.4: Pressure coefficient in tubes T1, T3 and D when periodic boundary conditions are used instead: phase lag is corrected.

Consequently, the periodic boundary conditions were finally employed for the rest of the cases. This symmetric pattern for the stream flow can also be appreciated in Figs.4.5 and 4.6, where typical (steady) contours of velocity and static pressure are shown.

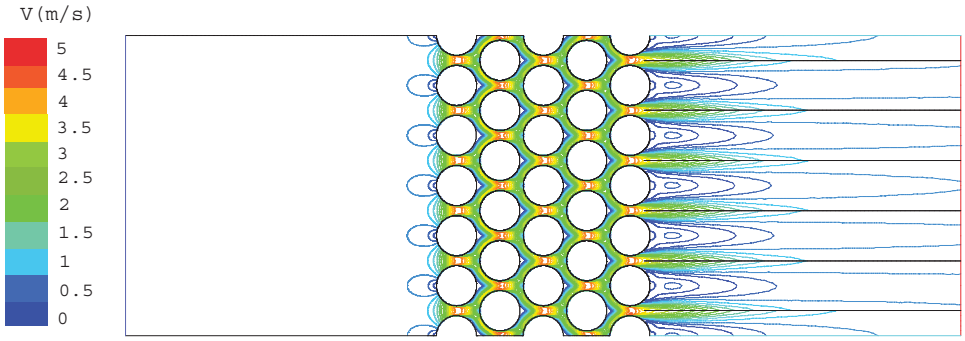

FIGURE 4.5: Contours of velocity magnitude. Typical steady air-flow simulation with P/d=1.25 and U0=0.89 m/s (P/d=1.25, U_0=0.89 m/s).

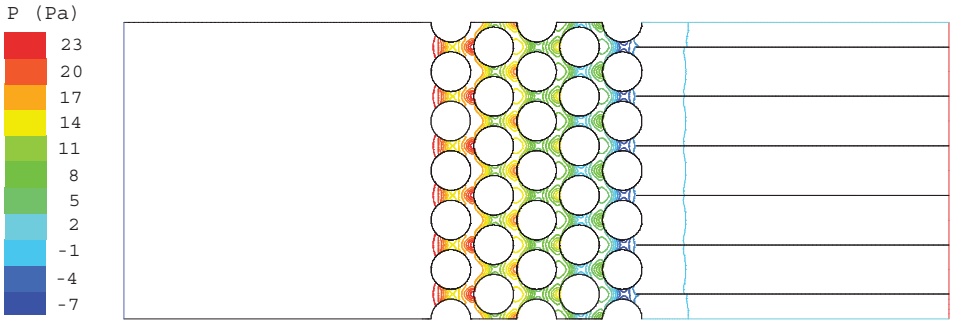

FIGURE 4.6: Contours of static pressure. Typical steady air-flow simulation with P/d=1.25 and U0=0.89 m/s (P/d=1.25, U_0=0.89 m/s).

4.2 CFD force coefficients + Quasi-unsteady model

4.2.1 Methodology

The governing equation of motion for a tube in an array subjected to a fluid elastic force can be expressed in a general way as:

$$m_s \ddot{} + \quad _s \dot{} + \quad _s \quad = \quad (\ddot{}, \dot{}, \quad , U_0) \tag{4.2}$$

This simple formulation ignores both turbulent buffeting and vortex shedding phenomena. However, because this general function is unknown, various models have proposed alternative procedures to determine its mathematical expression. One initial proposal [8] used the quasi steady approach, which assumes that the instantaneous force on the oscillating tube is equal to an equivalent time-lagged force on the cylinder when it is statically displaced to the same position.

This model was later improved in an unsteady fashion [9], to represent the time lag as a function (a memory function), which describes the relation between the instantaneous fluid forces and the static lift force. In this quasi-unsteady model, an expression for the instantaneous lift forces on the oscillating tube is given according to:

$$F_y(\ ) = -\frac{1}{2}\rho d^2 \quad C_M \ddot{} + \frac{1}{2}\rho U^2 \quad d(\frac{dC_L}{d} \quad * \quad - C_D \dot{}) \tag{4.3}$$

where d and L represent the diameter and length of the tube, rho is the fluid density, U is the free-stream velocity and C_M, C_L and C_D are the mass, lift and drag coefficients, respectively. Here, the tube displacement is convolved with the delay function . The drag, is considered to have an impact even in the y-direction (due to the quasi-unsteady assumption), although its influence is really small when compared to the lift force. The convolution integral can be expressed as

$$* \quad = \int_0^\tau \quad (\quad - \quad _0) \quad (\ _0) d \ _0 \tag{4.4}$$

with h representing the memory function

$$(\ ) = \frac{d\Phi}{d} \tag{4.5}$$

The transient evolution of this memory function, which is essential for accurate predictions under FEI phenomena, is controlled by the function Φ. This transient function converges towards 1 as approaches infinity. It can be represented as a series of decaying exponentials [9], based on Schwartz theorem:

$$\Phi = (1 = \sum_{i=1}^{N} \quad _i \quad ^{-\beta_i \tau}) \quad (\ ) \tag{4.6}$$

Previously [9] the parameters $_i$ and $_i$ were found by fitting the model response to experimental data observed in an array subjected to cross-flow. More recently, a simple wake model has been propesed by [20] to predict the values of $_1$ and $_1$ with a first-order theoretical model. This mathematical model assumes that the memory function is the normalized instantaneous bound circulation on the tube. Hence, modeling the wake as a discretized vortex sheet, an equation for the memory function is achieved. Combining this consideration with the solution of the equation of motion in the Laplace domain, a fourth-order polynomial for the critical velocity is obtained.

$$\sum_{i=1}^{4} \ _i U_c^i = 0 \tag{4.7}$$

in which $_i = \ _i(\ _0, m_r, C_D, \frac{dC_L}{dy}, \ _1, \ _1)$. A further description of the model and definition of these coefficients can be found in Appendix B.

With this model, the only required inputs for the model to predict critical velocities are: the structural properties $_0$, (the damping ratio) and m_r (the mass ratio), as well as the static fluid force coefficients C_D and $\frac{dC_L}{dy}$. Though force coefficients have been traditionally obtained via experimental testing, this study will deal with numerical simulations to provide a set of values for these coefficients (see Fig. 4.1). Finally, in order to obtain stability thresholds, equation 2.6 is used to complete the model.

4.2.2 Comparison #2: Critical velocity from static calculations of force coefficients + quasi-unsteady theory

A second validation test has been conducted to match the experimental tests presented in [1]. Two different array configurations with P/d=1.25 and P/d=1.37 have been simulated in air for the same Reynolds number range adopted in the experiments, ($= 2\ 1 \times 10^4 \rightarrow 7\ 4 \times 10^4$). Using the values for $\frac{dC_L}{dy}$ and C_D obtained from these simulations, the critical velocity was hence calculated, for the mass ratio and the structural damping range corresponding to the structural parameters of their experimental work, ($m_r = 493, \delta = 0\ 02 \rightarrow 0\ 14$).

The comparison between the numerical predictions and the experimental critical velocities is shown in Figures 4.7 and 4.8. Besides, the numerical values corresponding to the different mass damping parameters in those figures, can be seen in Tables 1 and 2, respectively, where the difference in the results is also given in the table, in terms of relative error.

It is observed that the hybrid methodology is consistenly underpredicting the critical velocity for both array configurations. The differences are larger for the P/d=1.25 configuration (relative differences ranging between 37 and 62%) than for the P/d=1.37 array (differences reduced to a closer range between 0 and 28%). However, in qualitative terms, it can be concluded that the thresholds trend are reasonably captured for the two arrays, which it is a promising result of the methodology if all the constraints of the current level of approach are considered. It was concluded that the approach is sufficient to conduct an analysis of dependence of different parameters.

$m_r\delta$	CFD	Experimental	Difference %
11 4229	8 8371	14 1477	−37 53
14 6031	9 1270	14 1477	−35 48
18 6686	9 5077	15 5518	−38 86
22 6754	9 8682	16 5645	−40 42
26 7096	10 1832	17 6431	−42 28
29 5877	10 3848	18 7920	−46 04
34 4967	10 7566	21 3190	−49 54
39 8107	11 1065	22 7072	−51 08
49 3552	11 6961	25 7608	−54 59
59 3381	12 2801	27 4382	−55 24
69 1831	12 8579	34 2174	−62 42

TABLE 4.1: Comparison of predicted critical elocit and e perimental data from [1] for the P/d=1.25 tube array

$m_r\delta$	CFD	Experimental	Difference %
11 4791	16 3019	14 8398	9 85
18 5047	18 8069	18 6822	0 01
25 1722	21 0993	23 5195	−10 29
33 1694	24 1279	30 5995	−21 15
42 3378	28 3505	39 8107	−28 78

TABLE 4.2: Comparison of predicted critical elocit and e perimental data from [1] for the P/d=1.375 tube array

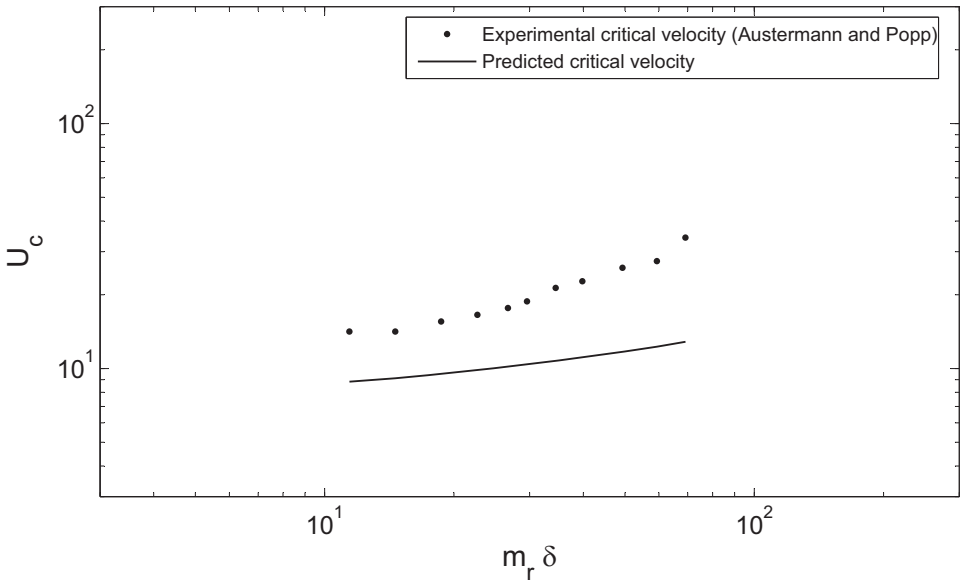

FIGURE 4.7: Predictions of the critical velocity with the hybrid theoretical-CFD methodology U_c. Comparison with experimental data from [1]. P/d=1.25 tube array.

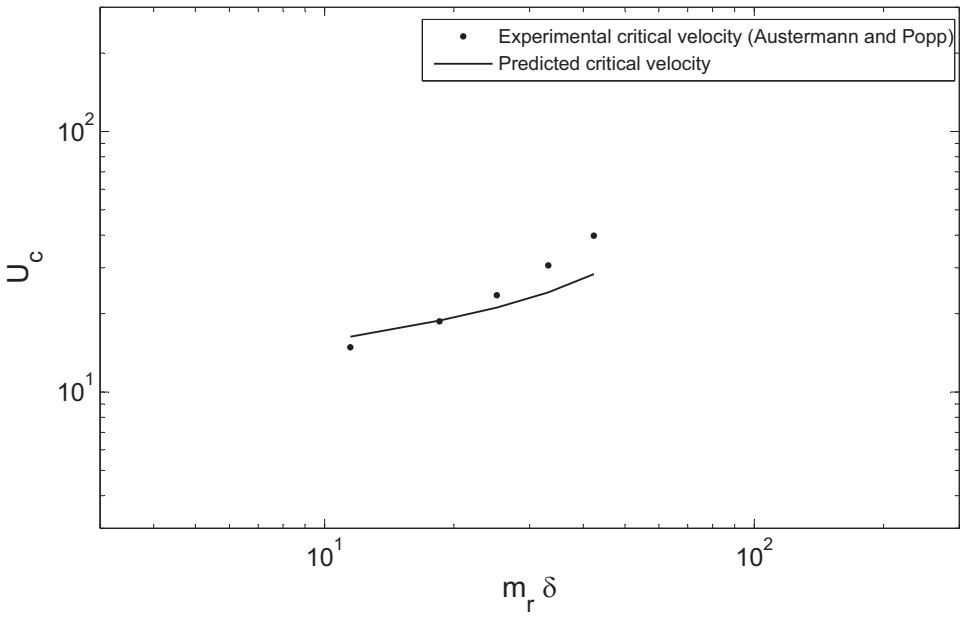

FIGURE 4.8: Predictions of the critical velocity with the hybrid theoretical-CFD methodology U_c. Comparison with experimental data from [1]. P/d=1.375 tube array.

4.2.3 Effect of different parameters in the prediction of the critical velocity

Predicted stability maps show a significant dependence on the Reynolds number and the mass ratio. Figs. 4.9 shows the effect of increasing the Reynolds number over a range of $= 10^4 \rightarrow 9 \times 10^4$ and the mass ratio over a range of ($m_r = 10 \rightarrow 10^7$), respectively. As can be seen, an increment in both parameters leads to a higher critical velocity, being evident for the threshold in the case of Re, but only for higher mass damping parameters in the case of m_r. A certain pitch ratio dependence can also be observed comparing Figures 4.5 and 4.6, corresponding to the thresholds of the the P/d=1.25 and $P/d = 1\ 375$ arrays.

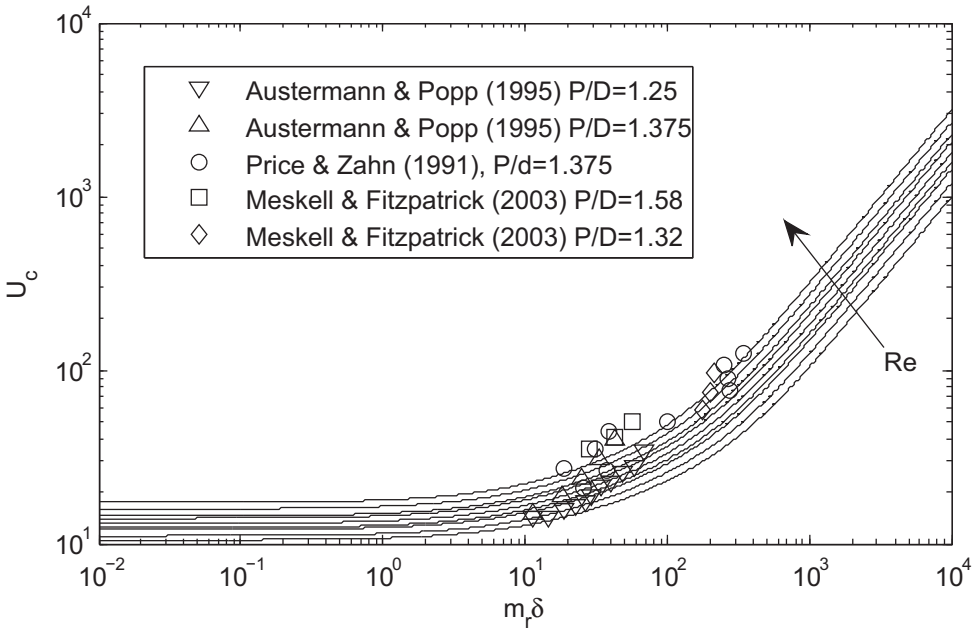

FIGURE 4.9: Effect of Reynolds number in the stability threshold. Comparison with experimental data.

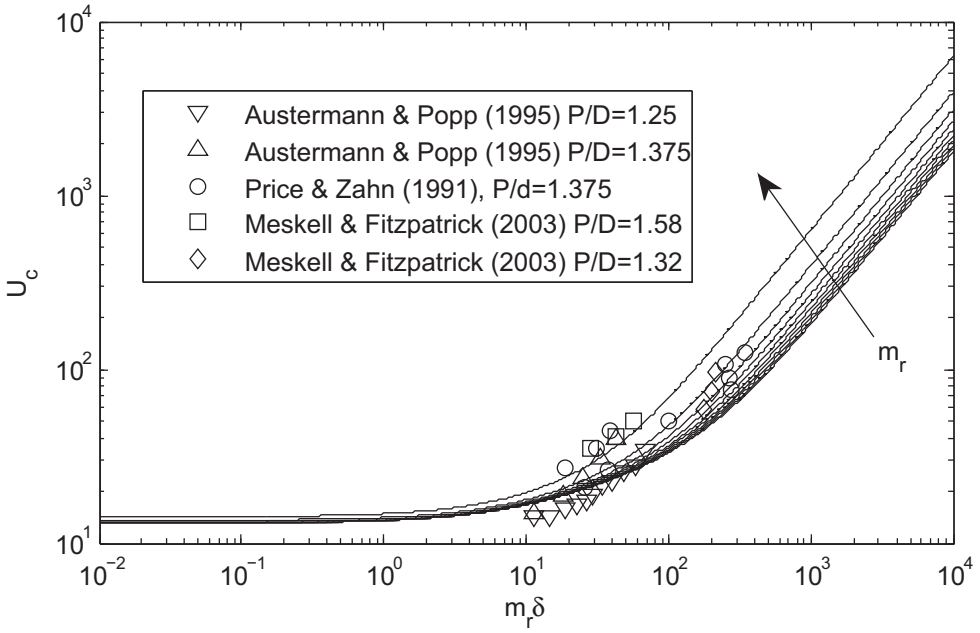

FIGURE 4.10: Effect of mass ratio in the stability threshold. Comparison with experimental data.

Furthermore, in order to quantify the specific dependency of the critical velocity on these parameters ($P/d, m_r,$), up to 90 steady simulations, corresponding to the 5 pitch-to-diameter ratios ($P/d = 1\,25, 1\,30, 1\,32, 1\,375, 1\,44$), 9 Reynolds numbers ($= 10^4 \rightarrow 9 \times 10^4$) and two positions of the displaced tube ($-0\,005d, 0\,005d$) were carried out. Following the same hybrid procedure, 6 mass ratios ($m_r = 10 \rightarrow 10^7$) and 13 structural damping values ($\delta = 10^{-9} \rightarrow 10^3$) were considered in this analysis. The combination of these parameters reported a total number of 3510 stability thresholds analyzed , which are summarized in Table 4.3.

Parameter	Range	Number of values
P/d	$(1\,25 \rightarrow 1\,44)$	5
	$(\quad = 10^4 \rightarrow 9 \times 10^4)$	9
m_r	$(m_r = 10 \rightarrow 10^7)$	6
δ	$(\delta = 10^{-9} \rightarrow 10^3)$	13
Stability thresholds		3510

TABLE 4.3: Parameters range and number of alues considered in the stud of the critical elocict dependenc .

4.2.3.1 Effect of Reynolds number

In this subsection, the effect of the variation of the Reynolds number on the prediction of the critical velocities is discussed. For that purpose, the Reynolds number is ranged over one order of magnitude (from 10^4 to $9*10^4$). Representation of the reduced critical velocity, Uc*, as a function of Re, is given for a wide range of the mass-damping parameter, i.e. from $m_r\delta = 10^{-2}$ to 10^4. Firstly, the mass ratio was modified, going from 10 to 10^7, to obtain Figure 4.11. Secondly, the structural damping was varied from 10^-4 to 10^-2 to get Figure 4.12 In this case the reduced critical velocity has been normalized as:

$$U_c^* = \frac{U_c}{U_c^{ref}} = \frac{U_c}{U_{c(Re=5\times10^4)}} \tag{4.8}$$

With this non-dimensional U_c^* velocity, the effect of a general increase of the critical velocity at higher $m_r\delta$ values is isolated, so the specific effect of the parameters and m_r is evaluated only.

Previously, it was shown that the predicted stability threshold increased with for all mass damping parameters (Fig. 4.9). It was also found that m_r affects to higher mass damping parameters, only (Fig. 4.10). This suggested a major impact of the parameter m_r for higher mass-damping parameter values that will be discussed hereafter.

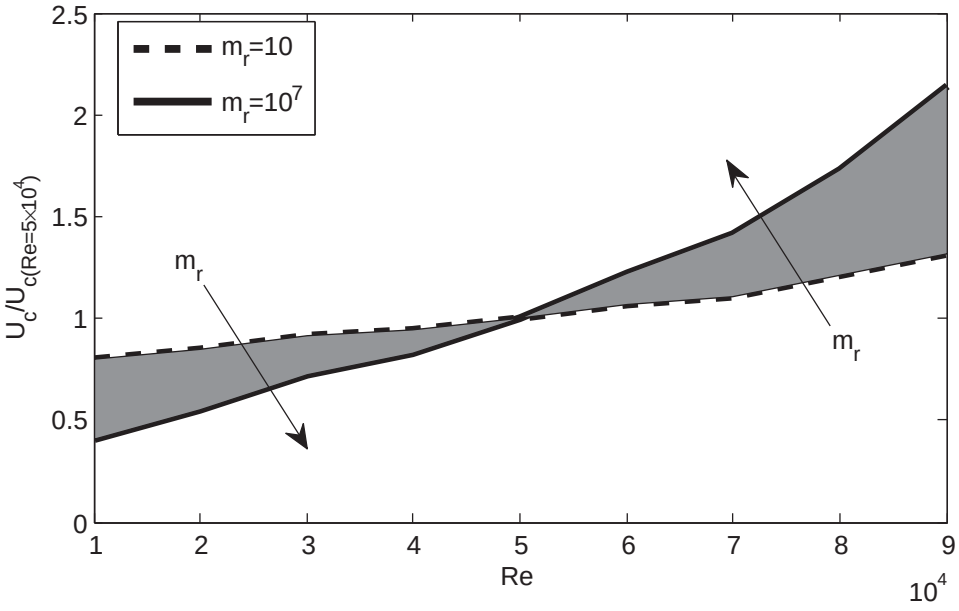

FIGURE 4.11: Effect of the Reynolds number in the critical velocity for different m_r values.

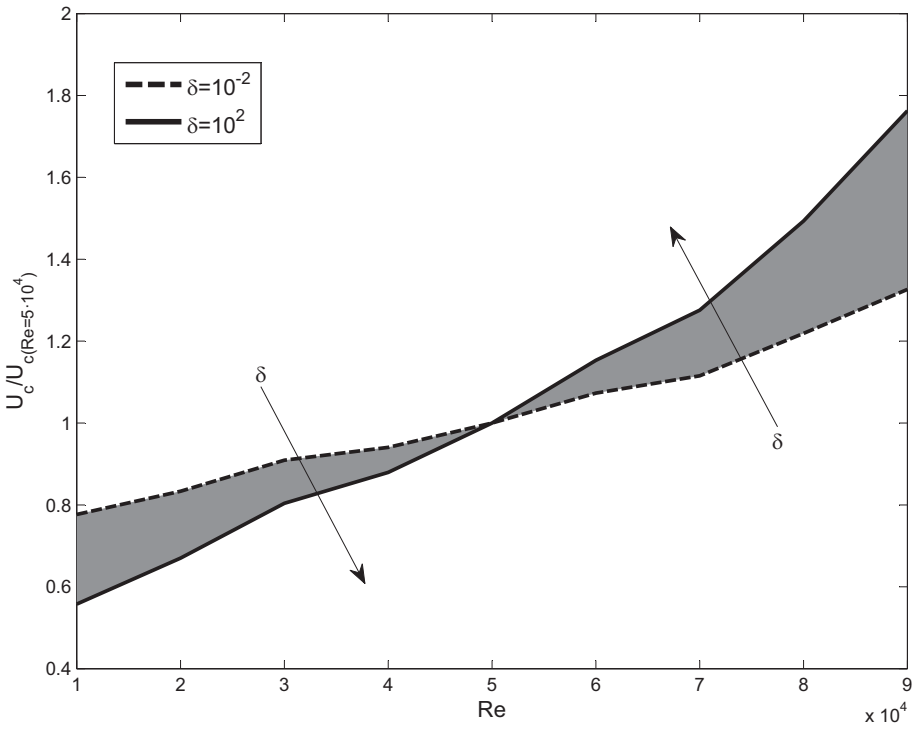

FIGURE 4.12: Effect of the Reynolds number in the critical velocity for different δ values.

In addition, previous figures 4.9 and 4.10 indicated that the case of the lower $m_r\delta$ value (in particular $m_r = 10$ and $\delta = 10^{-4}$ is not dependent to m_r variations, so this condition will be employed to study the effect of the Reynolds number.
Calculating the increase of the critical velocities in any of the two curves a factor of $\sim$ 1 6 is obtained. With the width of the evaluated in perspective, these results would indicate that Reynolds number effect is moderate and considering experimental or numerical inputs obtained at low Reynolds numbers in the theoretical models, would be a reasonable approach from the side of the security, at a design stage.

4.2.3.2 Effect of mass ratio

The effect of the mass ratio in the critical velocity will be discussed in this subsection. For each mass damping parameter, $m_r\delta$, in the stability threshold, we are interested in comparing U_c predictions obtained with different m_r values. However, m_r is one of the factors that compose the own mass damping parameter, so in order to obtain comparable

increased (and consecuently δ decreased) in seven orders of magnitude $m_r = 10 \rightarrow 10^7$. The three constant mass damping parameters considered were: $m_r\delta = 10^{-2}$, $m_r\delta = 10^4$ and $m_r\delta = 10^4$. Table 4.4 describes the particular values of the parameters in this study.

m_r	δ	$m_r\delta$
$10 \rightarrow 10^7$	$\delta = 10^{-3} \rightarrow 10^{-9}$	$m_r\delta = 10^{-2}$
$10 \rightarrow 10^7$	$\delta = 1 \rightarrow 10^{-6}$	$m_r\delta = 10$
$10 \rightarrow 10^7$	$\delta = 10^3 \rightarrow 10^{-3}$	$m_r\delta = 10^4$

TABLE 4.4: Mass ratio and damping values considered to obtain each constant mass damping parameter.

Fig. 4.13 shows the results of this study. As expected (see Fig. 4.10) different sensitivity of U_c to m_r was found depending on the zone of the map. For lowest $m_r\delta = 10^{-2}$, $-U_c^*$ curves are almost coincident. As the mass damping parameter increases, m_r influence becomes stronger and gradient of these curves increases more noticeably for higher m_r values. In the extreme situation, $(m_r\delta = 10^4)$, critical velocity predictions in the $-U_c^*$ curves obtained for $(m_r = 10 \rightarrow 10^7)$ increased 60%.

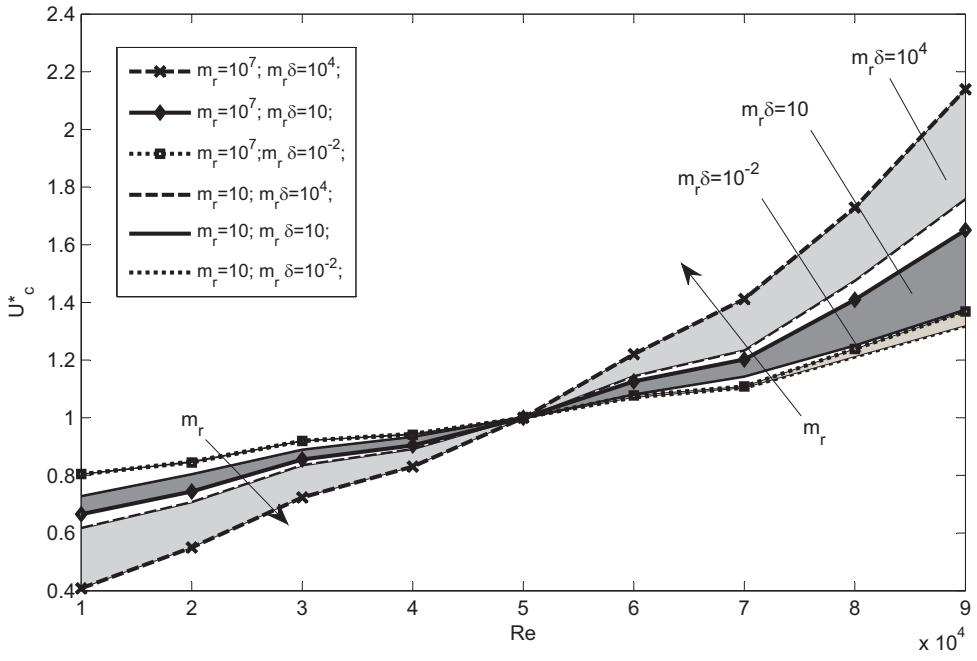

FIGURE 4.13: Mass ratio effect in U_c for constant $m_r\delta$.

Considering that the range of m_r evaluated was extremely width, these results would indicate that the mass ratio effect is very modest, only affecting to higher mass damping

parameters. Obviating the of m_r effect, or using coefficients obtained (numerically or experimentally) at low m_r values, as inputs for the the quasi-unsteady model, would be a reasonable simplification to obtain conservative predictions.

4.2.3.3 Effect of pitch ratio

Finally, the effect of the pitch ratio on the prediction of the critical velocity is discussed in Fig. 4.14. Five different pitch ratios have been studied ($P/d = 1\ 25, 1\ 30, 1\ 32, 1\ 375$, $1\ 44$). In this case, the non-dimensional critical velocity has been defined as: The effect of increasing the pitch ratio in the predicted critical velocity will be discussed in this subsection. Pitch ratio values evaluated were: $P/d = 1\ 25, 1\ 30, 1\ 32, 1\ 375$ and $1\ 44$. The normalized critical velocity in this subsection was defined as:

$$U_c^* = \frac{U_c}{U_c^{ref}} = \frac{U_c}{U_{c(P/d=1.375)}} \tag{4.9}$$

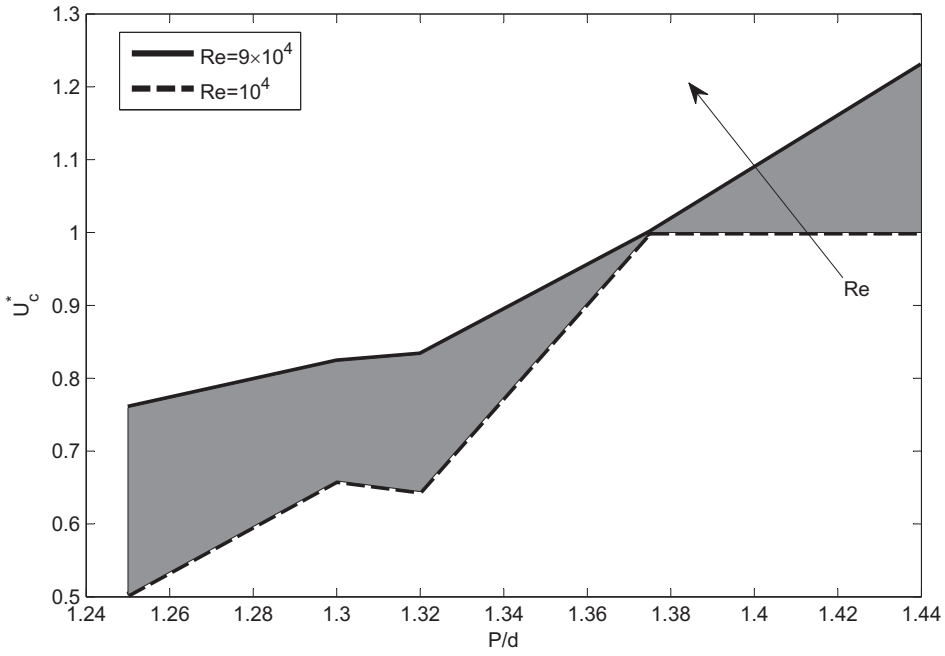

FIGURE 4.14: Pitch ratio effect in U_c at different Reynolds numbers ($= 10^4 \rightarrow 9 \times 10^4$).

The curves obtained at different Reynolds numbers (from $= 10^4$ to $9 * 10^4$ as before) reveal that for the range of P/d values evaluated, the critical velocity is consistently

increased (between a 50-60%) for all the Reynolds numbers. In other words, it can be suggested that the higher pitch-ratios contribute to increase the thresholds for critical velocities.

Chapter 5

Forced Oscillations

In this chapter, a series of dynamic simulations have been conducted with a tube in motion under harmonic forced oscillations in the traverse direction. For that purpose, a special routine (user defined function [93]) was coupled to the CFD code so position and velocity of the tube could be conveniently updated at every time step during calculations. Results of the CFD model in this level of calculations are compared with experimental data obtained in the present investigation and also to the empirical measurements given by Mahon and Meskell (2013) [2] and Khalifa et al. [3]. In particular, the amplitude and phase lag of the flow perturbations, the time delay between the tube motion and the force coefficients and the propagation velocity of the flow perturbations have been compared to the CFD results of the forced oscillations model. Finally, the flow pattern for the oscillating tube array has been analyzed and disused for different geometries as well as cross flow velocities. Contour maps of velocity and pressure, in terms of amplitude and phase lags, have been rendered for the analysis.

5.1 Comparison #3: Experimental data of the propagation of pressure perturbations.

A campaign of experimental tests under forced oscillations has been specifically developed in order to investigate the transmission of the flow perturbations in a triangular array, in terms of amplitude and time delay. A detailed description of the set up and the preliminary tests conducted in this experimental study can be found in Appendix A. The reasonable repeatability and the moderate dispersion observed for these results has allowed to develop a useful empirical study of the nature of the flow perturbations, as discussed in this section.

The experimental setup consisted in a parallel triangular array of 7 tube rows and 5

lines, with $P/d = 1\ 57$ and $d = 10mm$. The tube placed in the fourth row and the third line was forced to vibrate in the transverse direction. Static pressure perturbations were monitored in four points located in the static tubes around the vibrating cylinder in the channel between the third and the fourth lines of the array. Fig. 5.1 shows a sketch of the array with the location of the monitored points, indicated by green markers.

Series of tests were carried out for five different oscillation frequencies, ranging from 10 to 25 Hz and repeated twice to assure repeatability. The measurements reported by the pressure transducers (green markers in Fig. 5.1) were correlated with the tube motion data, via two accelerometers (monitoring X and Y components). Only the four first harmonics were analyzed in the post-processing routines (in the range of 10-75 Hz) because the data dispersion was found to be excessive at high frequencies.

The experimental measurements, regarding amplitude and phase lag, were compared with the results reported by the CFD methodology proposed with forced vibrations, four different frequencies in the range of the experimental tests (11, 20, 40 and 60 Hz) were simulated. In order to allow for the contrast with the empirical data, the numerical domain has exactly corresponded to the experimental conditions and geometry: $P/d = 1\ 57$, $d = 10mm$ and $U_g = 0$ (See Fig. A.1 in Apendix B). The results are discussed in Figs. 5.2-5.8, where the data corresponding to the two series of tests (repeatability) are plotted with red and blue square markers respectively. In addition, the CFD results are represented with black pentagonal markers. Data corresponding to those points located in symmetrical positions of the array (with respect to the tube motion) are discussed together, because they are expected to have the same value. In particular, this corresponds to the T1-T4 and T2-T3 pairs of tubes, located in symmetrical positions because the test was conducted with no cross-flow.

The non-dimensional pressure coefficient in these figures is defined according to:

$$P^* = \frac{\Delta P}{\Delta\ d\rho_w f^2} \tag{5.1}$$

where Δ is the amplitude of the vibration in the transverse direction, ΔP is the amplitude of the static pressure perturbations in the measurement point, d is the tube diameter, ρ_w is the water density and f corresponds to the oscillation frequency.

This non dimensional pressure was defined to allow for a realizable comparison of the results between the CFD simulations and the experiments. In the CFD, the amplitude of vibration was only $\Delta = 0\ 01d$ (in order to avoid excessive mesh deformation that would provoke degraded cells in the domain) while in the experimental test, the oscillations were an order of magnitude larger (approximately $\Delta = 0\ 1d$ for the first harmonic) in order to reduce the relative errors due to the uncertainty in the measurements.

Figs.5.2 and 5.3 show the amplitude of the pressure perturbations, comparing the results on tubes T2-T3 and T1-T4 respectively. An abrupt increase of several orders of

magnitude is observed for frequencies higher than 30-40 Hz (corresponding to data of high-order harmonics), due to the inability of the experimental set up to measure the low amplitude perturbations taking place above the first harmonic, when the amplitude of vibration falls to the order of magnitude of 10^{-7} (see also Fig. 5.4). Nevertheless, if the results of the higher order harmonics are not considered, CFD and experimental results show a reasonable good agreement in quantitative and qualitative terms, as can be seen in Figs. 5.5 and 5.6.Those figures represent a reduced range of values of P^* corresponding to the results within the first harmonic for both T2-T3 and T1-T4 cylinders. Obviously, the amplitude of the pressure perturbations is higher in tubes T2 and T3 than in the others, T1-T4, because its location in the channel is closer to the vibrating tube. Also, these amplitudes is seen to be directly related to the square of the vibrating frequency, being more clear in the case of the CFD results (the range of frequencies of the experimental values is lower), though they are also reasonably consistent. This result, which indicates that pressure perturbations depend only on the tube velocity, was to be expected since the experimental measurements were conducted under no cross-flow conditions.

Complementary, Figures. 5.7 and 5.8 show the phase lag of the flow perturbations with respect to the tube motion , for both T2-T3 and T1-T4 transducers). It can be seen that static pressure is in phase with the tube position, because the lag tends to zero when the frequency decreases. However, then for higher frequencies the phase lag increases linearly, revealing a constant propagation velocity of the pressure perturbations in the channel. As expected, phase lag in tubes T2 and T3 was lower than in tubes T1 and T4, as they are monitoring points of the channel closer to the source of perturbations. Also, this constant propagation velocity is in agreement with the experimental measurements obtained by Khalifa et al. [3] for a very similar geometry (parallel triangular array $P/d = 1\ 58$) under cross-flow conditions. Those authors observed very linear phase lag for the velocity of the flow perturbations estimating averaged values of 0 42m/s and 1 90 m/s (upstream and downstream the vibrating tube, respectively). In the present study the propagation velocity has been calculated with the data of tubes T1-T4 at f=70 (the phase lag is higher so the relative error in the estimation should be lower) obtaining a final estimation of $U_p = 1\ 04m/$. Note that this result, obtained with no cross-flow, is between the upstream and downstream values proposed in Khalifa et al. [3] under cross-flow conditions, which is coherent to the fact that for decreasing cross flow velocities upstream and downstream propagation rates should converge to an intermediate value.

Although the experimental data obtained in this these laboratory routines was quite limited, measurements of propagation velocity were found to be similar to those available in the literature [3]and coherent conclusions were reported for the specific conditions of our experiment. CFD model showed a satisfactory agreement with empirical measurements

for amplitude and phase lag parameters in both quantitative and qualitative terms. This fact, in addition to the good agreement found in the previous section with the experimental time delay of the lift force for the normal triangular tube array [2], allows the validation of the numerical model (under the calculation level of forced vibration) and encourages, to conduct the set of tests for the transmission of the flow perturbations and the analysis of the patterns which are discussed in the following section.

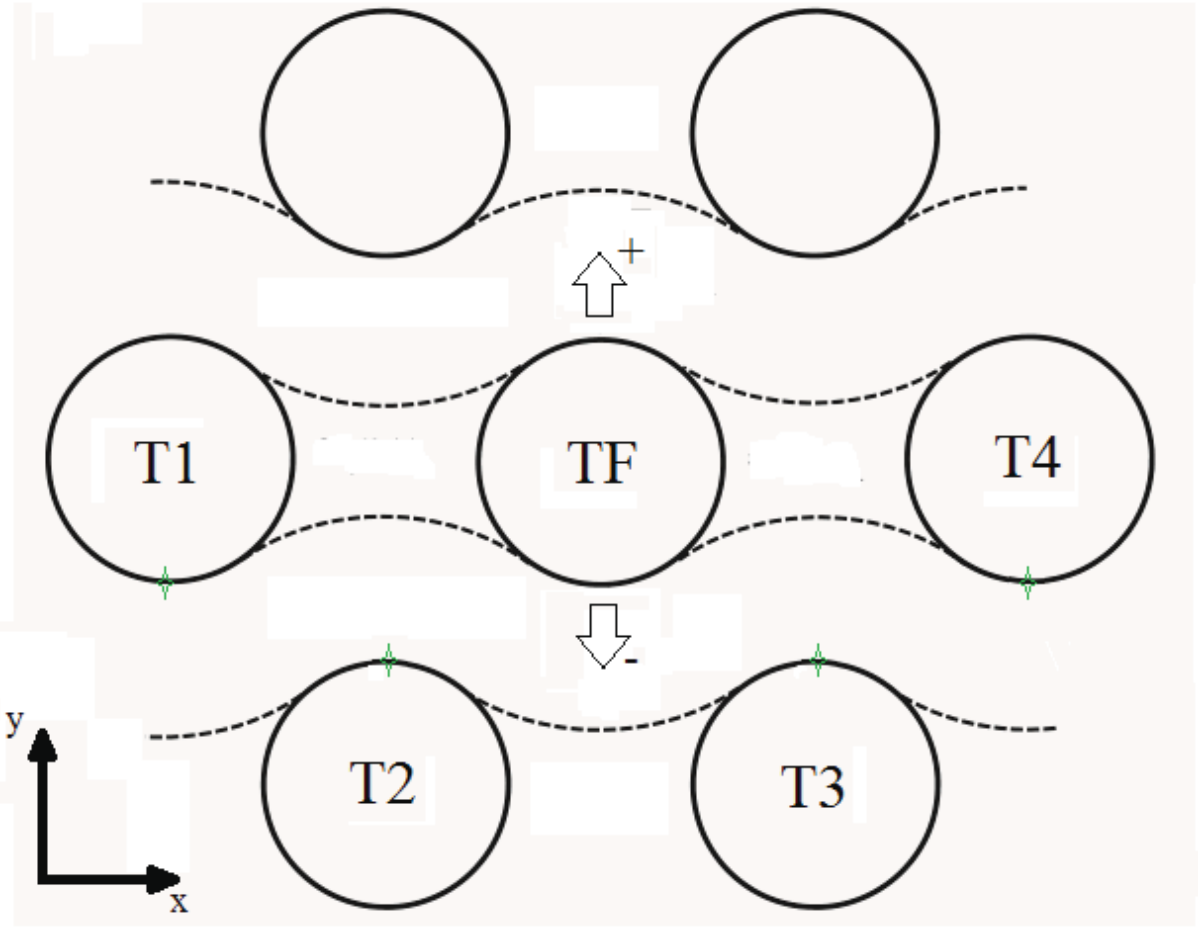

FIGURE 5.1: Location of the pressure transducers along the cylinders in the lower channel.

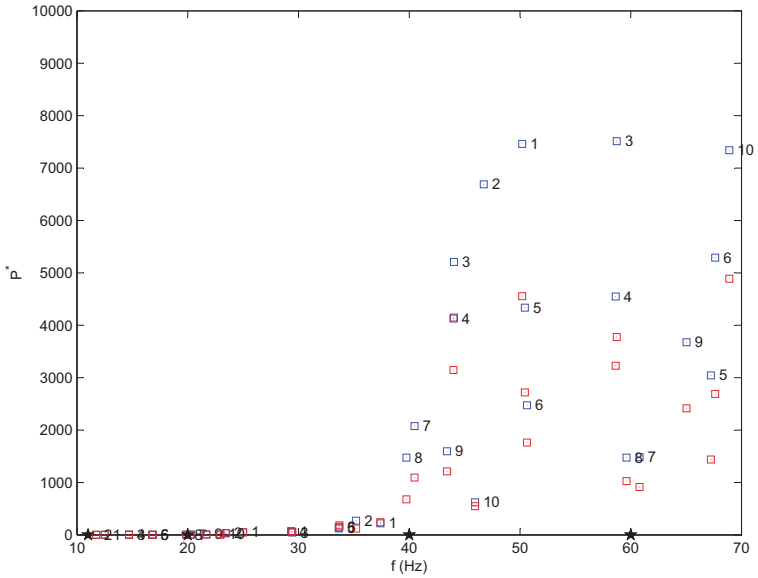

FIGURE 5.2: Amplitude of the pressure perturbations with the discarded higher harmonics for the tubes T2 and T3. Red squares: 1° series of tests; blue squares: 2^{nd} series of tests; black pentagrams: CFD results.

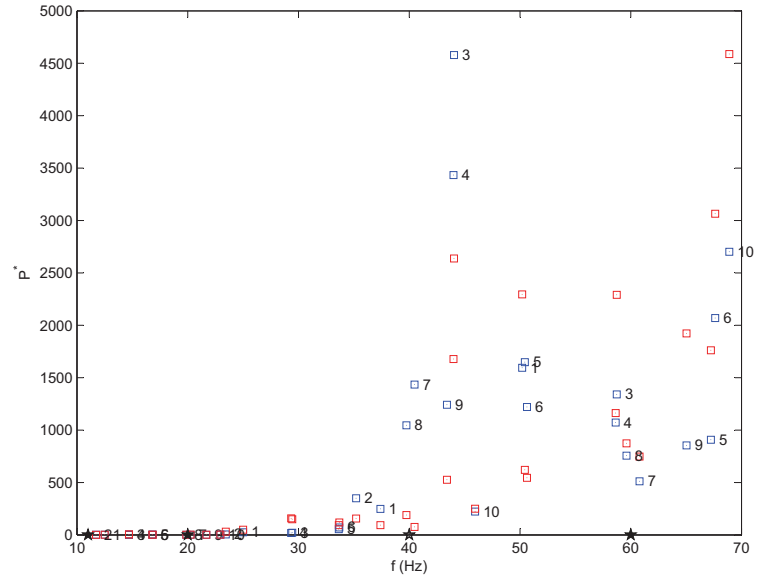

FIGURE 5.3: Amplitude of the pressure perturbations with the discarded higher harmonics for the tubes T1 and T4. Red squares: 1° series of tests; blue squares: 2^{nd} series of tests; black pentagrams: CFD results.

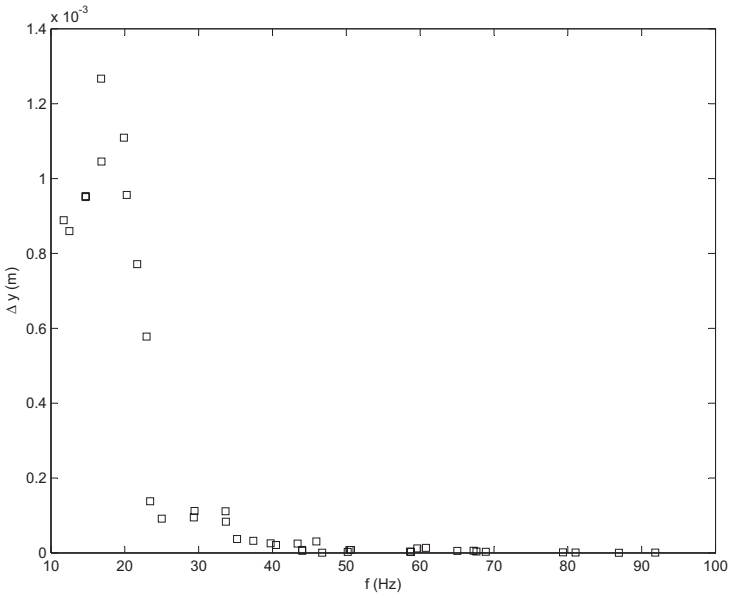

FIGURE 5.4: Amplitude of vibration for increasing frequencies showing magnitude of amplitude in the discarted higher harmonics ($\Delta \sim (10^{-7})$).

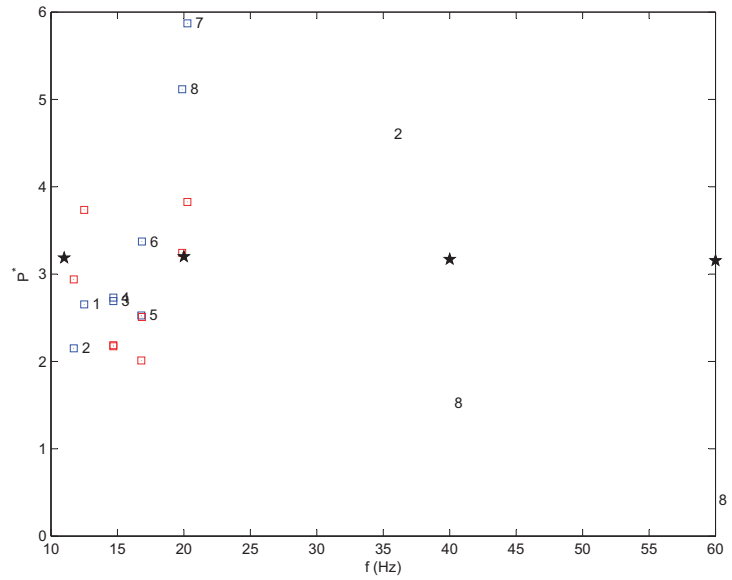

FIGURE 5.5: Amplitude of the pressure perturbations in tubes T2 and T3. Detail of the first harmonic and CFD amplitudes. Red squares: 1° series of tests; blue squares: 2^{nd} series of tests; black pentagrams: CFD results.

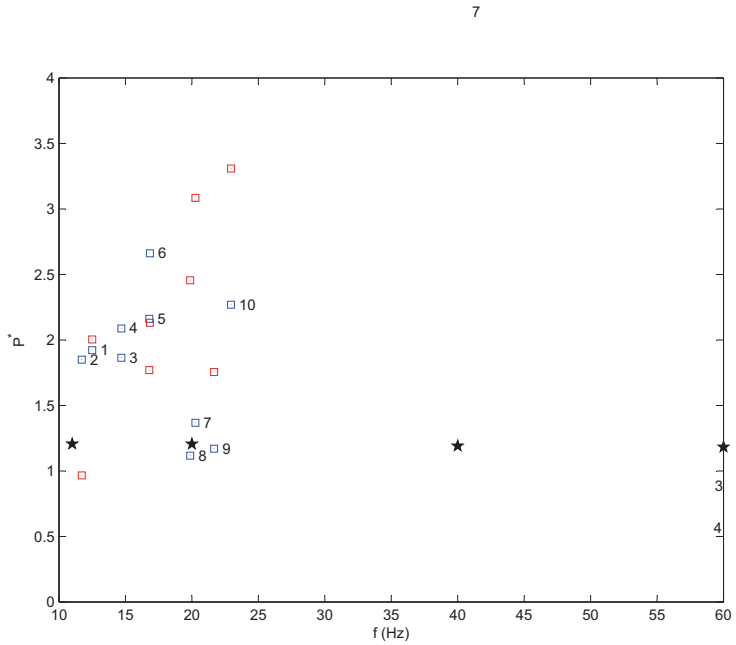

FIGURE 5.6: Amplitude of the pressure perturbations in tubes T1 and T4. Detail of the first harmonic and CFD amplitudes. Red squares: 1° series of tests; blue squares: 2^{nd} series of tests; black pentagrams: CFD results.

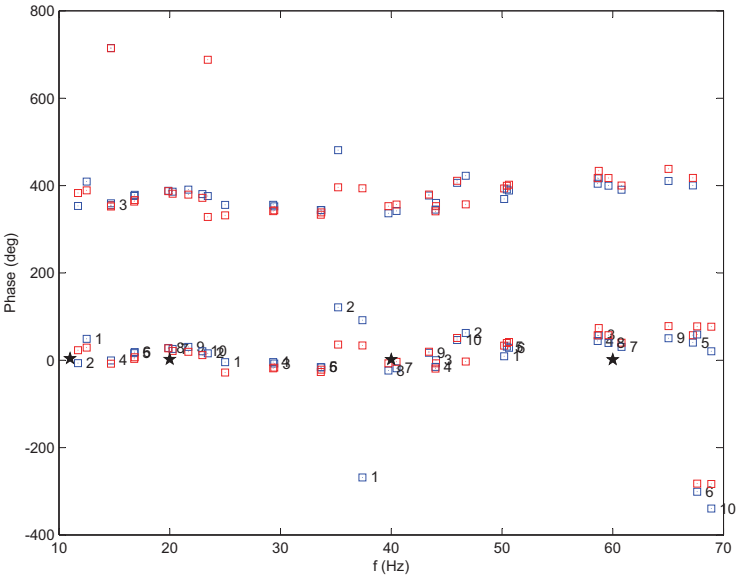

FIGURE 5.7: Phase lag of the pressure perturbations in tubes T2 and T3. Red squares: 1° series of tests; blue squares: 2^{nd} series of tests; black pentagrams: CFD results.

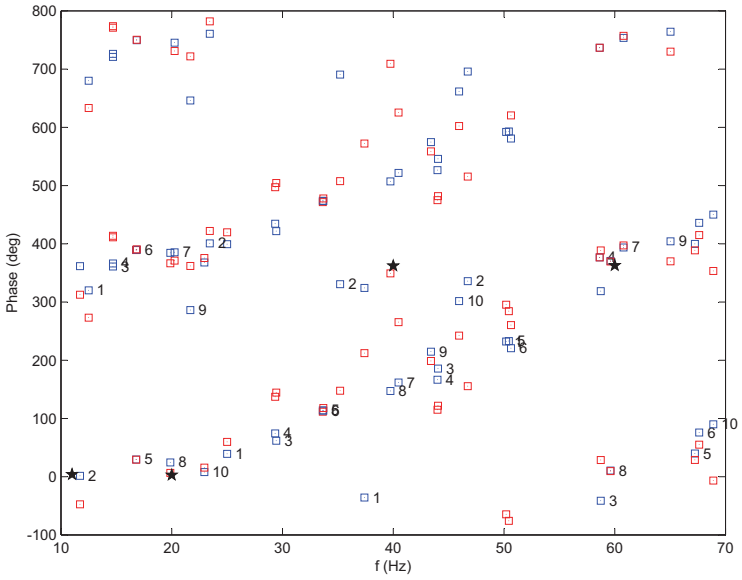

FIGURE 5.8: Phase lag of the pressure perturbations in tubes T1 and T4. Red squares: 1° series of tests; blue squares: 2^{nd} series of tests; black pentagrams: CFD results.

5.2 Comparison #4: Time delay of the lift force.

A second series of computationshas been completed to obtain the time delay between the lift force on the oscillating tube and its acceleration. Additionally, the experimental results by Mahon and Meskell (2013) [2] for a P/d=1.32 subject to air cross-flow have been employed for validation. Fig.5.9 presents the normalized time delays (t1) estimated via CFD for vibrations at 8.6 Hz (amplitude of 1% of tube diameter) under a range of cross-flow velocities. It is seen that the time delay is progressively reduced as the stream velocity increases, suggesting an asymptotic trend towards a zero delay value. The continuous line in Fig.5.9, which is the hyperbole defined by the flow retardation parameter $=\Delta U/d$=0.29, was proposed by [2] as the best fit of their experimental data. The trend and order of magnitude of that curve and the numerical data are similar to those of the numerical data, especially for the second half of the range of velocities. This agreement supports the validity of quasi-steady theoretical models incorporating a constant value for the flow retardation parameter ($=\Delta U/d$), as proposed by Paidoussis and Price [[10]], though they suggested $\sim$ (1), i.e, higher than the one obtained by [2] and also in the present study.

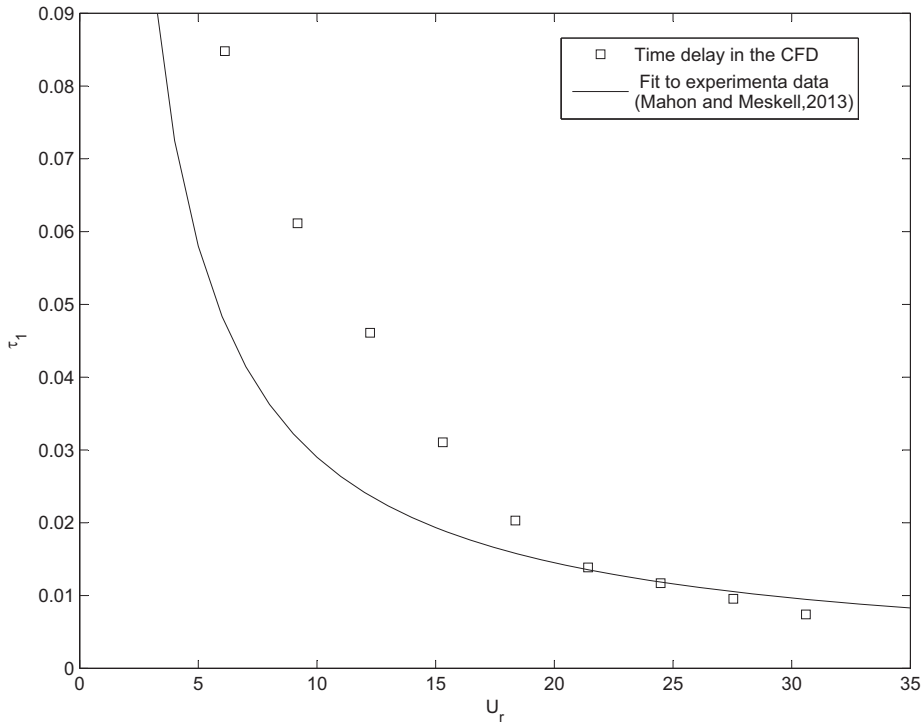

FIGURE 5.9: Normalized time delay of the lift coefficient on tube TV as a function of the reduced velocity (P/d=1.32, f=8.6HZ, vibration amplitude = 0.01 ×d): Current predictions and experimental data of [2].

5.3 Comparison #5: Propagation velocity of flow perturbations and flow pattern.

5.3.1 Parallel triangular tube array geometry

5.3.1.1 Maps of velocity and static pressure

Following a similar procedure to the previous one in the case of the normal triangular array, the average velocity magnitude and static pressure, as well as the amplitude and phase lag of the flow perturbations in the interstitial flow were analyzed for the parallel triangular tube array configurations ($P/d = 1\ 57$, $\Delta\ = 1\%$) at two different cross flow velocities, $U_r = 1\ 84$ and $U_r = 6\ 4$. The objective was to compare the flow perturbations when the relative significance of the tube velocity and the cross flow velocity varies. The first would be similar to the case of the experimental campaign conducted for the present work while the later could be compared to the empirical data reported by Khalifa et. al. [3].

Instantaneous time results in a cycle of the tube oscillation have been postprocessed ,

harmonics where the static pressure is found to be nearly in phase with the tube position. This can be attributed to the decrease of the kinetic energy because the velocity is in counter-phase with the tube motion, as previously discussed in this section (see Fig. 5.11), the lower phase in the area between the wake of tube TV and tube T3 could also be explained for the effect of the opposite velocity pattern in this concrete zones (velocity is in phase with the tube position in those regions causing the decrease of the pressure in the affected areas).

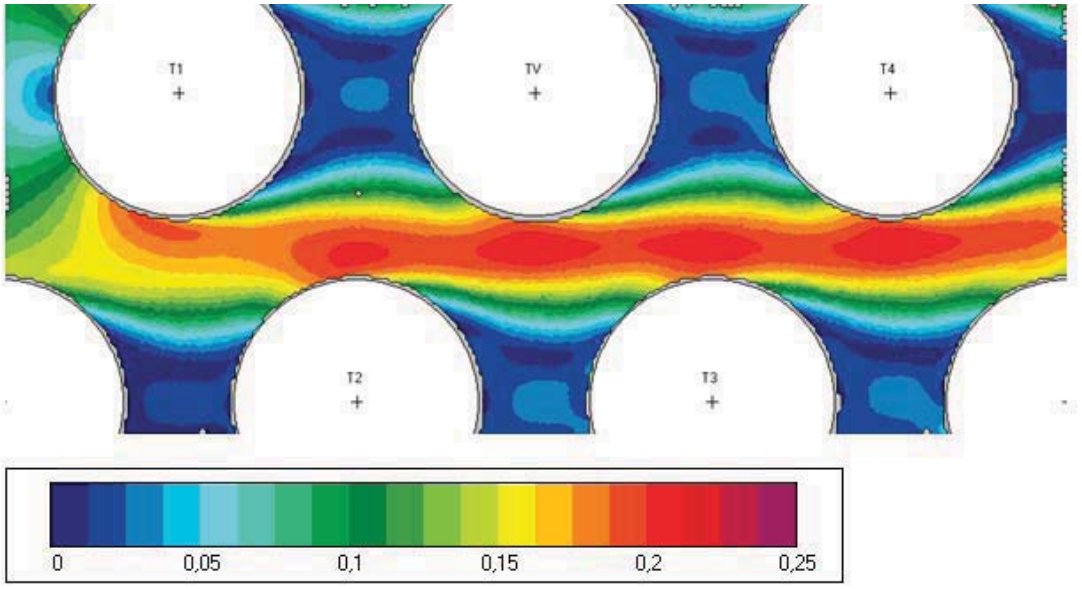

FIGURE 5.10: Averaged velocity magnitude [m/s]. Conditions for U_r = 1 84, f=7.81 Hz.

so the meantime values (averaged for a whole cycle) were obtained in the vicinity of the vibrating tube comprising three rows and two lines.

Parallel triangular tube array at low crossflow velocity

As in the previous section, only the first three harmonics were considered in the discussion. Figs. 5.10-5.23 show averaged maps of velocity and pressure amplitudes of perturbation and phase lag.

First of all, Fig. 5.10 shows the map corresponding to the averaged velocity. The figure reveals the high flow velocity streamtubes between lines of tubes. In addition, low flow velocity areas are located between consecutive tubes in the same line, where the wake of the preceding tube and the region affected by the stagnation point of the next tube coincides. Highest velocities in the streamtubes sections between the tubes are very homogenous, especially for this particular case $P/d = 1\ 57$ which corresponds to a convective velocity 2.75 times higher than the upstream velocity.

Following, Figs. 5.11, 5.12 and 5.13 show the fluctuation amplitude of the velocity vector for the first, second and third harmonics respectively. It can be seen that the most significant fluctuations take place in the detached points of the vibrating tube, as occurred in the normal triangular tube array. Note that this is in agreement with the experimental results obtained by Khalifa et al. [3].

Complementarily, Figs. 5.14-5.16 show the results for the three first harmonic, regarding the phase lag. The fluctuation of the velocity in the streamtube is inversily out-of-phase with respect to the tube motion, because the incremented section causes a velocity reduction which requires a finite time delay to adjust the flow rate distribution accordingly between the channels. On the contrary, both wake region in tube T1 and stagnation area in tube T3 present fluctuations in phase with the tube position due to the existing suction in those locations.

Next, Fig. 5.17 shows the map corresponding to the averaged static pressure. Maximum pressure values are associated to the stagnation points in the front of the tubes and, also, to the wakes in the rear, where the velocity is lower. Conversely, the pressure is lower in the high velocity tube streams where the high kinetic energy term is more significant. In addition, comparing different rows, it can be observed the progressive expected pressure loss as the flow crosses through the array.

Following, Figs. 5.18, 5.19 and 5.20 show the fluctuation of the fluctuation of the static pressure for the first, second and third harmonics respectively. It can be seen that the most significant pressure perturbations take place in the laterals of the tube, as a consequence of the transverse motion. In this case, the pressure oscillations are very lightly displaced downstream of the curvilinear coordinate origin ($-90°$) because the cross flow velocity is very slow with respect to the tube velocity.

Regarding the phase lag, Figs. 5.21-5.23 show the results obtained for the three first

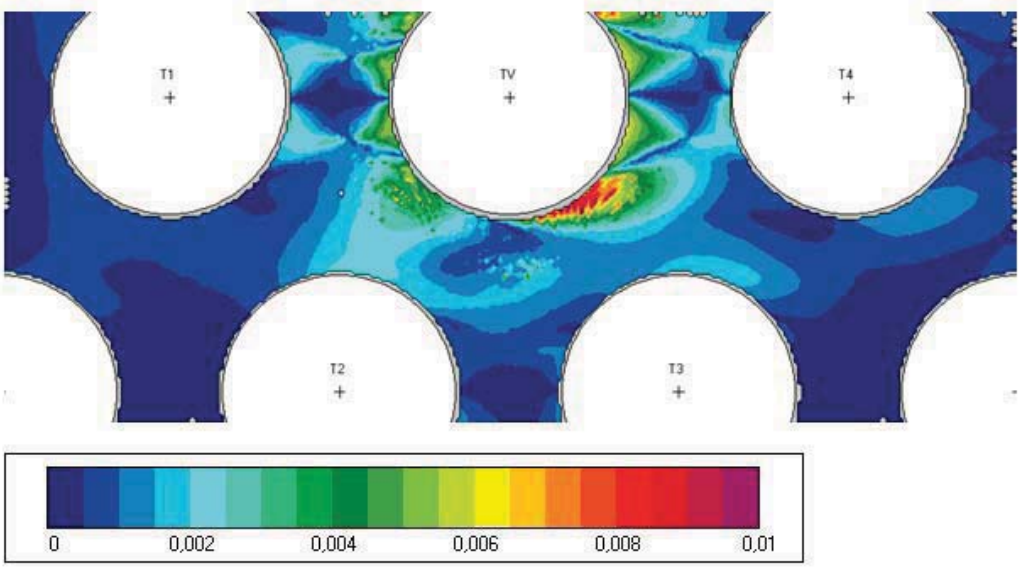

FIGURE 5.11: Fluctuation of the velocity magnitude. Amplitude [m/s] of 1st harmonic ($U_r = 1\ 84$, f=7.81 Hz).

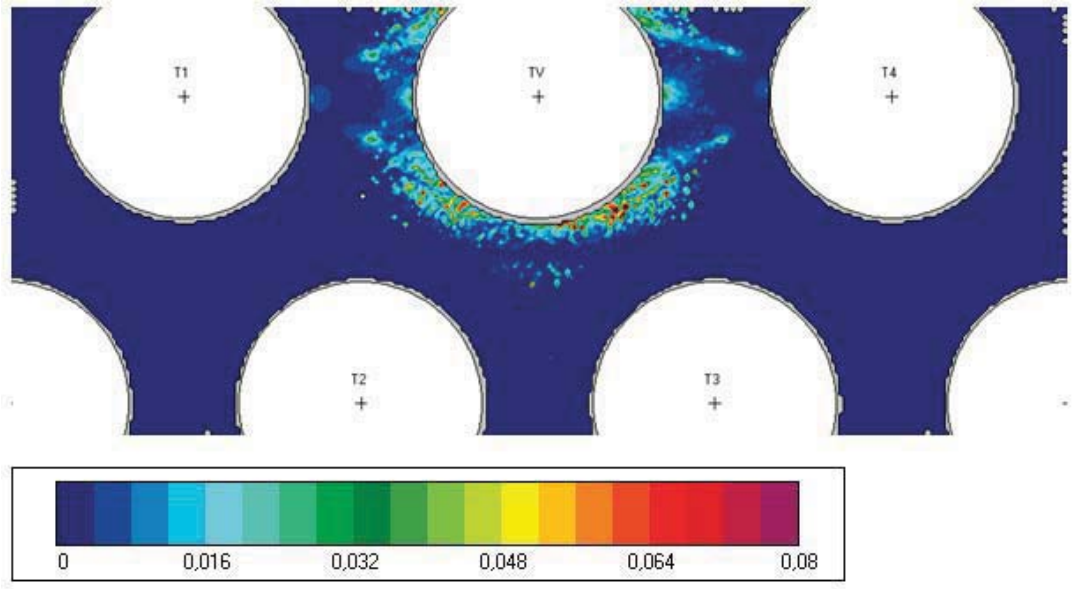

FIGURE 5.12: Fluctuation of the velocity magnitude. Amplitude [m/s] of 2nd harmonic ($U_r = 1\ 84$, f=15.63 Hz).

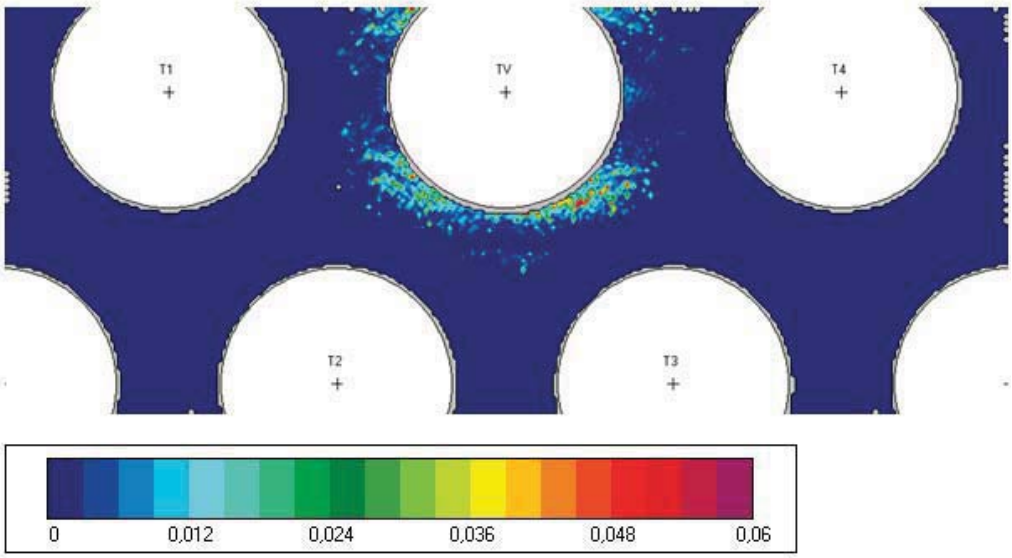

FIGURE 5.13: Fluctuation of the velocity magnitude. Amplitude [m/s] of 3rd harmonic (U_r = 1 84, f=23.44 Hz).

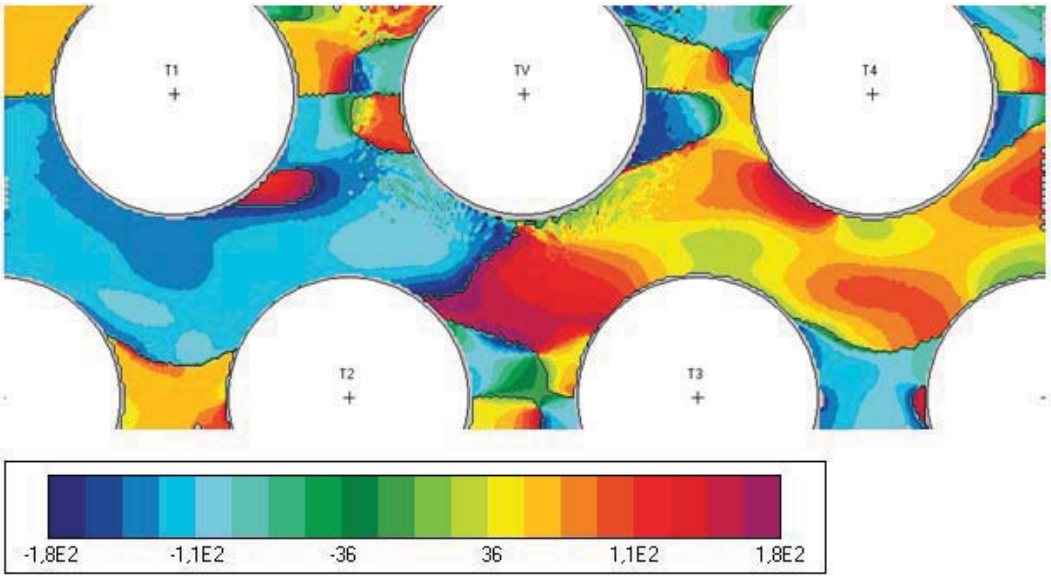

FIGURE 5.14: Fluctuation of the magnitude. Phase [deg] of 1st harmonic (U_r = 1 84, f=7.81 Hz).

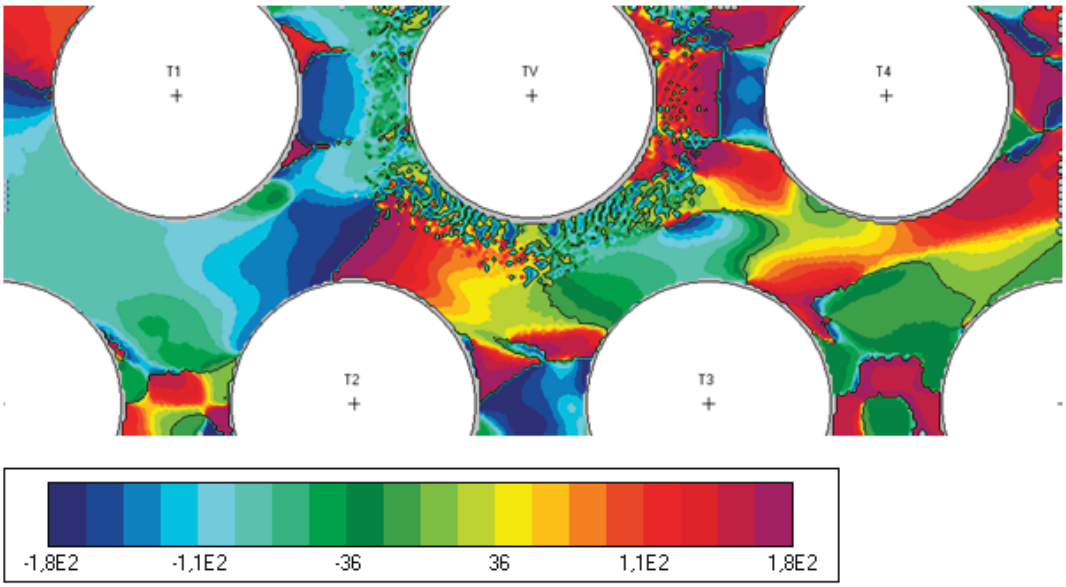

FIGURE 5.15: Fluctuation of the magnitude. Phase [deg] of 2nd harmonic ($U_r = 1\ 84$, f=15.63 Hz).

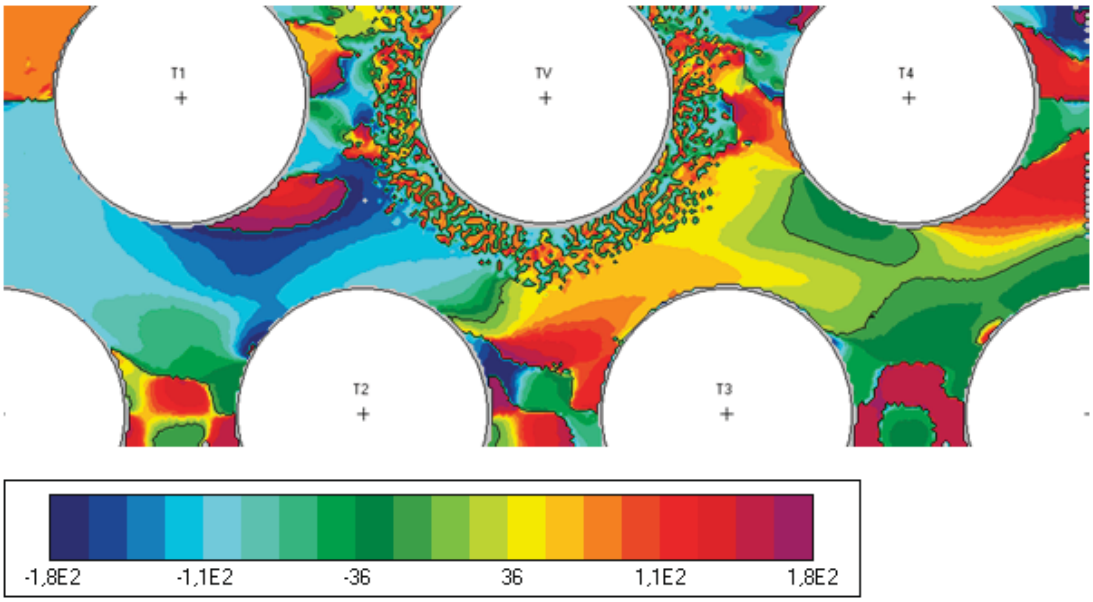

FIGURE 5.16: Fluctuation of the magnitude. Phase [deg] of 3rd harmonic ($U_r = 1\ 84$, f=23.44 Hz).

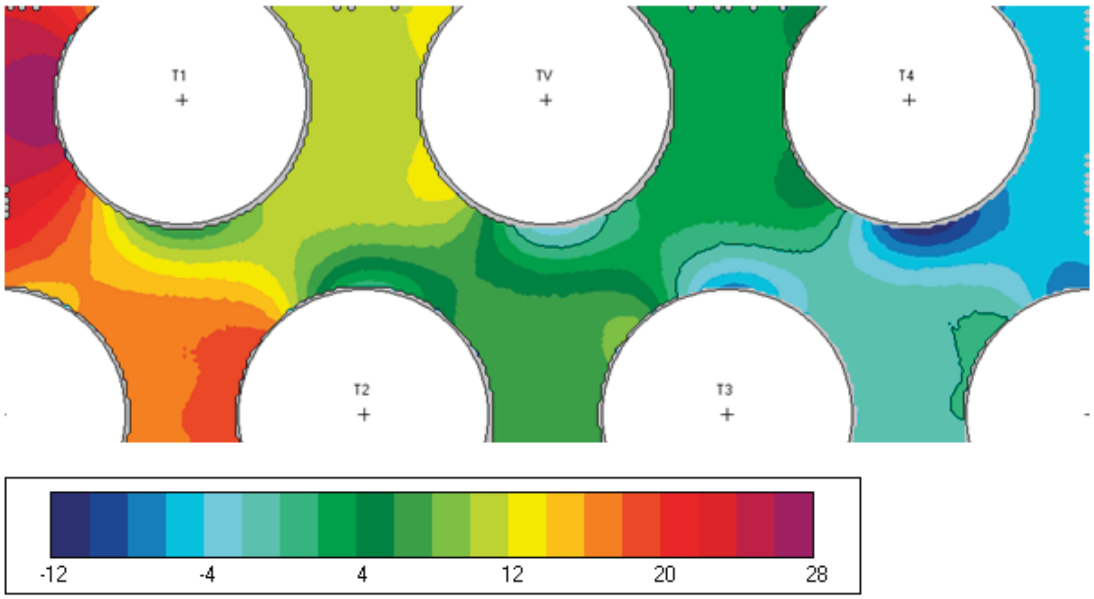

FIGURE 5.17: Averaged static pressure [Pa]. Conditions for $U_r = 1\ 84$, f=7.81 Hz.

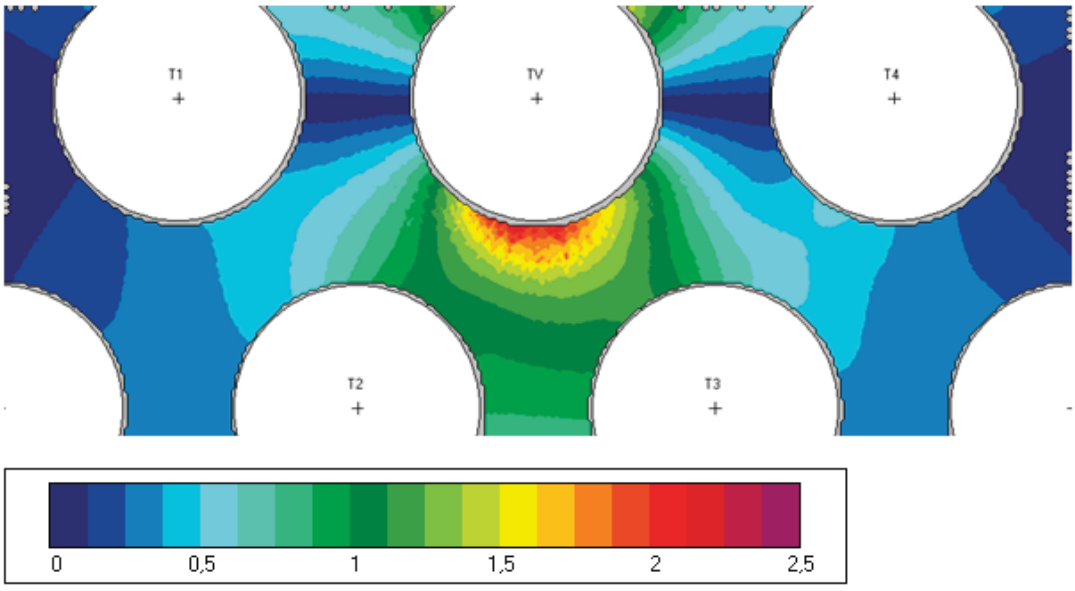

FIGURE 5.18: Fluctuation of the static pressure. Amplitude [Pa] of 1st harmonic ($U_r = 1\ 84$, f=7.81 Hz).

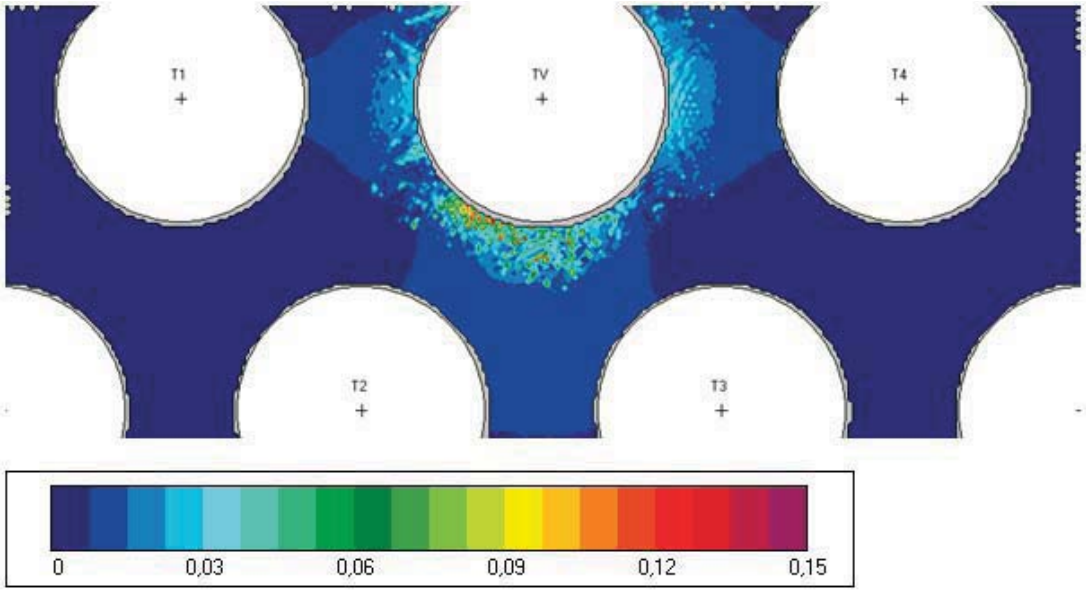

FIGURE 5.19: Fluctuation of the static pressure. Amplitude [Pa] of 2nd harmonic ($U_r = 1\ 84$, f=15.63 Hz).

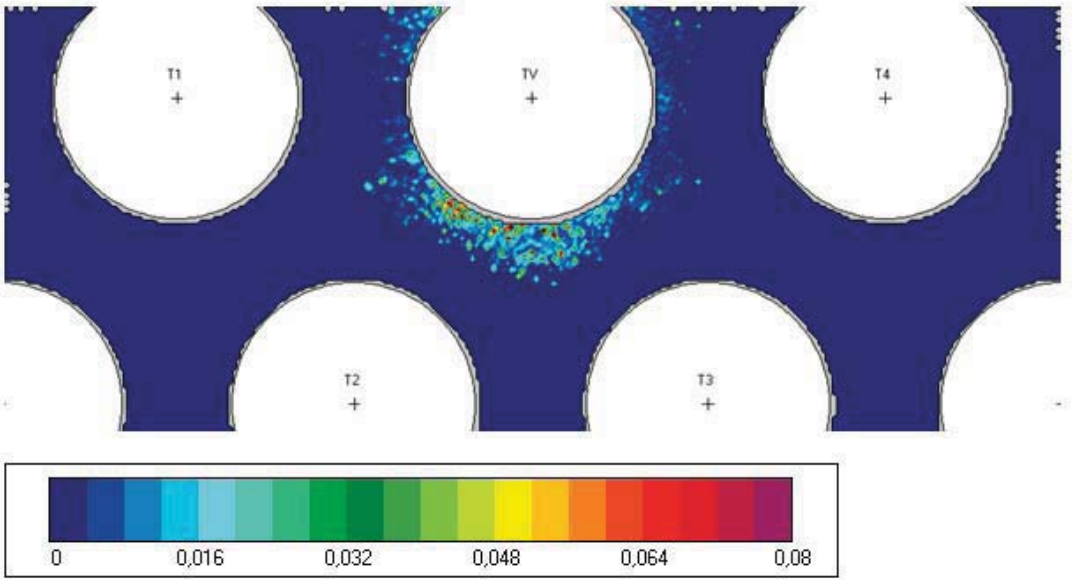

FIGURE 5.20: Fluctuation of the static pressure. Amplitude [Pa] of 3rd harmonic ($U_r = 1\ 84$, f=23.44 Hz).

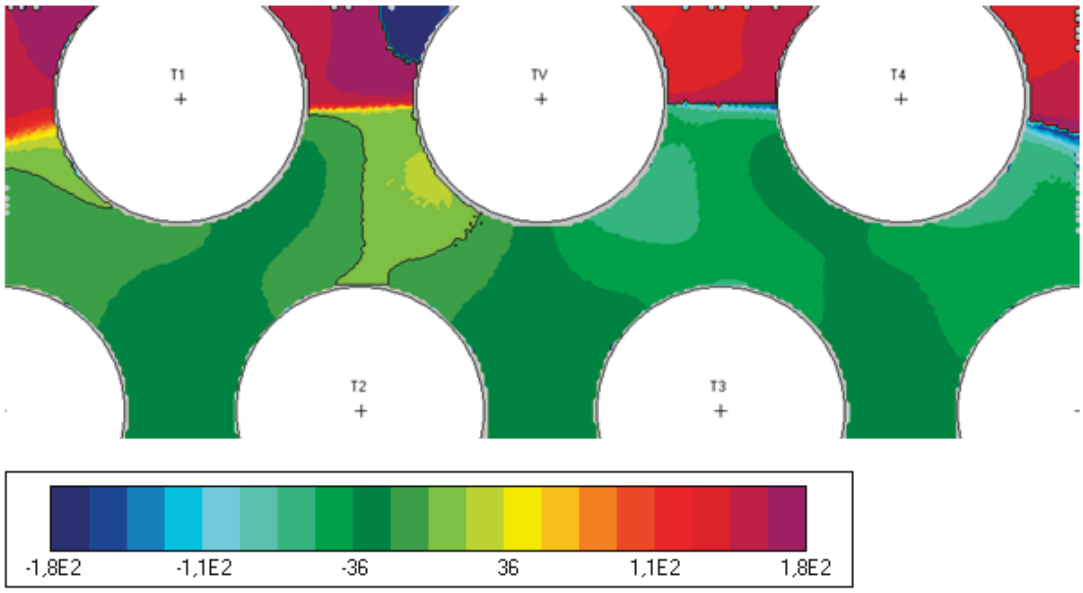

FIGURE 5.21: Fluctuation of the static pressure. Phase [deg] of 1st harmonic (U_r = 1 84, f=7.81 Hz).

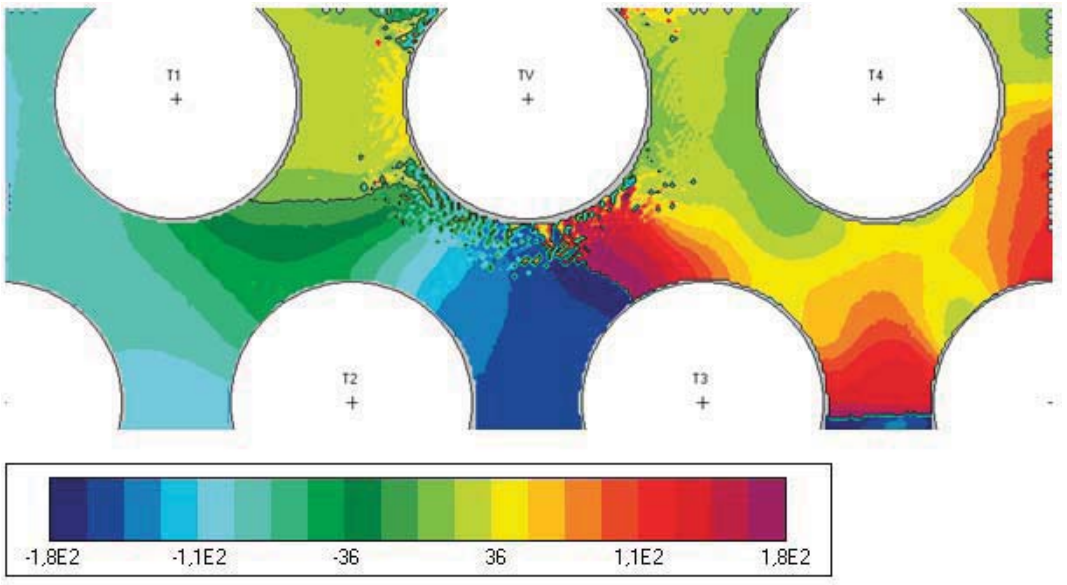

FIGURE 5.22: Fluctuation of the static pressure. Phase [deg] of 2nd harmonic (U_r = 1 84, f=15.63 Hz).

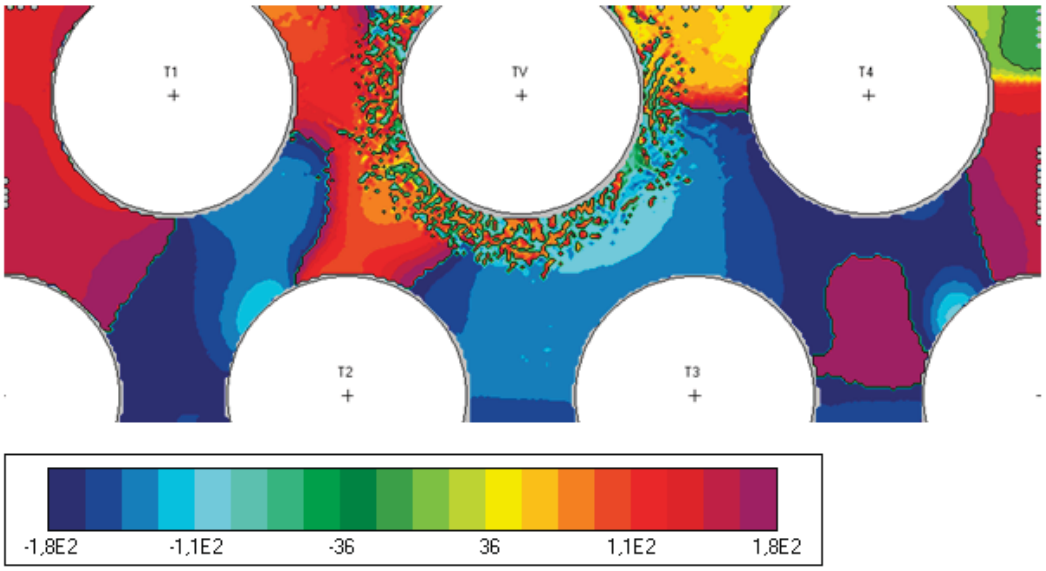

FIGURE 5.23: Fluctuation of the static pressure. Phase [deg] of 3rd harmonic (U_r = 1 84, f=23.44 Hz).

Parallel triangular tube array at high cross-flow velocity

Finally, 5.24-5.30 show similar maps with the amplitude and phase lag of the pressure fluctuations in the case of a cross-flow velocity of U_r = 6 4 (based on pitch velocity). Once again, only the first three harmonics were considered in the discussion.

Fig. 5.24 shows the map corresponding to the averaged velocity magnitude. In this case, velocity is very homogeneous in the stream-tube for this particular geometry (P/d = 1 57) which corresponds to a streamwise velocity that it is 2.75 times higher than the upstream velocity.

Figs. 5.25, 5.26 and 5.27 show the fluctuation in the amplitude of the velocity magnitude for the first, second and third harmonics respectively. It can be seen that the most significant fluctuations take place in the detached points of the vibrating tube (Khalifa et al. [3]). Moreover, because the cross-flow velocity is higher, the perturbations are rapidly propagated downstream the array, with lower attenuation than before. This can be seen in the area affected by the higher amplitude perturbations, with a downstream extension that it is reaching the tube in the next row.

Regarding the phase lag, Figs. 5.28-5.30 show the results for the three first harmonics, as usual. Precisely, the phase of the fluctuation of the velocity in the streamtube is opposite to that of the tube motion, due to the enlargement of the section. Conversely, the area affected within detached conditions for the tube TV is in phase with the tube position, as a consequence of the wake that it is oscillating (in and out of this section) in phase with the tube motion.

Fig. 5.31 shows the map corresponding to the averaged static pressure. The expected pressure loss as the flow crosses through the array is clearly noticeable in the representation. In a row, minimum pressure values corresponds to the stagnation points (in front of the tubes) and to the wakes (in the rear parts) where velocities are lower, . On the contrary, the pressure is lower in the stream-tubes due to the higher values of the kinetic energy.

Figs. 5.32, 5.33 and 5.34 show the amplitude of the fluctuation for the static pressure in the case of the first, second and third harmonics respectively. In addition to the pressure perturbations that take place in the sidewalls of the tube, as discussed in the previous section, pressure perturbations of high amplitude arise in this case in the surrounding areas of tube T4. Moreover, they can be inside or outside of the the wake of tube TV, depending on its instantaneous position, thus being then protected or exposed to the main stream.

Finally, Figs. 5.35-5.37 show the phase lag results for the three first harmonics of the time series. It can be seen that the static pressure is in phase with the tube position in the sidewalls of the tube and also in those points in the vicinity of tube T4 that are entering and leaving the wake of the vibrating tube. In fact, when the vibrating tube moves upwards the increased streamflow hits these surfaces so the rest of the channel is closer to the counter-phase and, at the same time, the enlargement of the section reduces the resistance to the flow. However, the effect of the surfaces that are in-phase with the motion are also extended through this area, resulting in an intermediate phase lag of about 110°.

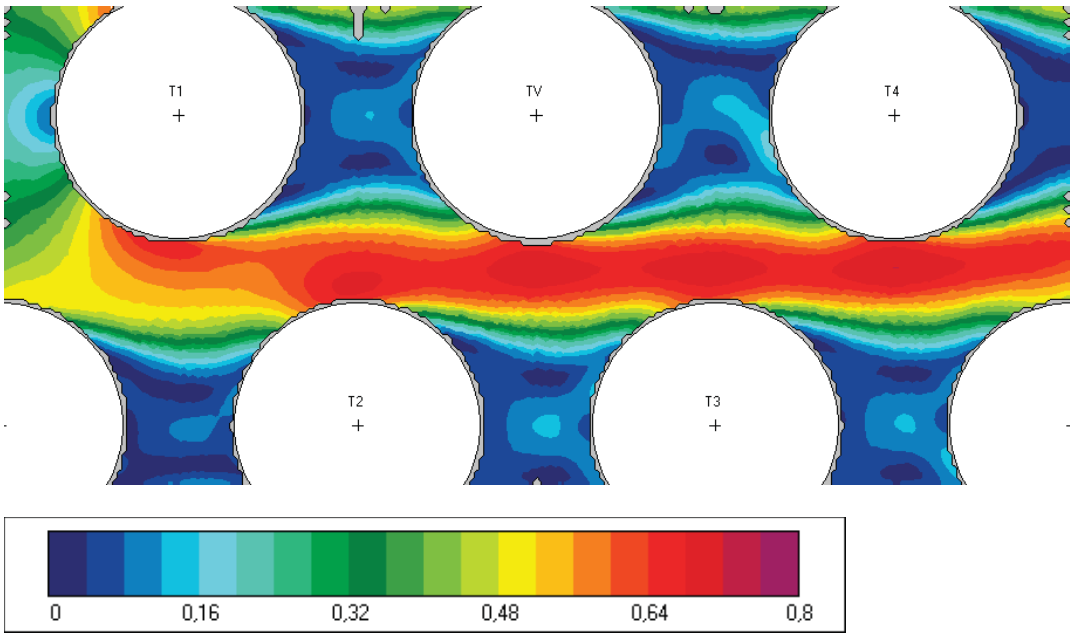

FIGURE 5.24: Averaged velocity magnitude [m/s] for $U_r = 6\ 4$, f=7.81 Hz.

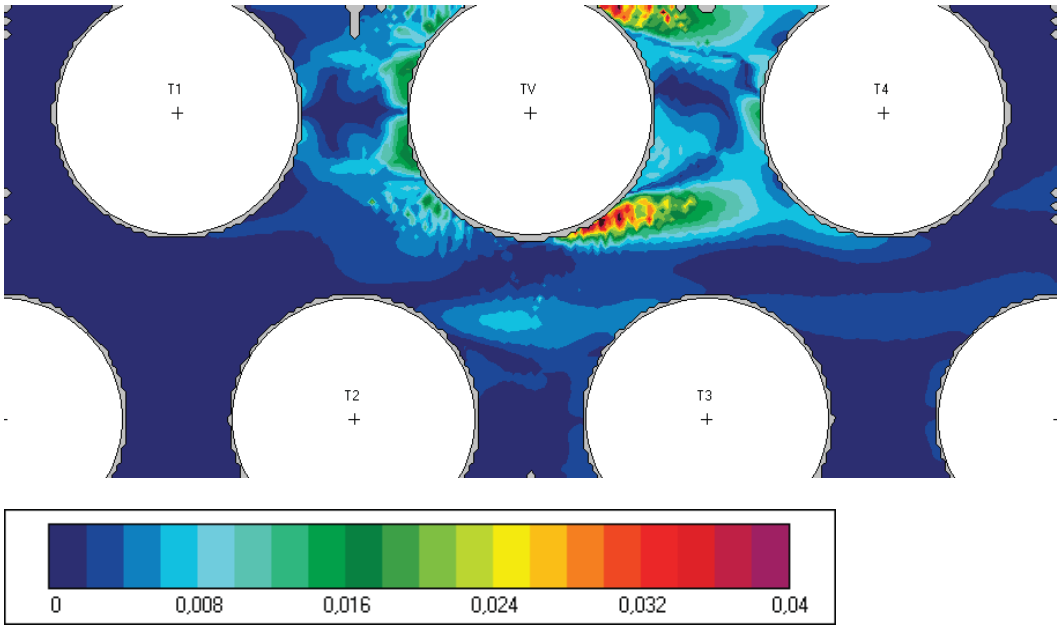

FIGURE 5.25: Fluctuation of the velocity magnitude. Amplitude [m/s] of the 1st harmonic ($U_r = 6\ 4$, f=7.81 Hz).

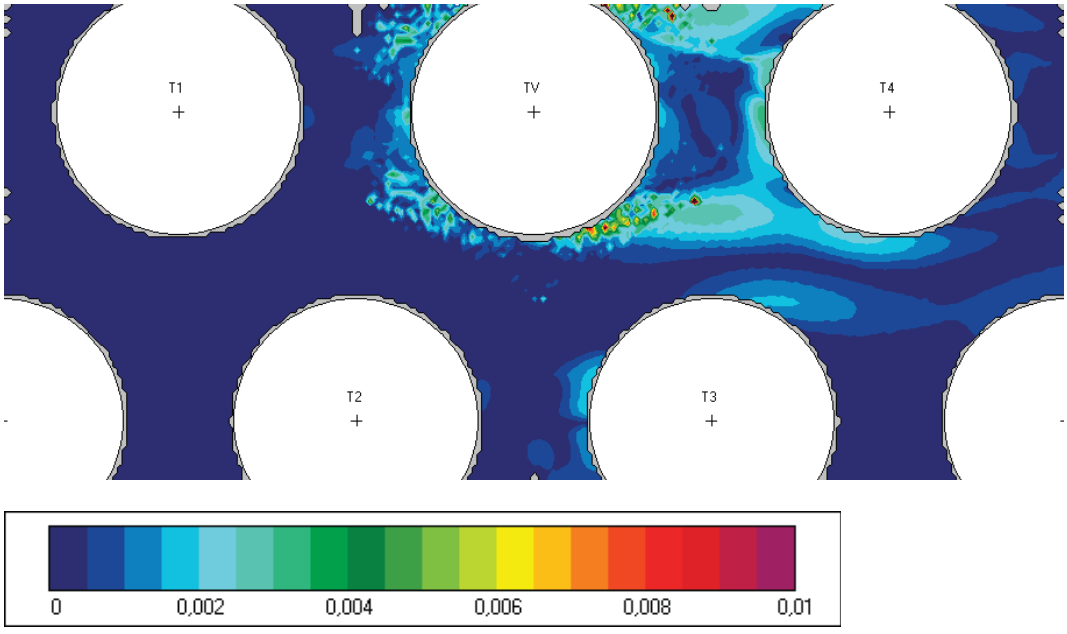

FIGURE 5.26: Fluctuation of the velocity magnitude. Amplitude [m/s] of the 2nd harmonic ($U_r = 6\ 4$, f=15.63 Hz).

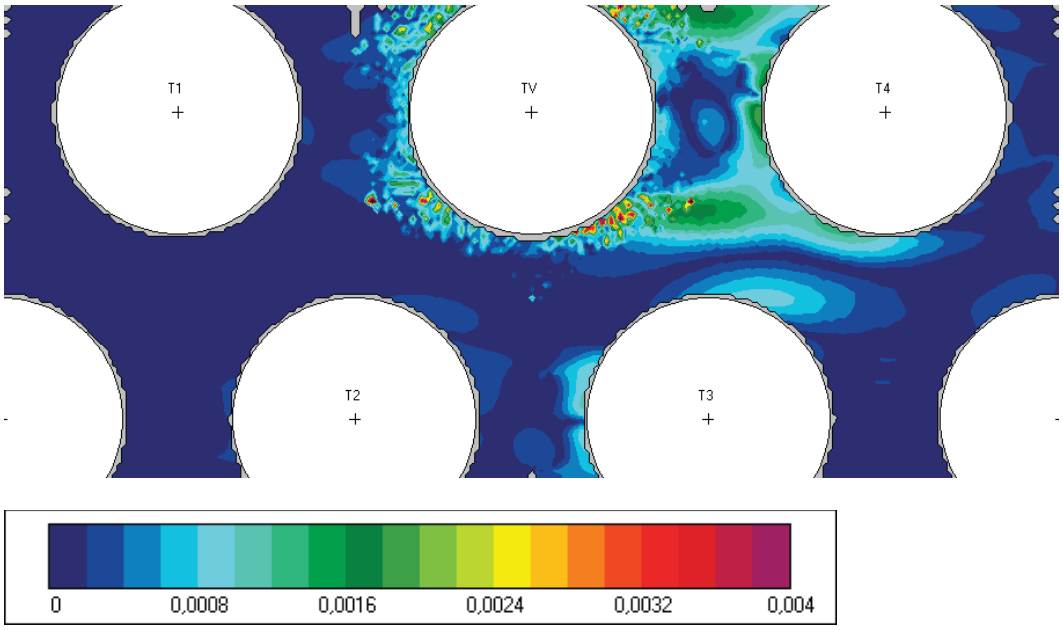

FIGURE 5.27: Fluctuation of the the velocity magnitude. Amplitude [m/s] of the 3rd harmonic (U_r = 6 4, f=23.44 Hz).

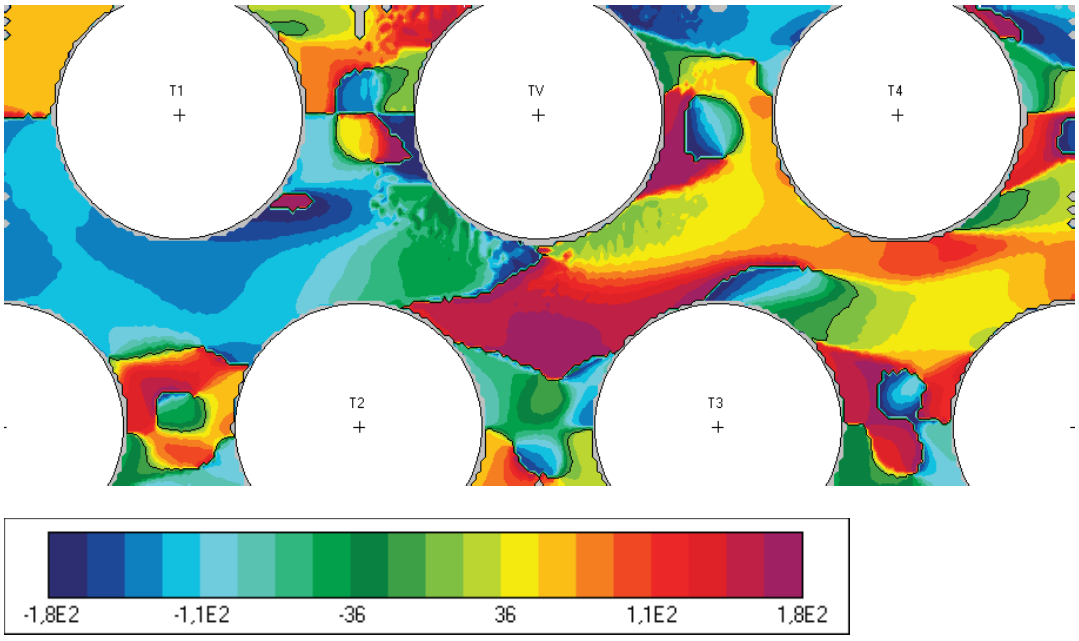

FIGURE 5.28: Fluctuation of the velocity magnitude. Phase [deg] of the 1st harmonic (U_r = 6 4, f=7.81 Hz).

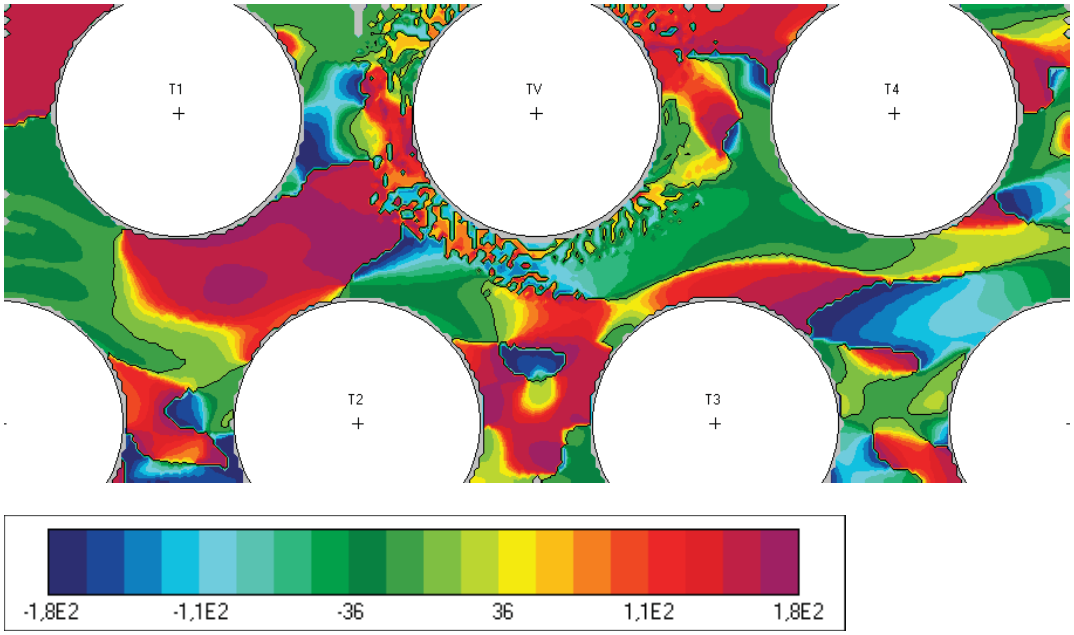

FIGURE 5.29: Fluctuation of the velocity magnitude. Phase [deg] of the 2nd harmonic ($U_r = 6\ 4$, f=15.63 Hz).

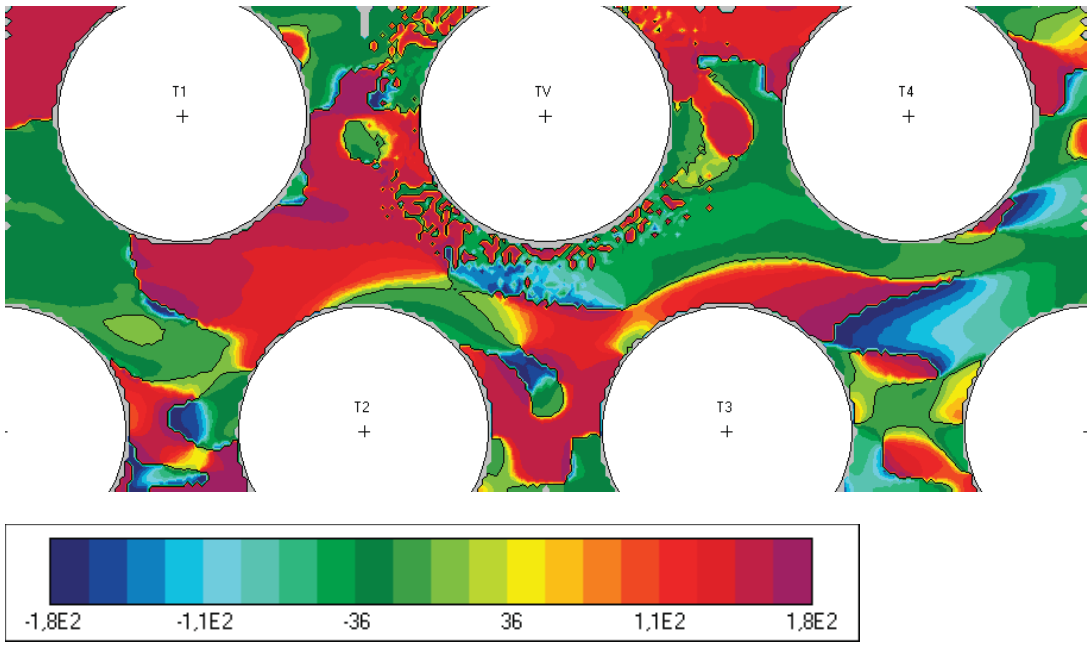

FIGURE 5.30: Fluctuation of the velocity magnitude. Phase [deg] of the 3rd harmonic ($U_r = 6\ 4$, f=23.44 Hz).

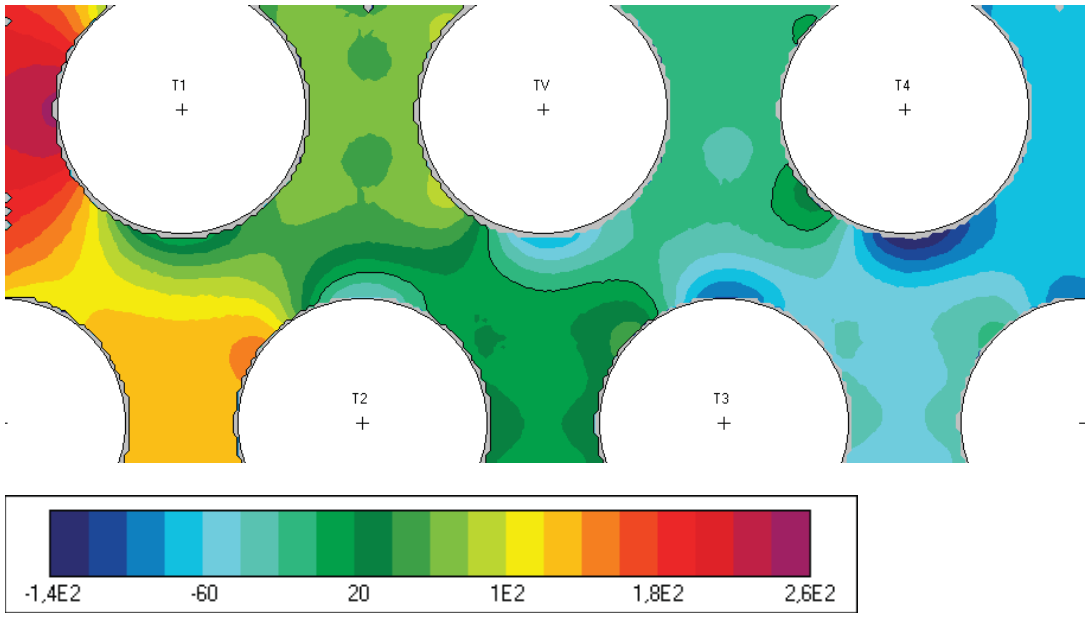

FIGURE 5.31: Averaged Static Pressure [Pa] for $U_r = 6\ 4$, f=7.81 Hz.

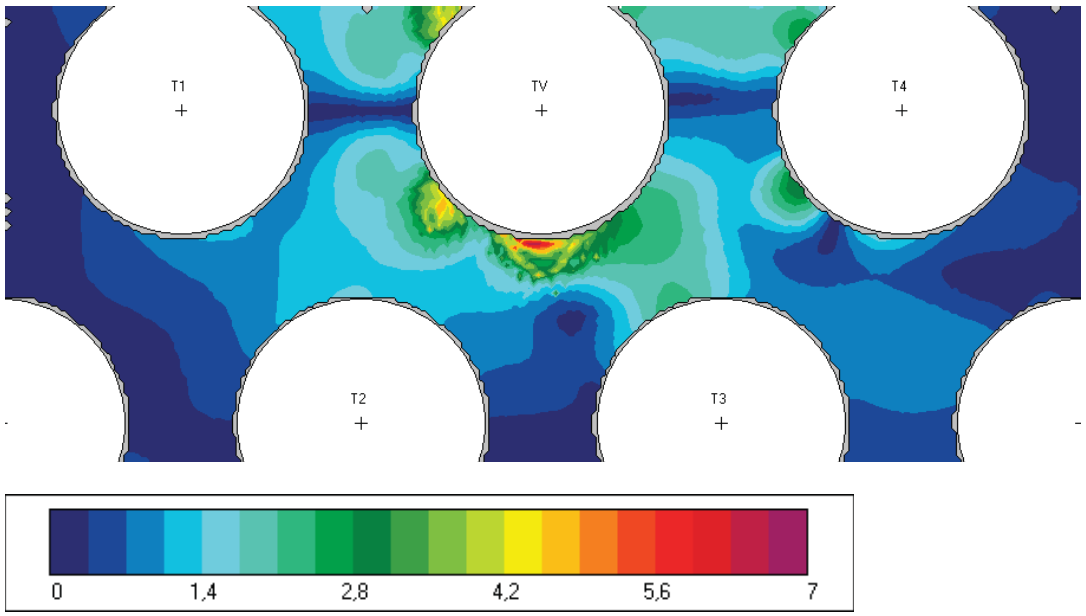

FIGURE 5.32: Fluctuation of the static pressure. Amplitude [Pa] of the 1st harmonic ($U_r = 6\ 4$, f=7.81 Hz).

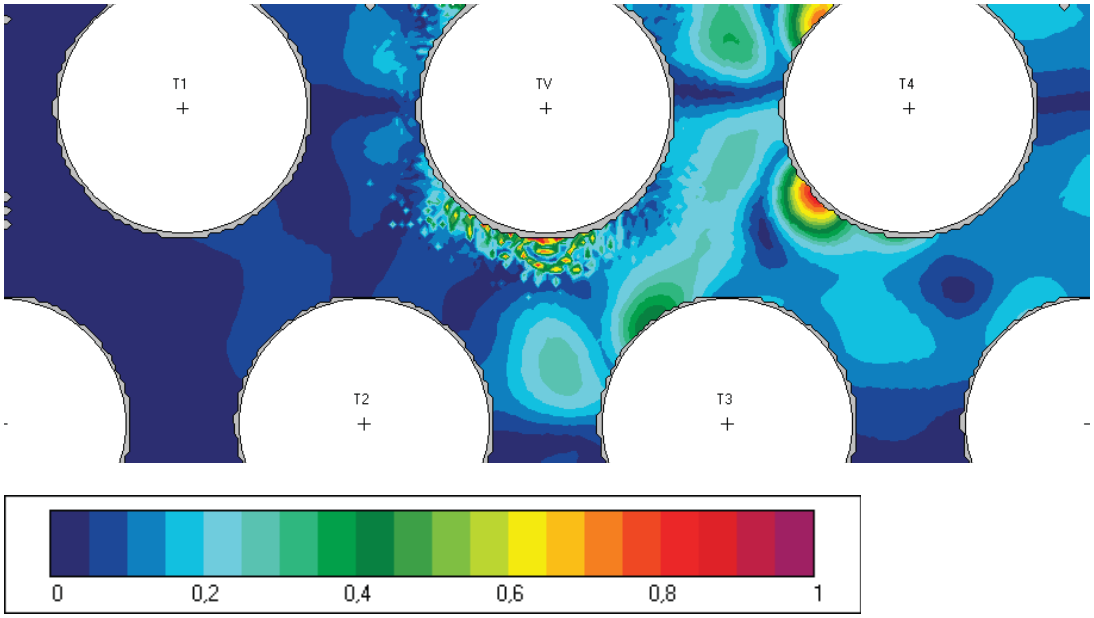

FIGURE 5.33: Fluctuation of the static pressure. Amplitude [Pa] of the 2nd harmonic ($U_r = 6\ 4$, f=15.63 Hz).

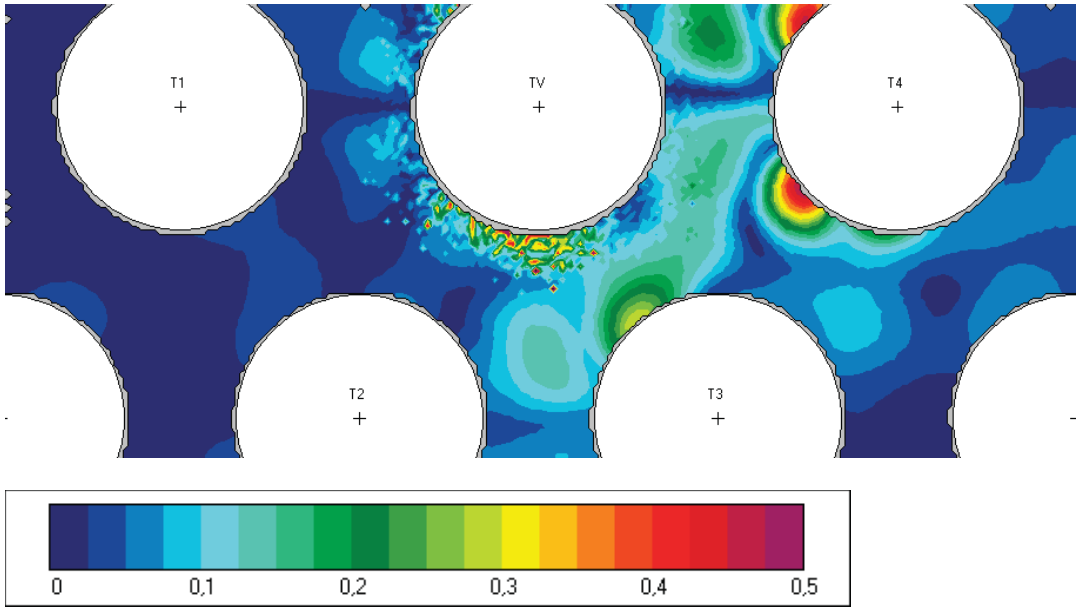

FIGURE 5.34: Fluctuation of the static pressure. Amplitude [Pa] of the 3rd harmonic ($U_r = 6\ 4$, f=23.44 Hz).

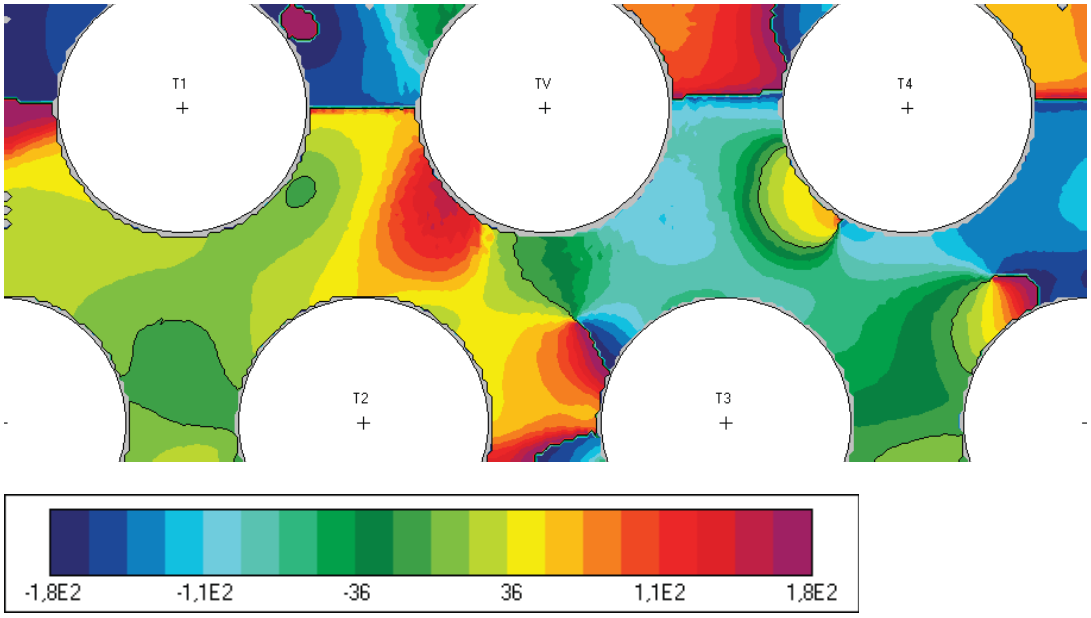

FIGURE 5.35: Fluctuation of the static pressure. Phase [deg] of the 1st harmonic ($U_r = 6\ 4$, f=7.81 Hz).

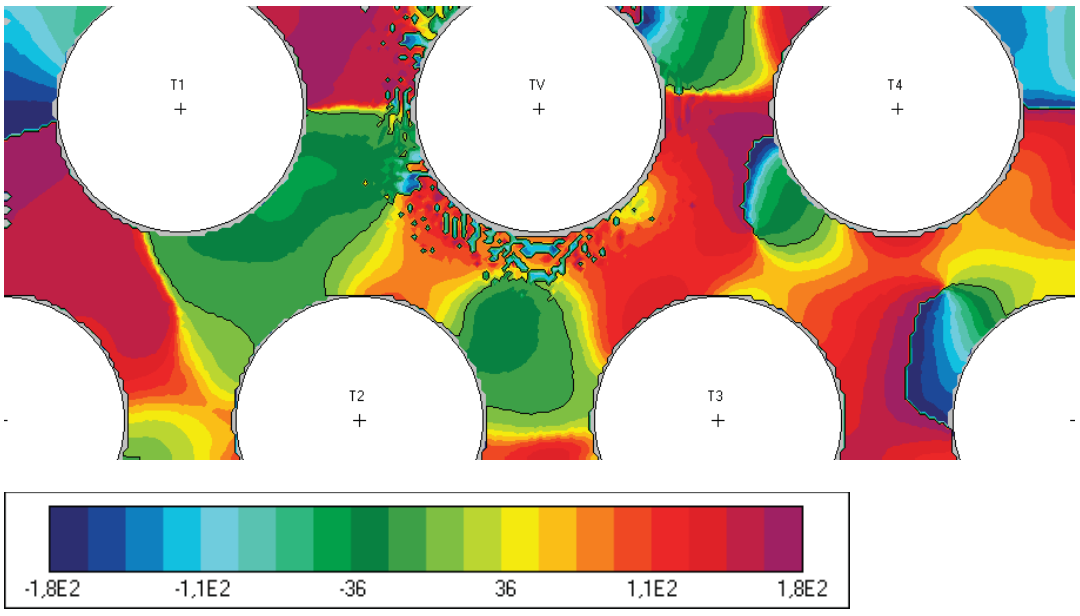

FIGURE 5.36: Fluctuation of the static pressure. Phase [deg] of the 2nd harmonic ($U_r = 6\ 4$, f=15.63 Hz).

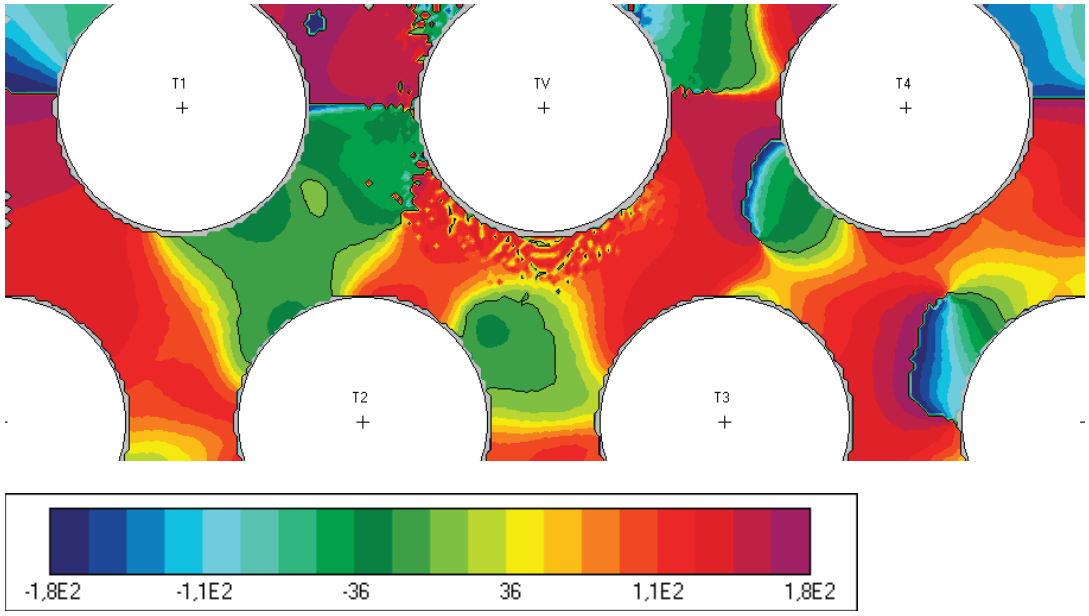

FIGURE 5.37: Fluctuation of the static pressure. Phase [deg] of the 3rd harmonic ($U_r = 6\ 4$, f=23.44 Hz).

5.3.1.2 Diagrams of normalized amplitude and time delay.

In order to explore the streamwise transmission of the perturbations along the array, several streamlines at increasing distances from the vibrating tube were selected to monitor the amplitude and phase lag of these perturbations. To identify every streamline, a coefficient "'k" ranging from k=0, (for a stream-line tangential to the tubes T1, TV and T4), to k=1 (for a streamline tangential to the tubes T2 and T3). Two different cross-flow velocities were considered in this study $U_r = 1\ 84$ and $U_r = 6\ 4$ (reduced velocities based on pitch velocity). Figs. 5.38- 5.51 show the results of these two cases in terms of normalized amplitude and phase lag of the velocity perturbations for different streamlines (with increasing k values). For the higher cross flow velocity, results were also compared to the experimental measurements obtained by Khalifa et al. [3] , because of their similar P/d values and cross flow velocities. A comparison of the paremeters of each study and their results is summarized in Table 4 and illustrated in Figs. 5.44 and 5.45.

Basically, the results reveal two peaks of high amplitude for the flow perturbations. These peaks correspond approximately on the detachment point on tube TV and to the wake of the preceding tube T2, that is suctioned by the tube motion, thus acting as a secondary perturbation source. As expected, when the stream line separates from tube TV (increasing k values) the relative importance of these two sources changes, being the streamlines closer to TV the most affected by its wake while those lines closer to T2 show stronger disturbances due to T2 wake.

Regarding the phase lag, , it can be observed that there is a finite time delay increasing from 0° at a curvilinear coordinate of about * =0.1-0.4 (except for a small interval centered approximately at * =-0.4 and shifted in 0°), This displacement in the phase lag could be attributed to the effect of the tubes in the preceding rows which disturbances propagate downstream and interfere with those of the tube TV.

Regarding the comparison with the experimental data by Khalifa et al. [3], the source of perturbations was found at similar locations in the numerical calculations, with amplitudes in the same order of magnitude and qualitatively similar (the lower value found in the simulations could be attributed to the higher P/d). The propagation velocity downstream the array was also found to be similar to the experimental values, as can be seen in Table 5.1. It must be adviced that, upstream the vibrating tube, the 180° shift observed in the present study was not found experimentally by these authors. However, this can be attributed to the different row where the vibrating tube was placed in the experiments. For Khalifa et al. [3] tube TV in Khalifa et al. [3] is closer to the non-disturbed uniform flow upstream, what helps to avoid the interference with these disturbances.

Parallel triangular tube array at low cross-flow velocity $U_r = 1\ 84$

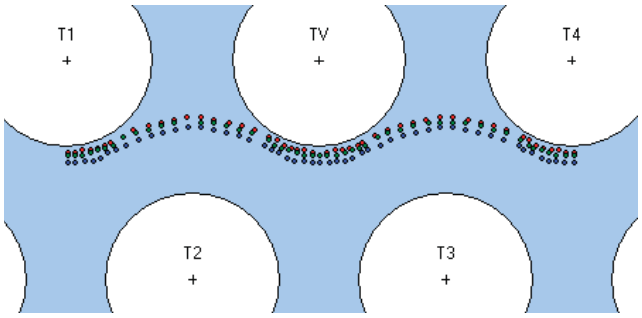

FIGURE 5.38: Location of the closer streamlines to the vibrating tube (k=0.11, 0.15 and 0.22) - numerical calculations. ($U_r = 1\ 84$).

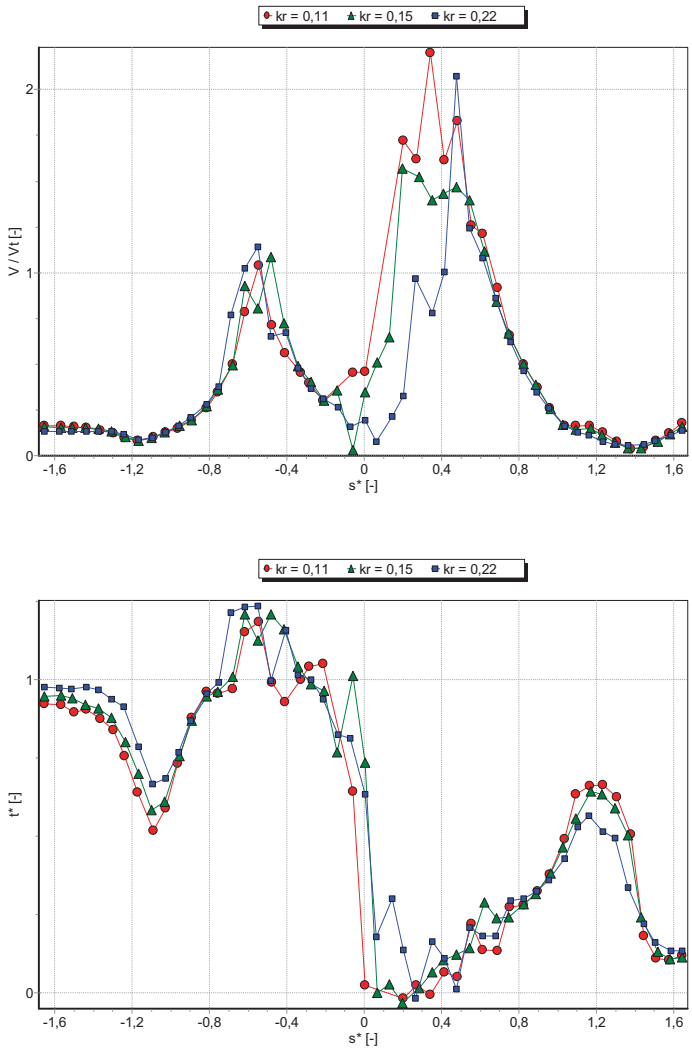

FIGURE 5.39: Normalized magnitude of velocity perturbations and phase lag of the fluctuations for the closer streamlines to the vibrating tube.

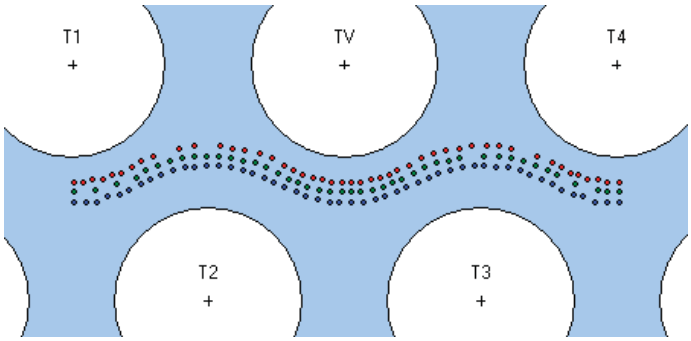

FIGURE 5.40: Location of the three stream-lines in the middle of the stream-tube (k=0.3, 0.4 and 0.5) - Numerical calculations (Ur =1.84).

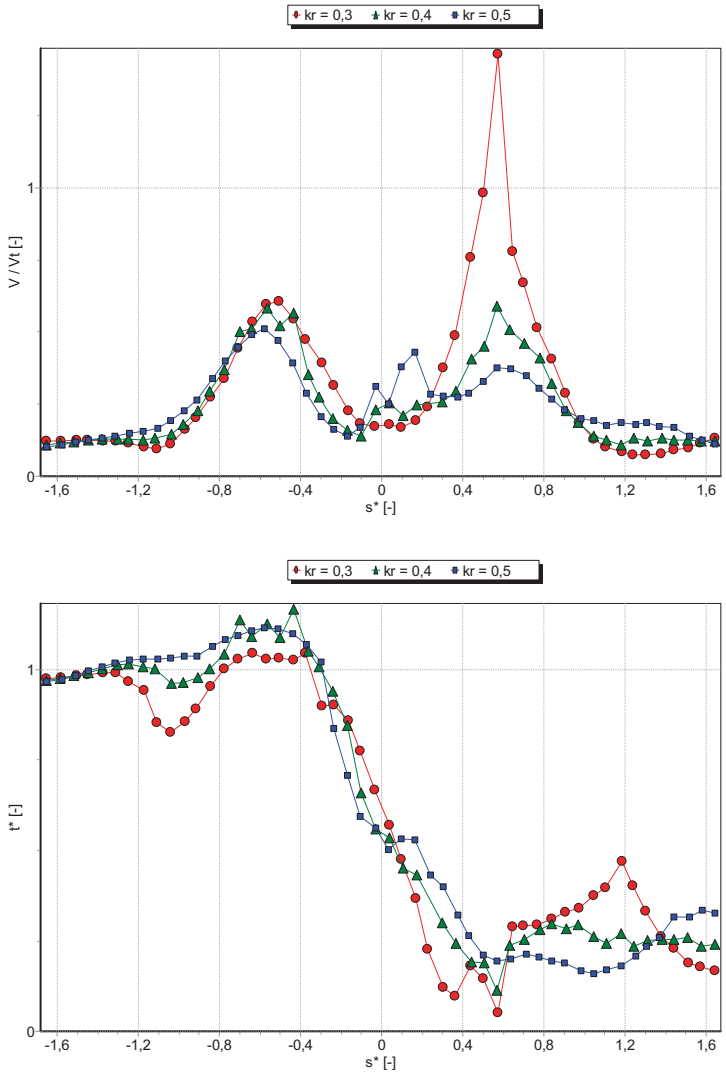

FIGURE 5.41: Normalized magnitude of velocity perturbations and phase lag for the three streamlines in the middle of the stream-tube.

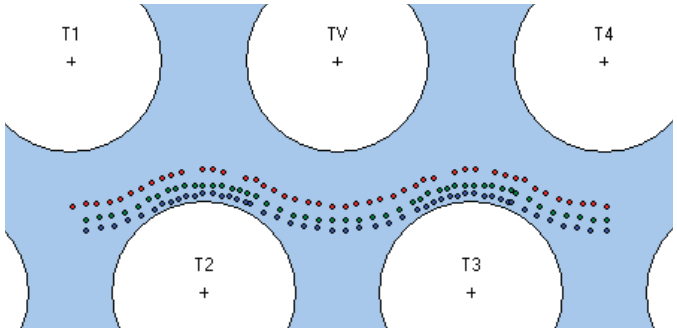

FIGURE 5.42: Location of the three stream-lines far from the vibrating tube in the stream-tube (k=0.6, 0.75 and 0.85) - Numerical calculations (Ur=1.84).

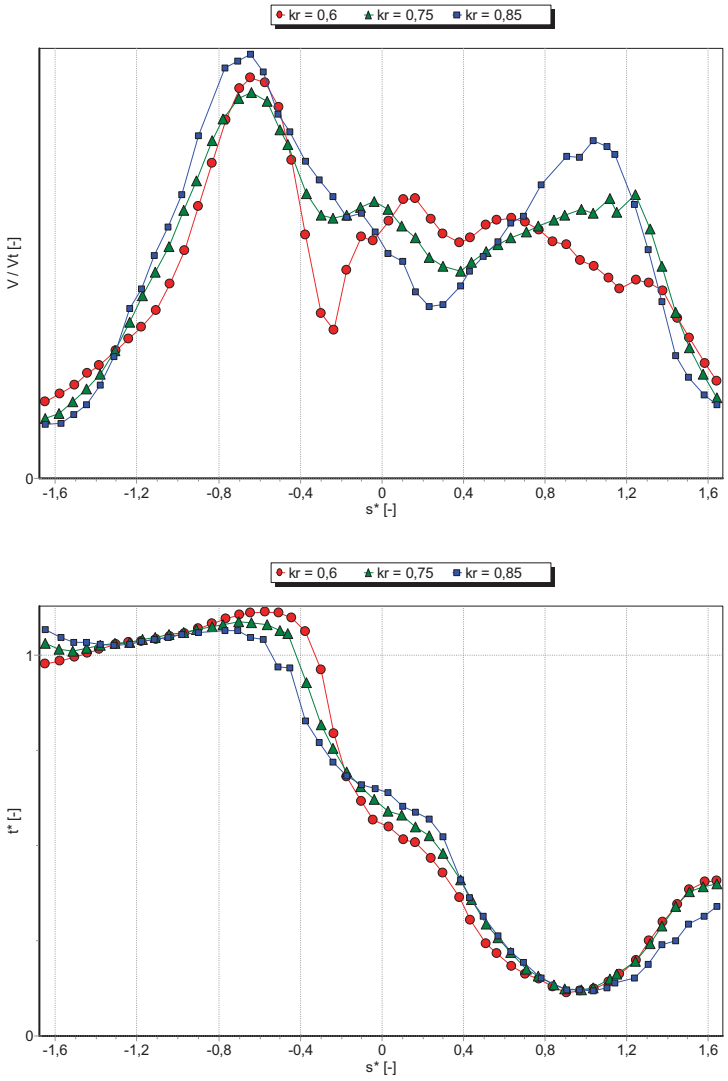

FIGURE 5.43: Normalized magnitude of velocity fluctuations and phase lag for the three streamlines far from the vibrating tube in the stream-tube.

Parallel triangular tube array at high cross-flow velocity $U_r = 6\ 4$

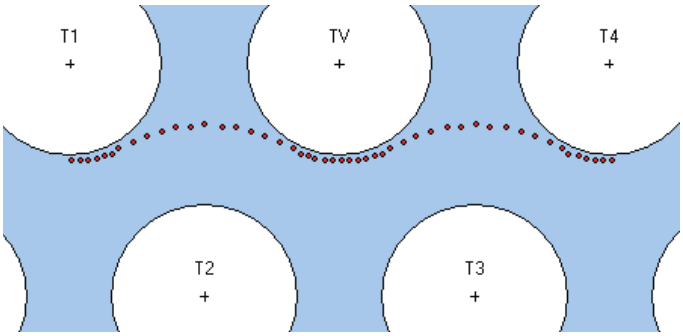

FIGURE 5.44: Streamline considered in the numerical calculations for the comparison with the experimental measurements [3] (k=0.11).

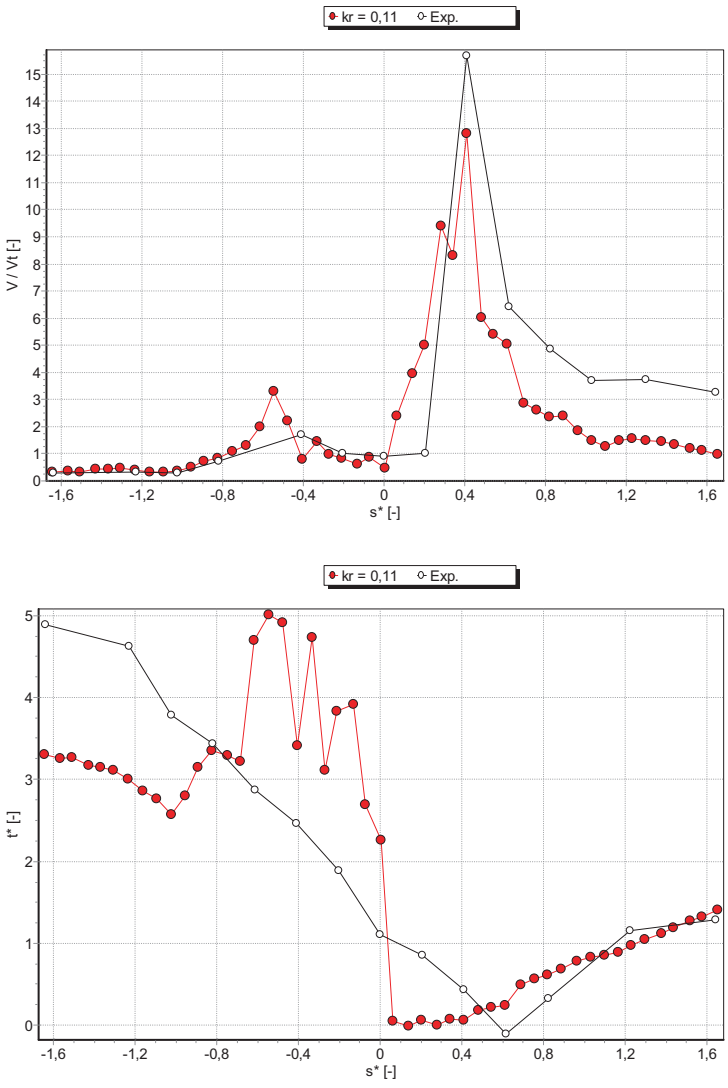

FIGURE 5.45: Normalized magnitude of velocity fluctuations and phase lag for the stream line k=1.11 compared to the experimental data.

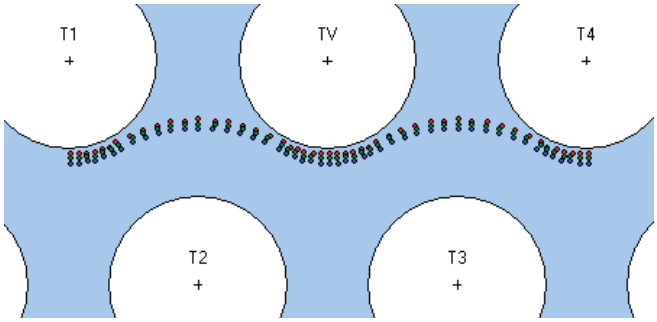

FIGURE 5.46: Location of the three stream-lines closer to the vibrating tube considered in the numerical calculations.

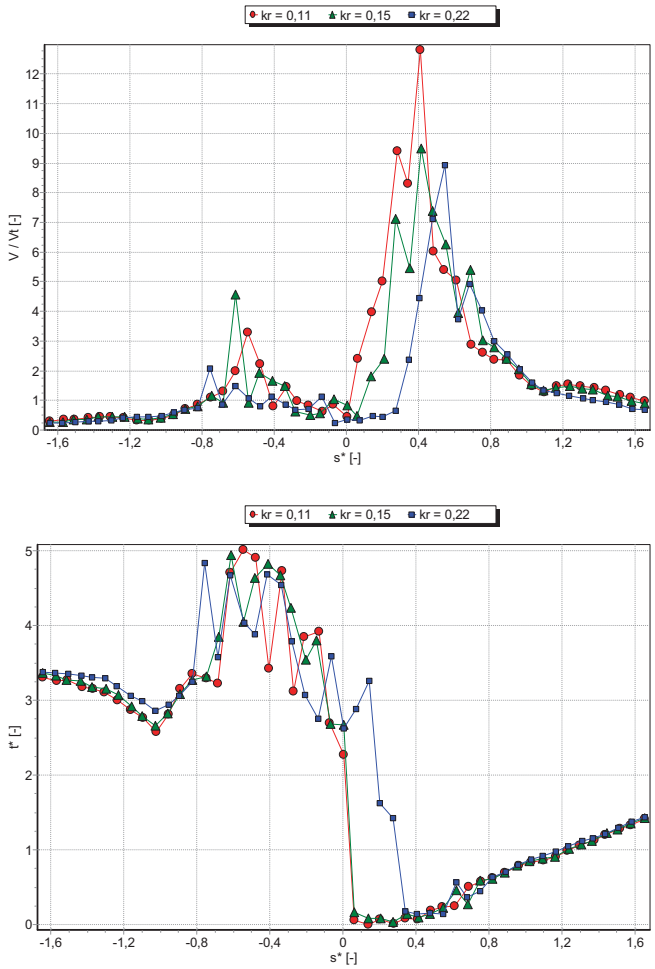

FIGURE 5.47: Normalized magnitude of velocity fluctuations and phase lag for the three streamlines closer to the vibrating tube.

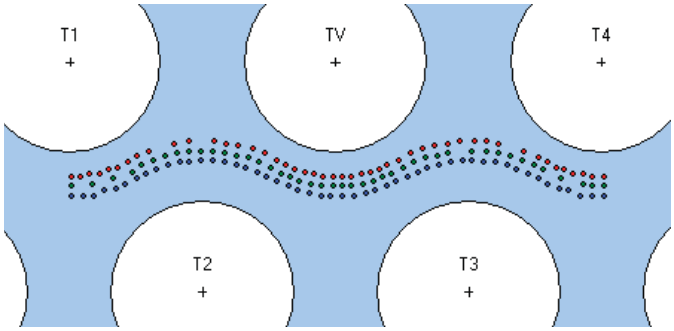

FIGURE 5.48: Location of the three stream-lines in the middle of the stream-tube considered in the numerical calculations.

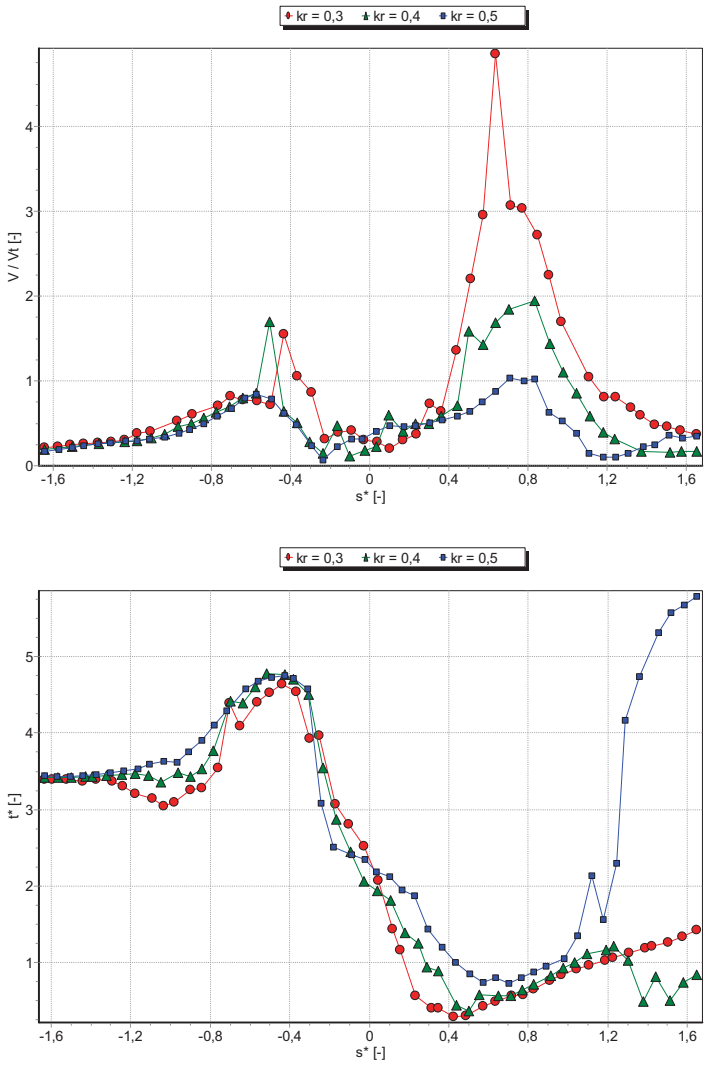

FIGURE 5.49: Normalized magnitude of velocity fluctuations and phase lag for the three streamlines in the middle of the channel.

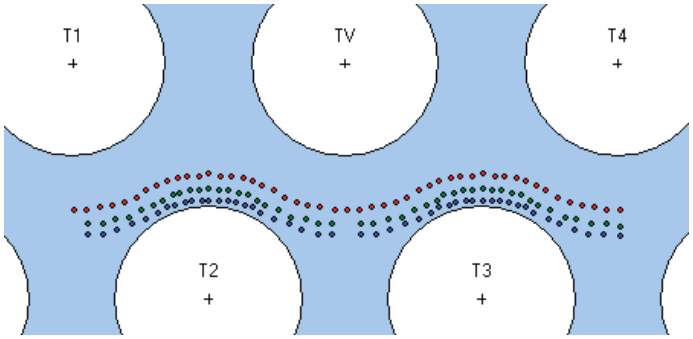

FIGURE 5.50: Location of the three stream-lines further to the vibrating tube in the channel considered in the numerical calculations.

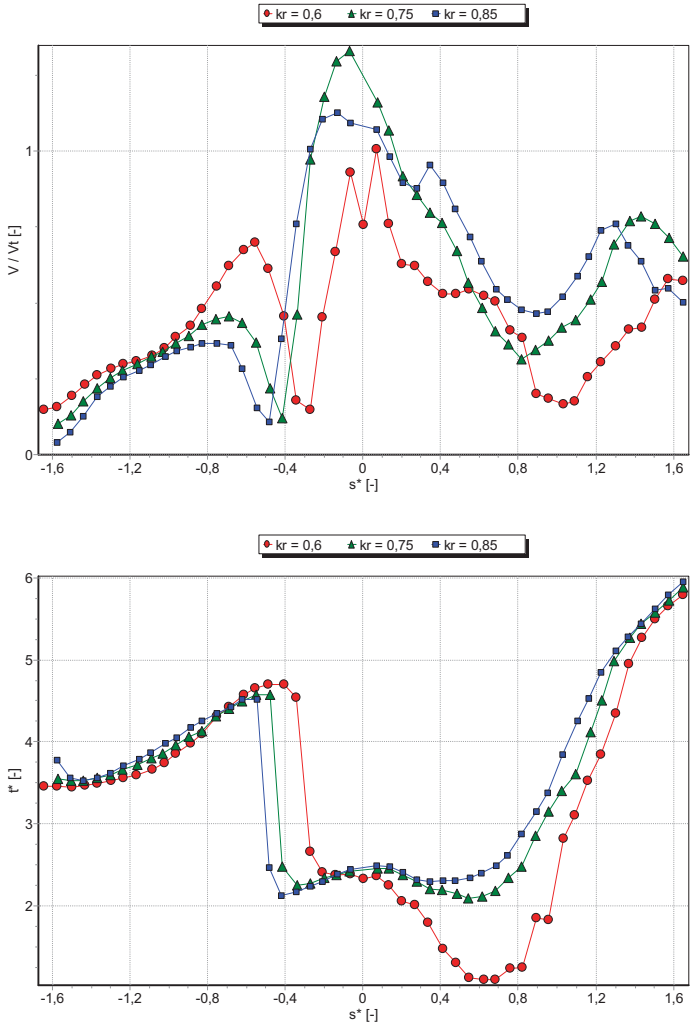

FIGURE 5.51: Normalized magnitude of velocity fluctuations and phase lag for the three streamlines further to the vibrating tube in the channel.

	P/d	Row (of the vibrating tube)	U_r	U_p/U_g
m l [3]	1 54	3	7 4	0 52
CFD	1.57	5	6 4	0 56

TABLE 5.1: Comparison of numerical and experimental parameters and propagation velocities U_P of the disturbances downstream the flow detachment region of tube TV.

5.3.2 Normal triangular tube array geometry

5.3.2.1 Maps of velocity and static pressure

Flow pattern oscillations for normal triangular tube arrays are investigated in this subsection. The discussion includes the analysis of average velocity magnitude, average amplitude of oscillations and also average phase lag with respect to the tube motion in the interstitial flow of these geometries. Firstly, velocity magnitude, amplitude of oscillation and phase lag of the flow perturbations in the interstitial flow of a normal triangular tube array with $P/d = 1\ 25$ were analyzed for a cross-flow reduced velocity of $U_r = 21\ 22$ and amplitude of the forced oscillations of $\Delta = 1\%$.

In particular, instantaneous time results were postprocessed so average values for a whole oscillation cycle were obtained in a region around the tube comprising three rows and two lines. Figs. 5.52-5.66 show the results of the study in maps of average amplitude and phase lag for the three fundamental harmonics.

Fig. 5.52 shows the map corresponding to the average velocity magnitude. In this figure the stagnation points in front of the tubes can be clearly appreciated, as well as the wakes in the rear and the detachment points that are located approximately at 110° and 250° in the angular coordinate. Highest velocities in the narrowest sections between the tubes are very homogenous, particularly in this case of $P/d = 1\ 25$, corresponding to four times the upstream velocity.

Figs. 5.17-5.19 show the amplitude of the fluctuations of velocity magnitude for the first, second and third harmonics respectively. The most significant fluctuations take place in the detachment points of tube TV. Precisely, this location for the source of perturbations was also proposed by Khalifa et al. [3] in their experimental study. It is also noticeable that second and third harmonics show much lower perturbations, with an amplitude that it is one order of magnitude lower than those of the first harmonic and with an area of influence much smaller. Regarding the phase lag, Figs. 5.20-5.23 show the results for the three first harmonics with different range scales in order to allow a more precise perception of the flow features in the different zones of interest. In general, the main stream in the channel is in phase with the tube motion, because the incremented section provokes the general increase of the flow velocity in the channel.

However both wake in tube T1 and stagnation point in tube T3 present 180° phase lag due to the upward motion of the tube. This produces in turn the suction of both wake and stagnation point areas making the affected area larger and even connecting the two zones (this can be seen around the angular position 270° in the figures, where the phase (90°) shows and intermediate behavior between the main stream and the wakes and stagnation point responses).

Fig. 5.24, showing the map corresponding to the average static pressure, this figure reveals the maximum pressure values in the stagnation points affectation areas in the front of the tubes, where the velocity is lower. Conversely, lower pressure values are located in the narrowest sections between the tubes, where the velocity is the highest.

Figs. 5.25, 5.26 and 5.27 show the amplitude of the fluctuation for static pressure at the contributions given by the first, second and third harmonics respectively. Large fluctuations arise between TV and T3, where the stagnation point of T3 is being suctioned by the vibrating tube motion. This produces that the flow is entering and leaving the area affected by the stagnation point with the tube motion (red zones in Fig. 5.25). Besides, maximum fluctuations also take place in the detachment points of the vibrating tube. Second and third harmonics shows much lower perturbations, with one and two orders of magnitude below the fundamental frequency.

Regarding the phase lag, Figs. 5.28-5.30 show the results for the three first harmonics. In the first map, it can be seen that the the static pressure in the stagnation point is in phase with the tube position, because of the suction-induced motion. Notice that the area affected by the suction of the stagnation point reaches downstream the narrowest section between the tube TV and the tube T3, while upstream it gets to approximately the 285° angular position of tube TV. Out of this region, the flow pressure is phase-inverted with the tube motion: the increment in the channel section produces the increment of the kinetic energy and consequently the decrement of the pressure. It is noticeable that the transition between these two areas is much abrupter downstream than upstream (there is an intermediate section upstream, between the 255°-285° angular positions in which the phase lag is around 90°). This is presumably attributed to a stronger effect of the velocity increment there: the section increase so both factors involved (increase of kinetic energy and the suction due to the T3 stagnation point) present similar importance, leading to an intermediate phase response (none of them is predominant for the flow behavior).

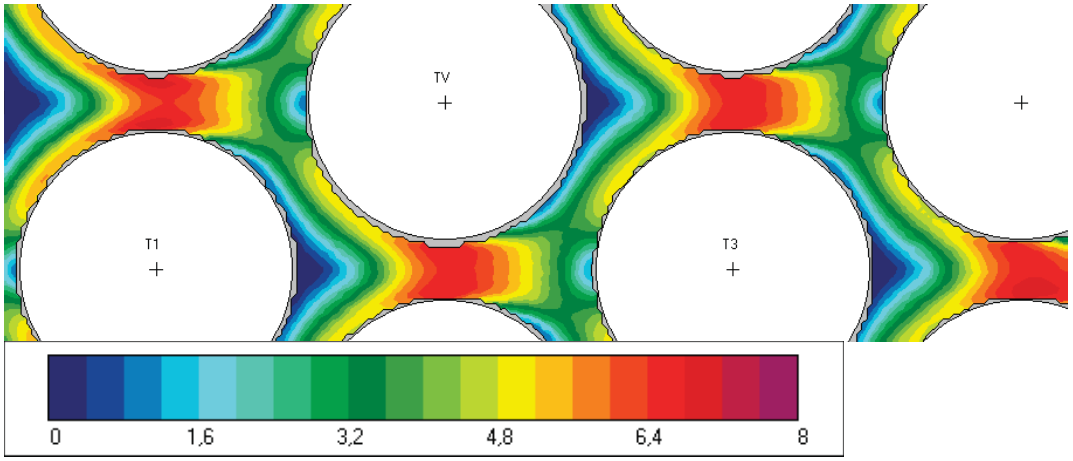

FIGURE 5.52: Average velocity magnitude [m/s].

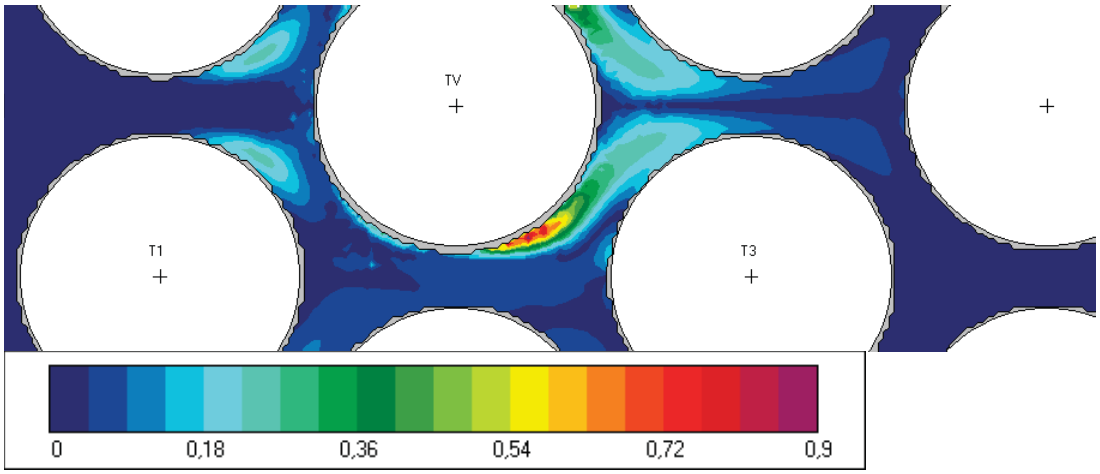

FIGURE 5.53: Fluctuation of the velocity magnitude. Amplitude of the 1st harmonic (f=7.81 Hz).

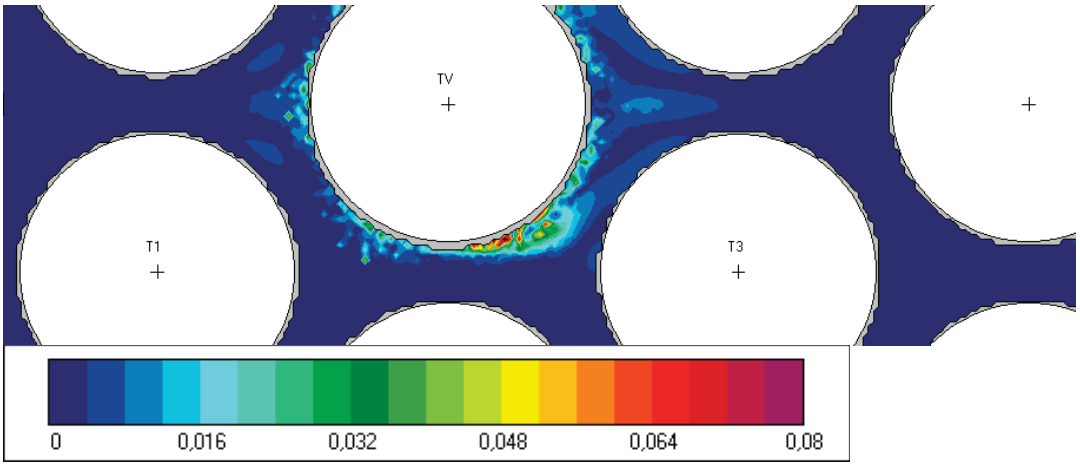

FIGURE 5.54: Fluctuation of the velocity magnitude. Amplitude of the 2nd harmonic (f=15.63 Hz).

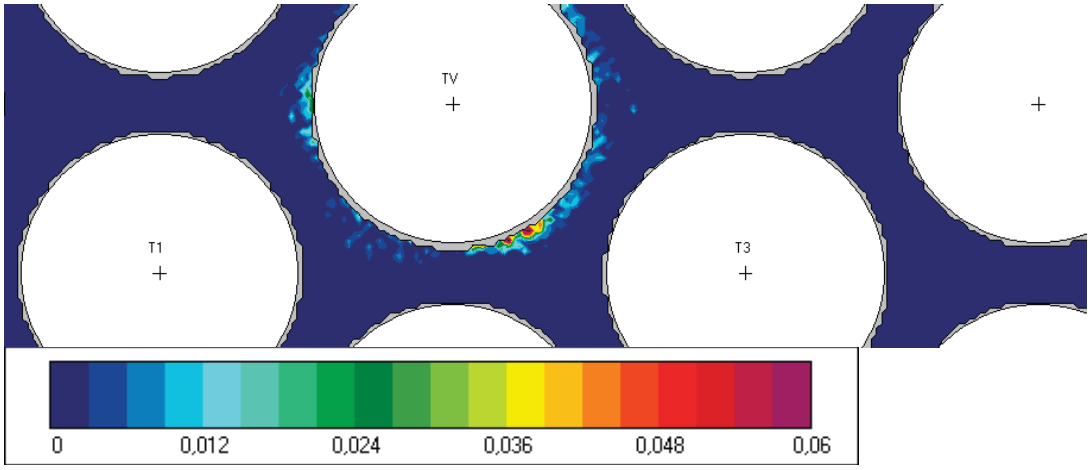

FIGURE 5.55: Fluctuation of the velocity magnitude. Amplitude of the 3th harmonic (f=23.44 Hz).

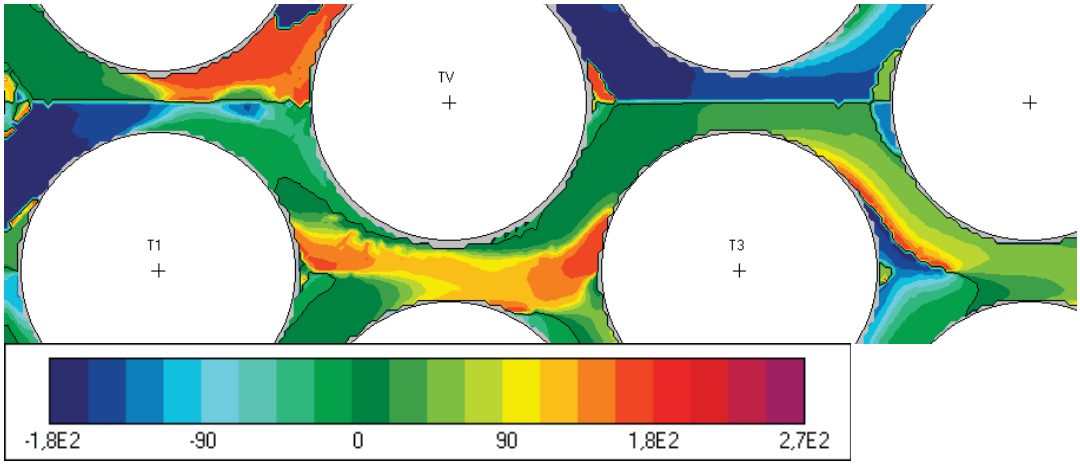

FIGURE 5.56: Fluctuation of the velocity magnitude. Phase of 1st harmonic (f=7.81 Hz).

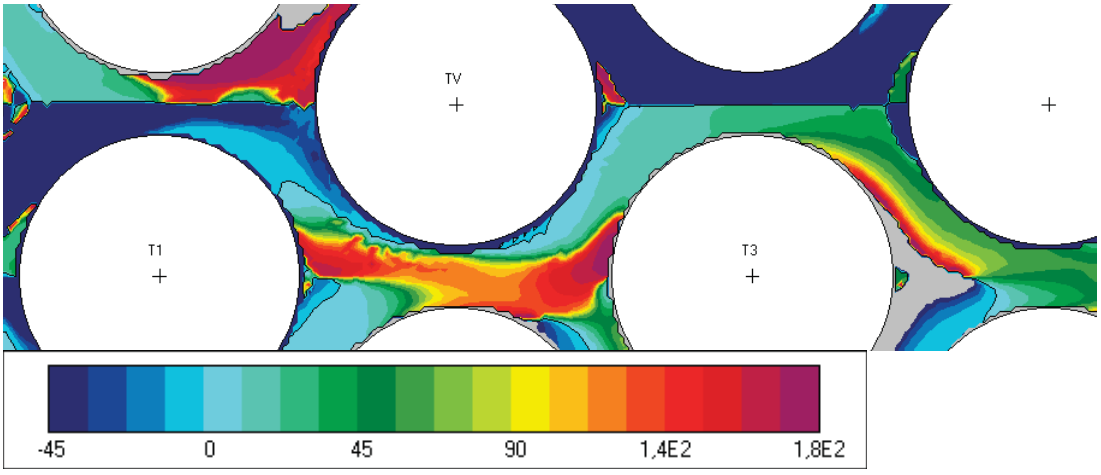

FIGURE 5.57: Fluctuation of the velocity magnitude. Detail of the phase of the 1st harmonic (f=7.81 Hz).

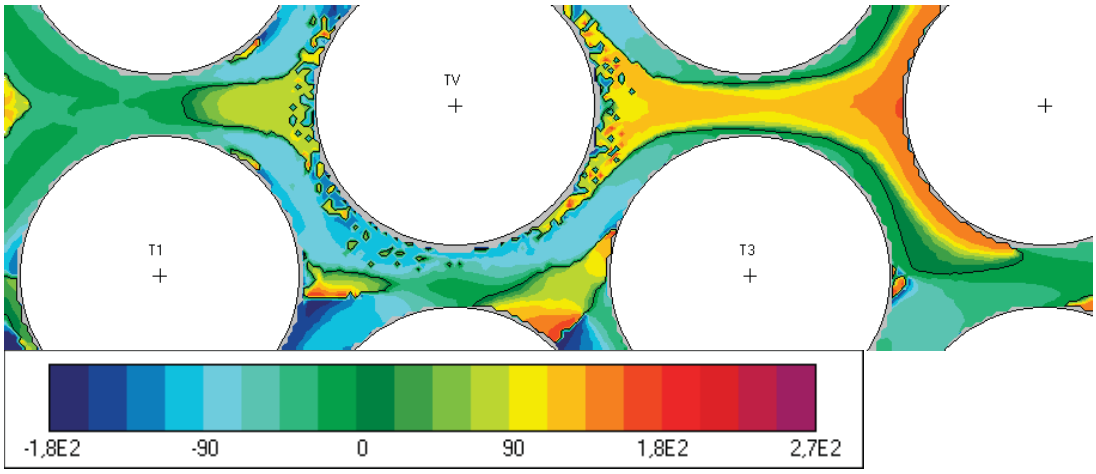

FIGURE 5.58: Fluctuation of the velocity magnitude. Phase of the 2nd harmonic (f=15.63 Hz).

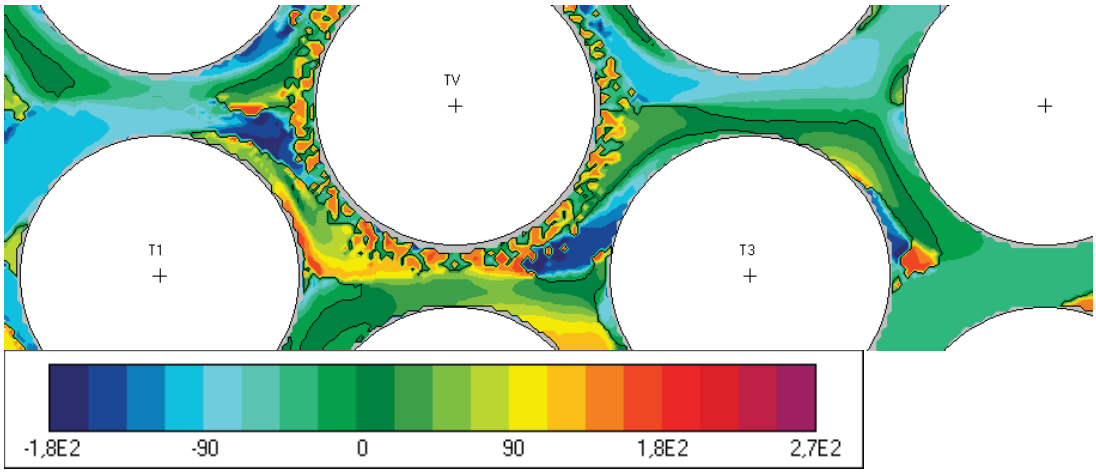

FIGURE 5.59: Fluctuation of the velocity magnitude. Phase of the 3th harmonic (f=23.44 Hz).

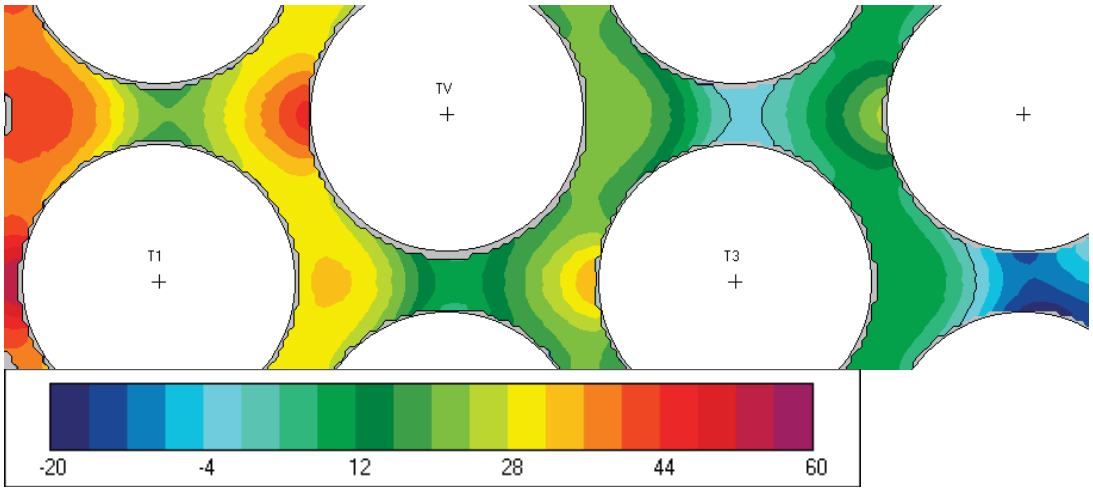

FIGURE 5.60: Averaged static pressure [Pa].

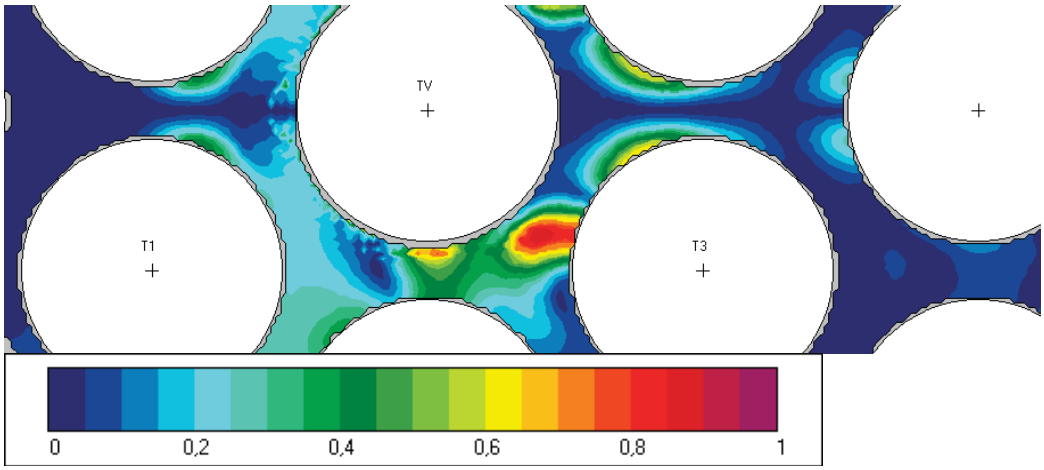

FIGURE 5.61: Fluctuation of the static pressure, amplitude [Pa] of the 1st harmonic (f=7.81 Hz).

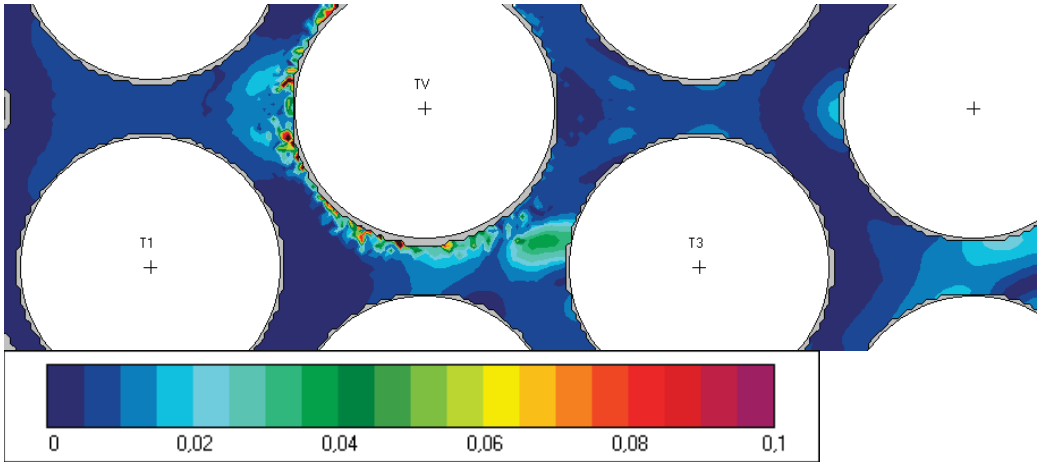

FIGURE 5.62: Fluctuation of the static pressure, amplitude [Pa] of the 2nd harmonic (f=15.63 Hz).

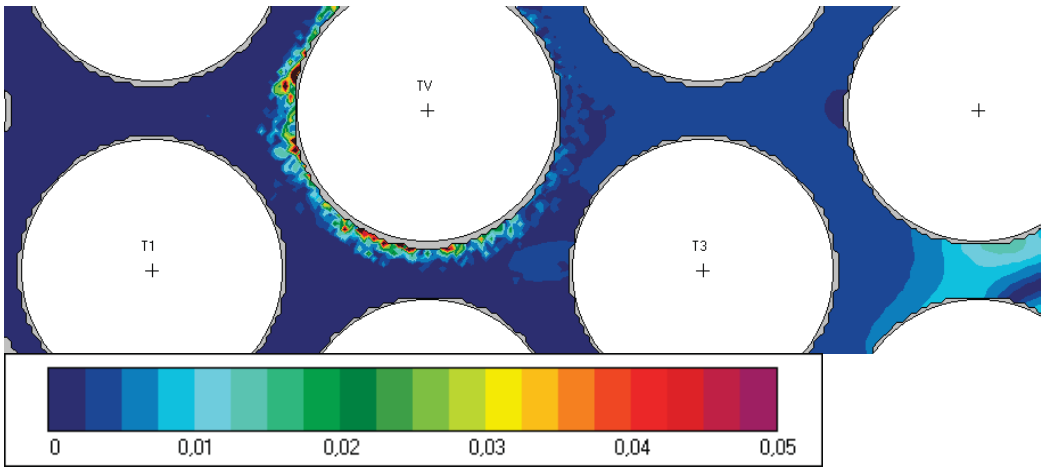

FIGURE 5.63: Fluctuation of the static pressure, amplitude [Pa] of the 3rd harmonic (f=23.44 Hz).

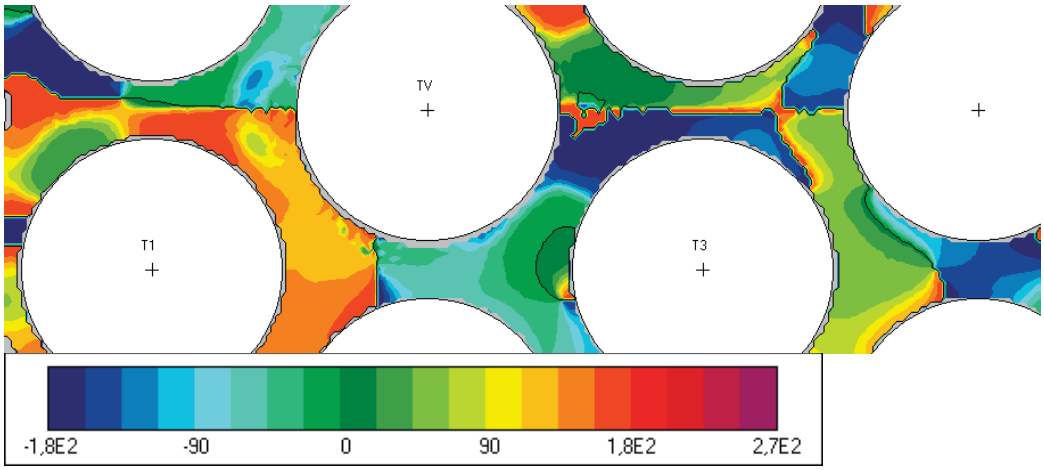

FIGURE 5.64: Fluctuation of the static pressure. Phase of the 1st harmonic (f=7.81 Hz).

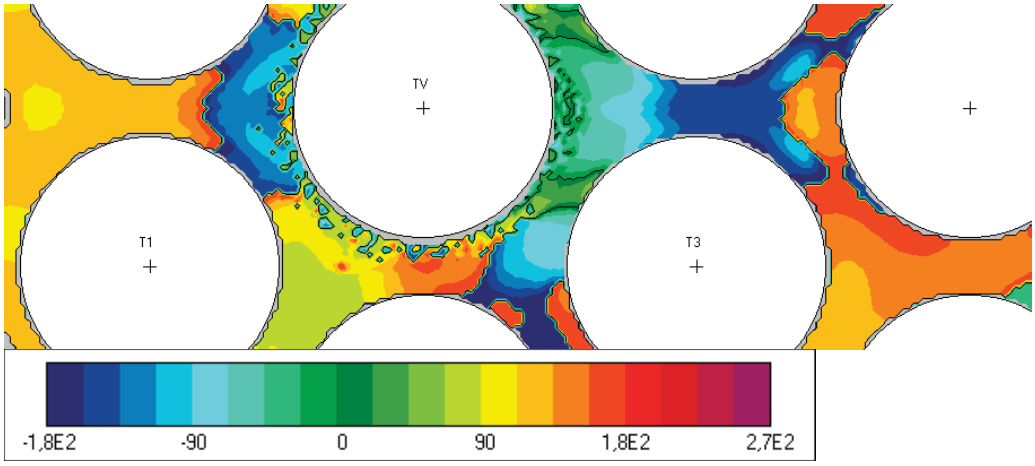

FIGURE 5.65: Fluctuation of the static pressure. Phase of the 2nd harmonic (f=15.63 Hz).

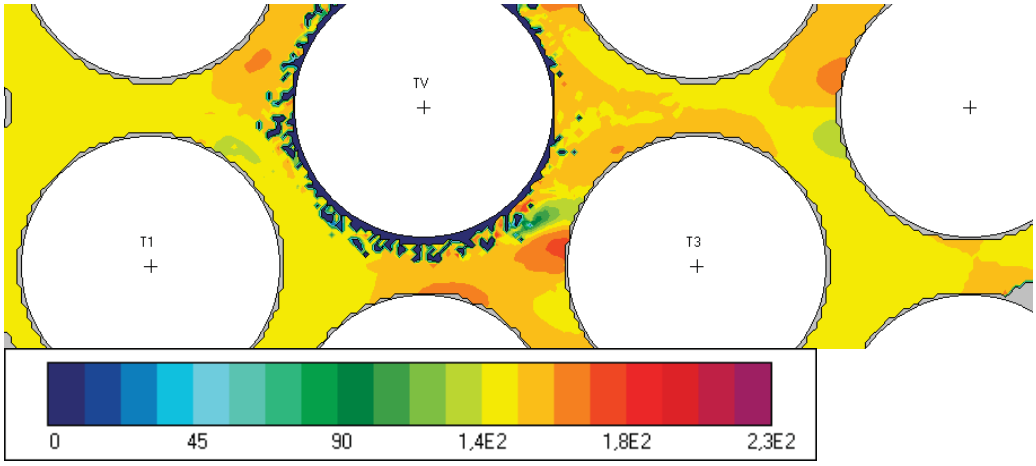

FIGURE 5.66: Fluctuation of the static pressure. Phase of the 3th harmonic (f=23.44 Hz).

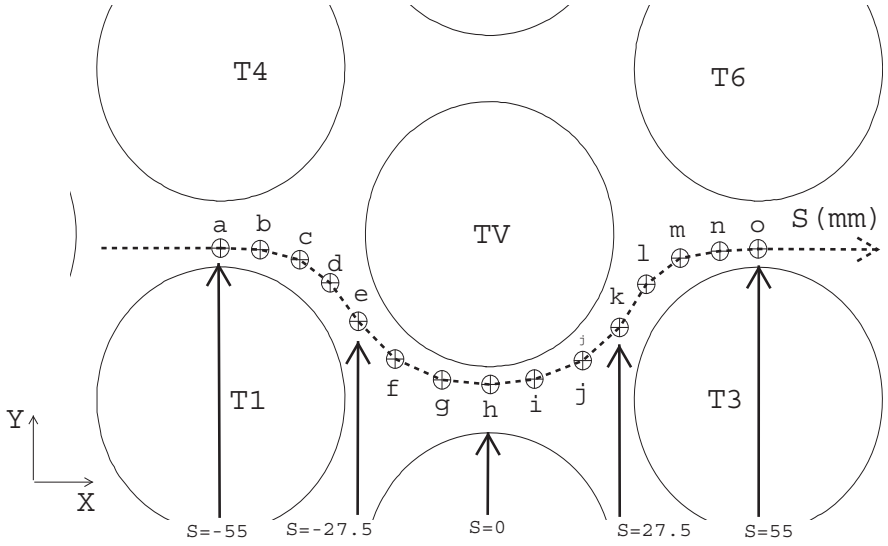

FIGURE 5.67: Position of the nodes for the velocity and pressure monitoring with the tube TV undergoing forced oscillations. S = curvilinear coordinate.

5.3.2.2 Propagation of the velocity and pressure perturbations

In order to explore the transmission of perturbations along the streamflow within the array, fifteen points (labelled a to o) were selected along a streamline surrounding the tube TV (Fig. 5.67), where the velocity magnitude and the pressure distributions have been monitored during the computations. Positions e-k are distributed in the region adjacent to tube TV at a radial distance between 5% (point h) and 12% (e and k) of the tube diameter (relative to the equilibrium position). The other nodes are located at similar positions with respect to the preceding and following cylinders (T1 and T3). Each of these nodes is associated to a linear coordinate along the stream, with =0 at the central point -node h. (Fig.5.67).

Figs.5.68 and 5.69 shows the calculated instantaneous contours of velocity magnitude and static pressure (P/d=1.25, U_0=1.26 m/s) in the region surrounding the vibrating tube (at 7.81 Hz) at the instant of maximum tube displacement (3% of tube diameter upwards). The general velocity pattern, which is in concordance with the visualization pictures obtained for the normal triangular tube array [94], clearly shows how the main stream detaches from the rear part of each cylinder (T1, T4, TV) to be later reattached to the next one after an inflexion region with a lower velocity. As expected, the pressure is the lowest in the gap region between cylinders of the same row, where the velocity is

the highest. Conversely, the pressure is higher at the stagnation zone on the front side of each cylinder (TV, T3, T6) as well as in the wakes (T1, T4, TV).

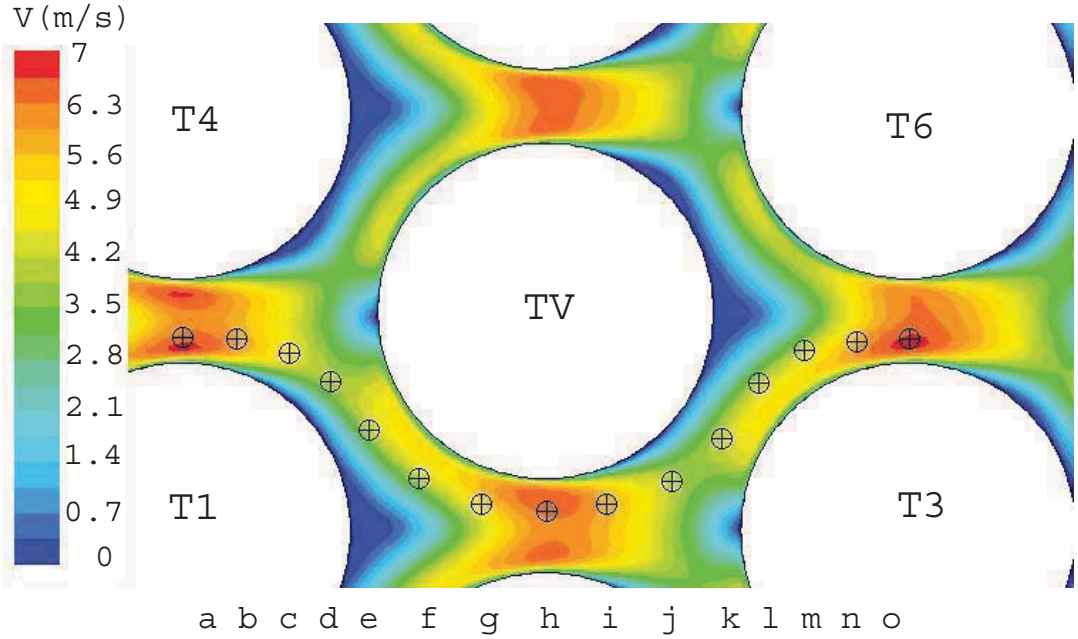

FIGURE 5.68: Instantaneous distribution of the velocity magnitude for P/d=1.25 U_0=1.26 m/s and tube TV oscillating transversely at 7.8Hz with amplitude of 3% of tube diameter, at the instant of maximum displacement upwards.

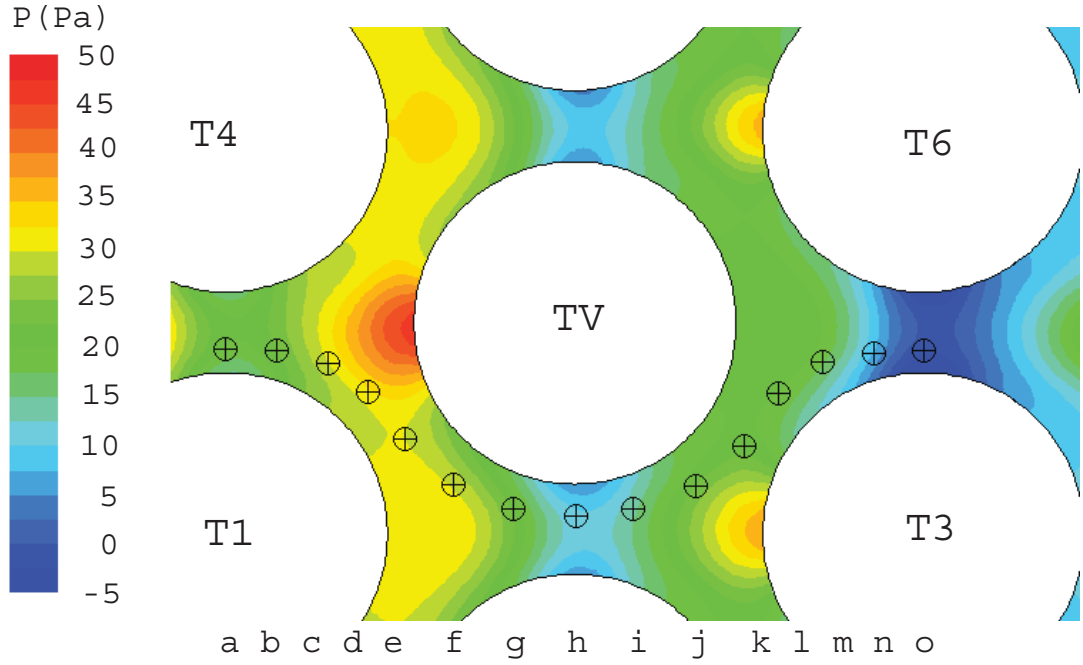

FIGURE 5.69: Instantaneous distribution of the static pressure for P/d=1.25 U_0=1.26 m/s and tube TV oscillating transversely at 7.8Hz with amplitude of 3% of tube diameter, at the instant of maximum displacement upwards.

The comparison of the upper and lower parts of both images in Figs.5.68 and 5.69 reveals asymmetries that are due to the shifted position of tube TV from equilibrium and also to the time lag required by the stream to accommodate to the tube motion. The latter produces a kind of wriggling effect at the border of the wake from the oscillating tube and also from the fixed cylinders. At the instant shown in Fig.5.68, the separation between tubes TV and T5 is the lowest while it is the largest between TV and T2. Because of that, the flow passing between cylinders T1 and T4 deviates downwards at a higher rate than upwards, and so the velocity of the main stream through tubes TV and T1 is higher than through TV and T4. Also, the wake from T4 has swelled until nearly merging with the stagnation zone on TV, creating a relatively large area at high pressure. However, despite the higher flowrate below tube TV than above, the average velocity at the gap between TV and T2 is lower than between TV and T5 (the opposite regarding average pressure), i.e. the flowrate distribution has not yet reached proportionality to the gap size. Downwards, the passage between TV and T3 is analogous to the region between TV and T1, whereas the passage between TV and T6 resembles the region between TV and T4, including the wake swelling effect toward the stagnation zone on tube T6, despite the low average pressure on top of tube TV.

Fig.5.70 shows the normalized amplitude of the velocity fluctuations at 7.8 Hz (x- and y-components) computed at each node for upstream velocities of 0.63 m/s (U_r=10.6), 1.26 m/s (U_r=21.2) and 1.89 m/s (U_r=31.8). Despite the range covered, the three curves are very similar for both velocity components. This can be attributed to the low value of the cylinder velocity with respect to the cross stream and, also, it indicates little dependence on the Reynolds number. As expected, the curves of velocity amplitude in both directions show decreasing values both up and downstream from the vibrating tube, with nearly no fluctuation at node a. However, the velocity amplitude is also low between nodes f and h, in spite of being close to the position of maximum channel constriction and enlargement when the cylinder vibrates. Highest fluctuations correspond to nodes c-e and, overall, i-m, which represent locations near the border of the wakes formed from tubes T1 and TV respectively, and hence they can be attributed to the wake oscillations lagging the motion of tube TV. In spite of tube V being oscillating only in the y-direction, the velocity fluctuations are considerably higher in the x-direction, except for the first upstream nodes a-c.

Fig.5.71 shows the amplitude and phase (relative to the position of tube TV) of the fluctuations of the velocity magnitude at the fifteen reference nodes. Not surprisingly, the amplitude distribution is similar to that for the x-component of the velocity, and, again, there is little dependence on the flowrate. In this regard, the most noticeable effect corresponds to node c: its velocity amplitude decays fast when increasing the flowrate because this provokes the wake stretch downstream so that node c gets out progressively from the wake border into the main stream.

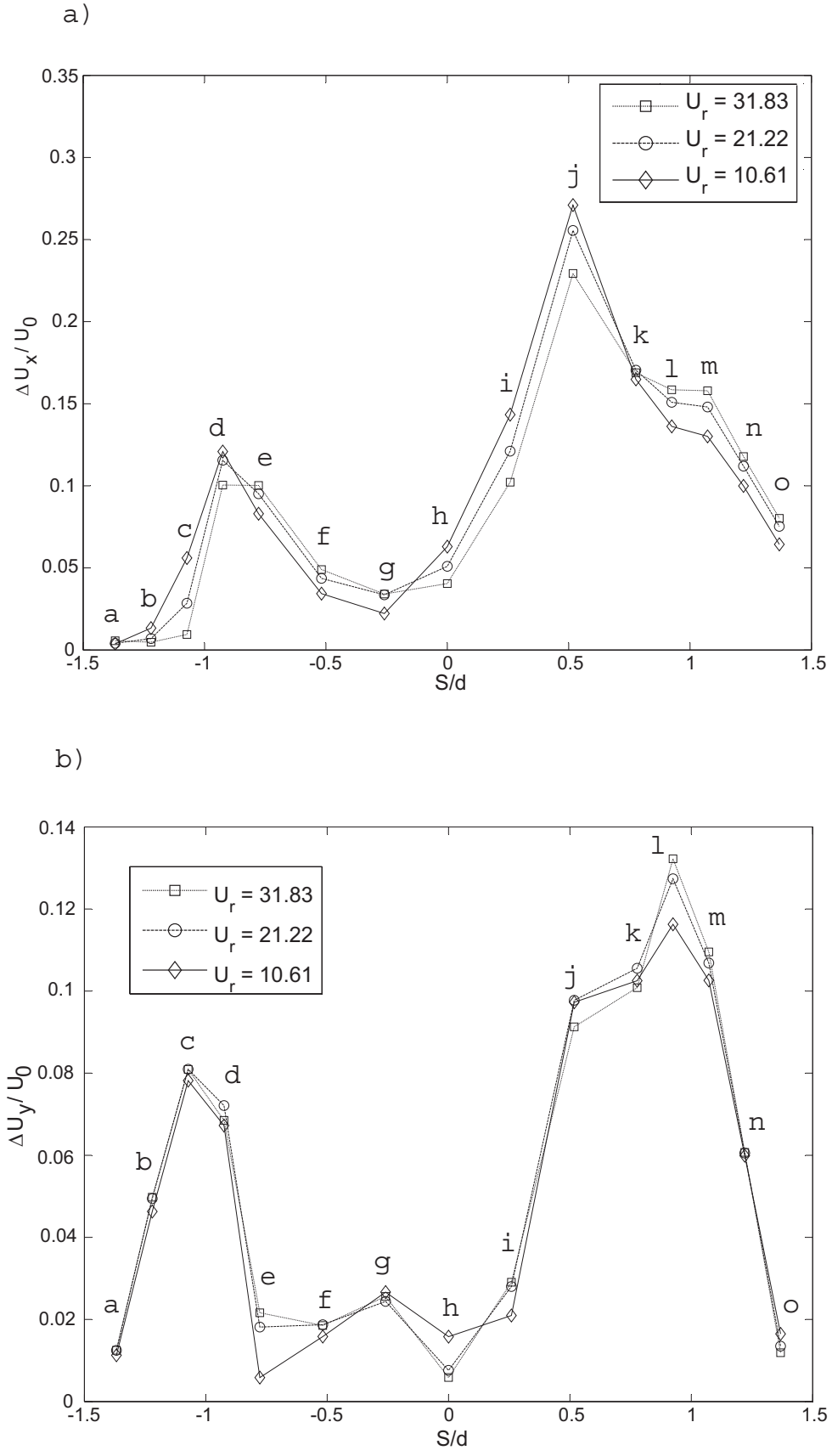

FIGURE 5.70: Amplitude of velocity fluctuations (x and y components) for three reduces velocities, with tube TV oscillating at 7.8Hz and amplitude of 0.01× d.

Regarding the velocity phase at the nodes with high amplitude, from c to e the phase is close to 0°, i.e., its velocity is approximately in phase with the motion of TV, whereas at node j (where the velocity amplitude is the highest) the phase is about 25°-30° and then increases downstream quite progressively up to about 60° at node o (for the smallest flowrate). This confirms that in the stream channels between T1 and TV and between TV and T3 the instantaneous flow-rate is highest or close to highest when tube TV is at top position during its oscillation. On the contrary, at node h the velocity phase is about 105°-115°, thus confirming that the increment in flow rate below TV when it is at top position is counterbalanced by the increment in cross-section between TV and T2.

Besides, the slope of the progression of the phase from node j to o is seen to be dependent on the reduced velocity U_r: the higher U_r, the lower the slope. This suggests that the velocity disturbances induced by TV travel downstream at a propagation speed that increases with U_r. For any given U_r, the phase curve is slightly less steep (i.e., faster propagation) before node l. This is so because nodes j-k are right in the area of disturbance formation (wake border close to separation point) and so they are affected very directly by the oscillations of tube TV. Table 1 presents the propagation speed estimated after performing a linear fit of the phase data for the last four nodes l-o, each at its curvilinear coordinate . For the three cases the determination coefficient ^{2} is above 0.985. The last column of Table 1 gives the ratio between the disturbance propagation speed and the gap velocity. This ratio is seen to take values between 0.8 for $U_r = 31\ 83$ and 0.88 for $U_r = 10\ 61$ (i.e. it changes little in spite of multiplying U_r 3 times).

U_r	U_g (m/s)	U_p (m/s)	^{2}	U_p/U_g
10 61	3 15	2 76	0 997	0 88
21 22	6 30	5 29	0 986	0 84
31 83	9 45	7 59	0 986	0 80

TABLE 5.2: Propagation velocities U_P of the disturbances downstream the flow detachment region of tube TV.

These results are comparable to the findings by [3] based on hot-wire measurements in the cross-flow through a parallel triangular array with P/d=1.54. Like in the present study, they identified the region of flow detachment from the vibrating cylinder as the source for flow disturbance propagation, and, besides, they observed that the propagation speed downstream was proportional to the gap velocity, with a factor of about 0.52. Certainly the higher value obtained for this factor in the present study can be attributed to the different array configurations regarding both geometry (normal triangular instead of parallel triangular) and P/d (1.25 instead of 1.54). However, [3] also observed clear

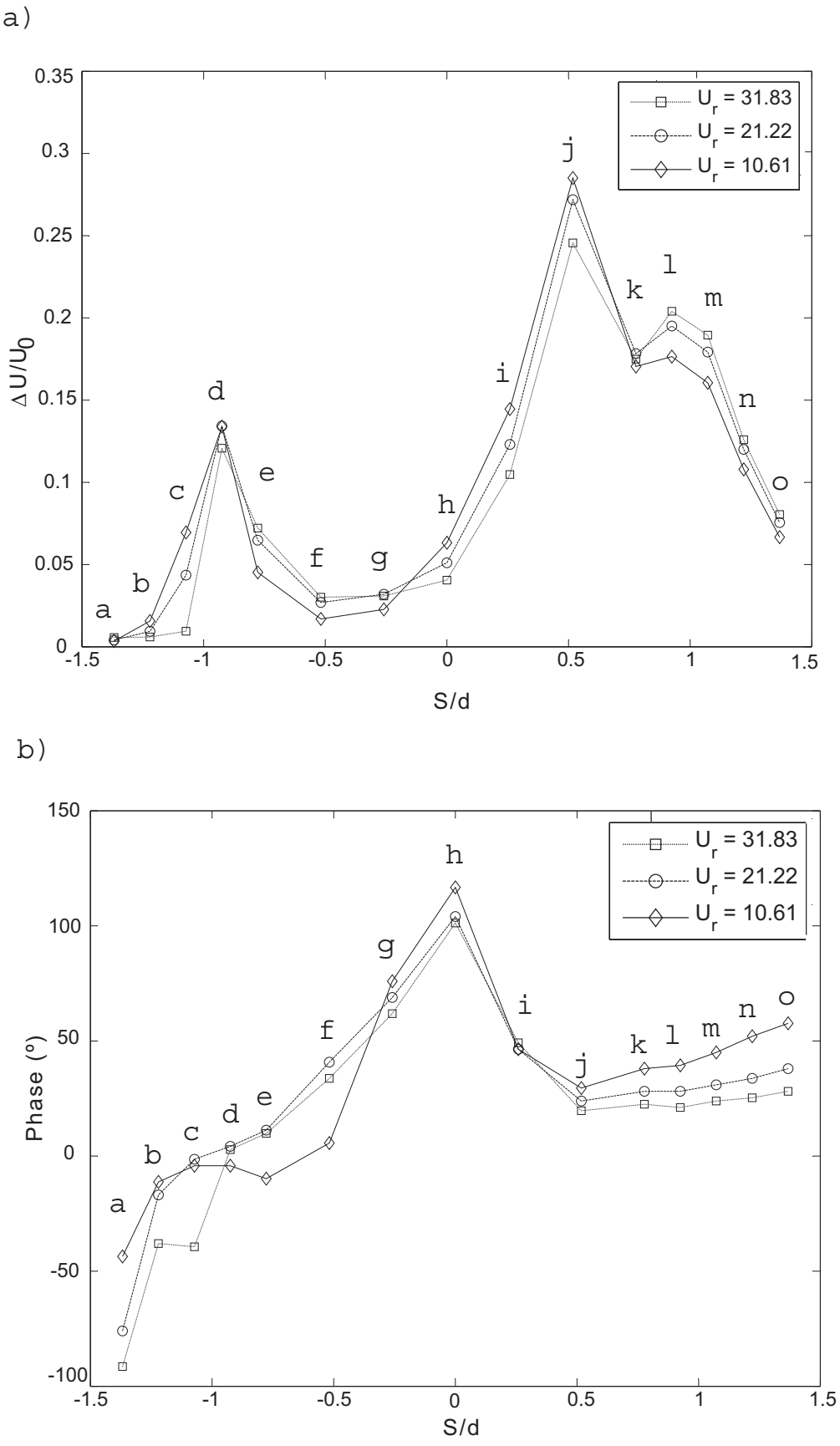

FIGURE 5.71: Amplitude and phase lag (relative to tube TV position) of the velocity magnitude. Conditions as in Fig. 5.13.

propagation upstream, at a speed about 20% lower than downstream. This is not so in the present study probably because of the array geometry: the oscillations of tube TV also induce significant oscillations in the wakes from upstream tubes T1 and T4, so that their wake borders can be considered as secondary disturbance sources that interfere with the main perturbations from tube TV.

Fig.5.72 shows the corresponding static pressure fluctuations in amplitude and phase (relative to the position of tube TV). Now the highest fluctuations are seen to correspond to nodes h-j for the three flowrates tested. That is the zone where flow decelerates while detaching from the oscillating tube, again in agreement with [3]. In fact, the pressure pattern of Fig. 5.72 resembles reasonably close the pressure measurements performed around a vibrating cylinder by [2] for a similar array (normal triangular, P/d=1.32), including the pressure dip at node i.

Considering the pressure phase, there is a minimum at node i that gets deeper for increasing values of U_r, while in the neighbor nodes (h, j, k) fluctuations are seen to be about in phase with the motion of tube TV, i.e. pressure there is the highest when tube TV is at the top position as in Fig.4.9b. This is so because at that instant the local cross-section is the largest and so the stream velocity is lowest, and, besides, the wake is well separated from nodes j-k and the stagnation region on cylinder T3 is growing towards tube TV. For that situation, the flowrate along the monitored stream is close

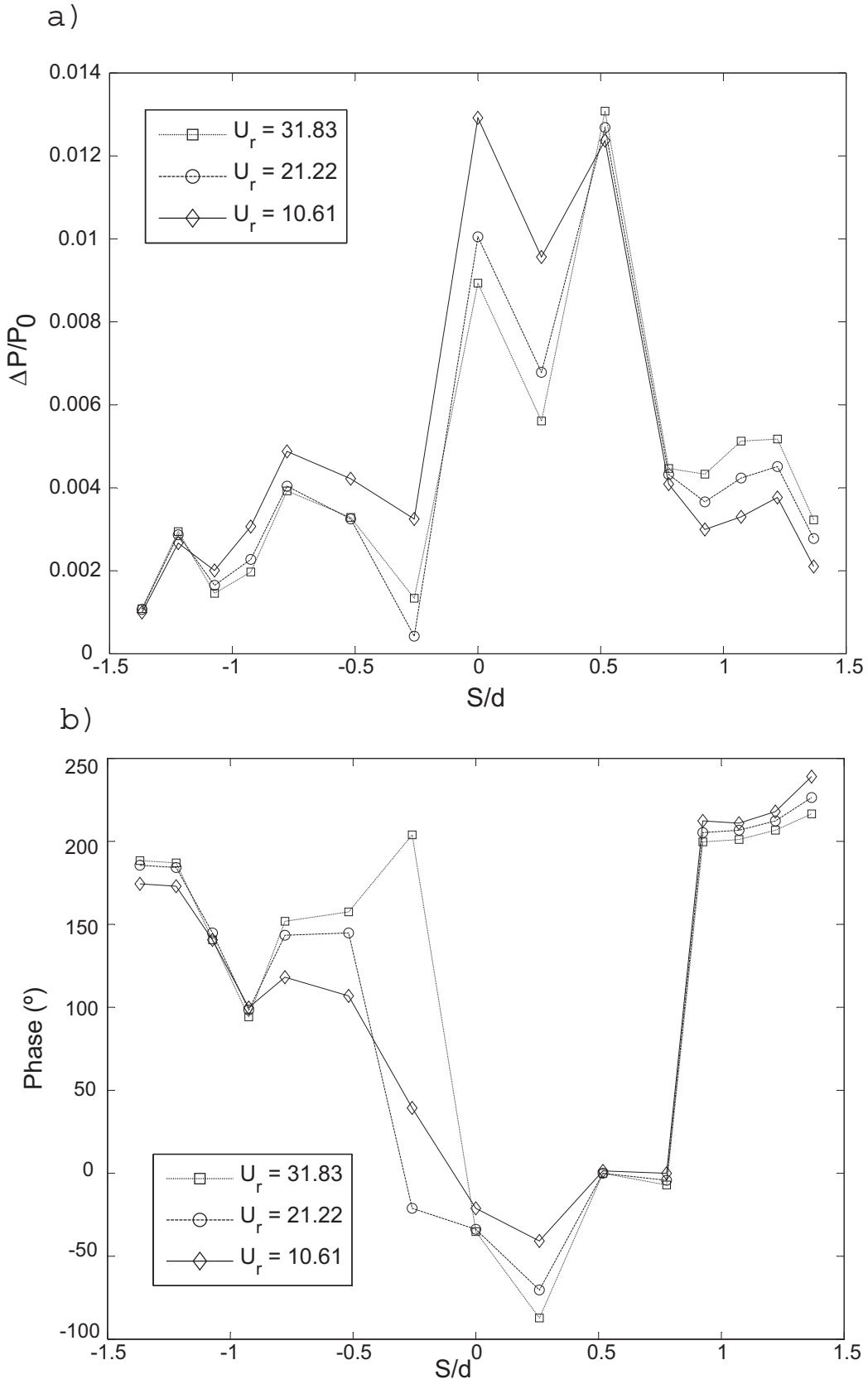

FIGURE 5.72: Amplitude and phase lag (relative to tube TV position) of the static pressure. Conditions as in Figure 5.13.

to the highest because of the enlarged cross-section at h-j, and that increases the velocity downstream (l-o) while pressure there reduces to a minimum. For that reason, the pressure phase shifts about 180° from k to l for the three flowrates tested. Upstream, the pressure phase also evolves towards values in the range of 180° at nodes a-b, but the progression is quite different depending on the flowrate. For the lowest U_r the variation in pressure phase is smoother, though there is some ridge at e-f that is related to the oscillations of the wake from the preceding cylinder T1. Increasing U_r, however, results in another 180° shift in the vicinity of node g, for which, besides, the pressure amplitude reduces nearly to zero.

Chapter 6

Self-excited Oscillations

6.1 Methodology and criteria for self-excited vibration

For the simulations reported in this section, the computed instantaneous fluid-dynamic forces that govern the vibrations of the tube were incorporated in the motion equation (Eq. 6.1) using a single degree of freedom scheme:

$$F(\ddot{}, \dot{}, \ , U_0) = m_s \ddot{} + \ _s \dot{} + \ _s \tag{6.1}$$

The modified user defined function allows the tube position and to be updated at each time step after using a discretized version of Equation 6.1 (derivatives approximated by finite difference ratios) which determines the new instantaneous tube velocity based on a second-order backward scheme.

The typical simulation procedure is initiated with a pre-calculation for steady flow and non-moving cylinders, in order to establish appropriate initial conditions for the dynamic calculations. Then the dynamic simulation for unsteady flow was launched, i.e. tube TV (Fig.3.2) was set free to move according to the fluid forces computed at each time step. Since the starting flow is not fully-symmetrical (due to small-scale asymmetries), the initial lift force was non-zero and the oscillation of tube TV about its equilibrium position was triggered from the beginning. As expected for air cross-flow, the added mass effects were small and the oscillations took place at the tube natural frequency as defined by its mass m and rigidity k. Depending on the cross flow velocity, the vibration amplitude could either decay progressively (Fig.6.1) or, on the contrary, amplify towards a state of limit cycle oscillations (Fig.6.2).

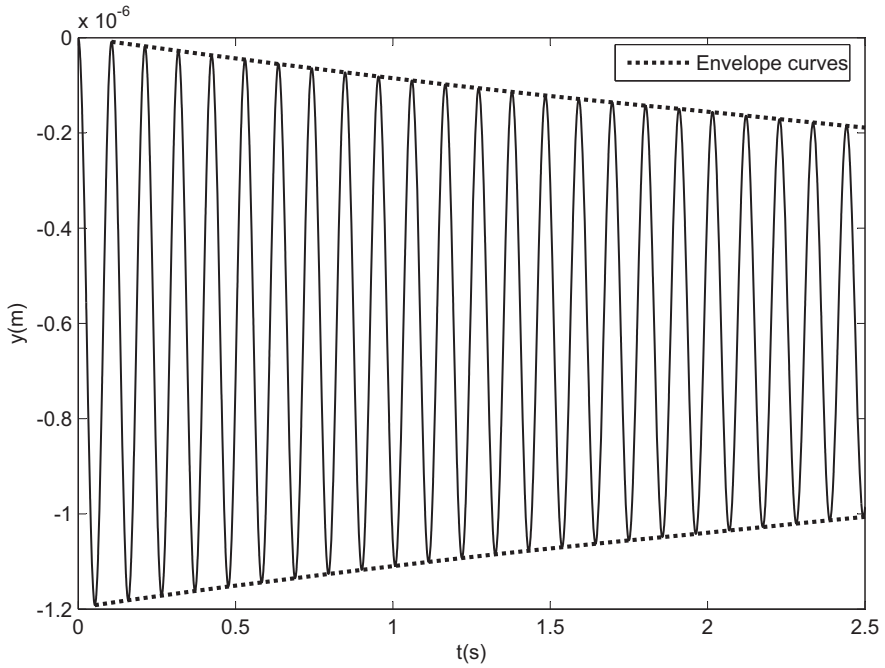

FIGURE 6.1: Example of tube response with decreasing vibration amplitude (stable regime).

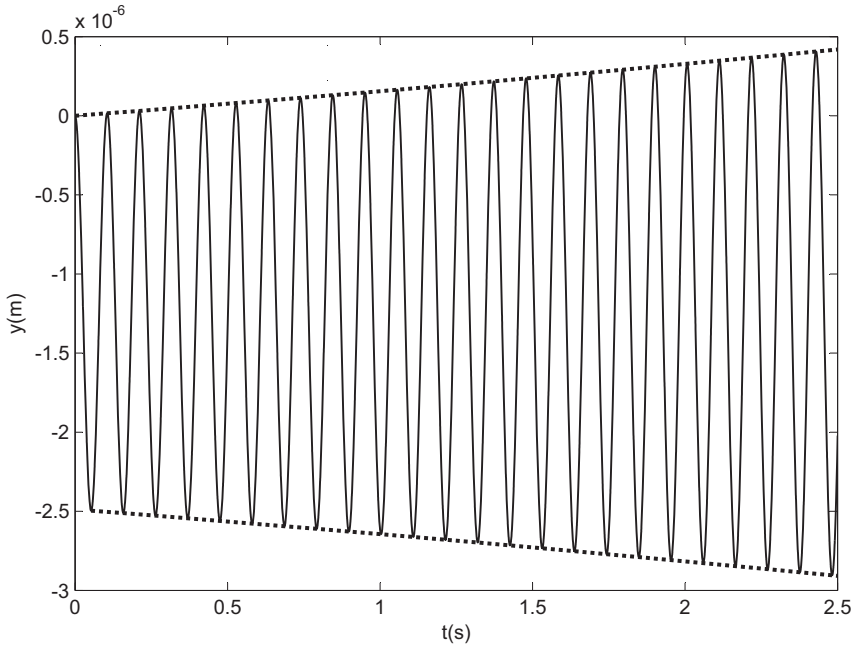

FIGURE 6.2: Example of tube response with increasing vibration amplitude (unstable regime).

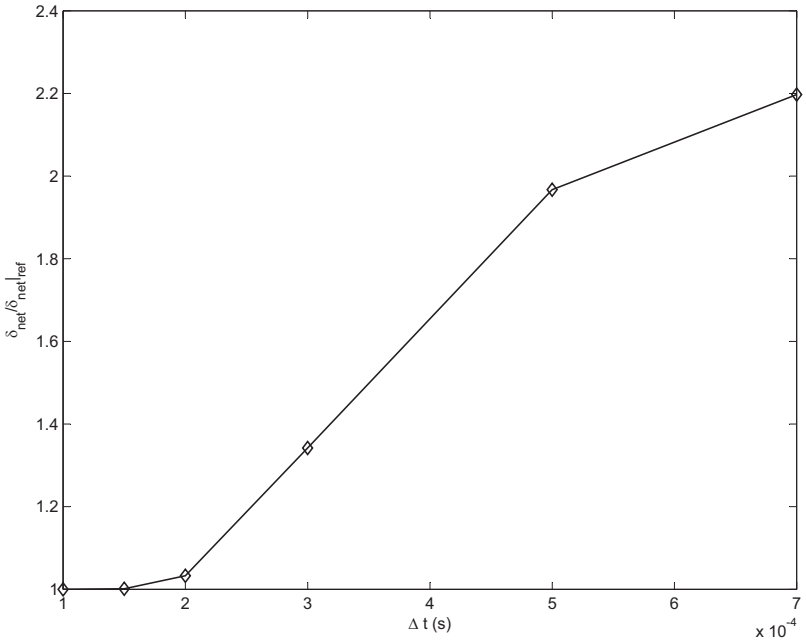

FIGURE 6.3: Effect of the time step on the computed damping of the coupled system. P/d=1.25, $m_r\delta$=26.7, U_0=1.26 and F_n=9.42Hz.

In the first case, the net damping of the system is positive so the system evolution is stable, whereas in the second case the net damping is negative and the system is dynamically unstable. The latter corresponds to damping controlled fluidelastic instability.
The corresponding system damping can be estimated by monitoring the tube motion and analyzing the amplitude decay (or growth). It was noticed that the resulting damping coefficient might be distorted depending on the time step employed in the simulations. Consequently, preliminary simulations were undertaken to explore that effect for the reference case of P/d=1.25, natural frequency f_n= 9.42 Hz and mass-damping parameter $m_r\delta$ = 26 7. The cross-flow had an upstream velocity of 1.58 m/s, for which this reference case is unstable. Fig.6.3 compares the predictions obtained for six time steps ranging from Δ =0.1 to Δ =0.7 ms, with the damping values normalized by the value for the time step of 0.1 ms. As expected, the predictions show very little variation for sufficiently small values of the time step, approximately below 0.2 ms. All subsequent simulations were conducted with a time step of Δ =0.15 ms, for which the relative deviation against the Δ =0.1 ms damping was 0.13%.

Fig.6.4 shows the time evolution of the tube vibration amplitude (as obtained from the envelope curves of the tube response) for the case (P/d=1.25, $m_r\delta$=18.7) when subjected to six cross-flows with velocities ranging from U_0=0.89 m/s to U_0=1.17 m/s. At low velocity the slope of the curves is negative, thus indicating that the net damping is positive and so the system is stable. Increasing the flow rate makes the slope more horizontal, i.e. the damping coefficient gets smaller, until a velocity at which the slope

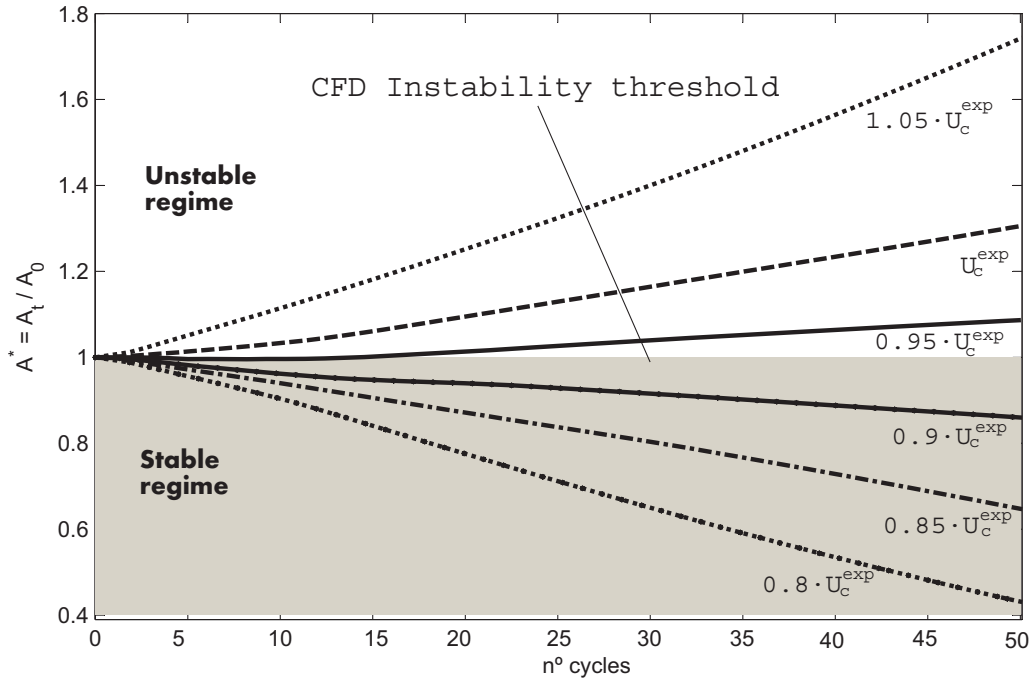

FIGURE 6.4: Envelope curves of tube response for increasing cross-flow velocity from stable to unstable regime (P/d=1.25,$m_r\delta$=26.7, U_c^{exp}=critical velocity determined by [1]).

turns positive and so the damping becomes negative and the system turns to be unstable. That velocity represents the critical threshold for fluidelastic instability.

6.2 Comparison #6: Critical velocity in self excited calculation mode

This method for delimiting the critical velocity was put into practice for the cases tested in wind tunnel by [1], who used arrays with P/d=1.25 and P/d=1.375 in which a single tube (located as tube TV in Fig.3.2) could oscillate in the transverse direction only. By means of a precise regulation of the damping of that tube, they obtained very accurate data of critical velocity for ranges of the mass-damping parameter from about 11 to 70 (P/d=1.25) and to 42 (P/d=1.375).

To prove the consistency of this enhanced methodology, a wide number of simulations have been performed, where the cross-flow velocity was progressively increased at intervals equivalent to 5% of the experimental critical value. Fig.6.5 compares Austermann and Popp's data of reduced critical velocity to the current CFD predictions, represented

by the highest U_r tested that showed stable regime behavior and the lowest U_r that showed unstable regime. The relevant data is collected in Tables 6.1 and 6.2.

$m_r\delta$	CFD highest stable U_r	CFD lowest unstable U_r	Experimental U_{cr}	Relative difference (%)
11 42	10 61	11 32	14 15	$-20\% \Leftrightarrow -25\%$
14 60	12 03	12 73	14 15	$-10\% \Leftrightarrow -15\%$
18 67	13 22	14 00	15 55	$-10\% \Leftrightarrow -15\%$
22 68	14 91	15 74	16 56	$-5\% \Leftrightarrow -10\%$
26 71	15 88	16 76	17 64	$-5\% \Leftrightarrow -10\%$
29 59	16 91	17 85	18 79	$-5\% \Leftrightarrow -10\%$
34 50	19 19	20 25	21 32	$-5\% \Leftrightarrow -10\%$
39 81	20 44	21 57	22 71	$-5\% \Leftrightarrow -10\%$
49 36	23 18	24 47	25 76	$-5\% \Leftrightarrow -10\%$
59 34	27 44	28 81	27 44	$0\% \Leftrightarrow 5\%$
69 18	29 08	30 80	34 22	$-10\% \Leftrightarrow -15\%$

TABLE 6.1: Comparison of predicted critical velocity and experimental data from [1] for the P/d=1.25 tube array.

$m_r\delta$	CFD highest stable U_r	CFD lowest unstable U_r	Experimental U_{cr}	Relative difference (%)
11 48	13 36	14 10	14 84	$-5\% \Leftrightarrow -10\%$
18 50	14 95	15 88	18 68	$-15\% \Leftrightarrow -20\%$
25 17	17 64	18 82	23 52	$-20\% \Leftrightarrow -25\%$
33 17	27 54	29 07	30 60	$-5\% \Leftrightarrow -10\%$
42 34	33 84	35.83	39 81	$-10\% \Leftrightarrow -15\%$

TABLE 6.2: Comparison of predicted critical velocity and experimental data from [1] for the P/d=1.375 tube array.

It is observed that the predictions underestimate systematically the experimental critical velocities, though in most cases it is only by about a 5-10%. Hence, the simulation procedure is quite consistent and can be regarded to give reasonable conservative estimations of the critical velocity for FEI. Following, this method will be exploited to explore the effect of different system parameters, as reported in the next section.

a)

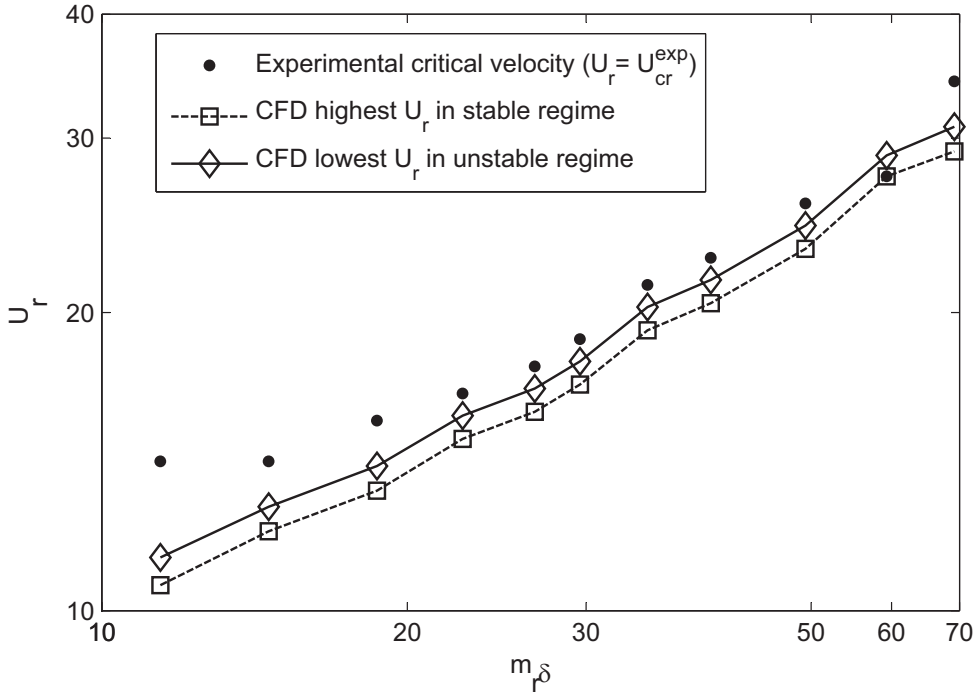

b)

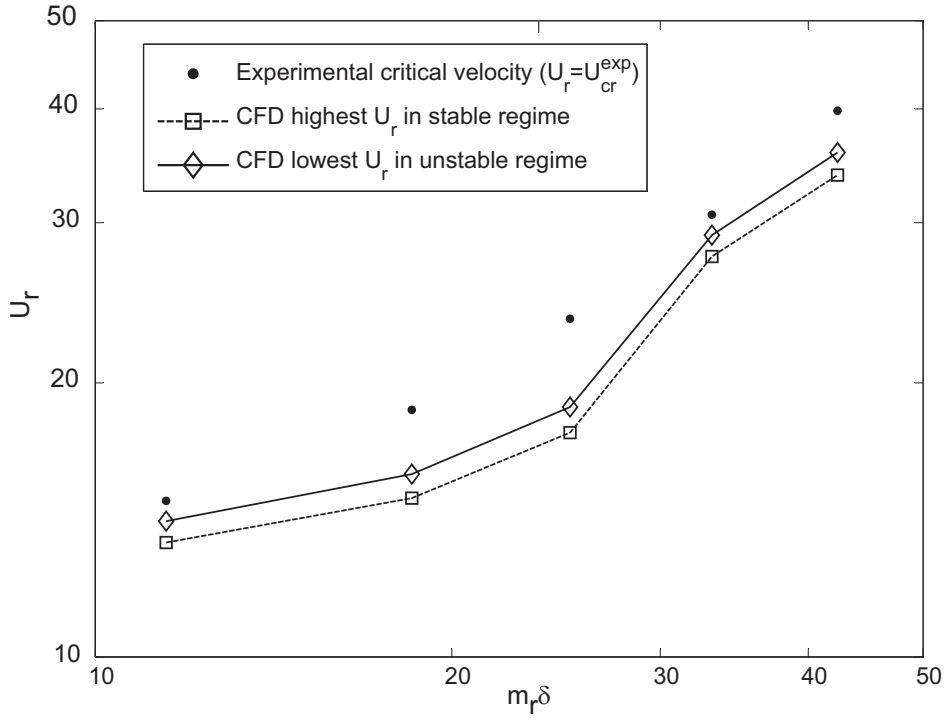

FIGURE 6.5: Experimental critical velocity ([1]) and CFD predictions of highest velocity in stable regime and lowest velocity in unstable regime for: (a) P/d=1.25, (b) P/d=1.375 .

6.3 Studies for the normal triangular tube array

6.3.1 Reynolds number

The reference case with P/d=1.25 and $m_r\delta$ = 26 7, subjected to air cross-flow, and corresponding to the experimental data by [1] has been considered for an analysis on the sensitivity to the Reynolds number. The baseline Reynolds number, based on tube diameter and gap velocity at experimental critical conditions, is 1 6$\times 10^4$. In this numerical database, the simulations were carried out for successive flow velocity increments of a 5% of the experimental critical value, but now the fluid viscosity was also increased accordingly, so that the Reynolds number did not change. This procedure of viscosity adaptation was repeated for four higher Reynolds numbers, up to 10^5. The results are presented in Fig.6.6. It is seen that the critical velocity for FEI (as delimited by the highest U_r in stable regime and the lowest U_r in unstable regime) increases by approximately a 20% within the range of Reynolds numbers tested. This conclusion is in concordance with the experimental study of [95] and also with the discussion in [26] about the applicability of the Connors equation, in which it was noted that a complete model of FEI should also include a Reynolds number dependency. Besides, the slope becomes progressively steeper when approaching the upper limit of Re=10^5. This trend is consistent with the high and scattered values of critical velocity usually determined in practice for tube arrays subjected to intensely turbulent flows ([96], [97],[98], between others). However, the predictions obtained under controlled low Reynolds numbers can still be considered as an appropriate low-bound estimation for the critical velocity [4][5].

6.3.2 Pitch ratio

Starting again from the reference conditions of P/d=1.25, $m_r\delta$ = 26 7 and air cross-flow, the previous simulation procedure was now applied on four new arrays with successively larger pitch ratios, up to 1.58. The significant results are presented in Fig.6.7. From P/d=1.25 to 1.375, the critical velocity is seen to increase about a 10%, whereas this effect appears to be much smaller in case of higher P/d values. In fact, the trend becomes uncertain because the variations observed are of the same order as the increments in streamwise velocity between consecutive simulations for a given P/d. Anyway, the effect of P/d within the range tested results to be so marginal that justifies no need for the inclusion of its variation in the typical engineering design criteria (as stated in [9]).

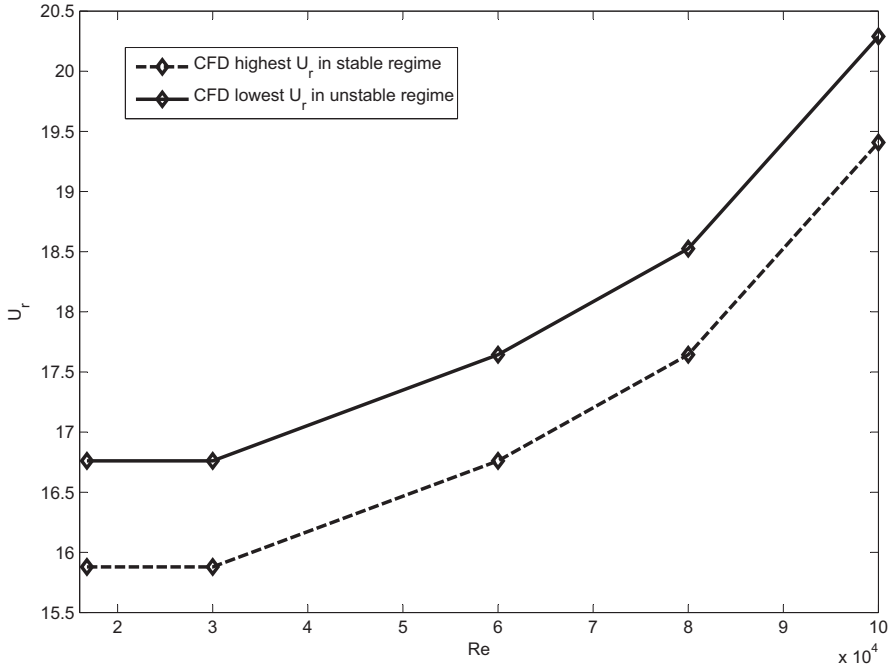

FIGURE 6.6: Effect of Reynolds number on the predicted critical velocity.(P/d=1.25, $m_r\delta = 26\ 7$)

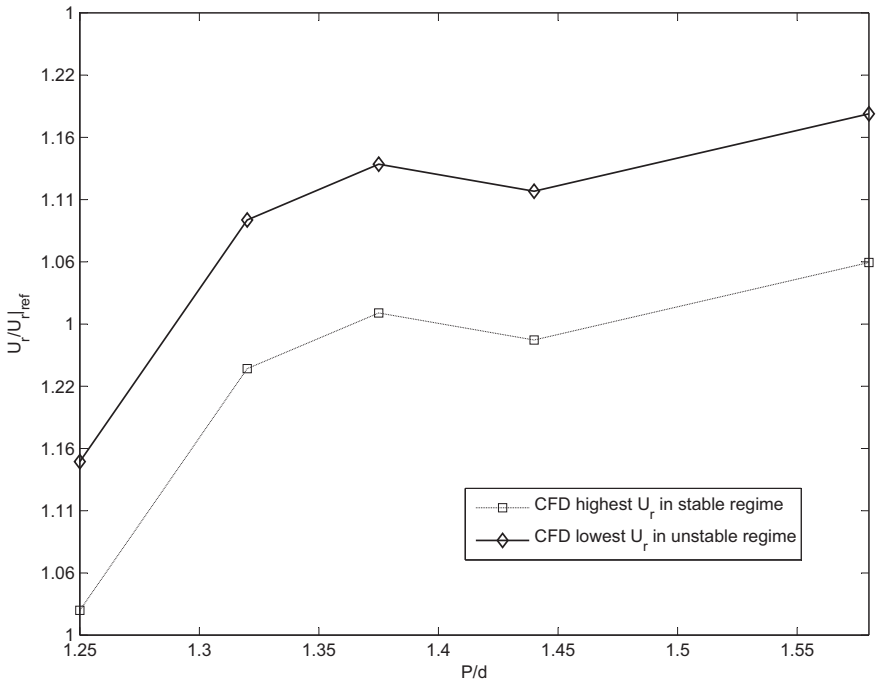

FIGURE 6.7: Effect of pitch ratio on the predicted critical velocity.($m_r\delta = 26\ 7$)

6.3.3 Degrees of freedom

Up to this point, the motion of the vibrating tube TV had been restricted to the transverse direction, only. Following, the user defined function will be modified to relax that condition and allow motion in the stream-wise direction as well. The motion equations considered for the two-degree-of-freedom tube are stated as follows:

$$F(\ddot{\ }, \dot{\ }, \ , U_0) = m_s \ddot{\ } + \ _s \dot{\ } + \ _s \tag{6.2}$$

$$F(\ddot{\ }, \dot{\ }, \ , U_0) = m_s \ddot{\ } + \ _s \dot{\ } + \ _s \tag{6.3}$$

with identical values of mass and structural damping and rigidity for the tube in both orthogonal directions. Figs.6.8 and 6.9 show a typical trajectory of TV after switching from the initial static conditions to full dynamic simulations with two degrees of freedom. Since the drag force on the tube is non-zero, first the tube crosses some distance downstream, searching for the new equilibrium position. The tube undergoes oscillations both streamwise and transversely to the main stream, thus composing an orbital motion. However, the amplitude of the streamwise oscillation decays fast, and very quickly the remaining vibrations take place mostly in the transverse direction (y-axis). Again, these transverse oscillations can be also reduced over the time, as is the case in Fig.6.8, or they can be increased, as is the case in Fig.6.9. The former corresponds to stable regime whereas the latter is characteristic at unstable conditions.

Another series of simulations was conducted to estimate the critical velocity corresponding to P/d=1.25 over the range of $m_r\delta$ tested by Austermann and Popp, now with two degrees of freedom allowed for tube TV. Fig.6.10 shows the new predictions, along with those obtained for one-degree of freedom conditions. The most noticeable effect is the drop from the previous predicted critical velocities, ranging from 25% for low $m_r\delta$ to more than 30% for high $m_r\delta$, thus exhibiting an average slope that is slightly less steep. Hence, according to these computations for damping-controlled instability in normal triangular arrays, the allowance of motion in the streamwise direction provokes a consistent and significant reduction in the critical velocities. In other words, these results point out that the instability thresholds estimated for one-degree of freedom can be unconservative. In consequence, though the instability is still associated to oscillations in the transverse direction, simulations intended to estimate FEI thresholds should incorporate cylinder motion with two degrees of freedom to obtain better predictions.

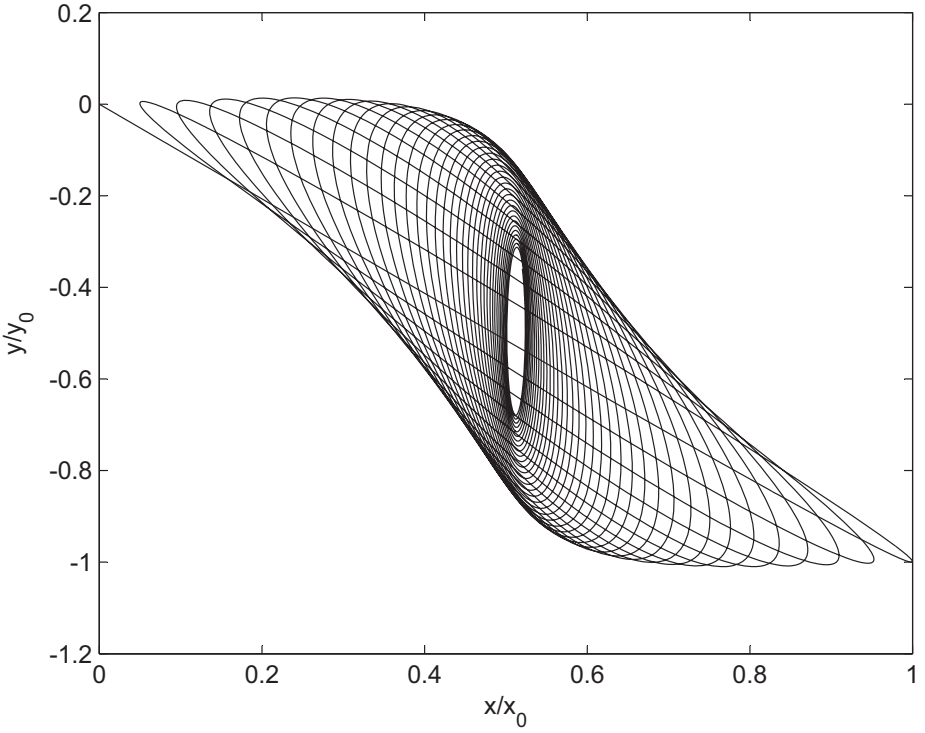

FIGURE 6.8: Orbital motion of tube TV with 2 degrees of freedom in stable regime (P/d=1.25, $m_r\delta$=26.7, U_r=22.2).

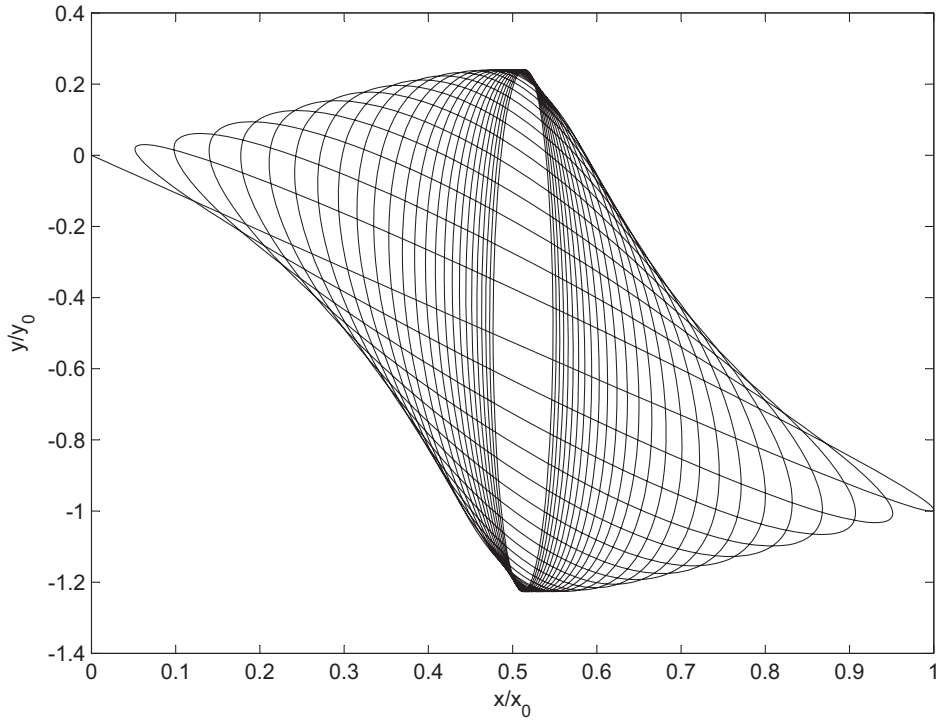

FIGURE 6.9: Orbital motion of tube TV with 2 degrees of freedom, showing instability in the transverse direction (P/d=1.25, $m_r\delta$=26.7, U_r=22.2).

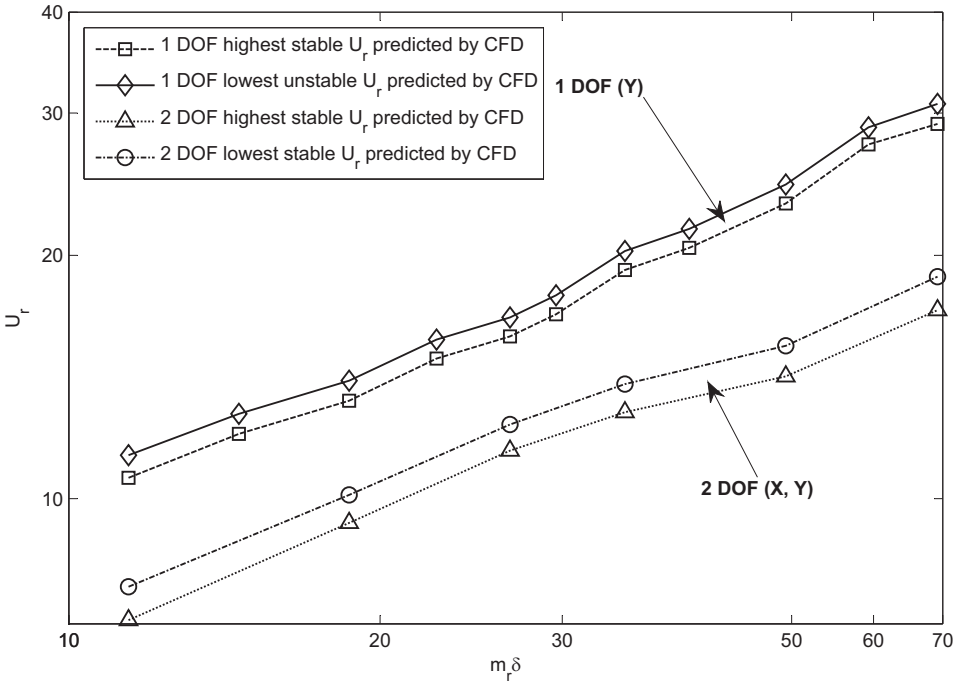

FIGURE 6.10: Comparison of instability thresholds obtained for the tube TV oscillating with one degree of freedom (transverse direction Y) and two degrees of freedom (motion with X and Y components).

6.4 Studies for the parallel triangular tube array

6.4.1 Results for one single flexible tube

The results presented in the following sections are based on the unsteady dynamic flow simulations through the parallel triangular array in the same conditions than the experimental test of the present investigation, i e. assuming water cross flow, $P/d = 1\ 57$ and $d = 10mm$ (see Apendix A). A first series of simulations was undertaken with only one flexible tube in the array, the one denoted as TF in Fig. A.1. Its main mechanical properties were established by imposing a natural frequency (vacuum conditions) $f_n = 15$ Hz and a logarithmic decrement of damping $\delta = 0\ 01$. In order to explore the dynamic response of the fluid-array system, seventeen CFD simulations were performed for increasing upstream velocities, in the range of $U_0 = 0\ 03$–$0\ 17m/\ $, so that the critical velocity value could be established when first observing instability in the results. During each simulation, the position and forces on the vibrating tube and its neighbors were recorded and analyzed both in time and frequency domains. As expected, when

exceeding a certain critical velocity any initial disturbance in the tube position does not disappear but rather amplifies.

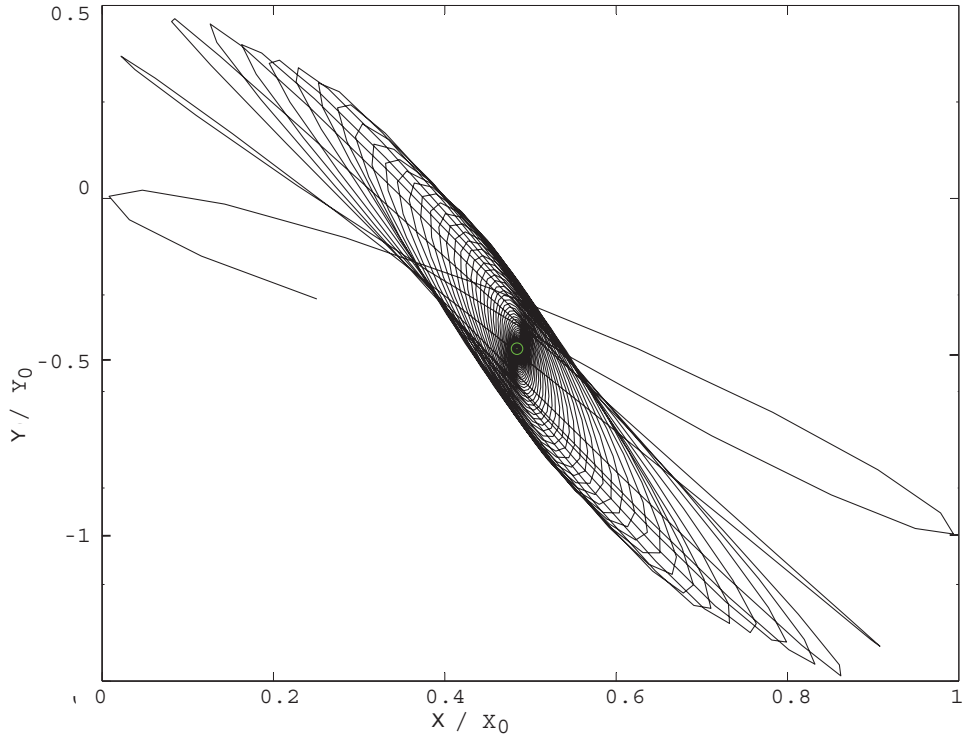

FIGURE 6.11: Orbital motion of tube TV with 2 degrees of freedom in stable regime ($P/d = 1\ 57$, U_0=0.03 m/s).

6.4.1.1 Behavior in stable conditions

Figs.6.11 and 6.12 present the orbital trajectory of the vibrating tube and the forces applied on it, calculated with the CFD model for an upstream water velocity $U_0 = 0\ 03m/$, corresponding to stable conditions. Fig. 6.11 shows that the vibrating tube describes orbits of progressively decreasing amplitude, with the final position highlighted with a green circle. The orbits rotate while both the in-line and traversal equilibrium positions are reached. Similarly, the lift and drag forces show decaying curves over time until nearly vanishing (Fig. 6.12).

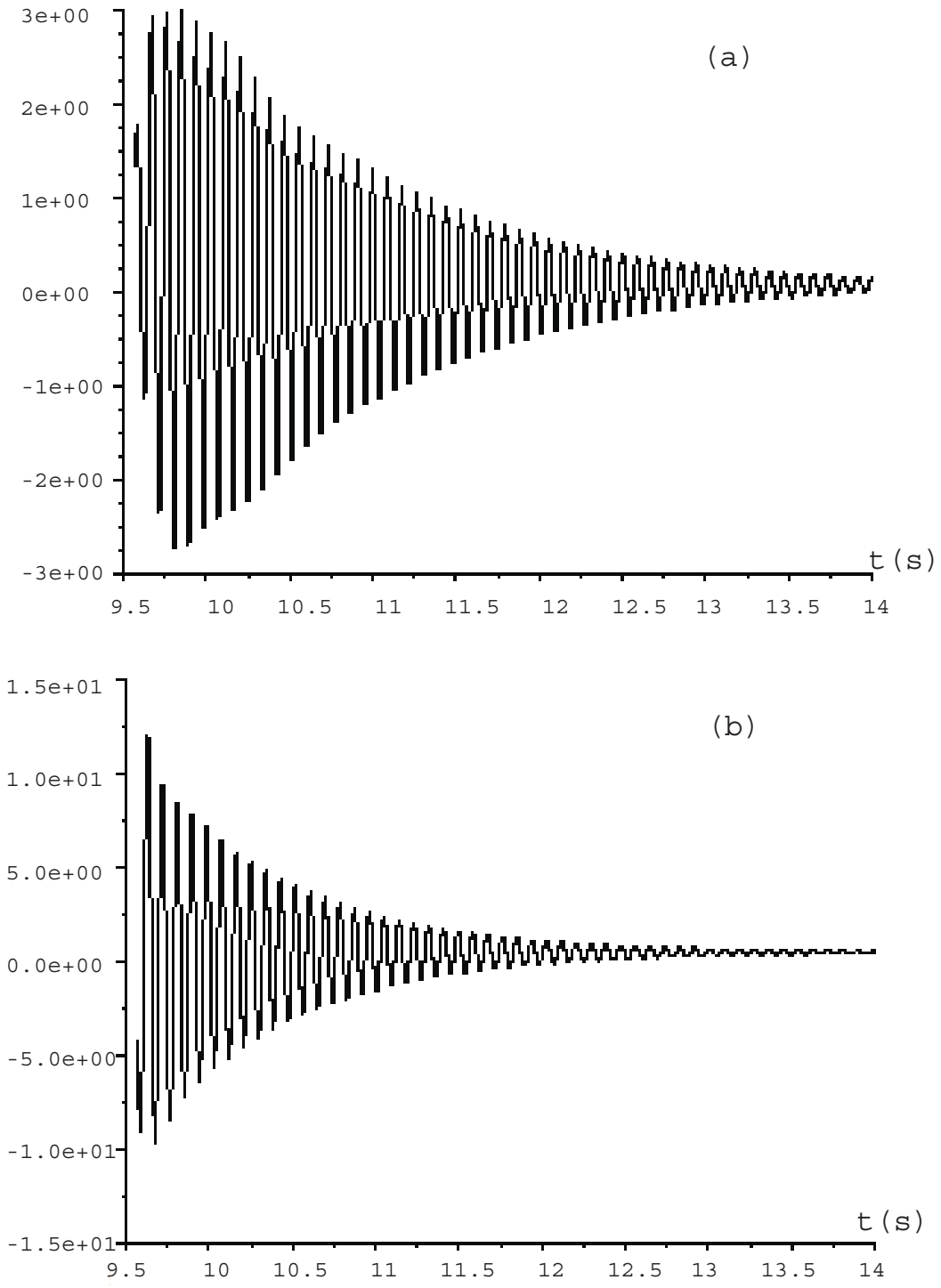

FIGURE 6.12: Temporal signals of force coefficients C_L and C_D in tube TF.(P/d = 1 57, U_0=0.03 m/s).

6.4.1.2 Behavior in unstable conditions

Fig. 6.13 presents the trajectory and forces calculated for an upstream water velocity $U_0 = 0\ 12m/\ $, which corresponds to unstable conditions. Unlike the decaying orbits of Fig. 6.11, the loops described by the vibrating cylinder in Fig. 6.13 are progressively larger.

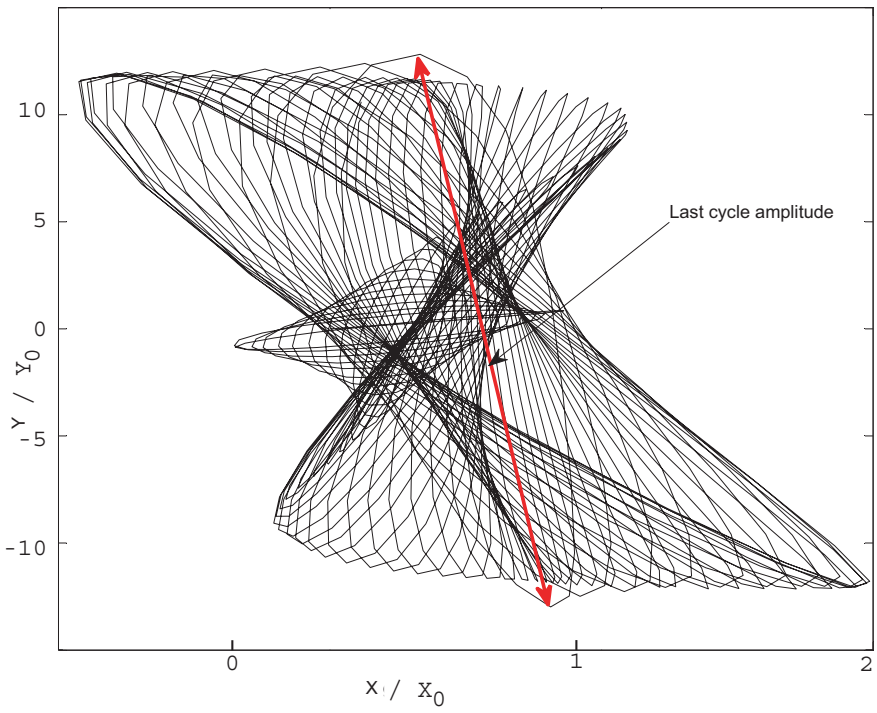

FIGURE 6.13: Orbital motion of tube TF with 2 degrees of freedom in unstable regime ($P/d = 1\ 57$, $U_r = 0\ 12m/\ $).

Although the final in-line equilibrium position is not reached in this case (note that the tube is still oscillating about the x-coordinate) it is observed that the transverse vibrations increase rapidly. Moreover, in a few seconds, the oscillations occur mostly in the transverse direction to the flow. The same amplification process is present in the temporal evolution of the lift and drag forces on the vibrating cylinder (Fig. 6.14), though the latter shows modulated transitions. The forces on the neighbouring tubes also exhibit similar behavior, as seen in Fig. 6.15 for tube T3.
Regarding frequency analysis, Fig. 6.16 shows the frequency spectra of previous lift and drag coefficients on the vibrating cylinder. It can be seen that the highest values appear at a frequency somewhat lower than the natural frequency specified for the tube ($f_n = 15$), which confirms the capacity of the model to estimate the effects of added mass.

6.4.1.3 Coupled system damping

In order to explore the damping of the coupled system, the temporal evolutions of the cylinder position and the forces exerted were analyzed for all the range of velocities tested. In particular, Figs. 6.17 and 6.18 show the evolution in the amplitude of the oscillations. It can be seen that, for increasing cross flow velocity values, the response decay becomes progressively less steep until a certain critical value is reached (Fig. 6.17). Then, if the cross flow velocity increases further, the vibration amplitude of the cylinder is seen to amplify until achieving limit cycle oscillations (Fig. 6.18). In this post-stable regime, increasing the cross-flow velocity produces a faster rate of amplitude increase and, besides, the limit cycle oscillations have larger amplitude.
Finally, damping of coupled system was calculated for every cross flow velocity, by means of fitting an exponential function to the previous curves with the time dependent amplitude of the oscillations. As expected, the damping value obtained is decreased for higher cross-flow velocities, becoming negative for the first unstable case. After that, its value is further reduced in the negative zone (Fig. 6.19).

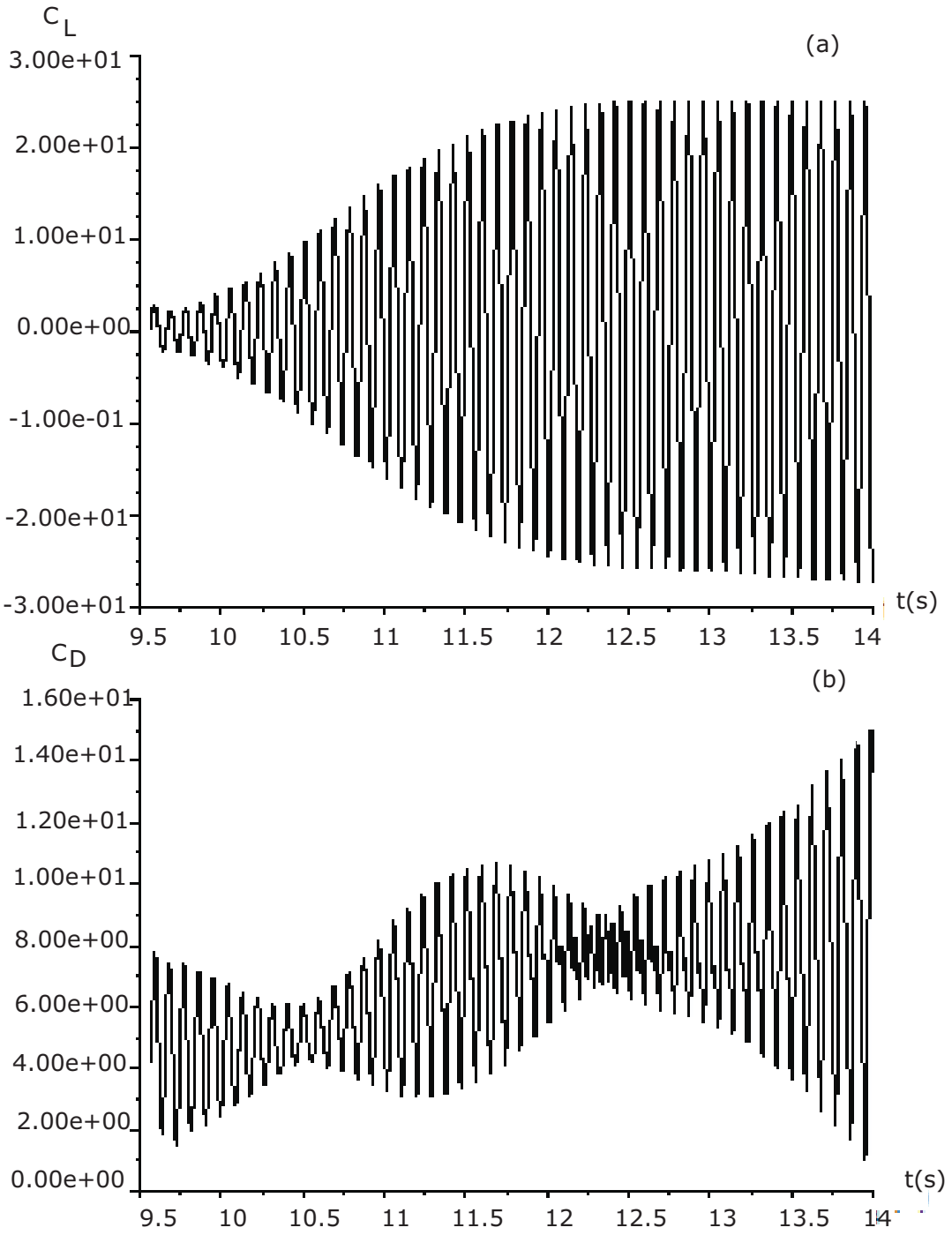

FIGURE 6.14: Temporal signals of force coefficients C_L and C_D in tube TF.(P/d = 1 57, U_0=0.12 m/s).

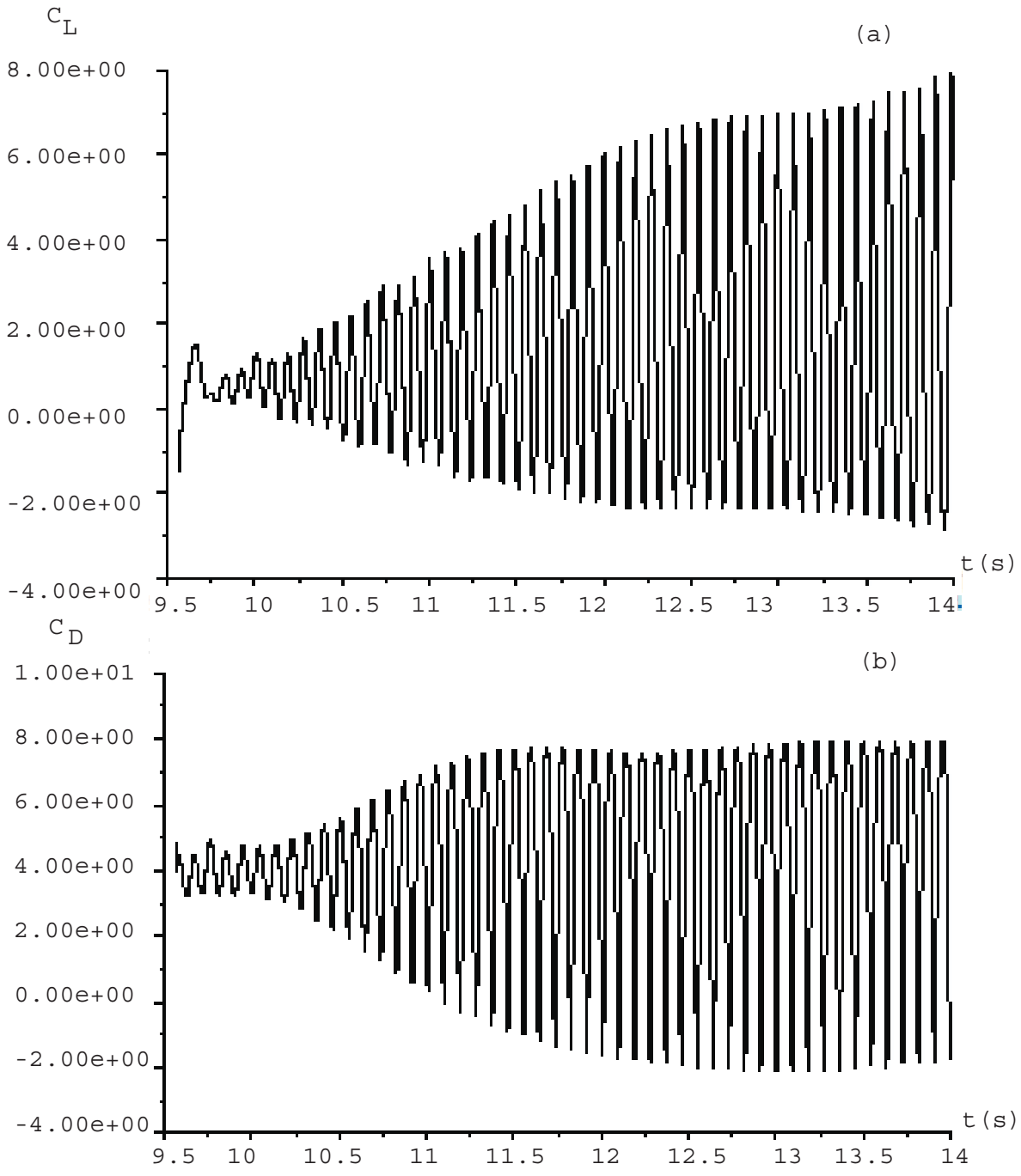

FIGURE 6.15: Temporal signals of force coefficients C_L and C_D in tube T3.(P/d = 1 57, U_0=0.12 m/s).

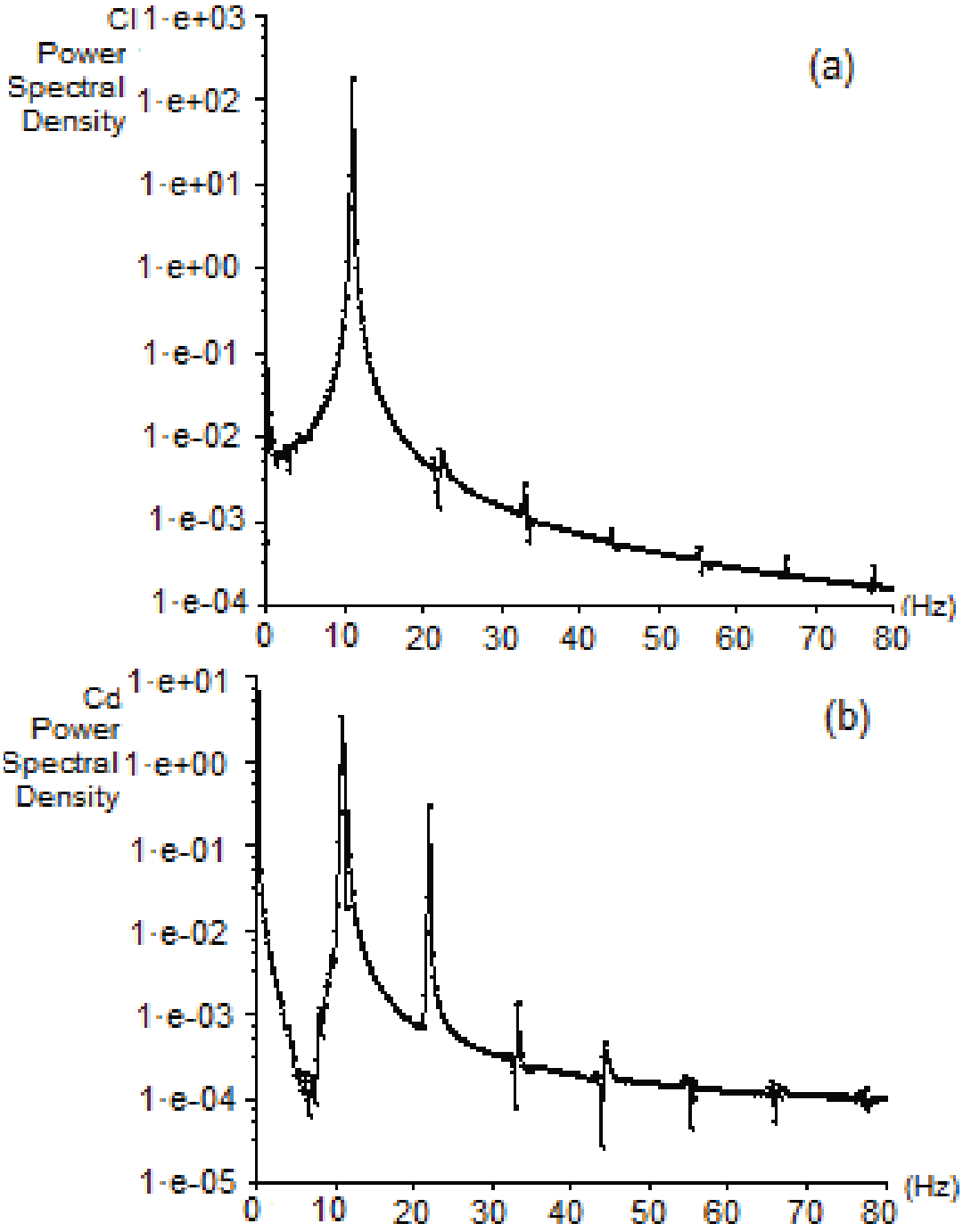

FIGURE 6.16: Spectral signals of force coefficients C_L and C_D for the vibrating tube ($P/d = 1\ 57$, U_0=0.12 m/s).

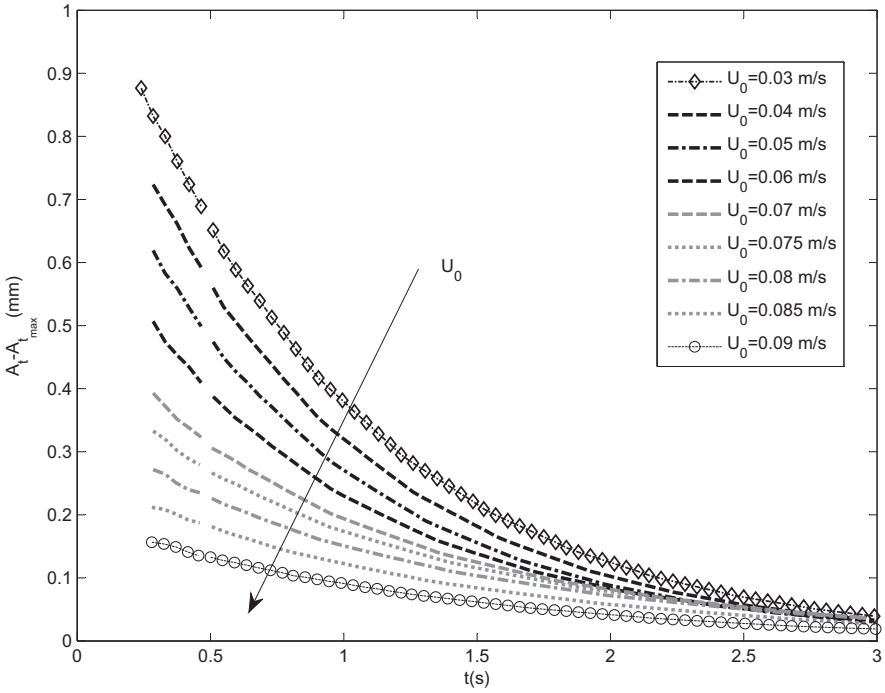

FIGURE 6.17: Amplitude of vibration on stable regime for increasing cross-flow velocities.

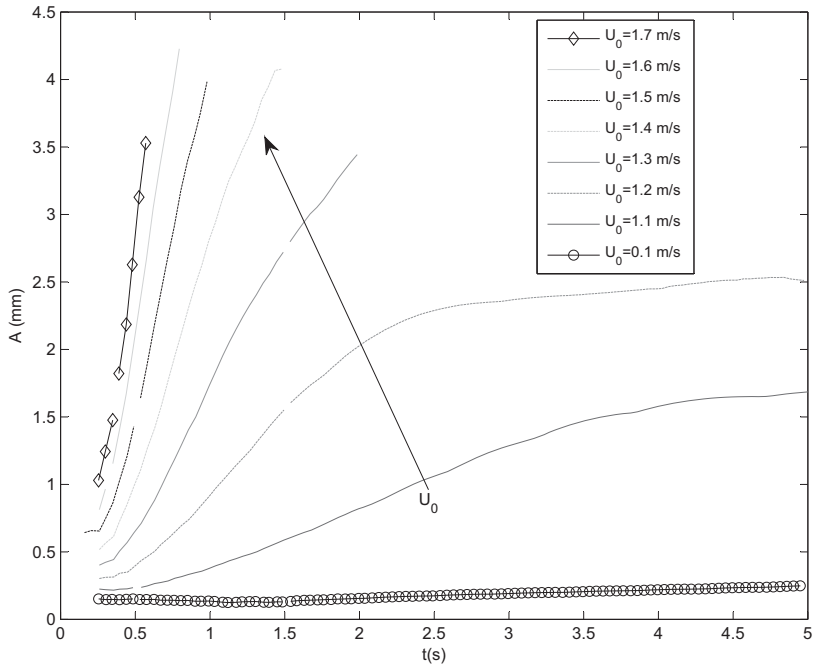

FIGURE 6.18: Amplitude of vibration on unstable regime for increasing cross-flow velocities.

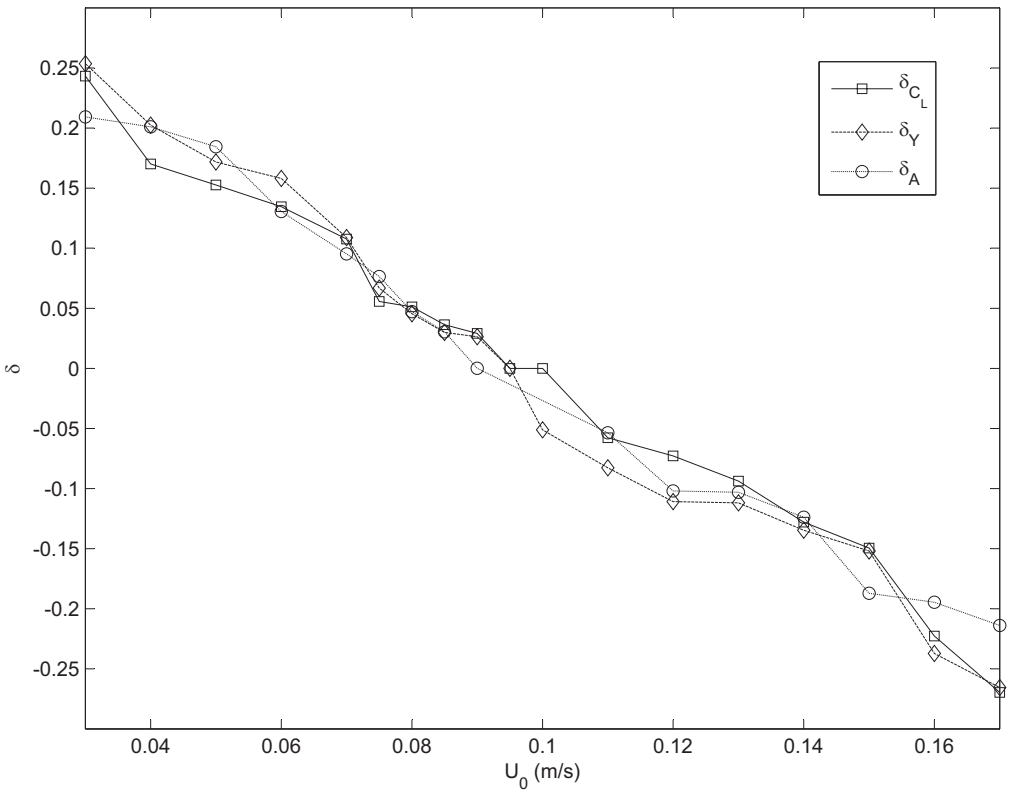

FIGURE 6.19: Net damping of the coupled system as a function of the cross-flow velocity.

6.4.2 Results for two in-line flexible tubes (T2-T3)

In this second part, results for simulations with two in-line flexible tubes will be shown. In particular, the pair of flexible tubes considered in these calculations were T2 and T3 (see Fig.A.1). As in the previous section, the natural frequency of the tubes and the damping value in air were $f_n = 15$ and $\delta = 0\,01$, respectively for both tubes. Seven simulations at different upstream velocities between $U_0 = 0\,05m/\ -0\,12m/$ were conducted. This range was chosen crossing the stability threshold previously obtained for one flexible tube so that the critical velocity value could be compared with the one obtained for two vibrating tubes. Fig. 6.20 shows the trajectory of the tubes calculated with the model for instability conditions. It can be seen that, for the cases analyzed in this relative position, vibrations are mainly transverse to the flow.

In Fig. 6.21 amplitude and phase of the tubes are represented. Note that the amplitude of the oscillations is between an 8% and a 13% larger in tube T2 than in tube T3 and this ratio seems to increase for higher cross flow velocities. Regarding the phase, it is found that tube T3 is around 20º delayed from T2. Comparison between the temporal

evolution of the amplitude of the oscillations for cases with the same cross flow velocity, namely 0.12m/s, and either one (TF) or two (T2 y T3) flexible tubes, is shown in Fig. 6.22. The results reveal that, under instability conditions, amplitude of vibration increases much faster and abruptly, reaching a higher limit cycle value, due to the presence of another flexible neighbour tube in the same line of the array (in flow direction).
Analogous data analysis to the one developed in case 1 returned the results, regarding amplitudes time evolution and net damping, showed in Figs. 6.23, 6.24 and 6.25. In Figs. 6.23, 6.24 it can be seen that critical velocity for these relative position is between $0\,9 - 0\,95m/$, which is a bit smaller than the value found for the single flexible tube simulations. In addtion, Fig. 6.25 shows the net damping of the coupled system. As in the single vibrating tube case, damping value obtained for higher cross flow velocities decreases, becoming negative for unstable cases and further reducing for higher values of U_0. Nevertheless, it is remarkable that the net damping value in the unstable zone reaches much more negative values, showing that the increase of the oscillations under instability conditions is faster and more violent than in the first case.

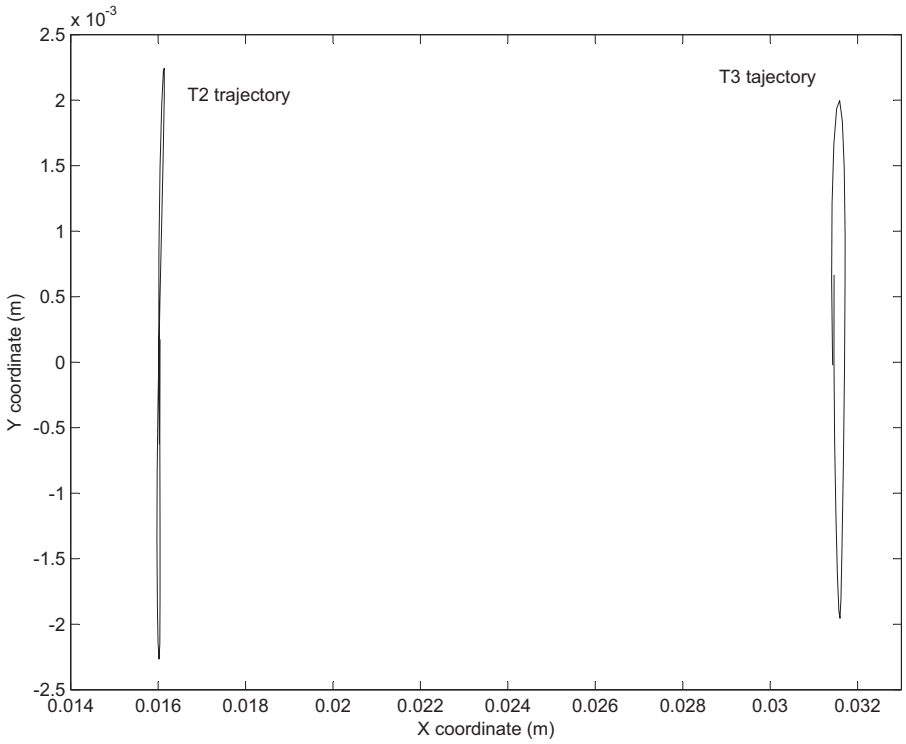

FIGURE 6.20: Trajectories of in-line tubes T2 and T3 under instability conditions.

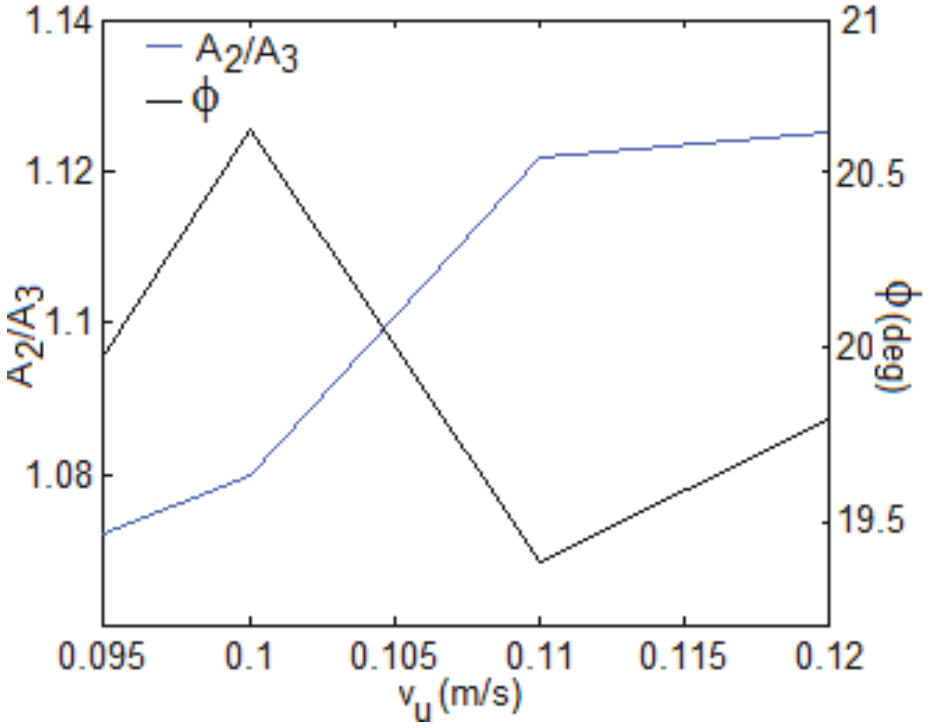

FIGURE 6.21: Ratio of vibration amplitudes of T2 and T3 and relative phase lag in their motion.

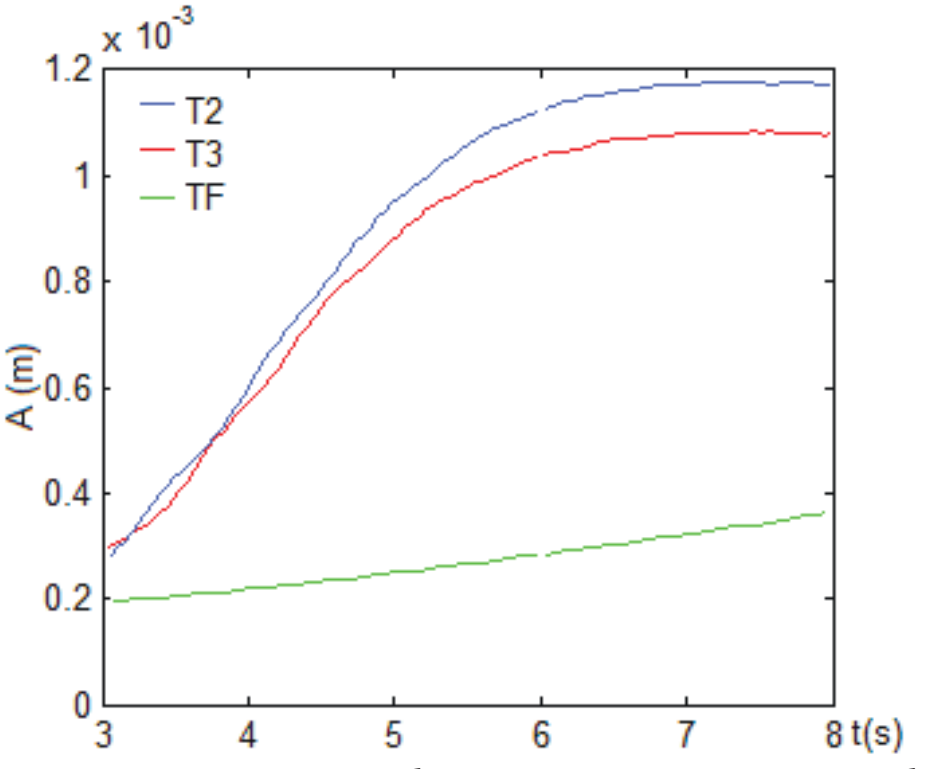

FIGURE 6.22: Temporal evolution of the amplitude of vibration in tubes T2 and T3 compared with the behaviour of one single flexible tube vibration TF in the same conditions ($P/d = 1\ 57$, U_0=0.12 m/s).

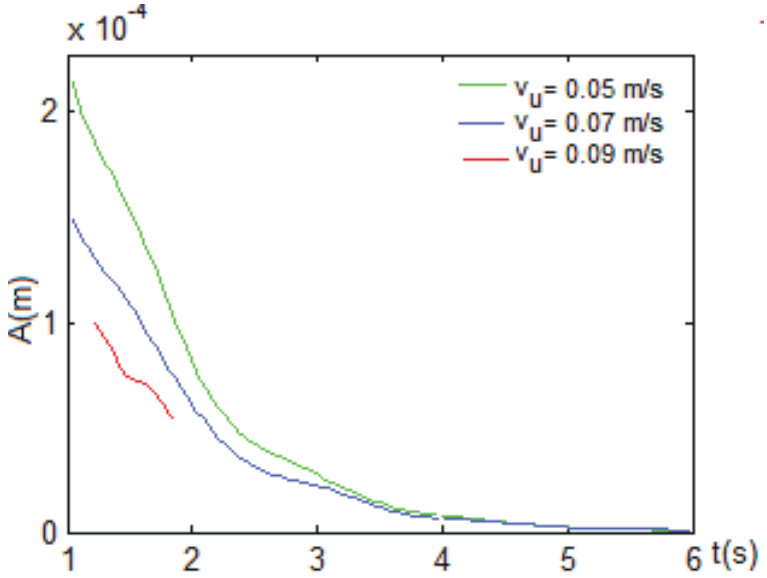

FIGURE 6.23: Temporal evolution of the amplitude in the vibration for two in-line flexible tubes T2 and T3 in stable regime.

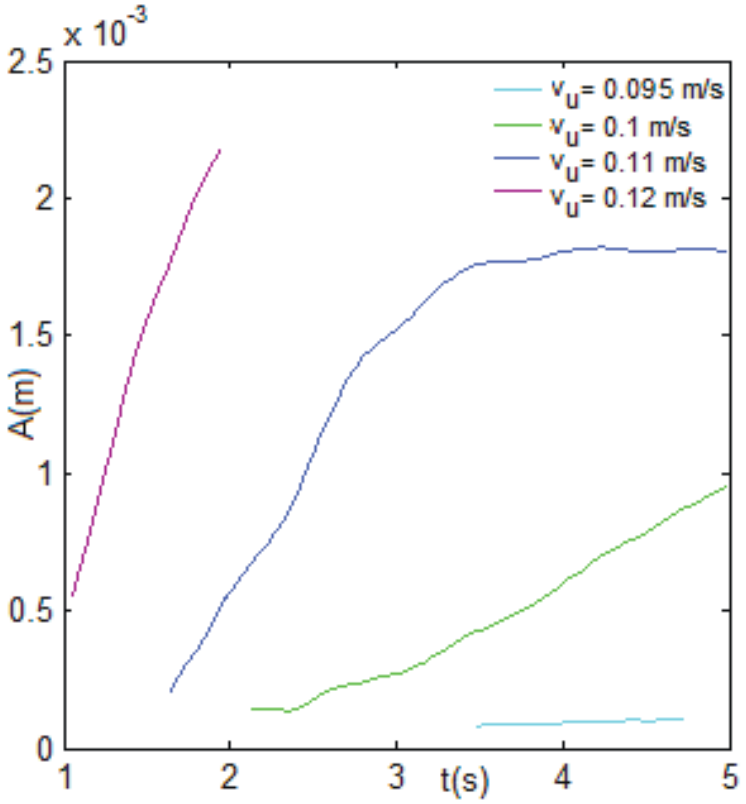

FIGURE 6.24: Temporal evolution of the amplitude in the vibration for two in-line flexible tubes T2 and T3 in unstable regime.

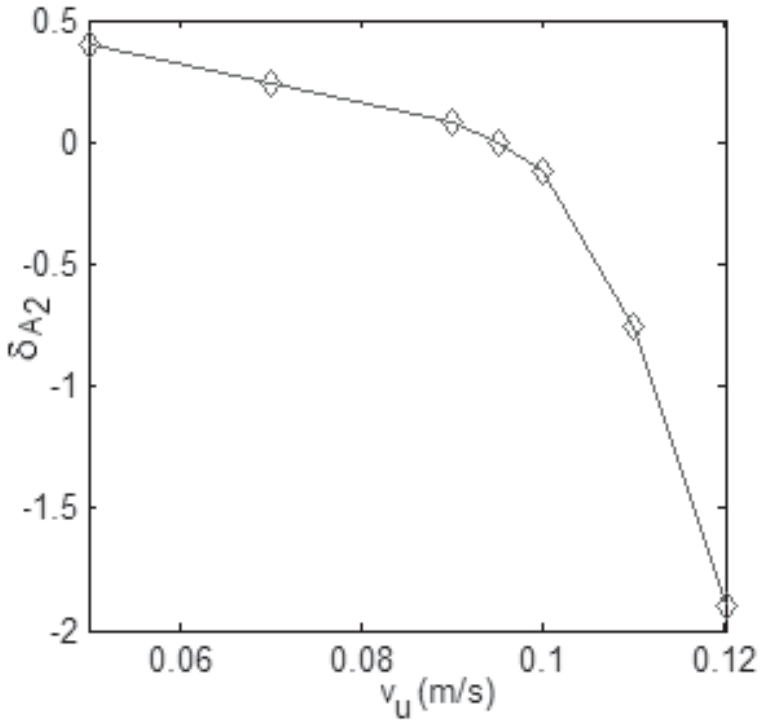

FIGURE 6.25: Net damping as a function of cross-flow velocities for two in-line flexible tubes T2 and T3.

6.4.3 Results for two flexible tubes in adjacent columns (T2-TF)

Finally, results from simulations with two neighbouring flexible tubes placed in adjacent rows, will be discussed in this section. The pair of flexible tubes considered in this case are T2 and TF (see Fig. A.1). Mechanical parameters of the flexible tubes were, $f_n = 15$ and $\delta = 0\ 01$, as in previous analysis.

Fig. 6.26 shows some of the orbits described by tubes T2 and TF in their trajectories under instability conditions. Regarding the amplitude of the oscillations, there is not a constant ratio between the amplitudes of the vibrating tubes. On the contrary, their values change with time (Fig. 6.27), so their ratio oscillates between 0.2 and nearly 2 (Fig. 6.28), with a characteristic frequency of approximately 10Hz (Fig. 6.29). Compared with the case with one flexible tube only, the maximum amplitudes observed in both tubes are similar to those registered in the single vibrating cylinder for the same cross flow velocity (Fig. 6.27).

These low frequency oscillations can be also seen in both stable and unstable temporal evolution of the amplitudes (Figs. 6.30 and 6.31), even showing a similar behavior to the previous cases with one single vibrating tube.

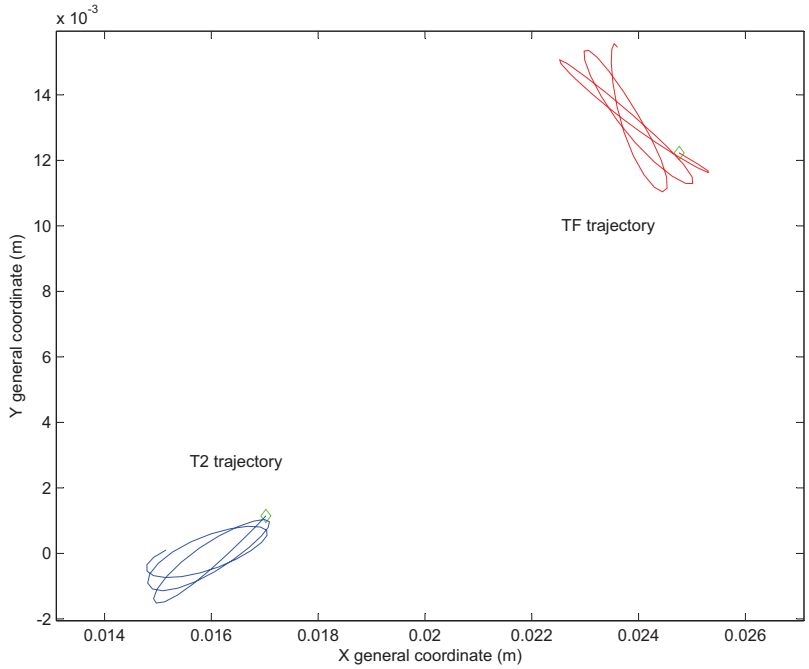

FIGURE 6.26: Trajectories of two flexible tubes in adjacent columns T2 and TF under instability conditions.

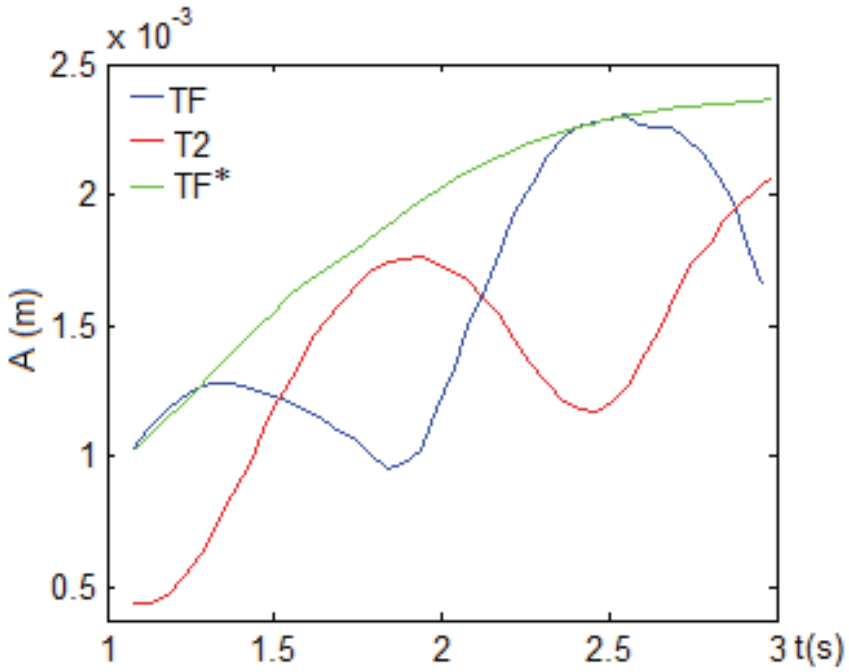

FIGURE 6.27: Amplitude of the temporal evolution of the vibration in tubes T2 and TF, compared with the amplitude of tube TF vibration when vibrating alone.

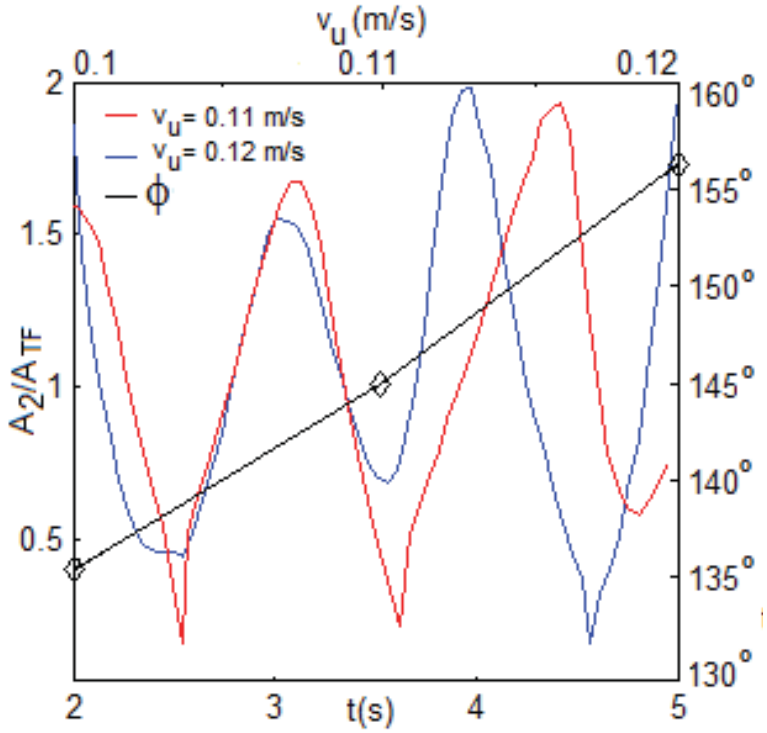

FIGURE 6.28: Ratio of amplitudes of vibration of tubes T2-TF and temporal evolution of their phase lag.

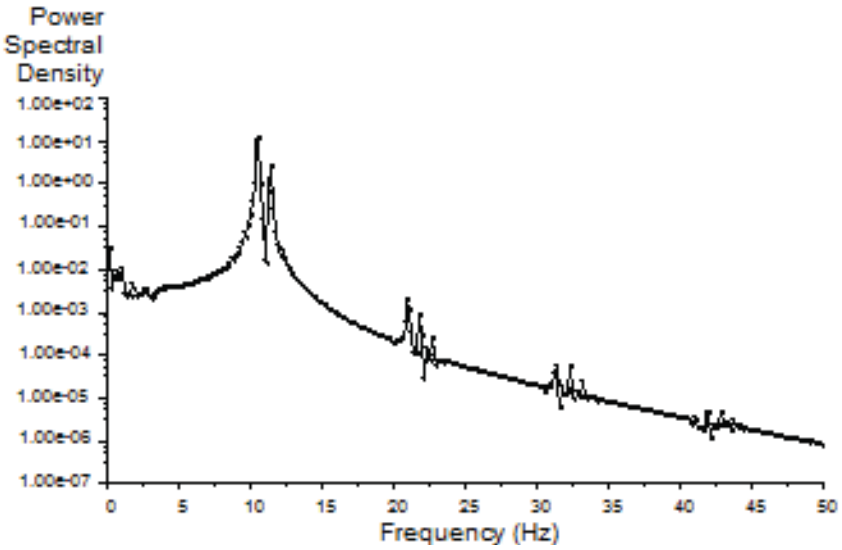

FIGURE 6.29: Typical spectral signal of flexible tubes T2-TF in self excited vibration.

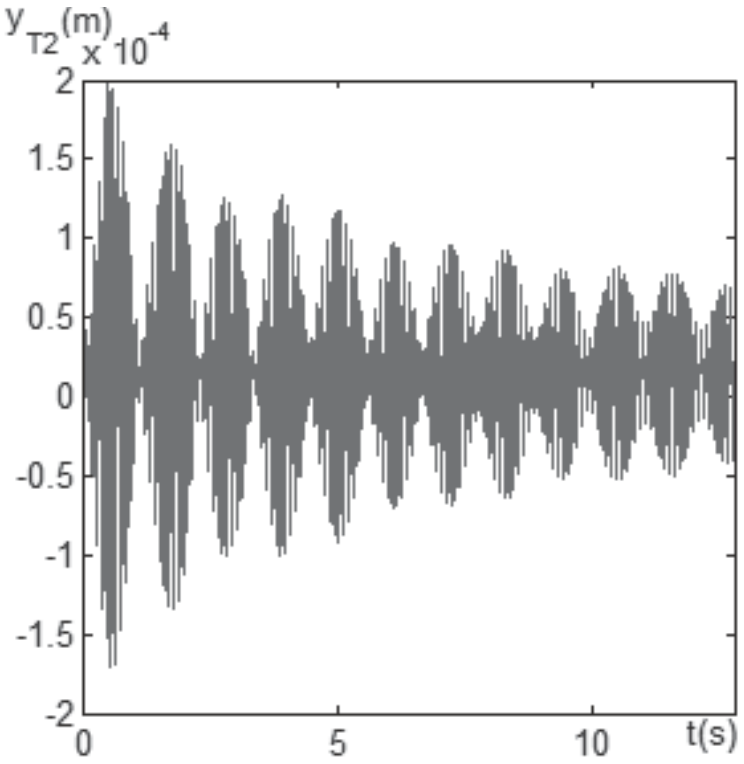

FIGURE 6.30: Temporal evolution of the amplitude of T2 vibration under stability conditions.

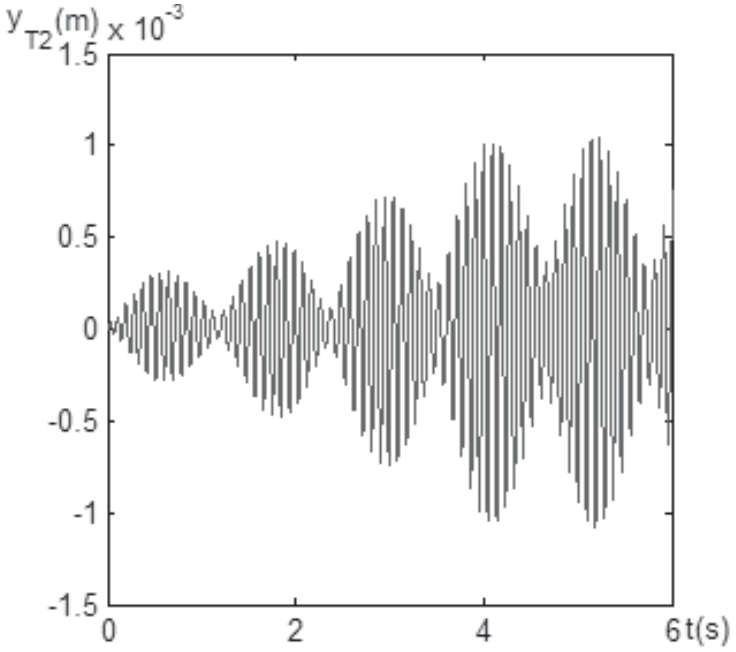

FIGURE 6.31: Temporal evolution of the amplitude of T2 vibration under instability conditions.

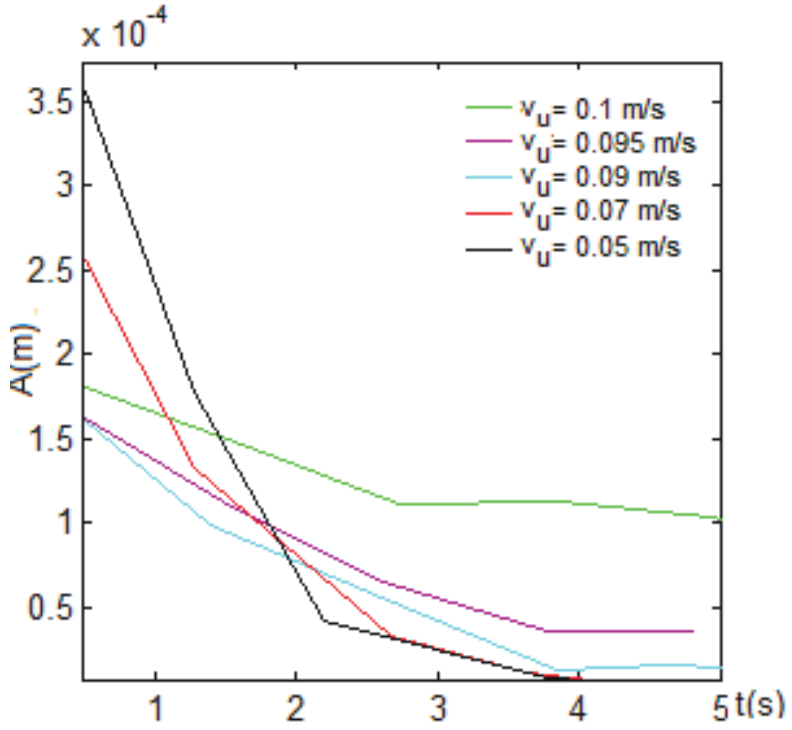

FIGURE 6.32: Temporal evolution of the amplitude of the vibration in tube T2 for increasing cross-flow velocities in stability regime.

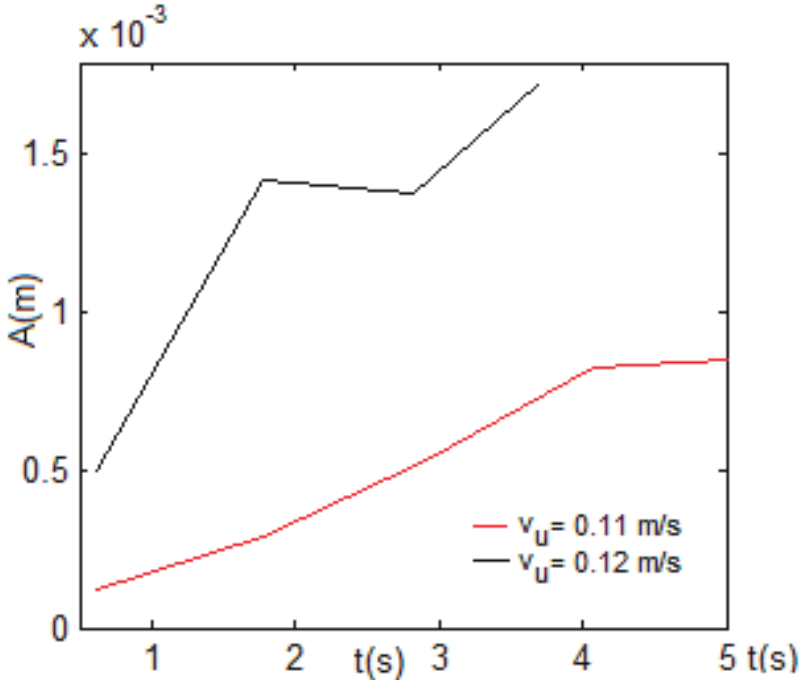

FIGURE 6.33: Temporal evolution of the amplitude of the vibration in tube T2 for increasing crossflow velocities in instability regime.

In order to compare the results of this system, (in terms of stability threshold and net damping), with those obtained in cases 1 and 2, the evolution of local maxima amplitudes

was considered as a representative indicator of the global behavior of the system. Seven different upstream velocities, in the range $U_0 = 0\ 05m/\ -0\ 12m/\text{s}$ (crossing the stability threshold) were simulated. In Figs. 6.32 and 6.33 the evolution of the amplitude in the oscillations, is shown in stability and instabilibty conditions, respetively. It is found that the critical velocity for these relative positions is between $0\ 1 - 0\ 11m/$, a higher value than the one observed for the single flexible tube simulations.

Regarding the net damping of the system (Fig. 6.34), the damping value obtained for high cross-flow velocities is decreased (as in previous sections) becoming even negative for unstable cases and with a further reduction for higher values of U_0. In contrast with case 2, the net damping for this pair of vibrating tubes is not too much lower in the instability zone than the value observed for a single vibrating tube.

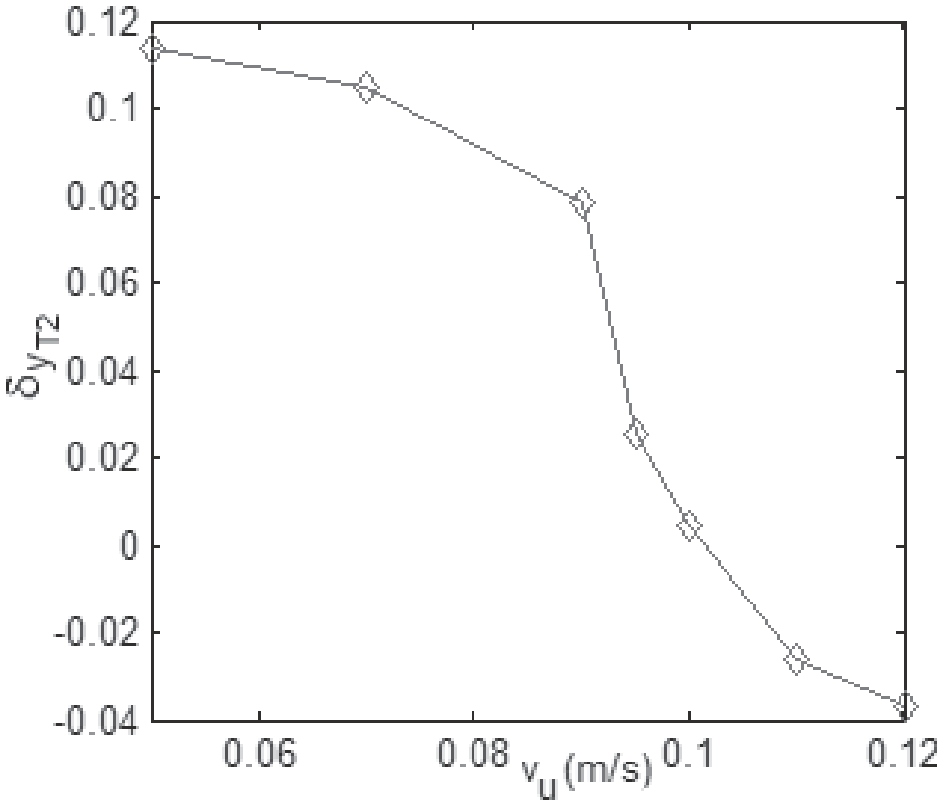

FIGURE 6.34: Net damping of the coupled system for increasing cross-flow velocities.

Chapter 7

Conclusions

Fluidelastic instability in shell and tube heat exchangers has been investigated both numerically and experimentally for a better understanding of the underlying mechanisms of the phenomenon and to deepen in the parameters determining the onset of the instability in practice. A critical review of the existing theoretical models in the literature has provided some answers regarding parameter dependence of the critical velocity but has also introduced some questions regarding the different stability behavior of a single flexible tube in a rigid array (depending on the row it is located) compared with a fully flexible array.

A new numerical methodology including structure motion and dynamic re-meshing has been proposed along with several experimental campaigns intended to investigate the key aspects involved in the phenomenon of FEI in tube arrays.

The CFD methodology proposed was contrasted by successively comparing the numerical predictions with successive experimental data including empirical data reported in the literature and also own measurements obtained for the present investigation. Several variables of interest have been analyzed in the study, regarding i) pressure distribution under static conditions ([19]), ii) time lag of lift coefficient under transverse forced vibrations ([2]) and iii) critical velocity for FEI for P/d=1.25 and P/d=1.375 over a range of the mass-damping parameter ([1]). The main conclusions and contributions of the present study, as well as proposals for future work are individually discussed in the following sections.

7.1 Conclusions

A CFD methodology involving structure motion and dynamic re-meshing has been put into practice to simulate the effect of self-excited vibrations due to damping-controlled

fluidelastic instability in a normal triangular cylinder array with a single flexible tube located in the third row. URANS 2D computations were performed with the commercial code Fluent 12.1 complemented with user defined functions to account for the flexible tube motion. Appropriate model parameters regarding mesh refinement, boundary conditions, turbulence model and time step were selected to ensure minimum influence on the predictions. In particular, spurious large-scale disturbances downstream the array were avoided by using parallel guide plates instead of truncating the computation domain at the last row like in other precedent models.

This CFD methodology was contrasted by successively comparing predictions to experimental data reported in the literature regarding i) pressure distribution under static conditions (Mahon and Meskell 2009[19]), ii) time lag of lift coefficient under transverse forced vibrations (Mahon and Meskell 2013 [2]) and iii) critical velocity for FEI for P/d=1.25 and P/d=1.375 over a range of the mass-damping parameters (Austermann and Popp 1995 [1]). In all cases the predictions can be considered satisfactory. In particular, the critical velocities estimated under Austermann and Popp's conditions resulted to be only 5-10% below the experimental values in most cases. Besides, the analysis of the velocity and pressure fluctuations streamwise suggests that the main flow disturbances are originated in the region of flow detachment from the vibrating tube, though the oscillations induced in the wake of the anterior cylinders can behave as secondary perturbation sources. Downstream the vibrating tube, perturbations were observed to propagate at a speed of about 0.84 times the gap velocity. These results are consistent with the experimental data obtained by Khalifa et al. (2013) [3]. Once this methodology has been validated as a useful tool to reproduce the fluidelastic instability phenomena, it has been extensively applied to investigate the effect of the modification of a number of system parameters. The following dependenices for the critical velocity were observed:

- Both static and self-excited calculation levels were used to investigate the specific dependence of the critical velocity on the pitch ratio and Reynolds number.For the self-excited calculation level, it was found a 10% increment of the critical velocity when the pitch ratio is increased from 1.25 to 1.4. Also, little variation was observed for higher P/d values. In a similar fashion, an increment of the Reynolds number also provoked the shift of the critical velocity towards higher values. These results are in agreement with those obtained, using the quasi-unsteady model of Granger and Paidoussis (1996) [11], with the memory function proposed by Meskell (2003) [78] and the force coefficients estimated with simple CFD simulations. In both cases, it can be considered that the estimations obtained for low tube spacing

and low Reynolds number constitute reasonable conservative bounds of the instability thresholds. Therefore, it is suggested not to include them in design formulas for engineering purposes.

- Using the self excited calculation level, the reliability of extrapolating results of calculations and tests with one single flexible tube (i.e., allowed to vibrate only in the transverse direction) was analyzed and discussed. The inclusion of a second degree of freedom in the flexible tube, thus allowing motion in both planar directions, showed that the critical velocities are reduced by a 25-30% though the instability still took place in the transverse direction. This result is in agreement with the differences found between the Austermann and Popp [1] predictions for the critical velocity with a tube position correction to avoid the streamwise displacement and the values obtained previously by Anjelic and Popp [98] for the same geometry and without any position correction. It was concluded that, the computations and experimental tests intended to estimate critical velocities for FEI should include two-degree-of-freedom tubes for a better prediction.
  In addition, differences between fully flexible arrays and rigid arrays with one single flexible tube (2 DOF) where also discussed, indicating that critical velocities would be similar if the single flexible tube is located in the first row presenting FEI (if it is previously identified).
  Finally, the scatter found in the stability maps throughout the literature is discussed to be partially attributed to different experimental conditions, regarding the number of degrees of freedom in the tubes, the number of vibrating tubes and its position, being the more conservative conditions for the tests the use of fully flexible tube arrays.

- The analysis of the interstitial flow pattern with = 1% tube oscillations suggested, for the P/d=1.25 normal triangular and the P/d=1.57 tube arrays, that the source of perturbations is located in the detachment point, in agreement with previous results by Khalifa et al. [3]. For the normal triangular tube array, the average ratio propagation velocity-flow velocity ratio was found to be $U_p/U_g = 0\ 84$. Maps of phase of the velocity fields and pressure perturbations were found to be affected by two effects: the increment of the kinetic energy in the channel with increasing sections and the suction of the stagnation point and the wake of the previous and next row tubes of the neighbour lines.

- Although the experimental data obtained in the laboratory campaign was limited, similar measurements to those available in the literature [3] with respect to the propagation velocity were reported and coherent conclusions for the specific conditions of the experiment were confirmed. The results from the CFD model showed satisfactory agreement with empirical measurements of the amplitude and phase lag, in both quantitative and qualitative terms.

7.2 Contributions

The contributions of the present research to the current state of knowledge in the field of fluidelastic instability in shell and tube heat exchangers are summarized as follows:

- A CFD methodology involving structure motion under different conditions, including forced or auto excited oscillations, has been proposed. Appropriate model parameters regarding mesh refinement, boundary conditions, turbulence model and time step were selected to ensure minimum influence on predictions. The model was validated with three different experimental measurements [19], [2] and [1] and also compared to the experimental data collected for the present study. The validated methodology could be a tool to investigate the fluidelastic instability in the future and provide useful modeling strategies in the numerical simulation of tube arrays.

- An hybrid theoretical-numerical methodology using the force coefficients obtained in steady numerical simulations as inputs of the the quasi-unsteady model of Granger and Paidoussis (1996) [11], with the memory function proposed by Meskell (2003) [78], was proposed. This procedure allows to predict stability thresholds without any experimental data and with a contained computational cost. Although this methodology reported less accurate results than the dynamic self-excited simulations in quantitative terms, it was found to be capable to predict the same sensitivity of the critical velocity to the parameters of the system, constituting a cost-and-time-efficient tool to analyze qualitatively the FEI behavior.

- The apparent contradictions and scatter of the experimental data reported in the literature for a single flexible tube in a rigid array were investigated and possible explanations were proposed. The Reynolds number and pitch ratio effect was found to be moderate, while it was concluded that the critical velocity is significantly affected by the streamwise motion. Although the tube still oscillates in the transverse direction, the displaced position it reaches due to the drag has the

effect of reducing the critical velocity nearly a 30%. Little differences were found in the critical velocity of the array with one flexible tube with respect to the fully flexible bundle when the flexible tube was located in the row that presents the lower threshold. However, this row may depend on the geometry and mass damping parameter and would not be known previously. Final recommendation would be that the computations intended to estimate critical velocities for FEI should include two-degree-of-freedom tubes and in order to use only one flexible tube, the row with lower critical velocity must be known for the same particular conditions.

7.3 Future work

As discussed in previous sections, it was found that the behavior of one single flexible tube in a rigid array would be representative of the stability threshold of a fully flexible tube array, as long as:
1. The more sensitive row to present instability is chosen for locating the tube and the motion is allowed both streamwise and in the transverse direction.
2. The damping controlled mechanism is dominant.
An interesting opportunity for future work would be the characterization of the row of lower critical velocity for different geometries, pitch ratios and mass-damping parameter, in order to investigate the relative importance of the damping and stiffness mechanisms in different operational conditions. Comparing critical velocity thresholds obtained with one single flexible tube, with those obtained with fully flexible bundles, would also allow to characterize the conditions for which simplified tests are representative of the real heat exchanger behavior, reducing the scatter of the stability maps.

Conclusiones

Se ha realizado una investigación tanto numérica como experimental acerca de la inestabilidad fluidoelástica en cambiadores de calor de carcasa tubos, con el objetivo de mejorar la actual comprensión de los mecanismos subyacentes en este fenómeno así como profundizar en los parámetros que determinan la aparición de la inestabilidad en la práctica. Se ha realizado una revisión crítica de los modelos teóricos existentes en la literatura que ha proporcionado algunas respuestas en lo referente a la dependencia de la velocidad crítica de ciertos parámetros y también planteado algunas cuestiones, como las posibles diferencias respecto a la estabilidad del comportamiento de un haz con un solo tubo flexible, en función de dónde éste esté localizado, frente a un haz completamente flexible.

Se a propuesto una nueva metodología numérica que incluye movimiento estructural con mallado dinámico y además se han realizado una serie de ensayos experimentales con el objetivo de investigar los aspectos clave involucrados en el fenómeno de inestabilidad fluidoelástica en haces de tubos. Para ello, se diseñó y construyó un motaje especifico en el laboratorio que investigaba la transmisión de perturbaciones de presión a través de un haz triangular paralelo, así como contrastar las predicciones del modelo CFD.

El modelo CFD propuesto fue contrastado por la comparación sucesiva de las predicciones numéricas con diferentes series de datos experimentales, incluyendo cinco series de datos empíricos publicados en la literatura y también las propias medidas obtenidas en el laboratorio durante la presente investigación. Se han analizado un conjunto de variables de interés de cara a validar el modelo numérico: distribución de presión, fluctuaciones de presión, retraso entre el movimiento del tubo y el coeficiente de sustentación, velocidad de propagación de las fluctuaciones de velocidad y velocidad crítica para la FEI.

Las principales conclusiones y contribuciones del presente estudio, así como propuestas de trabajo futuro, se discuten individualmente en las siguientes secciones.

1 Conclusiones

Se ha propuesto una metodología CFD que incluye movimiento estructural con mallado dinámico para simular el comportamiento de las vibraciones autoexcitadas debidas al mecanismo de inestabilidad fluidoelástica en un haz triangular normal con un único tubo flexible localizado en la tercera fila. Se realizaron simulaciones 2D URANS con el códido comercial Fluent 12.1 que se complementó un codigo de usuario udf para introducir el movimiento del tubo vibrante. Los parámetros del modelo más apropiados en lo referente al refinado de la malla, las condiciones de contorno, el modelo de turbulencia y el paso temporal fueron seleccionados de manera que garantizasen el mínimo efecto en los resultados del modelo. Una particularidad de el dominio computacional es que se instalaron placas guia tras los últimos tubos del haz para evitar la aparición de perturbaciones de gran escala, sin la necesidad de truncar el dominio aguas abajo del haz como se propuso en otros modelos precedentes.

La metodología CFD propuesta ha sido contrastada pos su comparación sucesiva con distintos datos experimentales, incluyendo cierto número de series de medidas publicadas en la literatura, así como los resultados empíricos obtenidos en el apartado experimental de la presente investigación. Se observaron: i) la distribución de presiones en condiciones estáticas (Mahon y Meskell, 2009), ii) las fluctuaciones de presión en la superficie de ciertos tubos estáticos de un haz triangular paralelo con P/d=1.57 y en el que un cilindro estaba sometido a vibración forzada. Este conjunto de medidas fueron realizadas para la presente investigación tras el diseño y construcción de un montaje experimental específico. iii) el retraso del coeficiente de sustentación respecto del movimiento del tubo, en condiciones de vibración forzada (Mahon and Meskell, 2013), iv) las fluctuaciones de la velocidad a lo largo de tubos de corriente a través de un haz triangular paralelo con P/d=1.54 con un tubo oscilando en inestabilidad fluido elástica FEI (Khalifa et al., 2013). iv) la velocidad crítica para la FEI con haces de P/d= 1,25 y P/d=1.375 a lo largo de un rango cierto rango de parámetros de masa amortiguamiento (Austermann y Popp, 1995). En todos los casos las predicciones pueden considerarse satisfactorias. Particularmente, las velocidades criticas estimadas en simulaciones que reproducían las condiciones de Austermann y Popp, en condiciones de vibración auto excitada, dieron resultados con un error relativo de solo el 5-10% por debajo del valor experimental en la mayoría de los casos. Además, el análisis de las fluctuaciones de velocidad y presión en la dirección del flujo sugiere que la fuente principal de perturbación se localiza en la zona de separación del tubo vibrante, aunque a su vez las oscilaciones inducidas en la cola le da fila precedente de cilindros también pueden actuar como fuente secundaria de perturbaciones. Aguas abajo del tubo vibrante, se observó que las perturbaciones

se propagaban a una velocidad de unas 0.84 veces la velocidad del gap. Estos resultados son consistentes con los datos experimentales obtenidos por Khalifa et. al. (2013). Una vez esta metodología fue validada como herramienta eficiente en la predicción del fenómeno de inestabilidad fluidoelástica, se empleó extensamente en la investigación el efecto de cierto número de parámetros del sistema en la velocidad crítica. Se observaron las siguientes dependencias en lo relativo a la estabilidad del sistema:

- Se emplearon simulaciones tanto estáticas (combinadas con el modelo teoríco quasi-no –estacionario) como auto excitadas (en las que se observaba directamente la respuesta libre del tubo en función de la velocidad del flujo) de cara a investigar la dependencia especifica de la velocidad crítica respecto a número de Reynolds y el ratio pitch-diametro.

  En el caso de las vibraciones auto excitadas, se encontró un 10% de incremento en la velocidad crítica para un rango de ratios pitch-diámetro creciente entre 1.25 y 1.4. Para ratios superiores se observó poca dependencia de éste parámetro. Del mismo modo se observó que un incremento en el número de Reynolds provocaba un desplazamiento hacia valores superiores del umbral de velocidades críticas. Estos resultados presentan un buen acuerdo con los obtenidos por Granger y Paidoussis (1996) con la función de memoria de Meskell (2003) y los coeficientes de fuerza estimados con las simulaciones CFD más sencillas. En ambos casos, puede considerarse que las estimaciones obtenidas con haces de tubos densos y números de Reynolds bajos pueden representar un límite razonable, por el lado de la seguridad, en la predicción de la velocidad crítica.

  En este caso, la conclusión del estudio apoyaría la simplificación de los modelos que excluyen la consideración de estos parámetros, ya que su efecto es limitado. Sin embargo, como estrategia para la determinación de la velocidad crítica, los resultados de esta investigación indicarían que tanto en la determinación de coeficientes de fuerza experimentales como en la implementación de modelos de cálculo numérico, lo más recomendable sería escoger condiciones de baja turbulencia y geometrías de pitch pequeño, ya que son indicadores de las condiciones más adversas para la inestabilidad.

- Empleando el nivel de cálculo auto-excitado, se analizó y discutió la fiabilidad en la extrapolación de resultados de simulaciones y ensayos experimentales con un solo tubo vibrante (que puede vibrar en dirección transversal únicamente). La inclusión de un segundo grado de libertad en el tubo vibrante, permitiendo movimiento en las dos direcciones del plano (axial y transversal), mostró que las

velocidades críticas se reducían en un 25-30%, aunque la inestabilidad siguió teniendo lugar en la dirección transversal. Estos resultados son coherentes con las diferencias en las predicciones de velocidad crítica encontradas entre Austermann y Popp (1995), con un solo tubo vibrante cuya posición respecto a la matriz de tubos había sido intencionadamente corregida para evitar que se viera desplazado aguas abajo debido al arrastre de la corriente, y Anjelic y Popp (1989), que ensayaron la misma geometría sin realizar esta corrección de la posición. Se concluye que, las simulaciones encaminadas a predecir la velocidad crítica deben incluir tubos de dos grados de libertad para una mejor predicción.

Además del efecto que genera la distorsión en el posicionamiento del tubo debido al arrastre, la fila en la que está localizado también afecta a las predicciones de velocidad crítica obtenidas con un solo tubo flexible, siendo en general la tercera fila la que desarrolla inestabilidad a velocidades más bajas. La velocidad crítica para un haz completamente flexible muestra pocas diferencias respecto a la obtenida con un único tubo flexible, siempre que este se encuentre localizado en la fila que desarrolla inestabilidad en primer lugar.

Finalmente, la dispersión presente en la literatura podría atribuirse, entre otros, a esta discrepancia en cuanto al número de grados de libertad de los tubos vibrantes o las distintas condiciones experimentales en cuanto al posicionamiento de los tubos, siendo las condiciones mas conservadoras las que corresponden a ensayos realizados con un haz totalmente flexible.

- El análisis del patrón de flujo intersticial con un $\Delta = 1\%$, para los haces de tubos de P/d=1.25 y P/d=1.57, sugiere que la fuente de perturbaciones se encuentra en el punto de separación, coincidiendo con los resultados de Khalifa et al.(2013). En el caso de la geometría triangular normal, la media del ratio entre la velocidad de propagación y la del gap fue $U_P/U_g = 0\,84$. Los mapas de campos de fases de las perturbaciones de velocidad y presión mostraron dependencia de los efectos: el incremento de la energía cinética en el cana con secciones crecientes y la succión del punto de estancamiento y la estela de los tubos de la filas anterior y posterior.

- Pese a que los datos experimentales obtenidos en el laboratorio fueron limitados proporcionaron medidas similares a las presentes en la literatura con respecto a la velocidad de propagación y confirmaron conclusiones coherentes de acuerdo a las condiciones específicas del experimento. Los resultados del modelo CFD mostraron un acuerdo satisfactorio con las medidas empíricas de amplitud y fase de retraso, en términos tanto cuantitativos como cualitativos.

2 Contribuciones

Las contribuciones de la presente investigación al estado del conocimiento en el campo de la inestabilidad fluidoelástica en cambiadores de calor de carcasa y tubos se enumeran a continuación:

- Se propone una metodología CFD con movimiento estructural que es capaz de simular distintitas condiciones experimentales, incluyendo vibraciones forzadas o autoexcitadas. Se seleccionaron los distintos parámetros del modelo, tales como refinado de la malla, condiciones de contorno, modelo de turbulencia y paso temporal, con objeto de garantizar que se minimiza su influencia en las predicciones. El modelo fue comparado con seis conjuntos de datos experimentales i) distribución de presión en condiciones estáticas (Mahon and Meskell, 2009), ii) fluctuaciones de presión en la superficie de tubos estáticos de un haz triagular paralelo P/d=1.57 con un cilindro en vibración forzada (estas medidas se realizaron en el laboratorio para este trabajo despues del diseño y construcción de un prototipo experimental específico), iii) retraso del coeficiente de sustentación respecto al movimiento del tubo (Mahon and Meskell, 2013), iv) fluctuaciones de velocidad a lo largo de tubos de corriente en un haz triangular paralelo de P/d=1.54 en el que un tubo desarrolla vibraciones por inestabilidad (Khalifa et.al.,2013) and v) velocidad crítica para la FEI con P/d=1.25 y P/d=1.375 en un cierto rango de parametros de masa amortiguamiento (Austemann and Popp, 1995). La metodología validada puede representar una herramienta útil en el estudio de la inestabilidad fluidoelástica en el futuro y proporciona estrategias de modelado útules para la simulación de haces de tubos.

- Se propone a su vez una metodología híbrida teorico-numérica que emplea coeficientes de fuerza obtenidos en simulaciones estacionarias como datos de entrada para el modelo quasi-no-estacionario de Granger y Paidoussis (1996), en el que se introduce la función de memoria propuesta por Meskell (2003). Este procedimiento permite la predicción de umbrales de inestabilidad sin la necesidad de ningún dato experimental y con un coste computacional moderado. Aunque esta metodología no proporciona unos resultados tan ajustados como las simulaciones auto excitadas en términos cuantitativos, se encontró que era capaz de predecir los mismos resultados en los estudios de dependencia de la velocidad crítica respecto de distintos parámetros del sistema, constituyendo una herramienta muy eficiente en términos de coste temporal y computacional para el análisis cualitativo del comportamiento de la FEI.

- Las aparentes contradicciones y la dispersión que se muestra en los datos experimentales presentes en la literatura para un solo tubo flexible en un haz de tubos rígidos fue investigada y se propusieron posibles explicaciones. El efecto del número de Reynolds y el ratio pitch-diámetro en la velocidad crítica del sistema fue evaluado como moderado, mientras que se encontró un efecto significativo del movimiento del tubo en la dirección del flujo. Pese a que el tubo con dos grados de libertad vibra igualmente sólo en dirección transversal, la posición desplazada que alcanza debido al arrastre al que se ve sometido tiene el efecto de reducir la velocidad crítica aproximadamente un 30%. Se producen pocas diferencias en la velocidad crítica entre haces con un solo tubo flexible respecto del caso de un haz completamente flexible siempre y cuando el tubo flexible se localice en la fila que presenta el umbral de inestabilidad más bajo. Sin embargo, la fila que presenta esa menor velocidad crítica puede depender de la geometría y del parámetro de masa amortiguamiento con lo que podría no ser conocida de antemano. La identificación previa de esta fila debe ser tenida en cuenta para la utilización de predicciones, numéricas o experimentales, obtenidas con haces con un solo tubo flexible.

3 Trabajo Futuro

Como se ha discutido en las secciones previas, el comportamiento de un único tubo flexible en un haz de tubos rígidos puede ser representativo del umbral de inestabilidad de un haz completamente flexible siempre y cuando:
1. Se escoja la fila más sensible a la inestabilidad a la hora de localizar el tubo.
2. El mecanismo de inestabilidad controlada por el amortiguamiento sea el dominante.
Una interesante oportunidad para futuros trabajos podría ser la caracterización de la fila con más baja velocidad crítica para diferentes geometrías, ratios de pitch y parámetros de masa amortiguamiento, con el objetivo de explorar la importancia relativa de los mecanismos de inestabilidad fluidoelástica controlada por el amortiguamiento y controlada por la rigidez en diferentes condiciones operacionales. La comparación entre umbrales de inestabilidad obtenidos con un solo tubo flexible y umbrales obtenidos pala haces totalmente flexibles también permitiría la caracterización de las condiciones en las que los tests simplificados son representativos del comportamiento real del intercambiador, reduciendo también la dispersión de los mapas de estabilidad.

References

[1] R. Austermann and K. Popp. Stability behaviour of a single flexible cylinder in rigid tube arrays of different geometry subjected to cross-flow. *Journal of Fluids and Structures*, 9(3):303 – 322, 1995.

[2] J. Mahon and C. Meskell. Estimation of the time delay associated with damping controlled fluidelastic instability in the normal triangular tube array. *Journal of Pressure Vessel Technology*, 135:1348–1368, 2013.

[3] A. Khalifa, D. Weaver, and S. Ziada. An experimental study of flow-induced vibration and the associated flow perturbations in a parallel triangular tube array. *Journal of Pressure Vessel Technology*, 135:030904 (9 pages), 2013.

[4] M. J. Pettigrew and C. E. Taylor. Vibration analysis of shell and tube heat exchangers: An overview-part 1: Flow, damping, fluidelastic instability. *Journal of Fluids and Structures*, 18(5):469–483, 2003.

[5] M. J. Pettigrew and C. E. Taylor. Vibration analysis of shell and tube heat exchangers: An overview-part 2: Vibration response, fretting-wear, guidelines. *Journal of Fluids and Structures*, 18(5):485–500, 2003.

[6] R. D. Blevins. *Flow-inducted Vibrations 2nd Edition. Krieger Publications, Malabar, Florida*, 1994.

[7] S. S. Chen. Instability mechanisms and stability criteria of a group of circular cylinders subjected to cross-flow. part 1: Theory. *Journal of Vibrations, Acoustics, Stress, Reliability and Design*, 105:51–58, 1983.

[8] S. S. Chen. Instability mechanisms and stability criteria of a group of circular cylinders subjected to cross-flow. part 2: Numerical results and discussion. *Journal of Vibrations, Acoustics, Stress, Reliability and Design*, 105:253–260, 1983.

[9] S. J. Price. A review of theoretical models for fluidelastic instability of cylinder arrays in cross-flow. *Journal of Fluids and Structures*, 9:463–518, 1995.

[10] S. J. Price and M. P. Paidoussis. An improved mathematical model for the stability of cylinder rows subject to cross-flow. *Journal of Sound and Vibration*, 97(4):615–640, 1984.

[11] S. Granger and M. Paidoussis. An improvement to the quasi-steady model with application to cross-flow-induced vibration of tube arrays. *Journal of Fluid Mechanics*, 320:163–184, 1996.

[12] J. Lever and D. Weaver. On the stability of heat exchanger tube bundles. part 1: modified theoretical model. part ii: numerical results and comparison with experiment. *Journal of Sound and Vibration*, 107:375–410, 1986.

[13] M. Hassan, A. Gerber, and H. Omar. Numerical estimation of fluidelastic instability in tube arrays. *Journal of Pressure and Vessel Technology*, 132(4):041307 (11 pp.) –, 2010.

[14] A. Khalifa, D. Weaver, and S. Ziada. Modeling of the phase lag causing fluidelastic instability in a parallel triangular tube array. *Journal of Fluids and Structures*, 43: 371–384, 2013.

[15] B. Anderson, M. Hassan, and A. Mohany. Modelling of fluidelastic instability in a square inline tube array including the boundary layer effect. *Journal of Fluids and Structures.*, 132(48):362–375, 2014.

[16] H. J. Connors. Fluid-elastic vibration of tube arrays excited by cross flow. *Proceedings, Flow-induced vibrations in heat exchangers, ASME, Chicago*, pages 42–56, 1970.

[17] M. P. Paidoussis. Real-life experiences with flow-induced vibration. *Journal of Fluids and Structures*, 22:741–755, 2006.

[18] D. S. Weaver. Some thoughts on the elusive mechanism of fluidelastic instability in heat exchanger tube array. *In: Proceedings of the 9th International Conference On Flow-Induced Vibration.Prague, Czech Republic.*, 1:290–297, 2008.

[19] J. Mahon and C. Meskell. Surface pressure distribution survey in normal triangular tube arrays. journal of fluids and structures. *Journal of Fluids and Structures*, 25: 1348–1368, 2009.

[20] C. Meskell. A new model for damping controlled fluidelastic instability in heat exchanger tube arrays. *Proceedings of the Institution of Mechanical Engineers, Part A: Journal of Power and Energy*, 223(4):361–368., 2009.

[21] S. S. Chen. Flow inducted vibration. *Pressure Vessel and Piping: Design Technology A decade of Prograss. ASME New York*, pages 301–312, 1982.

[22] M. P. Paidoussis. A review of flow inducted vibrations in reactors and reactor components. *Journal of Nuclear Engineering and Desing*, 74:31–60, 1983.

[23] M. P. Paidoussis and S. J. Price. The mechanisms underlying flow-induced instabilities of cylinder arrays in crossflow. *Journal of Fluid Mechanics*, 187:45–59, 1988.

[24] D. S. Weaver and J. A. Fitzpatrick. A review of cross-flow inducted vibrations in heat exchanger tube arrays. *Journal of Fluids ans Structures*, 1:73–93, 1988.

[25] H. Gelbe, Jahr M., and K. Schroder. Flow-inducted vibrations in heat-exchanger tube bundles. *Chemical Engineering and Processing.*, 34:289–298, 2009.

[26] S. J. Price. An investigation on the use of connors' equation to predict fluidelastic instability in cylinder arrays. *Journal of Pressure Vessel Technology*, 123:448–453, 2001.

[27] H. G. D. Goyder. Flow-inducted vibrations in heat-exchangers. *Chemical Engineering Research and Design.*, 80:226–232, 2002.

[28] D. R. Polak and D. S. Weaver. Vortex shedding in normal triangular tube arrays. *Journal of Fluids and Structures*, 9(1):1–17, 1995.

[29] G. Rzentkowski and J. H. Lever. An effect of turbulence on fluidelastic instability in tube bundles: A nonlinear analysis. *Journal of Fluids and Structures*, 12(5): 561–590, 1998.

[30] M. Rottmann and K. Popp. Influence of upstream turbulence on the fluidelastic instability of a parallel triangular tube bundle. *Journal of Fluids and Structures*, 18(5):595–612, 2003.

[31] E. Naudascher and D. Rockwell. Flow-inducted vibrations an engineering guide. *Dover Publications, Inc., Mineola, New York*, 1994.

[32] A. Khalifa. Fluidelastic instability in heat exchanger tube arrays. *PhD Thesis McMaster University Canadá*, 135, 2013.

[33] J. Parrondo. Vibraciones fluidodinámicas en haces de cilindros bajo flujo cruzado. inestabilidad fluidoelástica. *PhD. Thesis of the University of Oviedo*, 1992.

[34] M. A. Hassan, Weaver D.S., and Dokainish M. A. The effects of support geometry on the turbulence response of loosely supported heat exchanger tubes. *Journal of Fluids and Structures*, 18(5):529–554, 2003.

[35] F. Axisa, J. Antunes, and B. Villard. Random excitation of heat exchanger tubes by cross-flows. *Journal of Fluids and Structures*, 4(3):165–185, 1990.

[36] D. S. Weaver, S. Ziada, and M. K. Au-Yang. Flow-inducted vibrations in power ans process plant components progress and prospect. *Journal of Pressure Vessel Technology*, 122:339–348, 2000.

[37] D. S. Weaver. Vortex shedding and acoustic resonance in heat exchanger tube arrays. *Technology for the 90's. ASME, New York, Ch.*, 1:775–810, 1993.

[38] S. Ziada. Vorticity shedding and acoustic resonance in tube bundles. *Journal of the Brazilian Society of Mechanical Science Engineering*, 28, 2006.

[39] S. Ziada, A. Oengoren, and Buhlmann E. T. On acoustical resonance in tube arrays .1. experiments. *Journal of Fluids and Structures*, 3, 1989a.

[40] S. Ziada, A. Oengoren, and Buhlmann E. T. On acoustical resonance in tube arrays .2. damping criteria. *Journal of Fluids and Structures*, 3, 1989b.

[41] S. Ziada and A. Oengoren. Vorticity shedding and acoustic-resonance in an in-line tube bundle .1. vorticity shedding. *Journal of Fluids and Structures*, 6, 1992.

[42] S. Ziada and A. Oengoren. Flow periodicity and acoustic resonance in parallel triangle tube bundles. *Journal of Fluids and Structures*, 14, 2000.

[43] C. Sweeney and C. Meskell. Fast numerical simulation of vortex shedding in tube arrays using a discrete vortex method. *Journal of Fluids and Structures*, 18(5): 501–512, 2003.

[44] C. Liang and G. Papadakis. Large eddy simulation of cross- flow through a staggered tube bundle at subcritical reynolds number. *Journal of Fluids and Structures*, 23: 1215–1230, 2007.

[45] C. Liang, G. Papadakis, and X. Luo. Effect of tube spacing on vortex shedding characteristics of laminar flow past an inline tube array: A numerical study. *Journal of Computers and Fluids*, 38:950–964, 2009.

[46] S. S. Rao. *Mechanical Vibrations, 4th Edition. Pearson Education, Inc., Upper Saddle River, New Jersey, USA.*, 2004.

[47] M. P. Paidoussis, S. J. Price, and E. de Langre. Fluid-structure interactions. cross-flow-inducted instabilities. *Cambridge University Press*, pages 215–290, 2011.

[48] B. W. Roberts. Low frequency, self-excited vibrations in a row of cylinders mounted in an airstream. *PhD. Thesis, University of Cambridge*, 1962.

[49] B. W. Roberts. Low frequency, aeroelastic vibrations in a cascade of circular cylinders. *In: Mechanical Engineering Science. The Institute of Mechanical Engineers, London*, 4(5):1–28, 1966.

[50] D. J. Gorman. Experimental development of design criteria to limit liquid cross-flow-inducted vibration in nuclear reactor heat exchange equipment. *Nuclear Science and Engineering.*, 99:324–336, 1978.

[51] M. J. Pettigrew and C. E. Taylor. Flow-inducted vibration of nuclear power station components. atomic energy of canada report aecl-5852. *Journal of Fluids and Structures*, 18(5):469–483, 1978.

[52] M. P. Paidoussis. Flow-inducted vibrations in nuclear reactors and heat exchangers: Practical experiences and stage of the knowedge. *Practical experiences with flow inducted vibrations. Berlin, Springer-Verlag*, 76:329–360, 1980.

[53] M. K. Au-Yang. Flow-inducted vibrations of analysis of tube bundles. a proposed section iii appendix n non mandatory code. *ASME Journal of Pressure Vessel Technology*, 1991.

[54] M. J. Pettigrew and C. E. Taylor. Flow-inducted vibration of nuclear power station components. atomic energy of canada report aecl-5852. *ASME Journal of Pressure and Vessel Technology*, 113:242–256, 1991.

[55] D. S. Weaver and M. Elkashlan. The effect of damping and mass ratio on the stability of a tube bank. *Journal of Sound and Vibration*, 2:283–294, 1981.

[56] D. S. Weaver and M. Elkashlan. On the number of tube rows required to study cross-flow induced vibrations in tube banks. *Journal of Sound and Vibration*, 2: 265–273, 1981.

[57] D. S. Weaver and D. Koroyannakis. The cross flow response of a tube array in water - a comparison with the same array in air. *ASME Journal of Pressure Vessel Technology*, 10:136–146, 1982.

[58] R. D. Blevins. Fluid elastic whirling of a tube row. *Journal of Pressure Vessel Technology*, 96:263–267, 1974.

[59] R. D. Blevins. Fluidelastic whirling of tube rows and tube arrays. *Journal of Fluids Engineering.*, 99:457–460, 1977.

[60] R. D. Blevins. Fluid damping and the whirling instability of tube arrays. *In: Flow Induced Vibrations. American Society of Mechanical Engineers*, pages 35–39, 1979.

[61] S. J. Price and M. P. Paidoussis. A constrained-mode analysis of the fluidelastic instability of a double row of flexible circular cylinders subjected to cross-flow: A theoretical investigation of system parameters. *Journal of Sound and Vibration*, 105(1):121–142, 1986.

[62] H. Tanaka and S. Takahara. Unsteady fluid force in tube bundle and its dynamic effect on vibration. *ASME PVP Flow-inducted vibrations in power plants components. New York.*, 44:77–92, 1980.

[63] H. Tanaka and S. Takahara. Fluid elastic vibration of tube array in cross flow. *Journal of Sound and Vibration*, 77(1):19–37, 1981.

[64] H. Tanaka and S. Takahara. Flow-inducted vibrations in tube arrays with various pitch to diameter ratios. *ASME Journal of Pressure Vessel Technology*, 104:168–174, 1982.

[65] S. J. Paidoussis, M. P. Price and Mureithi W. N. On the virtual nonexistence of multiple instability regions for some heat-exchangers arrays in cross-flow. *Journal of Fluid Engineering*, 118:103–109, 1996.

[66] J. Lever and D. Weaver. A theoretical model for the fluidelastic instability in heat exchanger yube bundles. *Journal of Pressure Vessel Technology*, 104:147–158, 1982.

[67] D. S. Yetisir, M. Weaver. An unsteady theory for fluidelastic instability in an array of flexible tubes in cross-flow. *Journal of Fluids and Structures*, 7:751–766, 1993.

[68] J. Parrondo, E. Egusquiza, and C. Santolaria. Extension of the weaver's usteady analytical model to the fluidelastic instability of arrays of flexible cylinders. *Journal of Wind Engineering and Industrial Aerodynamics*, 49:177–186, 1993.

[69] H. Gross. Untersuchung aeroelastischer schwingungsmechanismen und deren berucksichtigung bei der auslegung von rohrbundelwarmetauschern. *PhD thesis, Technical University of Hannover*, 1975.

[70] D. S. Weaver and W. Schneider. The effect of flat bar supports on the cross flow induced response of heat exchanger u-tubes. *ASME Journal of Engineering for Power*, 105:775–781, 1983.

[71] A. J. Fricker. Vibro-impacting of fluid-elastically unstable heat exchangers tubes with support clearances. *Flow Inducted Vibrations*, 6:129–137, 1991.

[72] A. J. Fricker. Numerical analysis of the fluidelastic vibration of a steam generator tube with loose supports. *Journal of Fluids and Structures*, 58:85–108, 1992.

[73] S. S. Chandra S. Cai, Y. Chen. A theory for fluidelastic instability of tube-support-plate-inactive modes. *Journal of Pressure Vessel Technology*, 114:139–148, 1992.

[74] Y. Cai and S. S. Chen. Chaotic vibrations of non-linearly supported tubes in cross-flow. *Journal of Pressure Vessel Technology*, 115:128–134, 1993.

[75] Y. Cai and S. S. Chen. Non-linear dynamics of loosely supported tubes in cross-flow. *Journal of Sound and Vibration*, 168:449–468, 1993.

[76] S. S. Chen, S H Chen. Chaotic vibration in fluidelastic instability of a tube row in cross-flow. *ASME Flow-Inducted Vibration and Fluid-Structure Interaction.*, pages 11–20, 1993.

[77] M. P. Paidoussis and G. X. Li. Cross-flow-inducted chaotic motions of heat exchanger tubes impacting on loose supports. *Journal of Sound and Vibration.*, 152: 305–326, 1992.

[78] C. Meskell and J. A. Fitzpatrick. Investigation of nonlinear behaviour of damping controlled fluidelastic instability in a normal triangular tube array. *Journal of Fluids and Structures*, 18:573–593, 2003.

[79] T. K. Masri, S. F. Caughey. A non-parametric identification technique for nonlinear dynamic problems. *Journal of Applied Mechanics*, 54:918–929, 1979.

[80] C. Meskell and H. J. Fitzpatrick, J. A. Rice. Application of force-state mapping to a nonlinear fluid-elasteic system. *Mechanical Systems and Signal Processing*, 15: 75–95, 2001.

[81] D. S. Waring, L. F. Weaver. Partial admission effects on the stability of heat exchanger tube array. *ASME Journal of Pressure Vessel Technology*, 110:194–198, 1988.

[82] D. S. Weaver and H. G. D. Goyder. An experimental study of fluidelastic instability in a three span tube array. *Journal of Fluids ans Structures*, 4:429–442, 1990.

[83] D. S. Weaver and J. L. Parrondo. Fluidelastic instability in multispam exchanger tube arrays. *Journal of Fluids ans Structures*, 5:323–338, 1991.

[84] I. Marn, J. Catton. Flow-induced vibration problem in a simple cylinder array. one dimensional unsteady integral approach. *In: Winter Annual Meeting of the American Society of Mechanical Engineer.*, 102:19–21, 1990.

[85] I. Marn, J. Catton. Flow induced vibrations in cylindrical bundles. two dimensional analysis into normal modes. *In: Proceedings of the 28th National Heat Transfer Conference. Minneapolis, MN, USA,*, 165:9–14, 1991.

[86] M. S. M. Steininger D. A. Haslinger K. H. Eisinger, F. L. Rao. Numerical simulation of cross-flow induced fluidelastic vibration of tube arrays and comparison with experimental results. *Journal of Pressure Vessel Technology*, 117:31–39, 1995.

[87] V. Kassera and K. Strohmeier. Simulation of tube bundle vibrations induced by cross-flow. *Journal of Fluids and Structures*, 11:909–928, 1997.

[88] Y. A.. Barsamian, H. R. Hassan. Large eddy simulation of turbulent cross-flow in tube bundles. *Nuclear Engineering and Design*, (172):103–122, 1997.

[89] Schroder and H. K. Gelbe. Two- and three-dimensional cfd-simulation of owinduced vibration excitation in tube bundles. *Chemical Engineering and Processing*, 38(4-6): 621–629, 1999.

[90] Z. Souli M. Longatte, E. Bendjeddou. Methods for numerical study of tube bundle vibrations in cross-flows. *Journal of Fluids and Structures*, 18:513–528, 2003.

[91] M. Schneider, K. Farge. Numerical simulation of the transient flow behaviour in tube bundles using a volume penalization method. *Journal of Fluids and Structures*, 4(20), 2005.

[92] A. Khalifa, D. Weaver, and S. Ziada. A single flexible tube in a rigid array as a model for fluidelastic instability in tube bundles. *Journal of Fluids and Structures*, 34:14–32, 2012.

[93] ANSYS. Ansys fluent users guide. *ANSYS Fluent Users Guide*, 2013.

[94] R. P. Wallis. Photographic study of fluid flow between banks of tubes. *Engineering*, 148:423–426, 1939.

[95] D. Mewes and D. Stockmeier. A new model for damping controlled fluidelastic instability in heat exchanger tube arrays. *In Flow Induced Vibrations*, pages 231–242., 1991.

[96] H. J. Connors. Vibration of heat exchanger tube array. *ASME Journal of Mechanical Design*, 100:347–353, 1978.

[97] S. S. Chen and J. A. Jendrzjczyk. Experiments on fluid instability in tube banks subjected to liquid cross flow. *Journal of Sound and Vibration*, 78:355–381, 1981.

[98] M. Andjelic and K. Popp. Stability effects in a normal triangular cylinder array. *Journal of Fluids and Structures*, 3(2):165–185, 1989.

Appendix A

Experimental setup

A.1 Setup description

A.1.1 Geometry

A parallel triangular tube array of 7 rows and 5 columns of tubes made of PVC with $d = 12mm$ and $P/d = 1\ 57$ has been used in the present investigation for the experimental routines. Except for one vibrating tube (see Fig. A.1), the rest of the tubes are fixed to the top and to the bottom sidewalls of the channel. The test section was fabricated in methacrylate to allow a direct visualization of the flow, and the parallel triangular geometry was reproduced by means of a numerical controlled fabrication in order to achieve a high precision in the tubes location. Special care is desirable at this point because relatively small displacements from the ideal position of the tubes can affect the onset of the critical velocity fluidelastic instability [98] [1].
The equilibrium position of the vibrating tube is also determined by the numerical controlled machining, fixing it bottom extreme to the channel ground. The upper extreme of the tube is connected to a mechanism that induces a forced harmonic vibration in the transversal direction of the array. A guiding rod, is used to transfer that forced vibration getting out from the channel thought a hole in the top wall (see Fig. A.2).
Figs. A.3 A.4 and A.5 show photographs of the test section and also in perspective, top and front view, respectively, while Fig. A.6 shows the tube array filled with water.

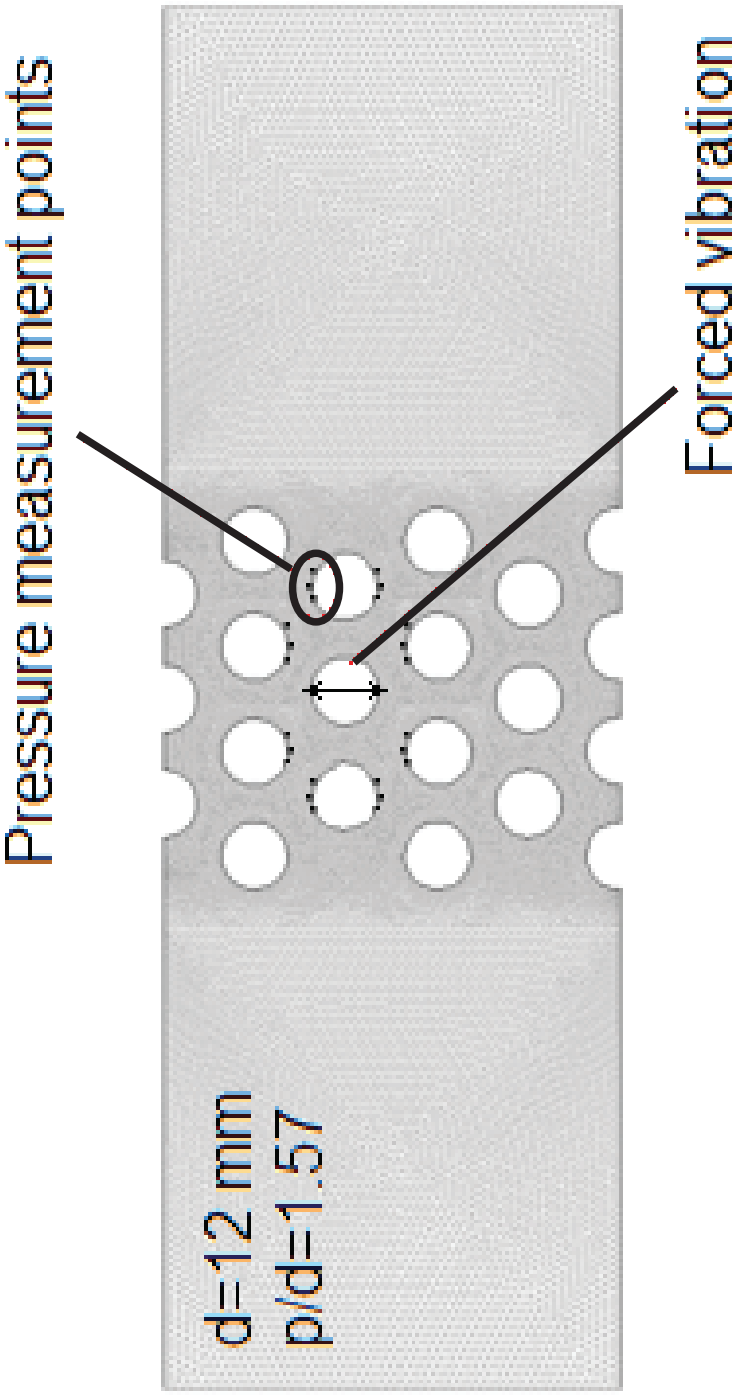

FIGURE A.1: Schematic of the array geometry and measurement points.

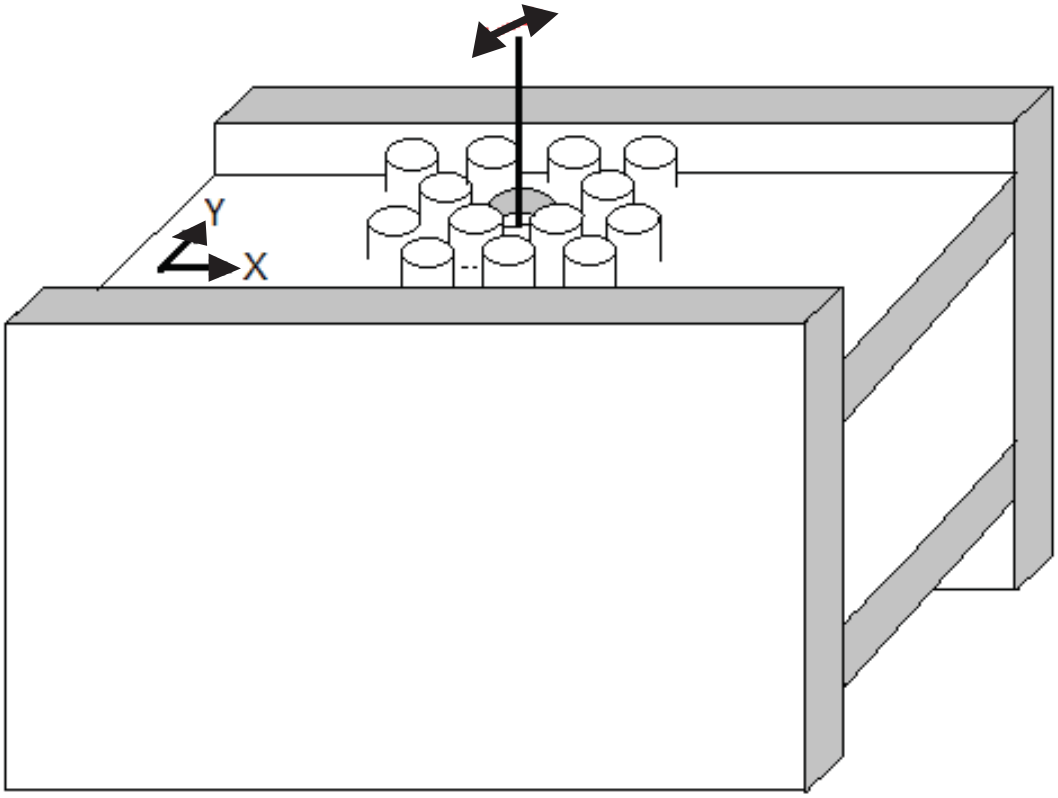

FIGURE A.2: 3D view of the tube array section and the mechanism to transmit the tube motion.

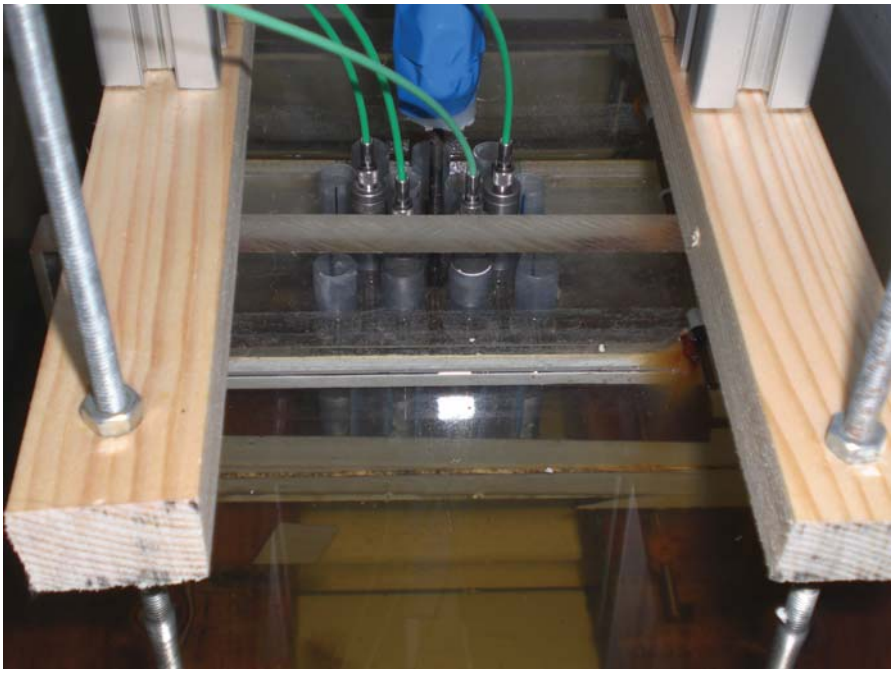

FIGURE A.3: Test section.

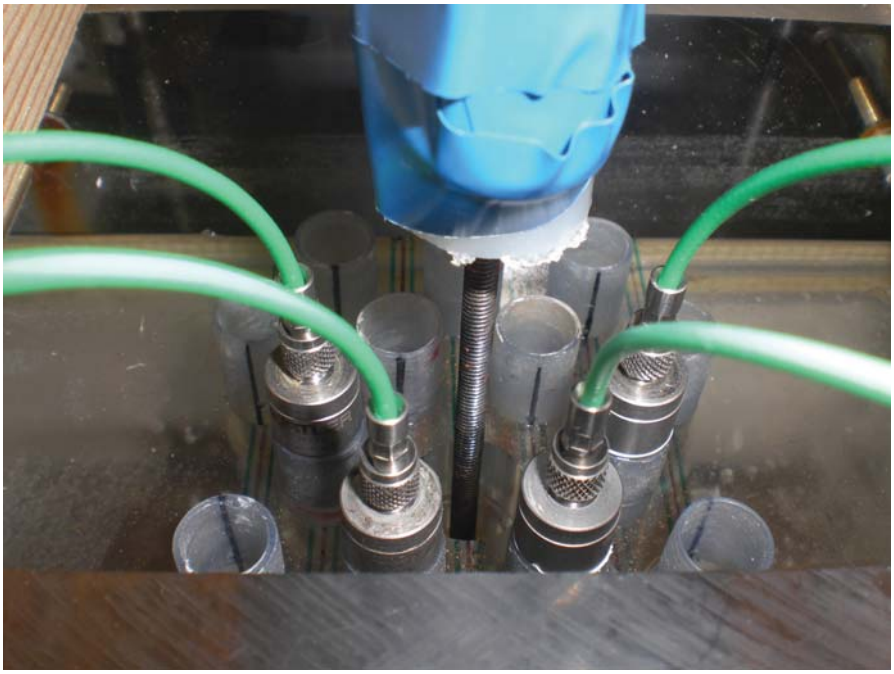

FIGURE A.4: Top view of the test section.

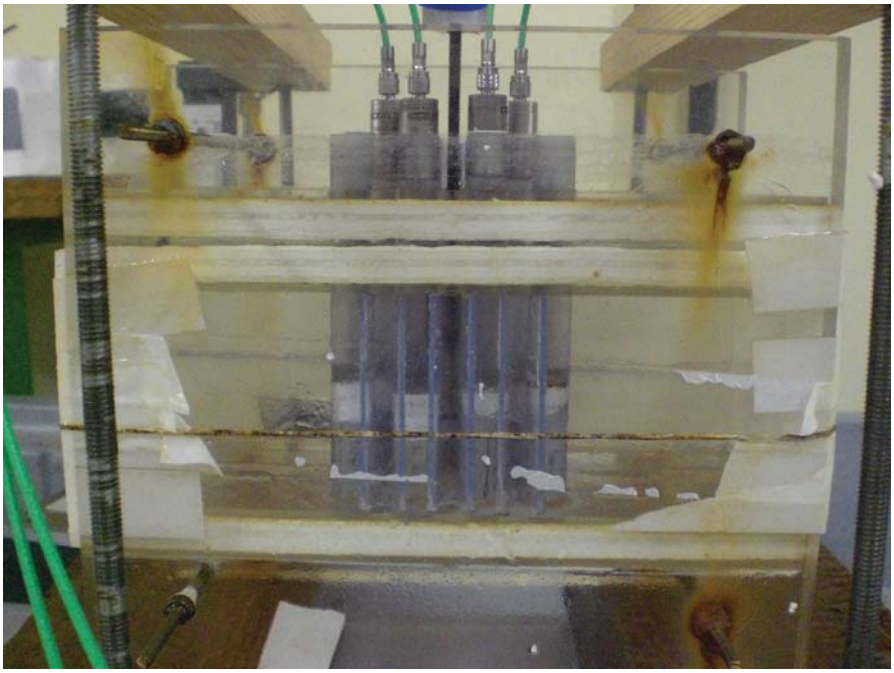

FIGURE A.5: Front view of the test section.

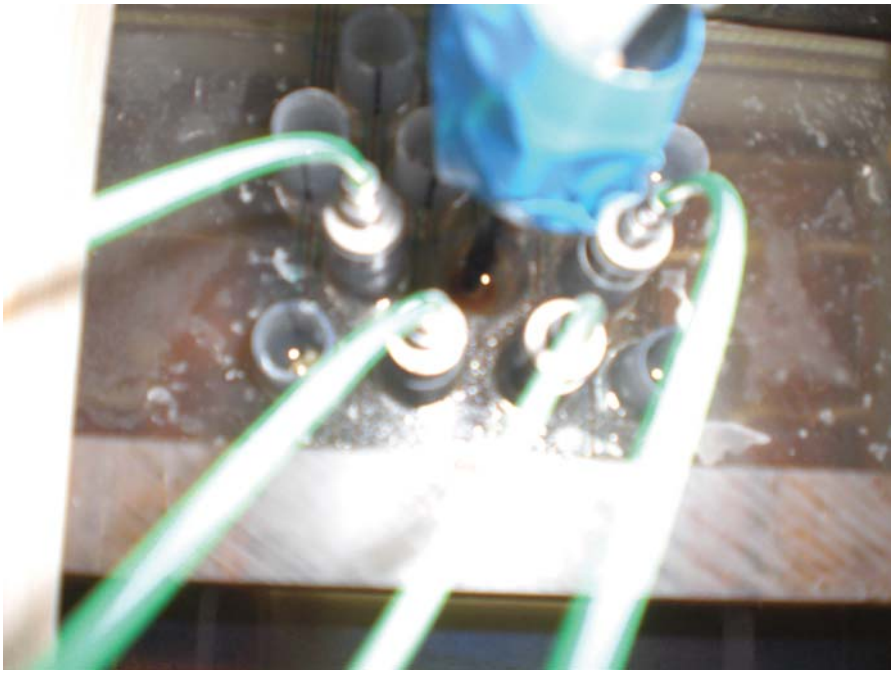

FIGURE A.6: Test section filled with water.

A.1.2 Mechanism for the excitation of forced oscillations

The mechanism to generate the forced vibration in the oscillating tube is composed by a drill, a ball bearing and a rail. The drill rotation axis was eccentrically connected with the interior piece of the ball bearing, while the outer casing of the bearing was assembled to the upper piece of a rail. On the other hand, the botton piece of the rail was fixed to the free ending of the flexible tube (see Fig. A.7). When the drill axes rotates, the ball bearing describes a circular motion due to the eccentricity in the assembly between the drill and the ball bearing, but only the transverse component is transmitted to the tube, because the rail, disposed in the in-line direction, acts as a filter to the axial component of the motion (see Fig. A.8).

Figs. A.9 and A.10 show photographs of the complete mechanism connected to the tube array and a zoom of the drill axis, ball bearing, rail and tube rod assembly. In Fig. A.11 the complete set-up is introduced in water.

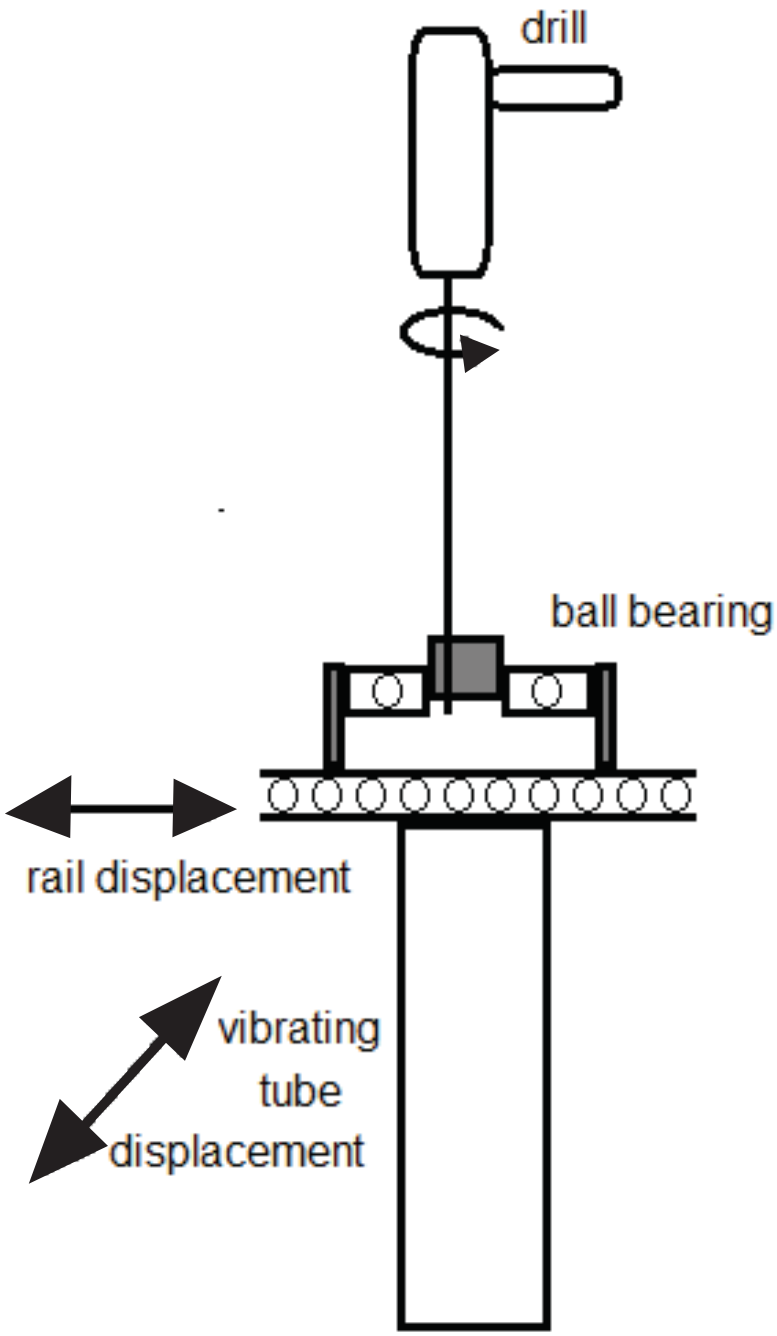

FIGURE A.7: Scheme of the front view of the mechanism inducing forced oscillations in the flexibe tube

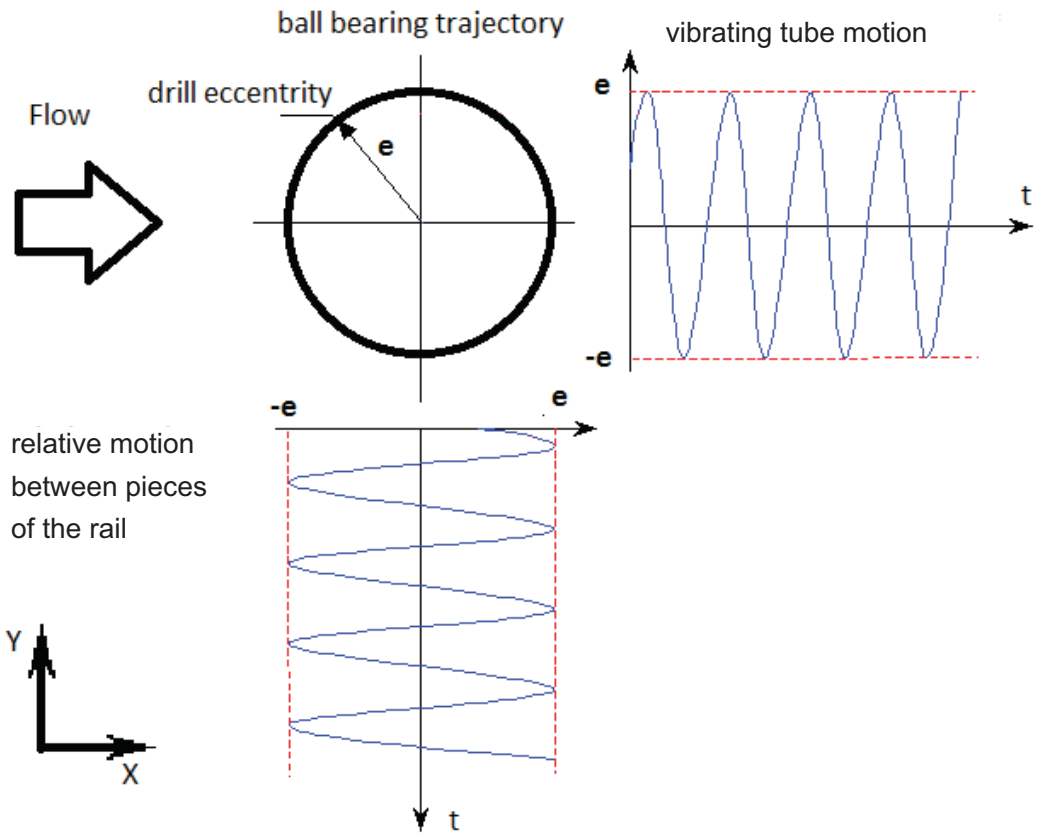

FIGURE A.8: Transverse harmonic oscillation obtained decoupling the circular motion components with a rail.

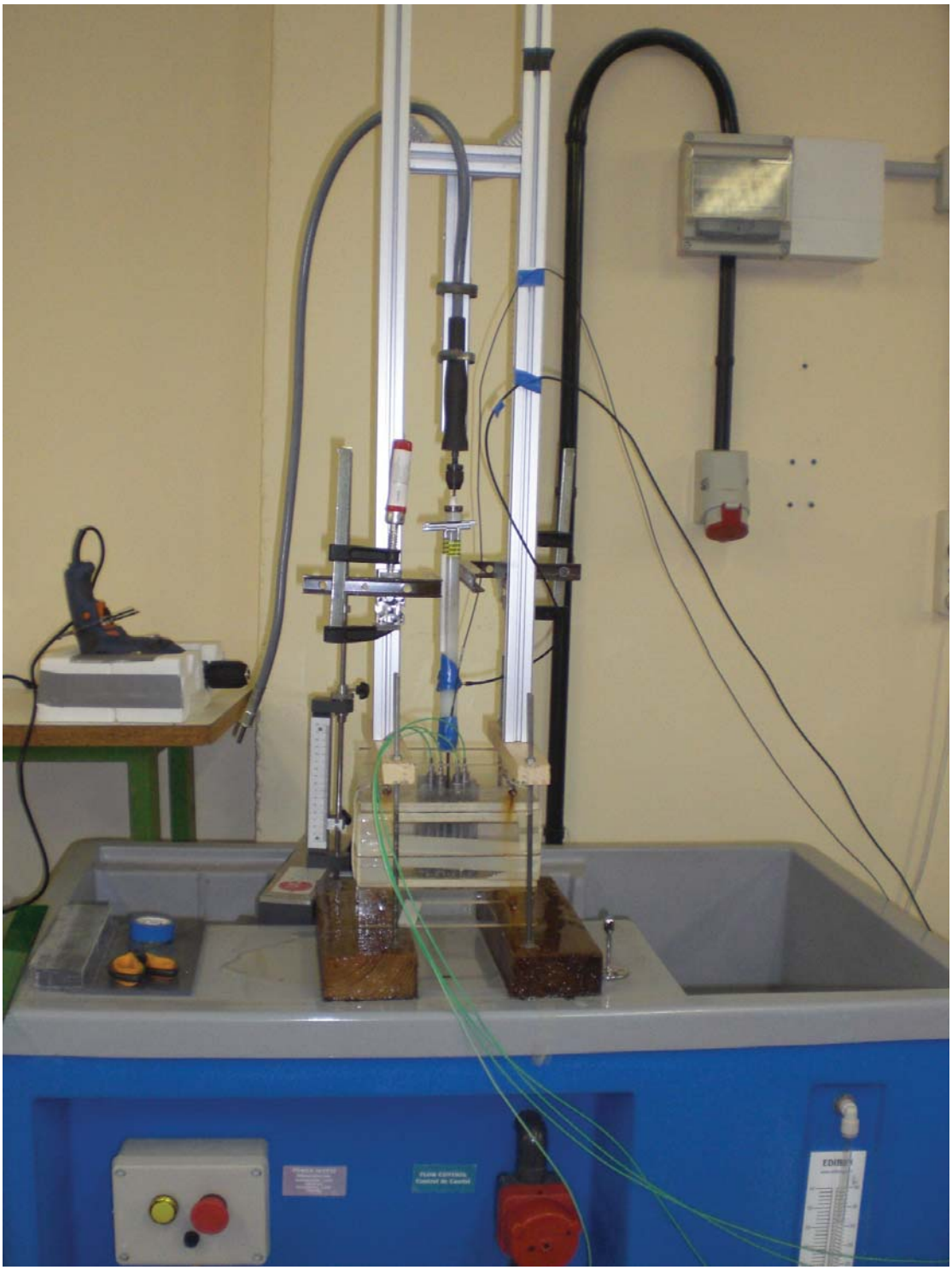

FIGURE A.9: Complete mechanism connected to the tube array.

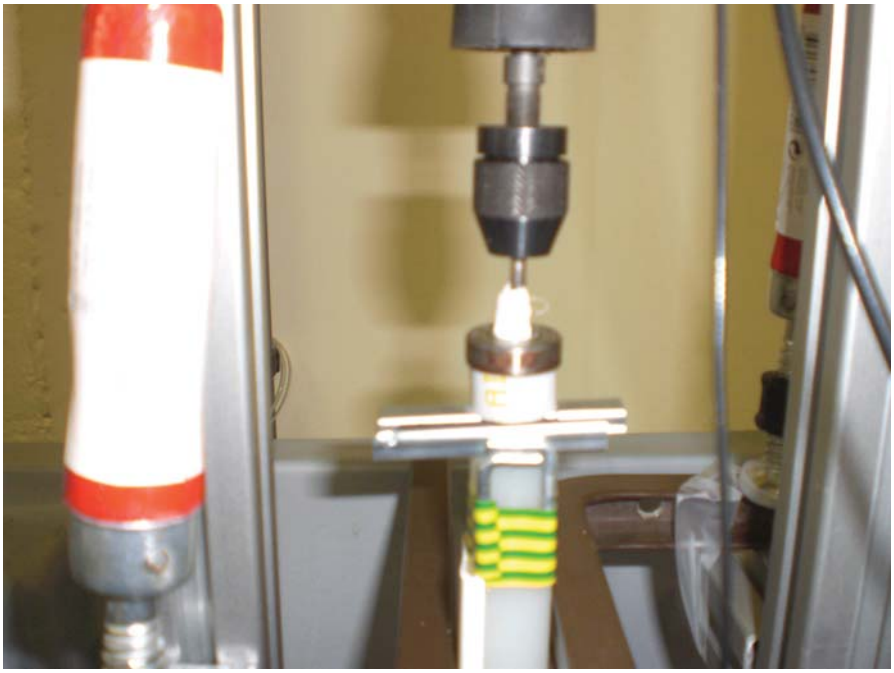

FIGURE A.10: Drill axis, ball bearing, rail and tube rod assembly.

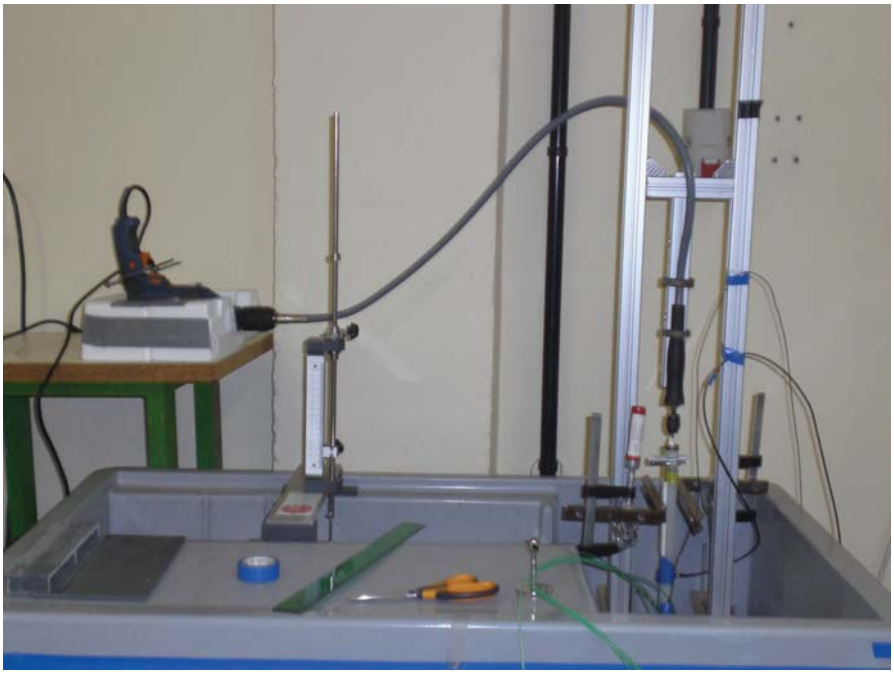

FIGURE A.11: Complete set-up is introduced in water (1).

FIGURE A.12: Complete set-up is introduced in water (2).

A.1.3 Instrumentation

The instrumentation used in the experimental measurements consisted in four pressure transducers and two accelerometers. The pressure transducers were located in the top of the tubes where a measurement point was selected for series of tests. The interior diameter of the tubes was selected to be the same as the transducer exterior diameter , thus matching exactly and allowing to place the sensors partially inside the tubes (see Fig. A.13).

The tube angular position could be rotated manually in order to change the orientation of the monitored point. In total, 12 points were monitored in different series of tests (see Fig. A.1). Note that only four points in different tubes can be monitored in every single test.

During the test, the monitored tubes were filled with water to the top, where the pressure transducer was located. The inner and outer flow were communicated through a small hole drilled in the middle section of the tubes (i.e., the measurement point). Below that point, the tubes were filled with solid to reduce the volume of the water chamber (preventing possible affection on the results).

The accelerometers were placed in the guiding rod above the tube section, measuring

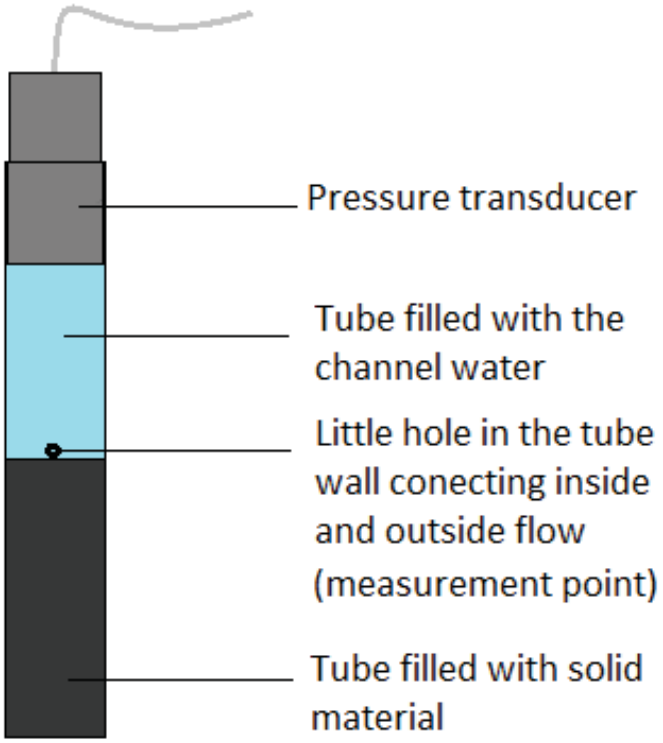

FIGURE A.13: Pressure transducer used in the experimental measurements.

transverse and in-line components of the tube motion (in-line motion was found to be negiligible compared to transverse oscillations). These measurements were transformed to values corresponding to the middle section of the tubes in the post-processing, taking into account the height of the sensors with respect to the measurement point.
Figs. A.14 and A.15 show photographs of the pressure transducers and accelerometers respectively. Finally the instrumented set-up is shown in Fig. A.16.

FIGURE A.14: Pressure transducer used in the experimental measurements.

FIGURE A.15: Accelerometer used in the experimental measurements.

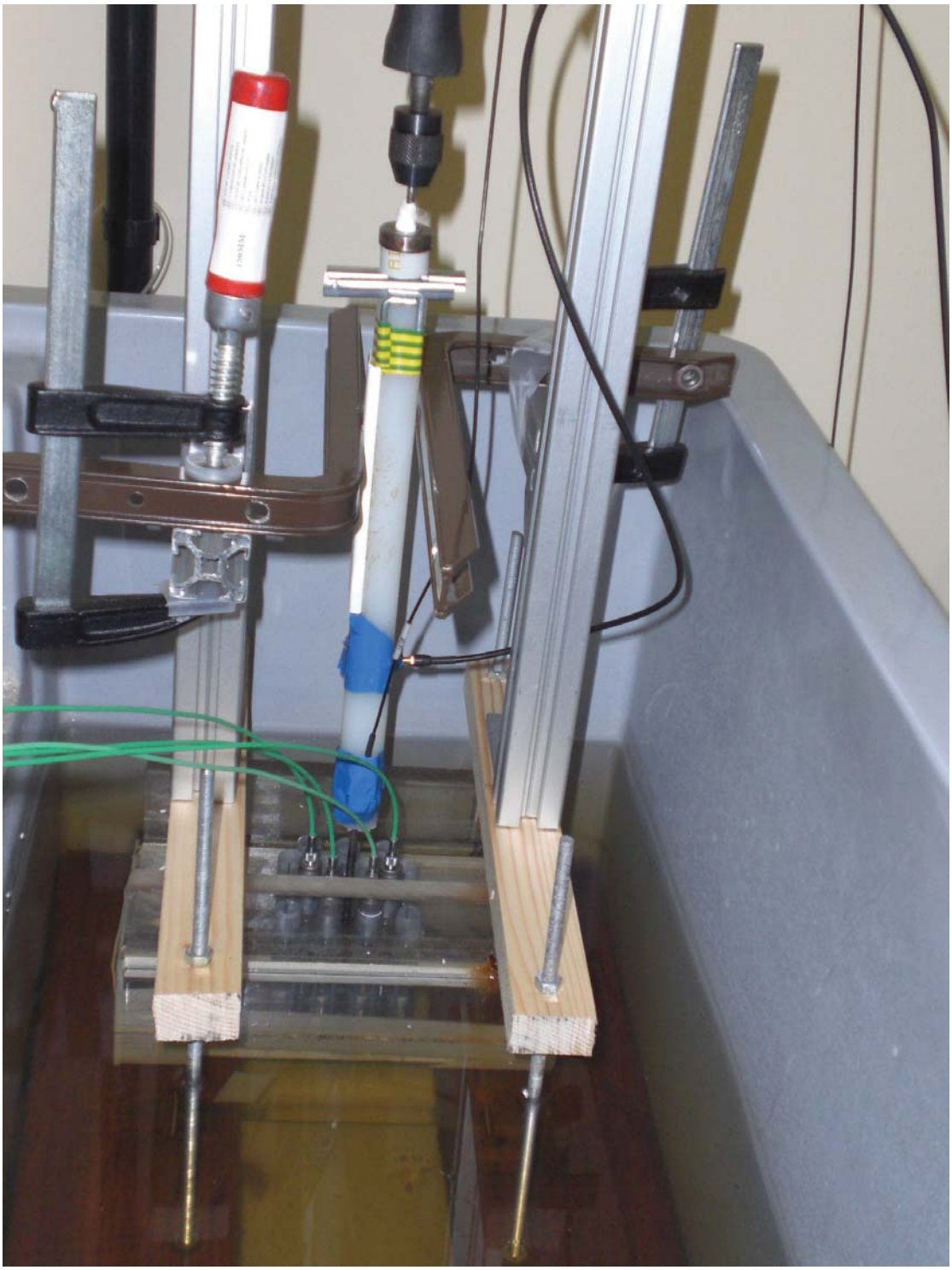

FIGURE A.16: Experimental setup with instrumentation.

A.1.4 Data acquisition

Six amplifiers were employed to recieve the pressure oscillations and the motion signals acquired with the transducers and the accelerometers. Also, the IMC software from FAMOUS was used to complete a just-in-time review of the results in every single test. Figs. A.17 and A.18 show photographs of the complete measurement chain in the laboratory, with the different devices and some of the typical results for a single frequency test processed with imc.

Temporal and spectral signals were collected in series of tests for increasing excitation frequencies, and later post-processes in order to correlate the pressure perturbations with the tube motion.

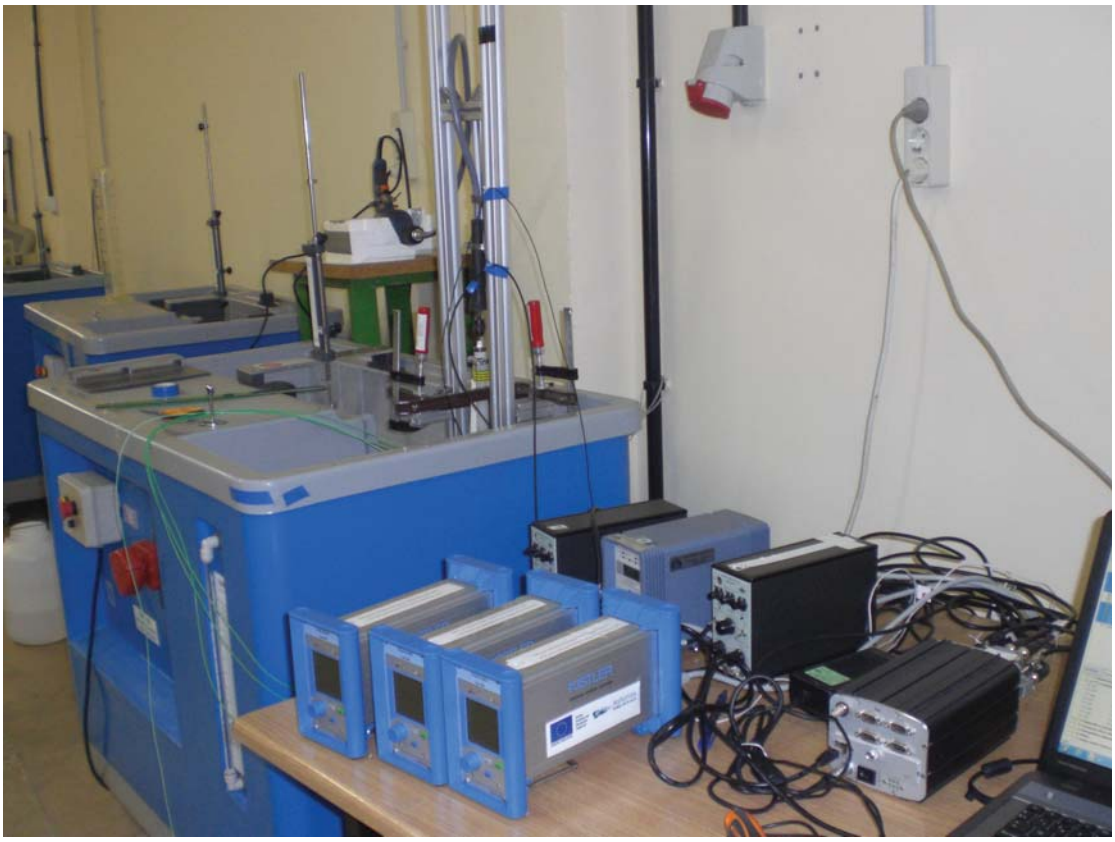

FIGURE A.17: Chain of laboratory devices for data acquisition.

FIGURE A.18: Typical results for a single frequency test processed with imc.

A.2 Preliminary test.

Data in time and frequency domains were analyzed in terms of amplitude of pressure perturbations and phase lag with respect to the tube motion. The tests were carried out for four different configurations, regarding the location of the four monitored points. For each configuration, series of tests was developed for five frequencies in the range of (10-25 Hz). In order to ensure the repeatability of the measurements, each series of tests was executed a second time in the same range of frequencies. The spectral signal reported by the transducers was then analyzed and correlated with spectral signal of the tube motion. The first four harmonics of the signals were then considered for postprocessing.

A.2.1 Configuration 1:

Fig. A.19 shows the location of the measurement points (red markers) in the first series of tests. In these measurements the neutral position (0 deg) of tubes T1 and T4 was monitored in the channel below the vibrating tube (see the figure), while the 0 deg locations of tubes T2 and T3 was monitoring in the channel above the vibrating cylinder. Figs. A.20 - A.23 show the results of this first series of tests. In these figures red and blue markers represent values obtained in the two different test campaigns, providing a reference of the repeatability obtained in these experimental measurements. As these tests were conducted under no flow conditions, pairs of points in tubes T1-T4 and T2-T3 are located in symmetric positions with respect to the tube motion. Consequently, they are expected to report the same results and their measurements are discussed together in the figures. Except for some minor dispersion in the results (specially regarding the higher harmonics) the tests reported reasonably good agreement comparing different experimental campaigns and equivalent positions in the geometry. Hence, it was considered that magnitude and specially tendency could be analyzed with this empirical methodology. As expected, both amplitude and phase increase with frequency, because tube velocity becomes more significant with respect to cross-flow velocity at higher frequencies. On the contrary, as frequency decreases both amplitude and phase tend to vanish because there is no vibration when the frequency is zero. Note that tubes T1 and T4 are representative of the channel above the vibrating tube, while T2 and T3 are located in the channel below, so their measurements are shifted 180°. As expected, amplitude of pressure perturbations is higher in tubes T2 and T3 than in tubes T1-T4, as they are closer to the source of perturbations. Regarding the trend in the phase lag, tubes T2 and T3 also have a lower increase rate (almost 0) than T1 and T4, because they account for closer curvilinear positions in the channel.

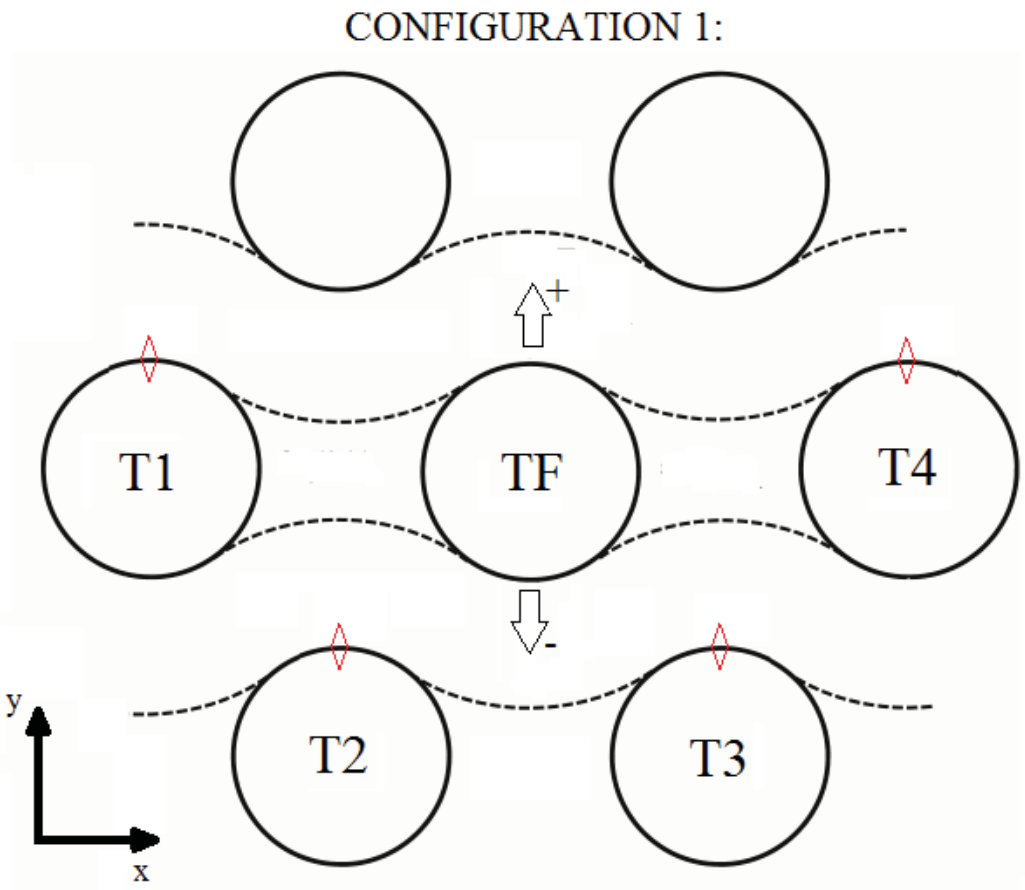

FIGURE A.19: Location of the measurement points in the first configuration.

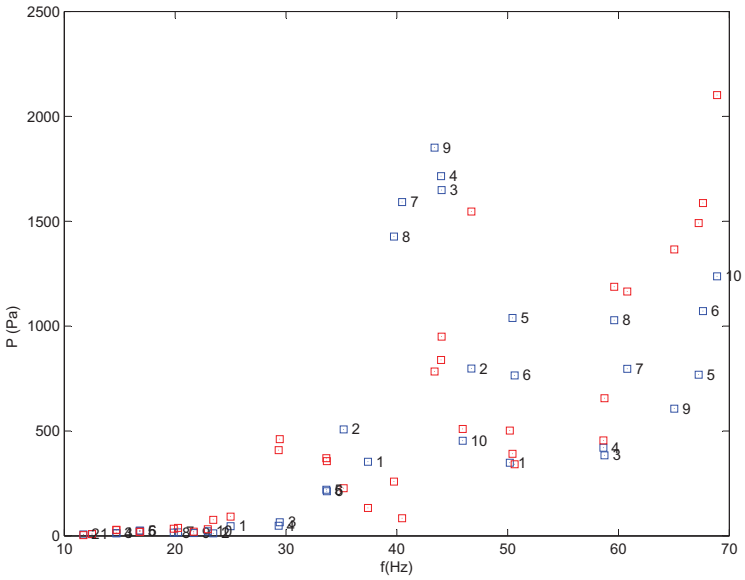

FIGURE A.20: Amplitude of vibration in tubes T1 and T4 in two series of tests (red and blue).

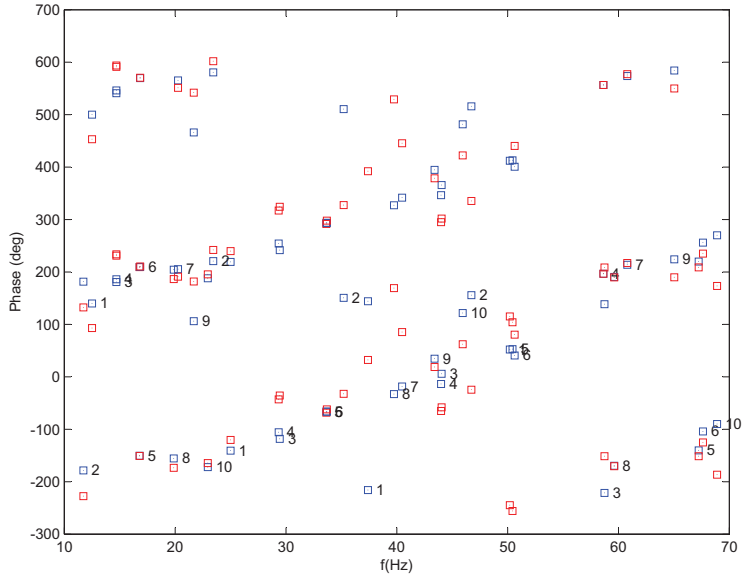

FIGURE A.21: Phase between tube motion and pressure fluctuations in tubes T1 and T4 in two series of tests (red and blue).

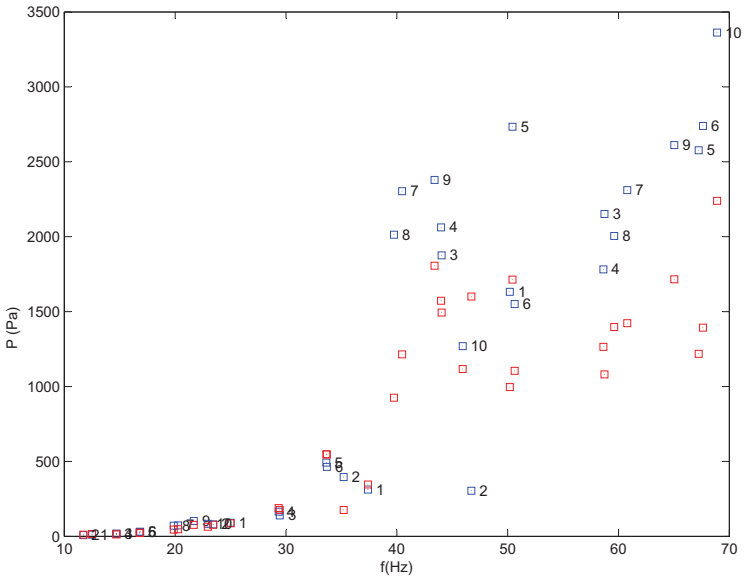

FIGURE A.22: Amplitude of vibration in tubes T2 and T3 in two series of tests (red and blue)

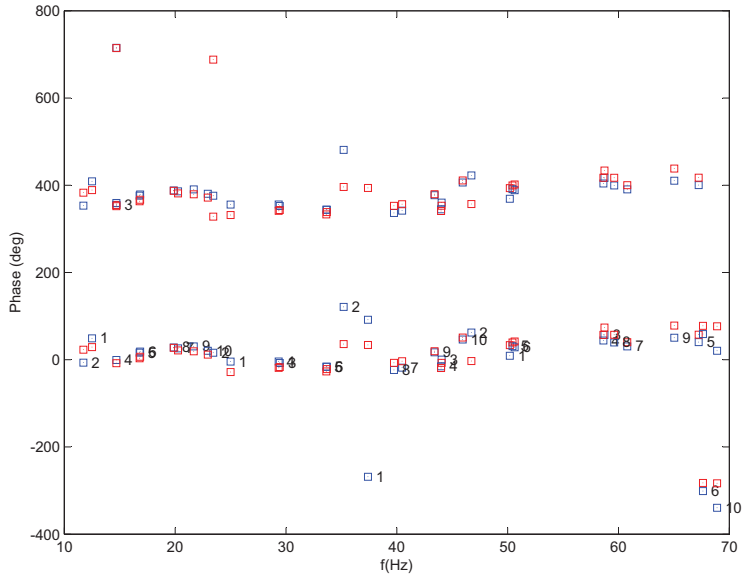

FIGURE A.23: Phase between tube motion and pressure fluctuations in tubes T2 and T3 in two series of tests (red and blue).

A.2.2 Configuration 2:

Fig. A.24 shows the location of the measurement points (green markers) in the second series of tests. In these measurements, the transducers in the the four tubes, T1, T2, T3 and T4 were monitoring their neutral position (0°) in the channel below the vibrating tube (see the figure).
Figs. A.25 - A.28 show the results of this second series of tests. Once again, red and blue markers represent values obtained in the two different test campaigns, providing a reference of the repeatability obtained in these experimental measurements. Also, tubes T1-T4 and T2-T3 are located in symmetric positions with respect to the tube motion so they report the same results and their measurements are discussed together in the figures. Some remarkable dispersion in the results was obtained, above 30 Hz, in these series of tests. However, magnitude and trend of amplitude and phase lag of flow perturbations is in reasonably good agreement with the previous experimental tests with configuration 1. Moreover, comparison between the two experimental campaigns and equivalent positions in the geometry reported satisfactory repeatability.
As expected, both amplitude and phase increased with the frequency, because tube velocity becomes more significant at higher frequencies with respect to cross-flow velocity (as discussed in previous section). Obviously, when frequency trend to 0 both amplitude and phase go to 0 as well. In these configuration, the four tubes are monitoring the same channel so there is no shift between the pair of tubes in the origin of phase lag lines. The increase rate of the phase lag in tubes T2 and T3 is again lower than in tubes T1 and T4 following the previous discussion. Regarding the amplitude, it was observed that an off-set appeared in the T2-T3 data. It was attributed to a progressive degradation of the vibrating mechanism setting during the experimental campaign. However, trend of amplitude and phase lag in the average data is in reasonably good agreement with the present experimental tests.

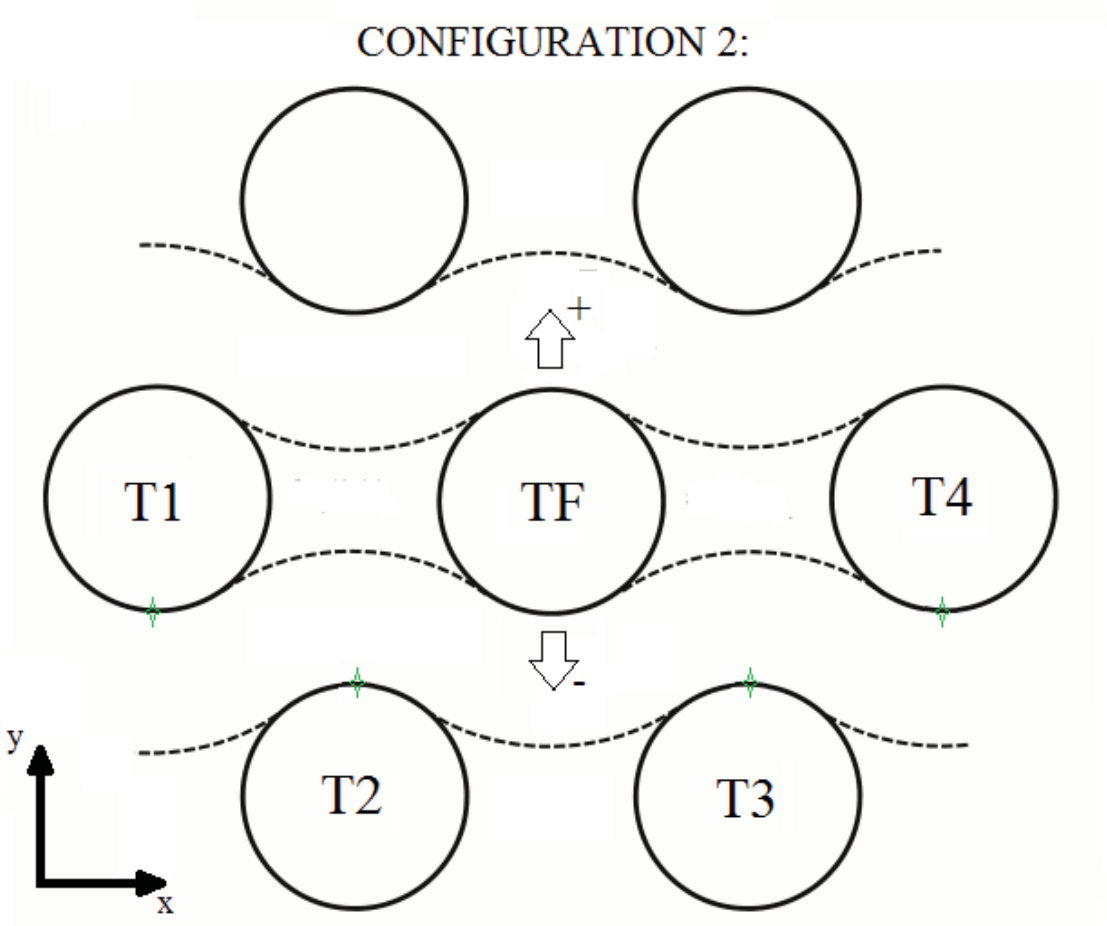

FIGURE A.24: Location of the measurement points in the second configuration.

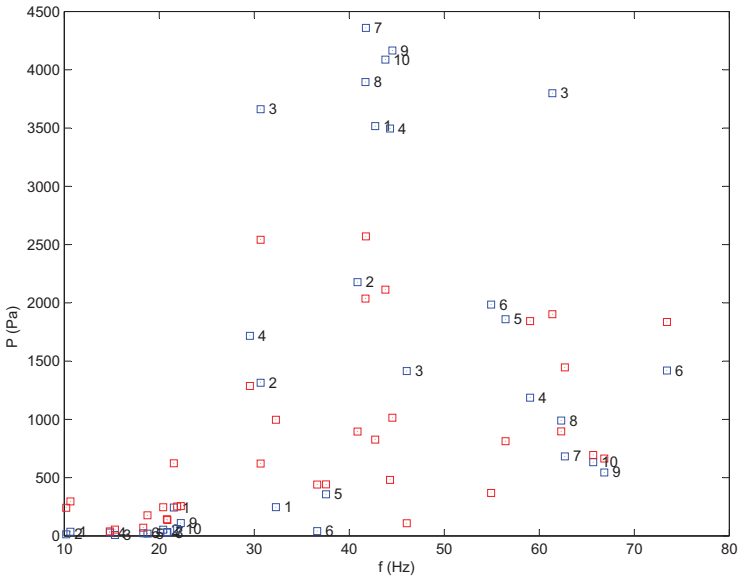

FIGURE A.25: Amplitude of vibration in tubes T1 and T4 in two series of tests (red and blue).

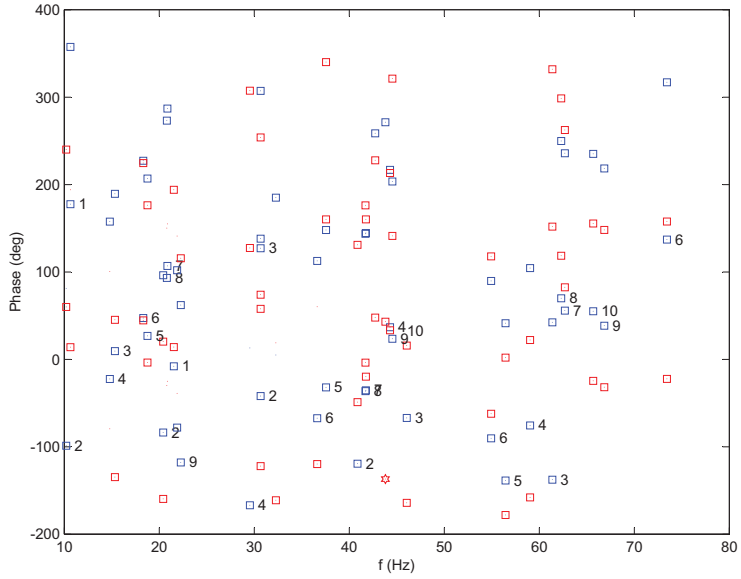

FIGURE A.26: Phase between tube motion and pressure fluctuations in tubes T1 and T4 in two series of tests (red and blue).

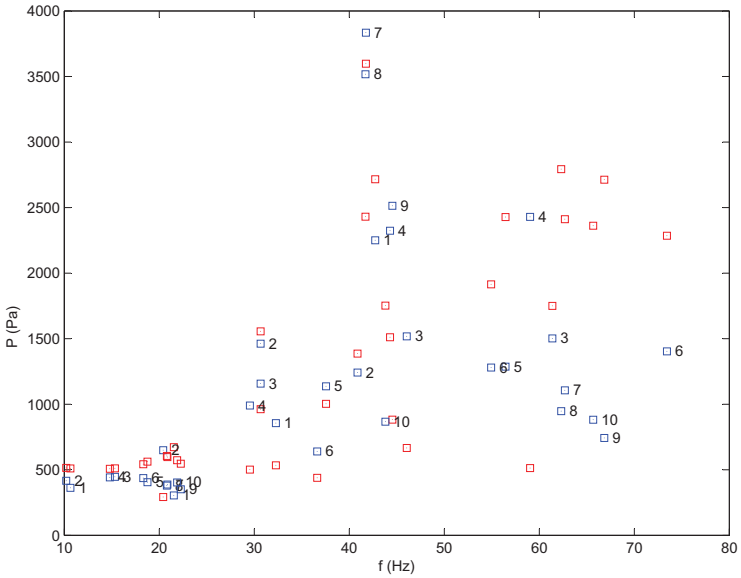

FIGURE A.27: Amplitude of vibration in tubes T2 and T3 in two series of tests (red and blue)

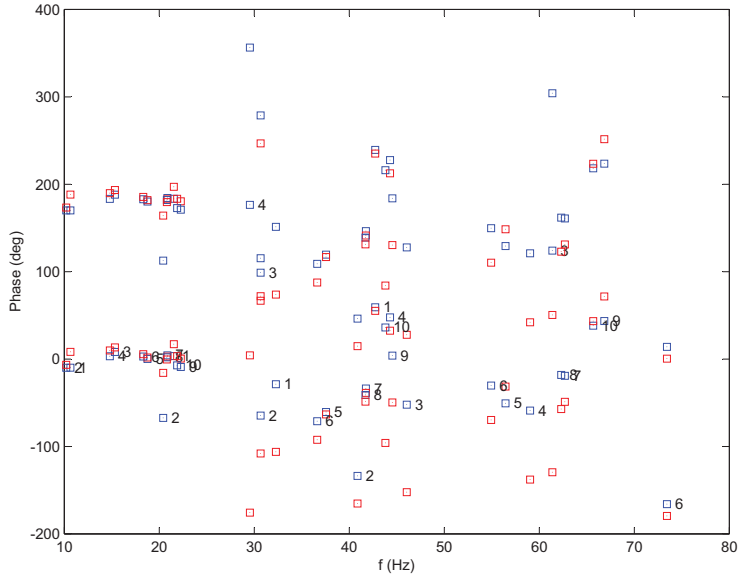

FIGURE A.28: Phase between tube motion and pressure fluctuations in tubes T2 and T3 in two series of tests (red and blue).

A.2.3 Configuration 3:

Fig. A.29 shows the location of the measurement points (purple markers) in the third series of tests. In these measurements tubes the four tubes, T1, T2, T3 and T4 were monitoring curvilinear positions 15° closer to the vibrating tube than the neutral point (0°).

Figs. A.30 - A.33 show the results of this second series of tests. Red and blue markers represent, as in previous sections, values obtained in the two different test campaigns. Again, couples of points located in symmetric positions with respect to the tube motion are discussed together in the figures (T1-T4 and T2-T3).

In these configuration the four tubes are monitoring the same channel so there is no shift between couples of tubes in the origin of phase lag lines. The set up in tubes T2 and T3 measurements was again obtained in these series of tests although it was found to be less significant due to a the improvement of the vibrating mechanism fixing. Otherwise no major differences were appreciated with respect to the previous configurations with the sensitivity reported by this experimental set up. Amplitude of pressure perturbations is higher in tubes T2 and T3 than in the couple T1-T4, and the increase rate of the phase lag in tubes T2 and T3 is again lower than in tubes T1 and T4.

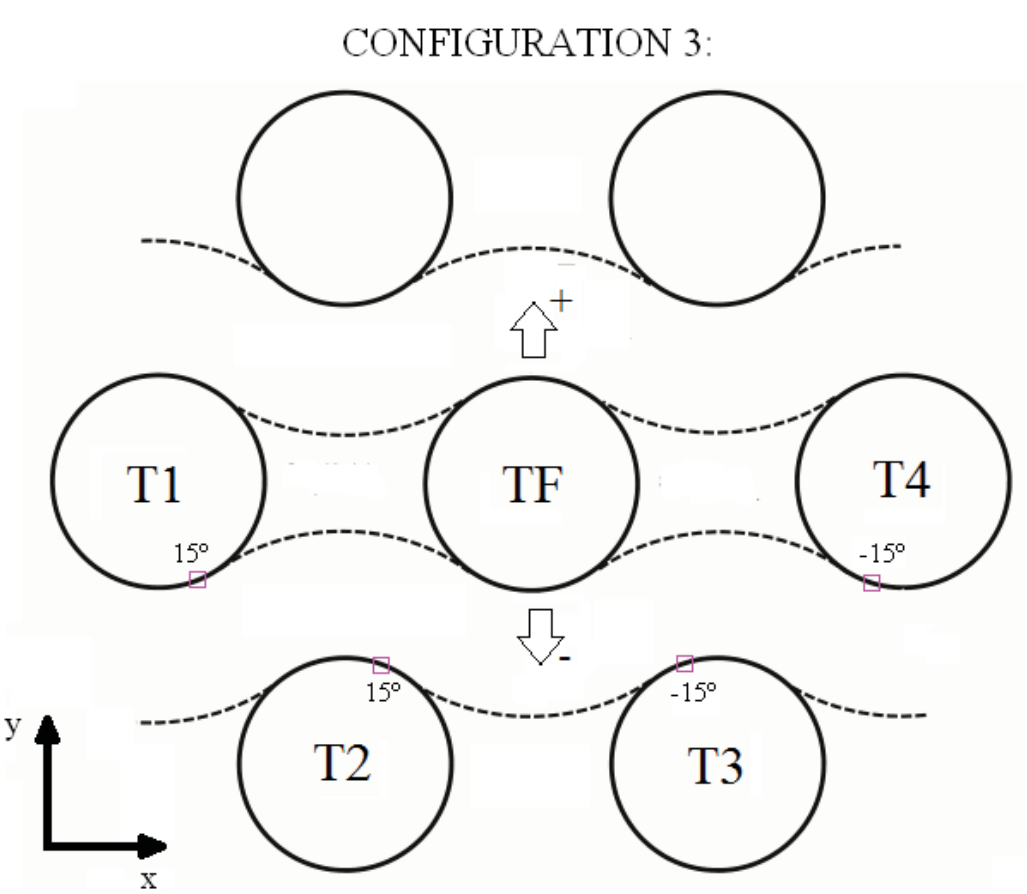

FIGURE A.29: Location of the measurement points in the third configuration.

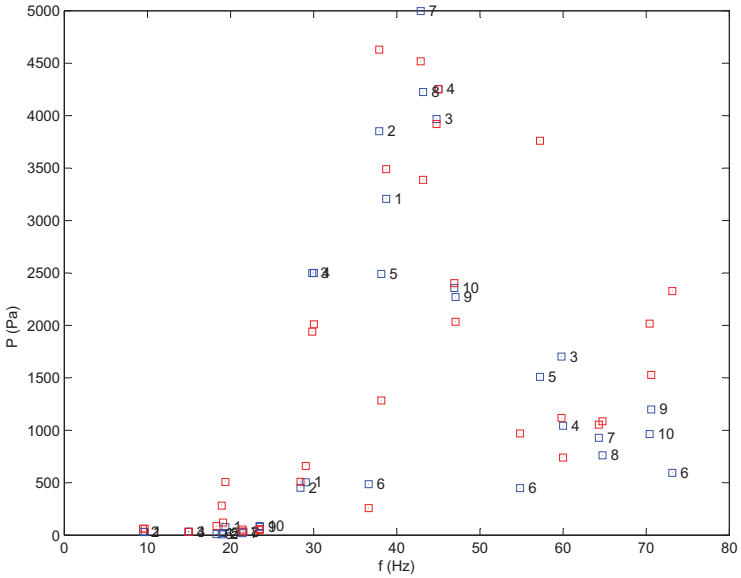

FIGURE A.30: Amplitude of vibration in tubes T1 and T4 in two series of tests (red and blue).

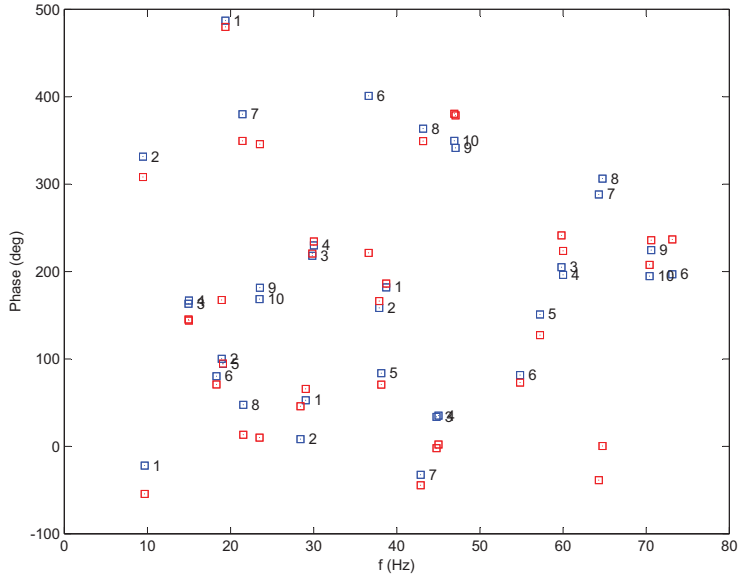

FIGURE A.31: Phase between tube motion and pressure fluctuations in tubes T1 and T4 in two series of tests (red and blue).

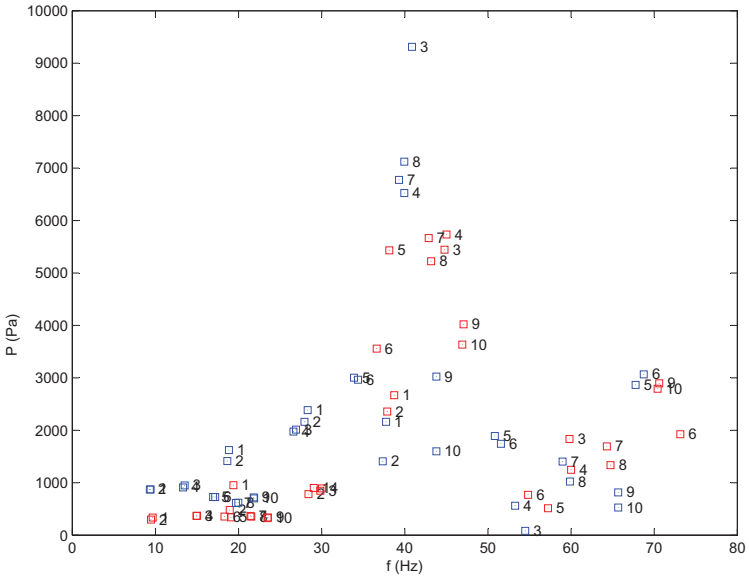

FIGURE A.32: Amplitude of vibration in tubes T2 and T3 in two series of tests (red and blue)

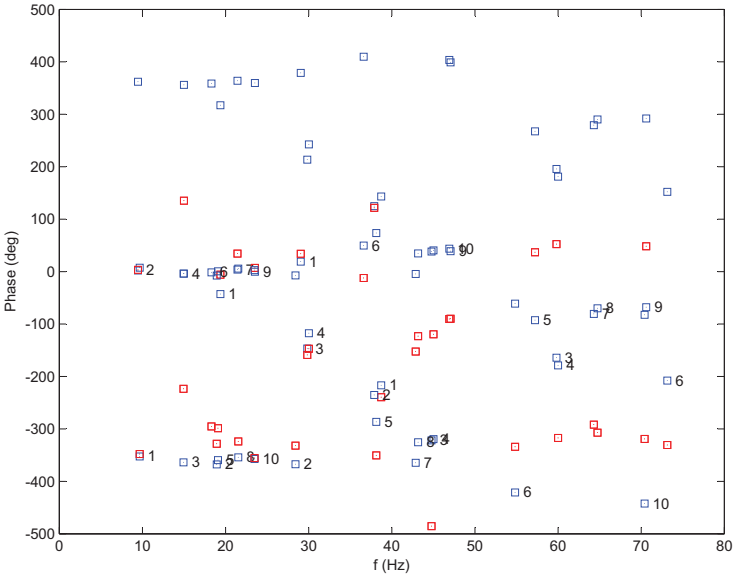

FIGURE A.33: Phase between tube motion and pressure fluctuations in tubes T2 and T3 in two series of tests (red and blue).

A.2.4 Configuration 4:

Fig. A.34 shows the location of the measurement points (blue markers) in the third series of tests. In these measurements the four tubes, T1, T2, T3 and T4 were monitoring curvilinear positions 15° far away from the vibrating tube than the neutral point (0°). Figs. A.35 - A.38 show the results of this second series of tests. Red and blue markers represent, as in previous sections, values obtained in the two different test campaigns. Again, couples of points located in symmetric positions with respect to the tube motion are discussed together in the figures (T1-T4 and T2-T3).
In these configuration the four tubes are monitoring the same channel so there is no shift between couples of tubes in the origin of phase lag lines. The set up in tubes T2 and T3 measurements was corrected in these series of tests by means of an improvement of the vibrating mechanism fixing. Otherwise no relevant differences were appreciated with respect to the previous configurations with the sensitivity reported by this experimental set up. Amplitude of pressure perturbations is higher in tubes T2 and T3 than in T1-T4, and the increase rate of the phase lag in tubes T2 and T3 is again lower than in tubes T1 and T4.

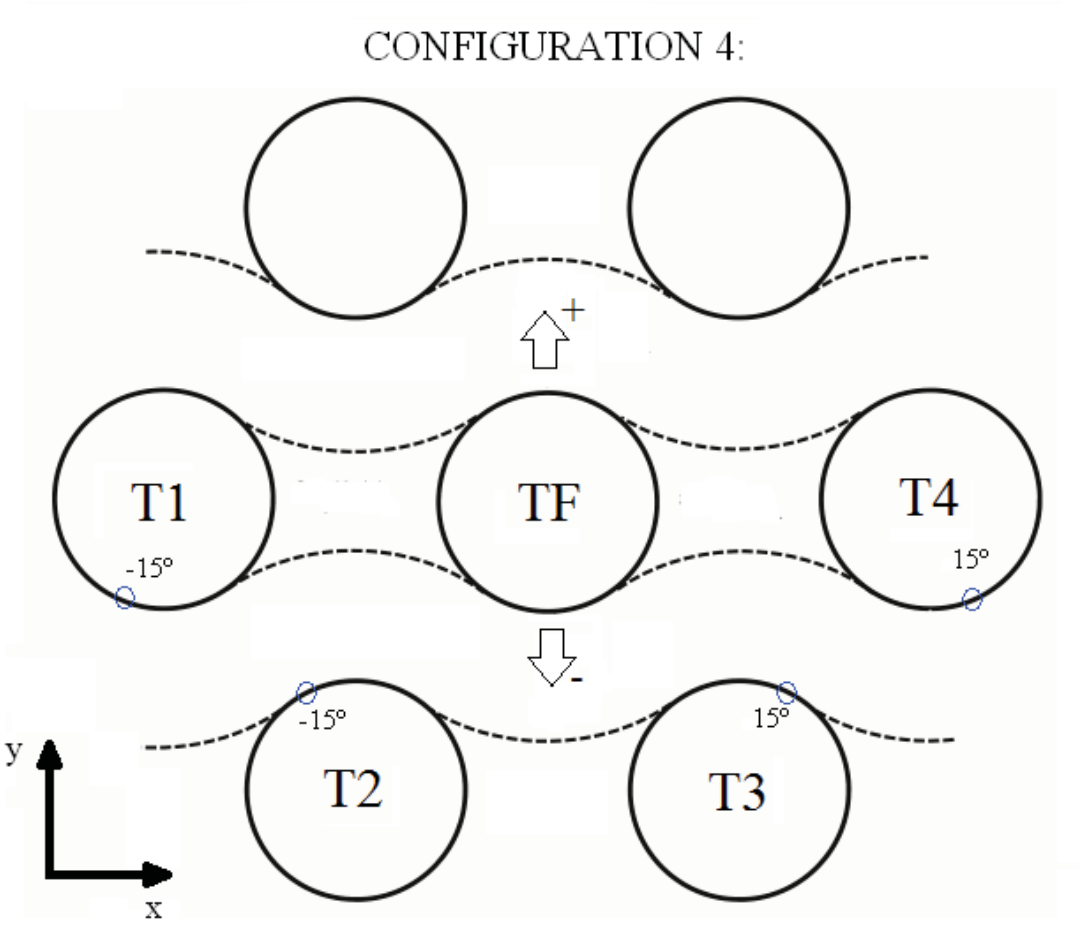

FIGURE A.34: Location of the measurement points in the fourth configuration.

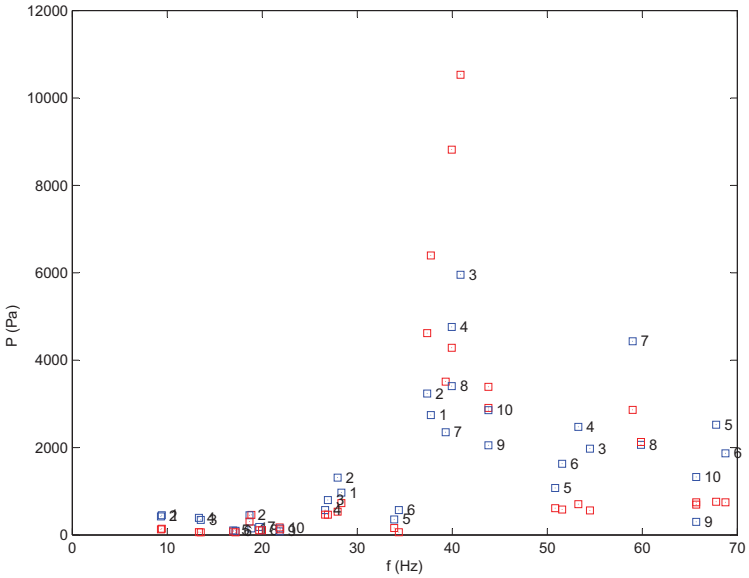

FIGURE A.35: Amplitude of vibration in tubes T1 and T4 in two series of tests (red and blue).

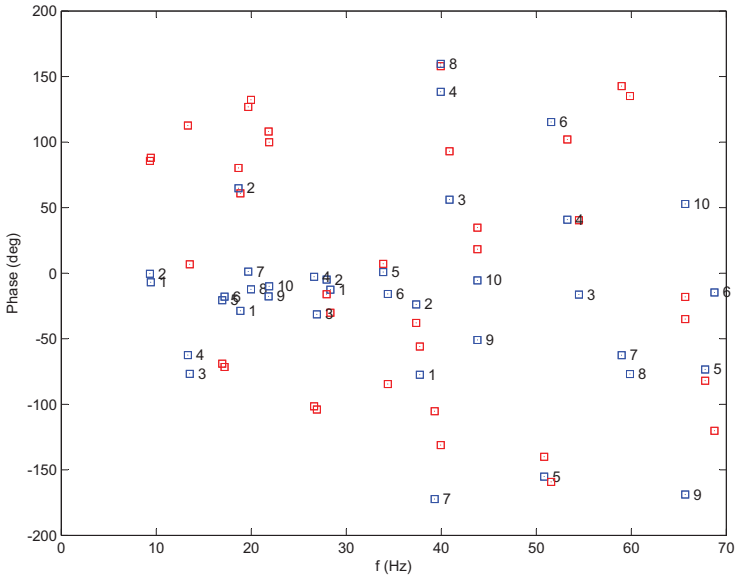

FIGURE A.36: Phase between tube motion and pressure fluctuations in tubes T1 and T4 in two series of tests (red and blue).

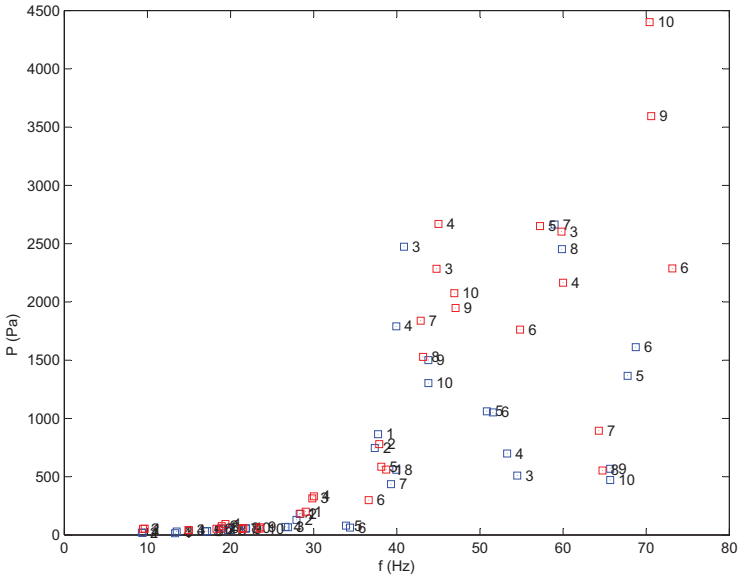

FIGURE A.37: Amplitude of vibration in tubes T2 and T3 in two series of tests (red and blue)

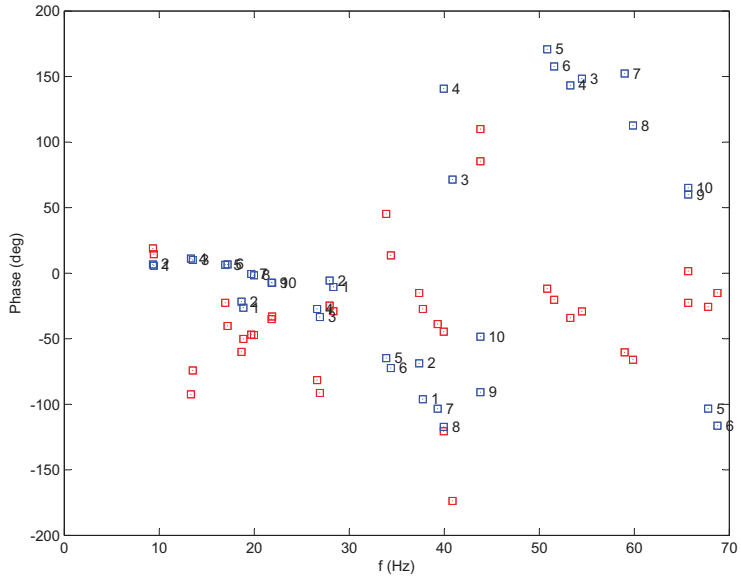

FIGURE A.38: Phase between tube motion and pressure fluctuations in tubes T2 and T3 in two series of tests (red and blue).

.

Appendix B

Quasi-unsteady model + CFD details

B.1 Solving for the critical velocity

Substituting the expression based on the quasi-unsteady model for the fluid elastic force (Eq. 2) into the equation of motion (Eq. 1), and taking the Laplace transformation after normalizing with the mass, it yields:

$$^2 + 2\ _o\ + 1 + \frac{1}{2m_r}\left[C_D U_r\ - \frac{C_L}{}U_r^2\left(1 - \frac{}{+\ U_r}\right)\right] = 0\ , \tag{B.1}$$

where,

$$= - \quad + \quad \sqrt{(1 - \ ^2)} \tag{B.2}$$

is the frequency of vibration of the coupled system.

The characteristic equation of the system is

$$\sum_{i=0}^{4}\ _i\ ^i = 0\ , \tag{B.3}$$

The coefficients $_i$ are polynomials of U_r. For convenience, the coefficients of these polynomials can be designated as $_{ij}$ where is the power of and is the power of U_r and are defined in Eqs. (B.5-B.8).

$$_4 = 1 \tag{B.4}$$

$$\begin{aligned} {}_3 &= \left(\quad + \frac{C_D}{2m_r} \right) U_r + 2 \ {}_0 \\ &= \ {}_{31} U_r + \ {}_{30} \end{aligned} \tag{B.5}$$

$$\begin{aligned} {}_2 &= \left[\frac{\beta}{2m_r} C_D + \frac{\alpha - 1}{2m_r} \frac{\partial C_L}{\partial y} \right] U_r^2 + 2 \quad {}_o U_r + 1 \\ &= \ {}_{22} U_r^2 + \ {}_{21} U_r + 1 \end{aligned} \tag{B.6}$$

$$\begin{aligned} {}_1 &= \frac{-\beta}{2m_r} \frac{\partial C_L}{\partial y} U_r^3 \ \ U_r \\ &= \ {}_{13} U_r^3 + \ {}_{11} U_r \end{aligned} \tag{B.7}$$

$$ {}_0 = 0 \tag{B.8}$$

At the fluidelastic threshold the net damping is zero (i.e. $\quad = 0$). Thus the value of the Laplace variable $\quad$ is

$$= \tag{B.9}$$

Substituting this into the characteristic equation (B.3) and balancing the complex part yields

$$- \ {}_3 \ {}^3 + \ {}_1 \quad = 0 \tag{B.10}$$

$$\Rightarrow \quad {}^2 = \frac{1}{3} \tag{B.11}$$

The real part of the characteristic equation yields an alternative estimate of $\quad$ at the threshold condition

$${}^2 = \frac{4}{2} \tag{B.12}$$

Equating, these two expressions eliminates $\quad$:

$$ {}_4 \ {}_1 - \ {}_2 \ {}_3 = 0 \tag{B.13}$$

The critical flow velocity U_{rc} is the reduced flow velocity, U_r, at the onset of instability, thus the functions $\quad {}_i$ in this equation are polynomials of the critical flow velocity. Substituting Eqs. (B.4-B.8) and after some manipulation, it yields a fifth-order polynomial in U_{rc},

$$\sum_{i=0}^{5} \ {}_i U_{cr}^i = 0 \ , \tag{B.14}$$

where the coefficients $_i$ are

$$\begin{aligned}
_5 &= - \ _{13} \ _{22} \ _{31} + \ _{13}{}^2 \\
_4 &= - \ _{13} \ _{21} \ _{31} - \ _{13} \ _{22} \ _{30} + 2 \ _{04} \ _{30} \ _{31} \\
_3 &= -2 \ _{11} \ _{13} - \ _{13} \ _{21} \ _{30} - \ _{11} \ _{22} \ _{31} - \ _{13} \ _{31} \\
_2 &= 2 \ _{11} \ _{12} - \ _{13} \ _{30} - \ _{11} \ _{22} \ _{30} - \ _{11} \ _{21} \ _{31} \\
_1 &= - \ _{11} \ _{21} \ _{30} + \ _{11}{}^2 - \ _{11} \ _{31} \\
_0 &= - \ _{11} \ _{20} \ _{30}
\end{aligned} \tag{B.15}$$

The terms of these polynomials, $_{ij}$ defined above in Eqs.(B.4-B.8), depend on: the steady flow force coefficients C_D and $\frac{\partial C_L}{\partial y}$; the memory function parameters and ; and the structural parameters $_0$ and m_r.

B.2 CFD Force coefficients obtained in steady simulations

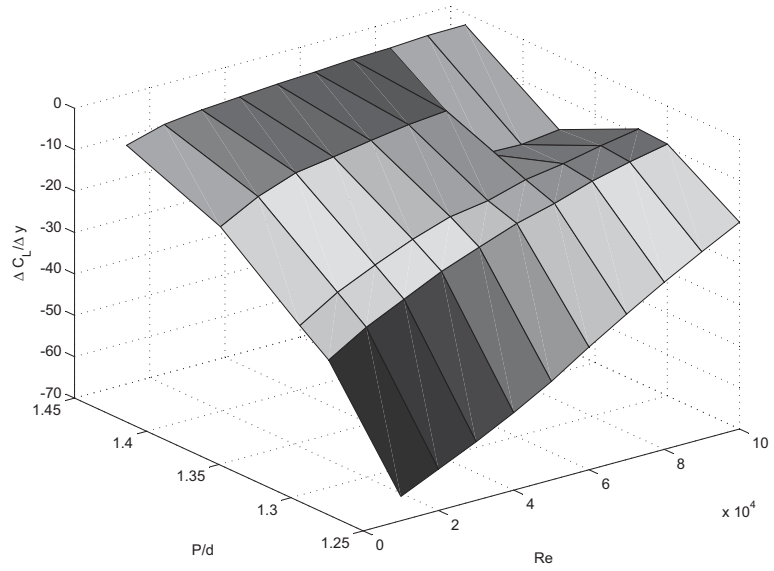

FIGURE B.1: Lift force coefficient gradient as a function of the Reynolds number and the Pitch ratio.

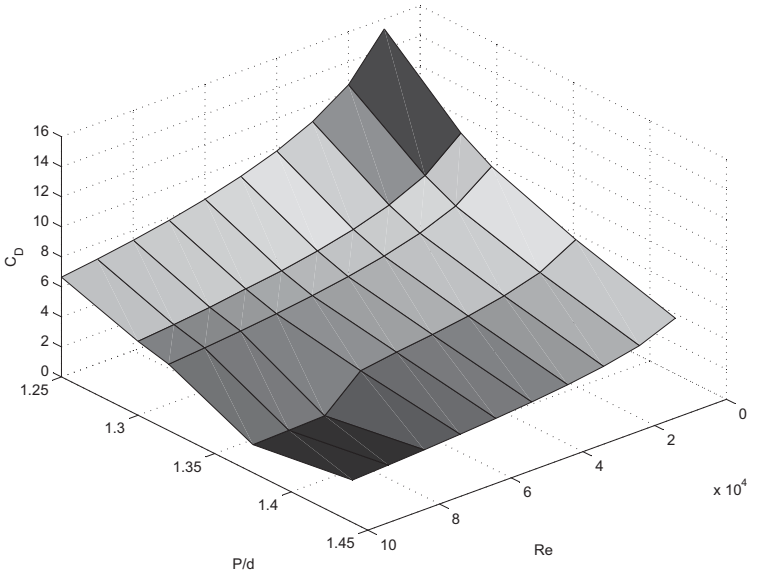

FIGURE B.2: Drag force coefficient as a function of the Reynolds number and the Pitch ratio.

B.3 Effect of complementary parameters

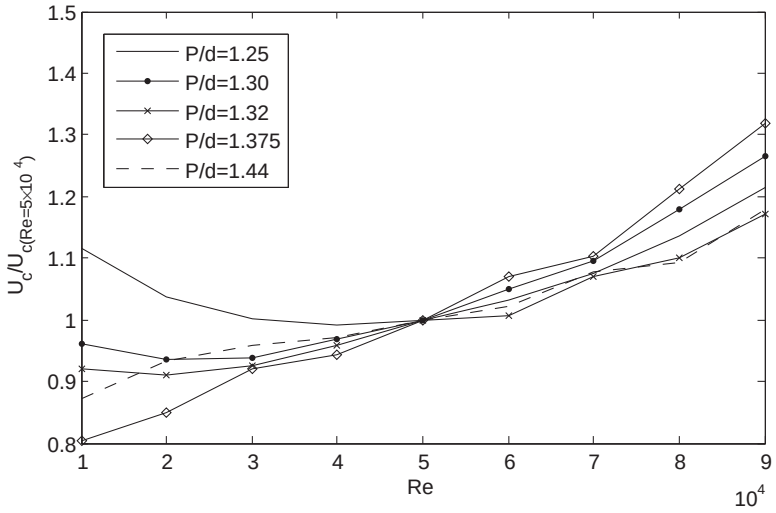

FIGURE B.3: Critical velocity Reynolds number curves for different P/d arrays.

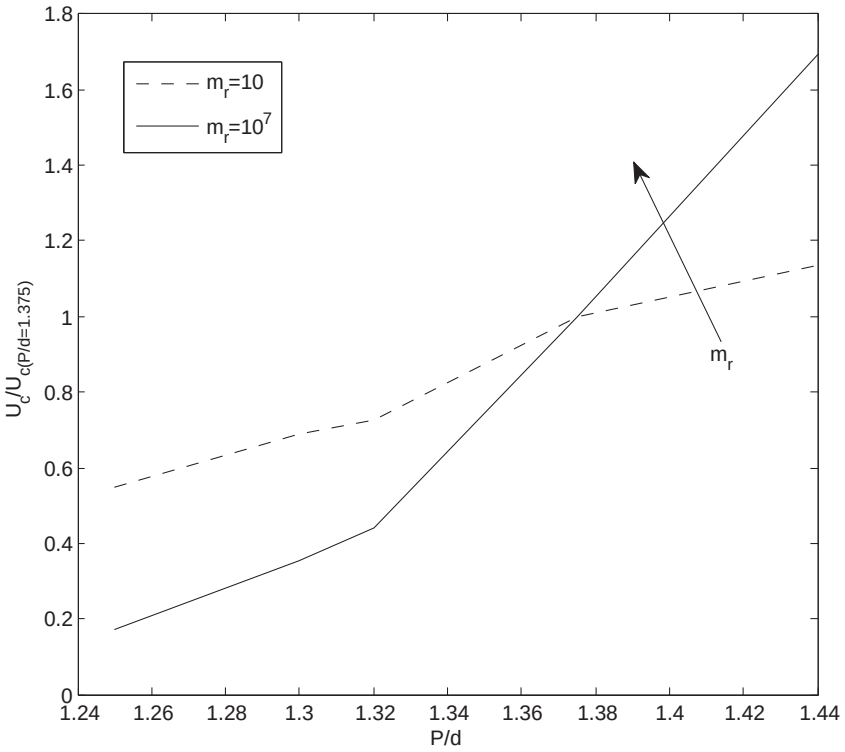

FIGURE B.4: Critical velocity Pitch ratio curves for different m_r.

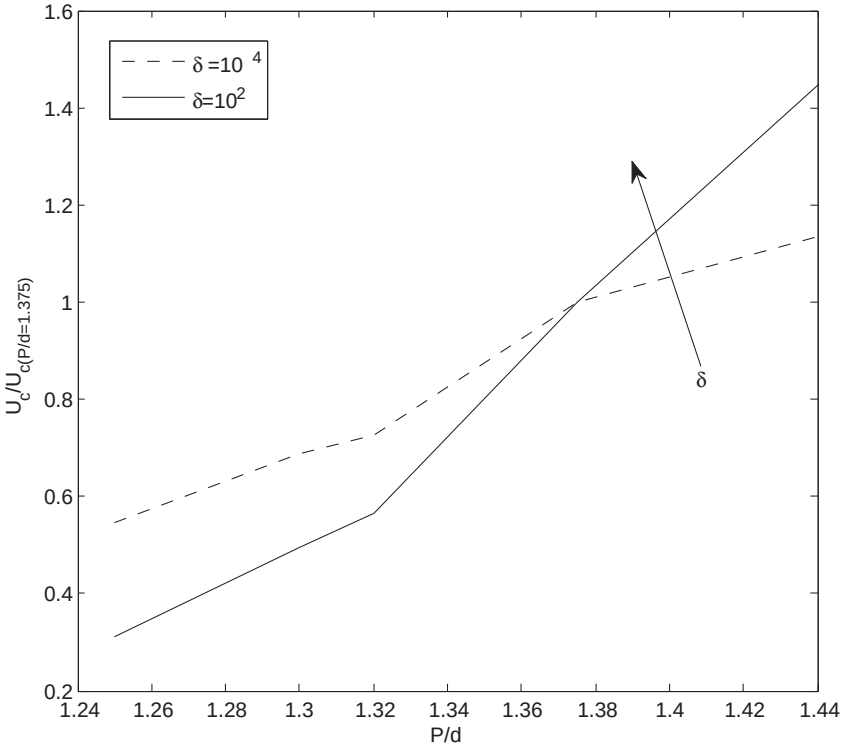

FIGURE B.5: Critical velocity Pitch ratio curves for different δ.

Appendix C

Source codes

C.1 Source code for the dynamic mesh

C.1.1 Forced vibrations

```
# include "udf.h"


DEFINE CG MOTION(tubo, dt, cg_v l,    _om    ,   m  ,d  m  )
{


real freq = f_n;
   l  m  =   ;
   ld   f     = Φ;


real omega;
real vel;


omega= 2.0*M_P  * f    ;
  l =  m  *  m    *    ( m    *  m  + d   f    );


cg_v  l[0] = 0 0;
   _v  l[1] =    l; / *  -   l      * /
   _v  l[2] = 0 0;
```

NV $_S$($_o m$,=,0 0); / * l m * /

DEFINE CG MOTION(capalimite, dt2, cg $_v$ $l2$, $_o m$ 2, m ,d m)
{

real freq = f;
real amp = A;
real desfase = 0;

real omega2;
real vel2;

omega2= 2.0*M $_P$ * f ;
$l2$ = m * m 2 * (m 2 * m + d f);

cg $_v$ $l2$[0] = 0 0;
$_v$ $l2$[1] = $l2$; / * − l * /
$_v$ $l2$[2] = 0 0;

NV $_S$($_o m$ 2,=,0 0);

C.1.2 Self-excited vibration

include ”udf.h”

static real vx = 0.0;
static real vy = 0.0;
static real vx_prev1 = 0.0;
static real vy_prev1 = 0.0;
static real vx_prev2 = 0.0;

```
static real vy_prev2 = 0.0;


DEFINE CG MOTION(fiv,dt,cg_vel,cg_omega,time,dtime)
Thread *t;
face_t f;


real NV_VEC(A);
real NV_VEC(cg_x);
real NV_VEC(force);
real NV_VEC(dv);
int i;
real rho = ρ;
real rext =  _e;
real rint =  _i;
real fn = f_n; /
real delta = δ;


real m = rho*M*(rext*rext-rint*rint);
real wn = 2*M*fn;
real psi = delta/(2*M);
real c = 2*m*wn*psi;
real k = m*wn*wn;

NV_S(cg_vel, =, 0.0);
NV_S(cg_omega, =, 0.0);


t = DT_THREAD(dt);


for (i=0; i2; i++)
cg_x[i] = DT_CG(dt)[i];
NV_S(force, =, 0.0);
begin_f_loop(f,t)

F_AREA(A,f,t);
force[0] = force[0] +F_P(f,t)*A[0] +F_STORAGE_R_N3V(f,t,SV_WALL_SHEAR)[0];
force[1] = force[1] +F_P(f,t)*A[1] +F_STORAGE_R_N3V(f,t,SV_WALL_SHEAR)[1];
```

```
end_f_loop(f,t)


dv = (force - cv -kx)*dt/m
for (i=0;
i2;
i++)

force[i] = force[i] - c*cg_vel[i] - k*cg_x[i];
dv[i] = dtime * force[i]/m;

vx_prev1 = 0;
vy_prev1 = vy;
vx = 0;
vy = (2*dv[1]+4*vy-vy_prev2)/3;
vx_prev2 = 0;
vy_prev2 = vy_prev1;


/* Actualizamos la velocidad para el cg_vel del dynamic mesh */
cg_vel[0] = vx;
cg_vel[1] = vy;


Message("Computed force: fx= %g, fy= %g ",force[0], force[1]);
Message("Computed velocity: vx= %g, vy= %g ",cg_vel[0], cg_vel[1]);
Message("Computed position: x= %g, y= %g ",cg_x[0], cg_x[1]);

DEFINE CG MOTION(capalimite,dt2,cg_vel2,cg_omega2,time,dtime)

Thread *t2;
face_t f2;
real NV_VEC(cg_x2);
real NV_VEC(dv2);
int i;
NV_S(cg_vel2, =, 0.0);
NV_S(cg_omega2, =, 0.0);
```

```
t2 = DT_THREAD(dt2);


for (i=0; i2; i++) cg_x2[i] = DT_CG(dt2)[i]; cg_vel2[0] = vx;
cg_vel2[1] = vy;


Message("Computed velocity: vx= %g, vy= %g ",cg_vel2[0], cg_vel2[1]);
Message("Computed position: x= %g, y= %g ",cg_x2[0], cg_x2[1]);
```

C.2 Source code for the postprocess of the experimental signals

Main code

```
%postproceso
factor = [f1 f2 f3 f4 f5 f6];
directorio='E:0';
apellido='*spec.ASC';
nombre=[directorio apellido];
list=dir(nombre)
nombre=[directorio 'resultados.txt'];
delete(nombre);
for k = 1:size(list,1)
% for k = 1:135
datos=importdata (list(k).name,' ',1);
%resultados(datos.data,5,list(k).name);
resultados(datos.data,5,nombre,k,factor);
end
datos= load (nombre);
for k = 1:size(datos,1)
for l = 1:6
if datos(k,1+2*l)0
datos(k,1+2*l)=datos(k,1+2*l)+360;
end
end
end
```

```
s1=8;
s2=12;
for k = 1:size(datos,1)
if datos(k,1)75
plot (datos(k,1),datos(k,s1),':squarer')
hold on
text(datos(k,1),datos(k,s1),[' ' num2str(datos(k,14))])
plot (datos(k,1),datos(k,s2),':squarer')
end
end
figure


for k = 1:size(datos,1)
if datos(k,1)75
plot (datos(k,1),-datos(k,s1+1)+360+180,':squarer')
hold on
text(datos(k,1),-datos(k,s1+1)+360+180,[' ' num2str(datos(k,14))])
plot (datos(k,1),-datos(k,s2+1)+360+180,':squarer')
plot (datos(k,1),-datos(k,s1+1)+2*360+180,':squarer')
plot (datos(k,1),-datos(k,s2+1)+2*360+180,':squarer')
end
end
```

Function *resultados*

```
function [res]=resultados(coeficiente,finicial,nombrearch,referencia,factor)
f=coeficiente(1:size(coeficiente,1),1);
s1=coeficiente(1:size(coeficiente,1),2);
res = zeros(4,14);
i=2;
while (isize(f,1))(f(i)finicial)
i=i+1;
end
if i==size(f,1)
str = [ 'ERROR: f inicial = ' , num2str(fincial),'  fmax =',num2str(f(size(f,1)))]
else
n=i;
s1max=s1(i);
while i=((size(f,1))-1)
if s1(i)
```

```
¿s1max
s1max=s1(i);
n=i;
end
i=i+1;
end
%for p = 1:6
%factor(p)=1;
%end
for ifr = 1:4
in=ifr*n;
if ifr
¿1
s1max = s1(in-5);
p=in-5;
for im = (in-6):(in+5)
if s1(im)
¿s1max
s1max=s1(im);
p=im;
end
end
in=p;
end


if insize(coeficiente,1)
res (ifr,1)=f(in);
for is = 1:6
res(ifr,(is-1)*2+2)= coeficiente(in,(is-1)*3+2)*factor(is);
res(ifr,(is-1)*2+3)= coeficiente(in,(is-1)*3+3)-(coeficiente(in,3)-360);
end
for is = 3:6
%res(ifr,(is-1)*2+2)= res(ifr,(is-1)*2+2)/res(ifr,2);
res(ifr,(is-1)*2+2)= res(ifr,(is-1)*2+2)/((((res(ifr,2))^2) + ((    ( f ,4))^2))^(1/2));
  d
  ( f ,14) =   f          ;
  d
  d
```

d

(m ,′ ′,′ − $d′$,′ − ′,′ − ′)

Publications

- ”CFD Modelling of the Cross-Flow through Normal Triangular Tube Arrays with one Tube Undergoing Forced Vibrations or Fluidelastic Instability.”. Beatriz de Pedro , Jorge Parrondo, Craig Meskell and Jesús Fernández Oro. Journal of Fluids and Structures, 2016.

- “CFD study on the Propagation of Disturbances in the Flow Through a Parallel Triangular Array with One Oscillating Tube”. Beatriz de Pedro, Jorge Parrondo, Jesús Fernández Oro and Eduardo Blanco. In Proceedings of the 11th International Conference on Flow-Induced Vibration - FIV 2016. The Hague, Nederland.

- “Investigation of the Effect of Mass Ratio and Reynolds Number on Damping Controlled Fluidoelastic Instability”. Beatriz de Pedro and Craig Meskell. In Proceedings of the 11th International Conference on Flow-Induced Vibration - FIV 2016. The Hague, Nederland.

- ”Fluidelastic Instability in a Parallel Triangular Tube Array. Dynamic CFD and Experimental Study”. Beatriz de Pedro, Jesús Fernández Oro, Eduardo Blanco and Jorge Parrondo. International congress on Water, Waste and Energy Management (WWEM). Oporto, 2014.

- “Acoustic Characteristics of a Hydraulic Pump and Noise Reduction due to Pump-Circuit Interaction”. Jens Keller, Raúl Barrio, Eduardo Blanco, Beatriz de Pedro and Jorge Parrondo. International Congress on WWEM. Oporto, 2014.

- ”Stable and Unstable Behavior of Cylinder Arrays Subject to Cross-Flow from CFD Simulations”. Beatriz de Pedro , Jesús Fernández Oro and Jorge Parrondo. WWEM. Lisboa , 2013.

- ”Flow Kinetic Energy Conversion from Vibration of Cylinder Arrays Due to Fluidelastic Instability”. Beatriz de Pedro, Jesús Fernández Oro and Jorge Parrondo. Internatonal congress on WWEM. Salamanca, 2012.//